

From supernovae to galaxy clusters

Observing the chemical enrichment in the hot
intra-cluster medium

François Mernier

ISBN: 978-94-6233-622-3

© 2017 François Mernier

From supernovae to galaxy clusters, Observing the chemical enrichment in the hot intra-cluster medium, Thesis, Universiteit Leiden

This work was supported by Leiden Observatory and SRON Netherlands Institute for Space Research.

Cover: Composite image of the Phoenix cluster (Credit: NASA / CXC / MIT / STScI). The X-ray emission (blue) shows the hot intra-cluster medium, while the cluster galaxies and star-forming filaments can be seen in optical (yellow and red). The front image shows an artist impression of the *XMM-Newton* satellite (Credit: ESA), together with metal lines derived from EPIC X-ray spectra (see Chapter 3 and summary).

From supernovae to galaxy clusters

Observing the chemical enrichment in the hot
intra-cluster medium

Proefschrift

ter verkrijging van
de graad van Doctor aan de Universiteit Leiden,
op gezag van Rector Magnificus prof.mr. C.J.J.M. Stolker,
volgens besluit van het College voor Promoties
te verdedigen op woensdag 31 mei 2017
klokke 13.45 uur

door

François Denis Marin Mernier

geboren te Ukkel (Brussel), België
in 1989

Promotiecommissie

Promotor: Prof. dr. Jelle S. Kaastra
Co-promotor: Dr. Jelle de Plaa

Overige leden: Prof. dr. M. Franx
Prof. dr. H.J.A. Röttgering
Prof. dr. J. Schaye
Dr. A. Simionescu (ISAS, JAXA, Sagamihara, Japan)
Dr. J. Vink (Universiteit van Amsterdam)

À mes parents

Contents

1	Introduction	1
1.1	The stellar nucleosynthesis: a brief history...	2
1.2	The role of Type Ia and core-collapse supernovae	3
1.2.1	Core-collapse supernovae (SNcc)	5
1.2.2	Type Ia supernova (SNIa)	6
1.3	Metals in clusters of galaxies	8
1.3.1	The legacy of past X-ray missions	10
1.3.2	The recent generation of X-ray missions	12
1.3.3	Constraining supernovae models by looking at the intra-cluster medium	13
1.3.4	Stellar and intra-cluster phases of metals	16
1.3.5	Where and when was the ICM chemically enriched?	17
1.4	Spectral codes for a collisional ionisation equilibrium plasma	20
1.5	This thesis	21
2	Abundance and temperature distributions in the hot intra-cluster gas of Abell 4059	25
2.1	Introduction	26
2.2	Observations and data reduction	28
2.2.1	EPIC	28
2.2.2	RGS	31
2.3	Spectral models	32
2.3.1	The <code>cie</code> model	32
2.3.2	The <code>gdem</code> model	33
2.3.3	Cluster emission and background modelling	33
2.4	Cluster core	34

2.4.1	EPIC	34
2.4.2	RGS	40
2.5	EPIC radial profiles	41
2.6	Temperature, σ_T , and Fe abundance maps	48
2.7	Discussion	52
2.7.1	Abundance uncertainties and SNe yields	52
2.7.2	Abundance radial profiles	55
2.7.3	Temperature structures and asymmetries	57
2.8	Conclusions	60
2.A	Detailed data reduction	63
2.A.1	GTI filtering	63
2.A.2	Resolved point sources excision	63
2.A.3	RGS spectral broadening correction from MOS 1 image	64
2.B	EPIC background modelling	65
2.B.1	Hard particle background	65
2.B.2	Unresolved point sources	67
2.B.3	Local Hot Bubble and Galactic thermal emission . . .	69
2.B.4	Residual soft-proton component	69
2.B.5	Application to our datasets	69
2.C	S/N requirement for the maps	72
3	Origin of central abundances in the hot intra-cluster medium	
I.	Individual and average abundance ratios from <i>XMM-Newton</i> EPIC	75
3.1	Introduction	76
3.2	Observations and data preparation	78
3.2.1	Data reduction	78
3.2.2	Spectra extraction	80
3.3	EPIC spectral analysis	81
3.3.1	Background modelling	83
3.3.2	Global fits	85
3.3.3	Local fits	85
3.4	Results	86
3.4.1	Estimating reliable average abundances	89
3.4.2	EPIC stacked residuals	90
3.4.3	Systematic uncertainties	92
3.5	Discussion	96
3.5.1	Discrepancies in the S/Fe, Ar/Fe and Ni/Fe ratios .	100
3.5.2	Comparison with the proto-solar abundance ratios .	101

3.5.3	Current limitations and future prospects	102
3.6	Conclusions	104
3.A	EPIC absorption column densities	107
3.B	Radiative recombination corrections	107
3.C	Effects of the temperature distribution on the abundance ratios	110
3.D	Best-fit temperature and abundances	113
4	Origin of central abundances in the hot intra-cluster medium	
	II. Chemical enrichment and supernova yield models	119
4.1	Introduction	120
4.2	Observations and spectral analysis	123
4.3	Chemical enrichment in the ICM	124
4.3.1	Abundance pattern of even-Z elements	126
4.3.2	Mn/Fe ratio	139
4.3.3	Fraction of low-mass stars that become SNIa	144
4.3.4	Clues on the metal budget conundrum in clusters	146
4.4	Enrichment in the solar neighbourhood	149
4.5	Summary and conclusions	153
4.5.1	Future directions	155
4.A	The effect of electron capture rates on the SNIa nucleosynthesis yields	158
4.B	List of SN yield models used in this work	159
5	Origin of central abundances in the hot intra-cluster medium	
	III. The impact of spectral model improvements on the abundance ratios	163
5.1	Introduction	164
5.2	The sample and the reanalysis of our data	166
5.2.1	The sample	166
5.2.2	From SPEXACT v2 to SPEXACT v3	167
5.3	Results	170
5.3.1	The Fe bias in cool plasmas	171
5.3.2	The Ni bias	176
5.3.3	Updated average abundance ratios	177
5.4	Discussion	179
5.4.1	Implications for the iron content in groups and clusters	179
5.4.2	Implications for supernovae yield models	182
5.5	Conclusions	188

6 Radial metal abundance profiles in the intra-cluster medium of cool-core galaxy clusters, groups, and ellipticals	193
6.1 Introduction	194
6.2 Observations and data preparation	198
6.3 Spectral modelling	199
6.3.1 Thermal emission modelling	199
6.3.2 Background modelling	201
6.3.3 Local fits	202
6.4 Building average radial profiles	203
6.4.1 Exclusion of fitting artefacts	203
6.4.2 Stacking method	203
6.4.3 MOS-pn uncertainties	205
6.5 Results	206
6.5.1 Fe abundance profile	206
6.5.2 Abundance profiles of other elements	208
6.6 Systematic uncertainties	214
6.6.1 Projection effects	218
6.6.2 Thermal modelling	218
6.6.3 Background uncertainties	220
6.6.4 Weight of individual observations	223
6.6.5 Atomic code uncertainties	225
6.6.6 Instrumental limitations for O and Mg abundances .	227
6.7 Discussion	228
6.7.1 Enrichment in clusters and groups	228
6.7.2 The central metallicity drop	230
6.7.3 The overall Fe profile	236
6.7.4 Radial contribution of SNIa and SNcc products .	242
6.8 Conclusions	250
6.A Cluster properties and individual Fe profiles	255
6.B Average abundance profiles of O, Mg, Si, S, Ar, Ca, and Ni .	255
7 Future prospects for intra-cluster medium enrichment studies	265
7.1 Current limitations of abundance measurements	265
7.2 The future of <i>XMM-Newton</i> in intra-cluster enrichment studies	267
7.2.1 Nearby clusters and supernova models	267
7.2.2 High redshift clusters	269
7.3 Future work on atomic data and spectral modelling	269
7.4 X-ray micro-calorimeters	270

7.5	The upcoming generation of X-ray missions	273
7.5.1	<i>Hitomi</i>	273
7.5.2	XARM	275
7.5.3	<i>Athena</i>	277
7.6	Concluding remarks	279
	Bibliography	281
	Nederlandse samenvatting	293
	English summary	301
	Résumé en français	309
	Curriculum Vitae	317
	List of publications	319
	Acknowledgements	321

*Quand on me demande: «À quoi sert l'astronomie?»
il m'arrive de répondre: «N'aurait-elle servi qu'à révéler tant de beauté,
elle aurait déjà amplement justifié son existence.»*

*When people ask me: "What is the use of astronomy?"
I sometimes answer: "If its use was only to reveal such beauty,
astronomy would have already amply justified its existence."*

– Hubert Reeves, *Patience dans l'azur*

1

Introduction

All along the 20th century, many discoveries have revolutionised our current view of the Universe. The success of the special and general relativity predicted by Albert Einstein more than hundred years ago (Einstein 1905, 1916) is probably one of the most famous examples. A second major result is certainly the discovery of other "island universes" by Edwin Hubble in 1926, extending our conception of the entire cosmos from the only Milky Way to a universe full of galaxies (Hubble 1926). Even more surprising is that, as also found by Hubble, these galaxies escape away from each other (Hubble 1929). This provided a solid piece of evidence that the Universe is actually expanding. A third major discovery, which quickly became a major issue for physicists and astronomers, was the evidence for missing (or "dark") matter, suggested independently in individual galaxies by Vera Rubin (1970) and in galaxy clusters by Jacobus Kapteyn (1922) and Fritz Zwicky (1933). Fourth, the accidental discovery of the cosmic microwave background by Arno Penzias and Robert Woodrow Wilson (1965; see also Dicke et al. 1965) provided a decisive proof of the Big Bang theory. Finally, the discovery of the acceleration of the expansion of the Universe by looking at distant Type Ia supernovae (Riess et al. 1998) suggests that the Universe is dominated by a mysterious "dark" energy, whose fundamental nature remains unknown.

All these above discoveries are now fully part of the basic history of sciences, as they have had an extraordinary impact on the current way we conceive the Universe. Nevertheless, some past discoveries are somewhat less known to a large public, although they have not contributed less to fundamentally revisit our relation to astronomy. One of them deals with

the question of the origin of the chemical elements.

1.1 The stellar nucleosynthesis: a brief history...

Only one hundred years ago, the origin of the chemical elements was still a total mystery for the scientific community. It had to wait until the progresses of quantum mechanics in the 1920's, before Sir Arthur Eddington (1920) and Jean Perrin (1922) proposed that the nuclear fusion of light elements like hydrogen could be a source of stellar energy. Later on, significant progress was achieved by Hans Bethe (1939) who set the first basis of the stellar nucleosynthesis theory by selecting two channels as the source of energy of stars:

1. The proton-proton chain reaction, believed to occur in low mass stars, where two protons eventually form a helium nucleus;
2. The CNO cycle, where carbon, nitrogen, and oxygen serve as catalysts to produce helium from protons in more massive stars.

At the time, however, stellar fusion theories did not explain how elements heavier than helium could form. Many years later, George Gamow (1946) proposed that these heavy elements, or "metals", had formed at the very first moments of the Universe. This was quantified more in the now well-known Alpher-Bethe-Gamow paper, published two years later (Alpher et al. 1948, which was found later to have correctly predicted the relative cosmic abundances of hydrogen and helium). On the contrary, Fred Hoyle suggested that metals are forged in the core of collapsing stars, after their hydrogen burning phase (Hoyle 1946). Finally, in 1952, Paul Willard Merrill detected absorption lines of technetium ($Z = 43$) in the spectra of R Andromedae and in other red variable stars. Since all the isotopes of technetium are unstable and thus short-lived, the natural conclusion was that significant amounts of this heavy element have been produced within the studied stars. While all the pieces slowly started to fit together with considerable progress from theories and observations, a complete and unified nucleosynthesis theory was still lacking.

The year 1957 has been decisive for the question of the origin of the elements. Almost simultaneously, two publications definitely gave birth to the modern stellar nucleosynthesis theory (Cameron 1957a; Burbidge et al. 1957). In particular, the second one — commonly named B²FH following

the authors (Margaret Burbidge, her husband Geoffrey Burbidge, William Fowler, and Fred Hoyle) — explicitly detailed all the processes responsible for the synthesis of all the heavy elements, from lithium to uranium. Two spectacular conclusions could be drawn from that paper.

1. It was definitely demonstrated that metals are synthesised in the cores of stars and, especially, in supernovae. On the contrary, the primordial nucleosynthesis is capable of creating hydrogen and helium only (as well as traces of lithium and berilium).
2. Perhaps even more importantly, the authors showed for the first time that when a star explodes as a supernova, it enriches its surrounding interstellar medium with its freshly created metals, thus participating actively in the formation of a new generation of stars.

In summary, about sixty years ago, evidence was provided that interstellar dust, planets, the Earth, living and human beings are all made of stars and supernovae, thereby revolutionising even further our conception of the Universe.

1.2 The role of Type Ia and core-collapse supernovae

Since 1957, stellar and supernova nucleosynthesis theories considerably improved (for an evolution of reviews, see e.g. Arnett 1973; Tinsley 1980; Arnett 1995; Nomoto et al. 2013). With the increase of computing performance (in synergy with the increasing number and quality of supernovae observations) from the end of the 1970’s, several research groups started to simulate explosive nucleosynthesis in massive stars and supernovae while taking observational features into account (e.g. Arnett 1977; Weaver et al. 1978; Weaver & Woosley 1980; Nomoto et al. 1984).

Nowadays, it is well established that the production of metals can be distinguished as follows.

- Asymptotic giant branch stars synthesise carbon (C), nitrogen (N), as well as traces of neon (Ne) and magnesium (Mg) — e.g. Karakas (2010).
- Core-collapse supernovae (SNcc; Fig. 1.1 left panel) and their massive star progenitors synthesise almost all the oxygen (O), Ne, and Mg of the Universe, as well as a non-negligible fraction (about one half) of silicon (Si) and sulfur (S) — e.g. Kobayashi et al. (2006).



Figure 1.1: *Left:* Composite X-ray image of the (core-collapse) supernova remnant G292.0+1.8. Oxygen-dominated ejecta are shown in yellow and orange, magnesium-dominated ejecta are shown in green, and silicon and sulfur-dominated ejecta are shown in blue (Credit: NASA/CXC/SAO). *Right:* Composite image (red: mid-infrared; green and yellow: ejecta seen in X-ray; blue: shock front seen in X-ray; white: optical) of the (Type Ia) Tycho supernova remnant (Credit: X-ray: NASA/CXC/SAO, Infrared: NASA/JPL-Caltech; Optical: MPIA, Calar Alto, O.Krause et al.).

- Type Ia supernovae (SNIa; Fig. 1.1 right panel) synthesise the major part of argon (Ar), calcium (Ca), as well as the Fe-peak elements, in particular chromium (Cr), manganese (Mn), iron (Fe), and nickel (Ni) — e.g. Iwamoto et al. (1999). Moreover, as for SNcc, about one half of Si and S is produced in SNIa explosions.
- Heavier elements are thought to be synthesised via the *r*- and *s*-processes, plausibly in peculiar events like neutron star mergers (e.g. Martin et al. 2015) or during compact stellar binary assembly (e.g. Ramirez-Ruiz et al. 2015).

Throughout this thesis, we focus on the chemical elements produced by SNIa and SNcc (see Sect. 1.5). In the next subsections, we detail further the nucleosynthesis predicted for these two classes of objects, as well as the parameters and uncertainties that may affect it.

1.2.1 Core-collapse supernovae (SNcc)

When a massive star ($\gtrsim 8\text{--}10 M_{\odot}$) has burned about 10% of its hydrogen into helium, it reaches the end of its life on the main sequence (typically within a few million years). Heavier elements (C, Ne, O, Si) are successively created, then burn in turn, building an onion-like structure in the core of the star, where heavier elements are synthesised in deeper layers. This burning process stops at ^{56}Ni (which further decays into stable ^{56}Fe), because nuclear fusion becomes energetically inefficient for higher isotopes. Consequently, Fe accumulates in the core and increases its density up to the electron degeneracy. When the core density reaches the Chandrasekhar limit ($\sim 1.4 M_{\odot}$), the electron degenerate pressure is not sufficient anymore to counter gravitational contraction, and the core quickly collapses. Neutrons and neutrinos are then massively created by electron capture. This collapse suddenly stops when the core reaches the neutron degeneracy pressure, producing a powerful reverse shock from the core toward the upper layers. As the shock traverses the less dense external layers, its velocity increases and can reach about 25% to 50% of the speed of light, heating the upper stellar material (which rapidly synthesises more elements) and violently ejecting it into the interstellar medium. A core-collapse supernova is born. For recent reviews on the mechanisms driving SNcc explosions, see e.g. Janka (2012); Burrows (2013).

SNcc are commonly associated to Type II supernovae (i.e. supernovae showing hydrogen in their spectrum), but also to Type Ib (if the star has lost its hydrogen layer) and Type Ic supernovae (if the star has lost its hydrogen and helium layers). As mentioned above, their main nucleosynthesis products are O, Ne, and Mg which are created almost exclusively in SNcc, as well as Si and S whose production originates from both SNcc and SNIa (see also Sect. 1.2.2). Heavier elements like Ca, Ar, Fe, and Ni may also be synthesised during SNcc explosions, but at much lower quantities.

How much mass of these elements are created by a SNcc or, in other words, what are the typical yields that a single SNcc produces? According to the current SNcc models, the answer to this question depends on two main parameters:

1. The mass of the stellar progenitor;
2. The initial metallicity of the progenitor or, in other words: was the progenitor previously enriched by past supernovae?.

Of course, instead of considering only one SNcc, one can also address the same question for a collection of SNcc resulting from a same single stellar population. In this case, one must integrate the above parameters over the whole stellar population. Generally speaking, the integrated yields of a population of SNcc will depend on the initial mass function (IMF) of the progenitor population, and on its average initial metallicity, supposed to be very similar for all the population members (Fig. 1.2 top).

1.2.2 Type Ia supernova (SNIa)

Type Ia supernovae are different from SNcc in many aspects. In particular, they are not the result of the end-of-life of a massive star. Instead, is it generally admitted that SNIa progenitors are binary systems including at least one carbon-oxygen white dwarf, i.e. the stellar remnant of a low-mass ($\lesssim 8 M_{\odot}$) star, which suddenly gets (re-) ignited by mass accretion from the companion object. Unlike sometimes claimed, and because they do not result from a gravitational collapse, SNIa or their progenitors approach the Chandrasekhar limit, but never reach it. Although the precise mechanism is still unknown, the ignition is thought to be triggered by the explosive burning of carbon and newly synthesised nuclei. Because the electron degeneracy is independent of temperature, the white dwarf is unable to regulate its thermonuclear fusion, e.g. by expanding and cooling down, as a main sequence star supported by thermal pressure would naturally do. This somehow triggers one or several ignition flames, resulting in a violent explosion entirely disrupting the object (contrary to SNcc, where the remaining stellar core collapses into either a neutron star or a black hole), and ejecting its material into the interstellar medium. For reviews on the mechanisms driving SNIa explosions, see e.g. Hillebrandt & Niemeyer (2000); Hillebrandt et al. (2013). Within a couple of seconds, many heavy elements are created from the multiple explosive burnings. In particular, SNIa are thought to synthesise most of the Ar, Ca, Cr, Mn, Fe, and Ni, and about half of the Si and S present in the Universe. On the contrary, because lighter metals like C, O, Ne, and Mg are actually the fuel that is being burned during the explosion, not many of these elements remain after the explosion.

Although SNIa are widely used as standard candles to measure cosmological distances (and provide thus crucial help to estimate the acceleration of the expansion of the Universe, e.g. Riess et al. 1998), they are poorly understood astrophysical objects.

First, the physics of the explosion, or more precisely the precise propagation of the burning flame, is poorly known. Among the supernova community, two (or three) models are currently competing:

- The deflagration model, in which the flame is assumed to propagate subsonically through the exploding white dwarf;
- The delayed-detonation model, in which below a certain critical density, the flame becomes supersonic before reaching the surface;
- A third model, the pure detonation, in which the flame propagates always supersonically, is less plausible, though sometimes evoked.

In parallel to the mass and initial metallicity of the SNcc progenitors (Sect. 1.2.1), it is important to note that the nucleosynthesis yields of SNIa are very sensitive to the explosion model considered. In particular, deflagration explosions should produce significantly more Ni and less Si, S, Ar, Ca, and Cr with respect to delayed-detonation explosions (Fig. 1.2 bottom). This means that an accurate measure of SNIa yields may help to favour specific models, and thus better constrain the explosion mechanism.

Second, and perhaps even more embarrassingly, the precise nature of the progenitor companion is still unclear. The reason is that the observed variation in properties of SNIa is not well understood. In practice, it appears to be difficult to derive the nature of the progenitor from the SNIa lightcurve and spectrum (for recent reviews, see Howell 2011; Maoz & Mannucci 2012; Maoz et al. 2014). Currently, the two main progenitor channels proposed are:

- The single-degenerate channel, in which the companion is a non-degenerate star. Its material is progressively accreted by the white dwarf via Roche lobe overflow until carbon ignition of the latter;
- The double-degenerate channel, in which the companion is another white dwarf. The ignition can then be triggered either by a violent merger, or by slow accretion if one white dwarf gets disrupted before reaching the other.

Whereas many observational constraints may be useful to favour/disfavour one particular channel, each of these two scenarios has its strengths and weaknesses, and the situation is still far from being clear. Among these constraints, a promising one is the determination of the delay time distribution, i.e. when do SNIa explode after the formation of an initial single

stellar population. While it is clear that the delay time between a star birth and a supernova is longer for SNIa than for SNcc since (i) low-mass stars live longer and (ii) there may be substantial time between the white dwarf phase and the SNIa explosion within the binary system, its distribution for SNIa is still poorly constrained, yet very dependent on the dominant channel.

Unfortunately, a precise link between the progenitor scenarios and the explosion channels is still somewhat unclear. Indeed, each progenitor scenario allows both deflagration and delayed-detonation explosions (sometimes also called near-Chandrasekhar explosions; e.g. Nomoto et al. 2013). However, and interestingly, the scenario of a violent merger between two white dwarfs should in principle produce a sub-Chandrasekhar explosion, namely a pure detonation (Seitenzahl et al. 2013a). In principle, this specific scenario can thus be tested via an accurate measure of the SNIa yields.

1.3 Metals in clusters of galaxies

Because SNIa and SNcc eject freshly processed metals into their surroundings, it is not surprising to detect these elements within galaxies, whether in the form of interstellar gas or dust grains, thereby forming planets and even life. However, metals also enrich the circumgalactic medium, where their presence is confirmed even at high redshifts via their metal lines absorbing the light of background quasars ($2 \gtrsim z \gtrsim 5$; for a review, see McQuinn 2016). Even more surprisingly, metal enrichment is also found well beyond this (circum-) galactic limit; that is to say, the scale of clusters of galaxies.

Galaxy clusters are in fact the largest gravitationally bound structures known in our Universe. Since the Big Bang (about 13.7 billion years ago), they have assembled from local gas and dark matter over-densities, and grow continuously in hierarchical structures via mergers. The major component (~85% in mass) of galaxy clusters is in the form of dark matter, whose precise nature is still unknown. Stars, planets, interstellar gas, and galaxies constitute only about ~10–20% of the remaining baryonic content. The other ~80–90% of the baryonic mass is found in the form of a very hot (10^7 – 10^8 K), extended, highly ionised, and tenuous (10^2 – 10^4 atoms/m³) gas, which fills the very large gravitational potential well of the whole cluster. This plasma, namely the intra-cluster medium (ICM, Fig. 1.3) is hot enough to emit X-ray radiation, essentially via bremsstrahlung ("free-free"

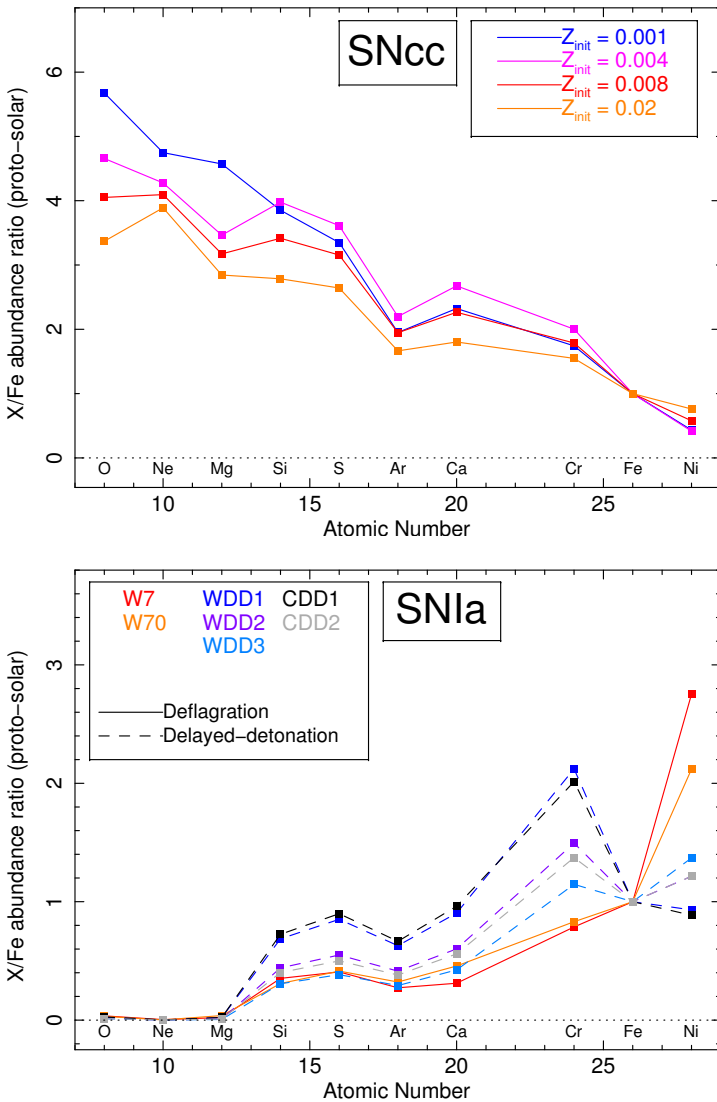


Figure 1.2: Predicted X/Fe abundance ratios from various SNcc (top) and SNIa (bottom) yield models. The SNcc yield models are adapted from Nomoto et al. (2013) and integrated over a Salpeter IMF between $10 M_{\odot}$ and $40 M_{\odot}$, and are shown for different assumed progenitor initial metallicities (Z_{init}). The SNIa yield models are directly adapted from Iwamoto et al. (1999). The W7 and W70 models reproduce a pure deflagration explosion while the other models (WDD1, WDD2, WDD3, CDD1, and CDD2) reproduce a delayed-detonation explosion. More details on all these models (and others) are provided in Chapter 4.

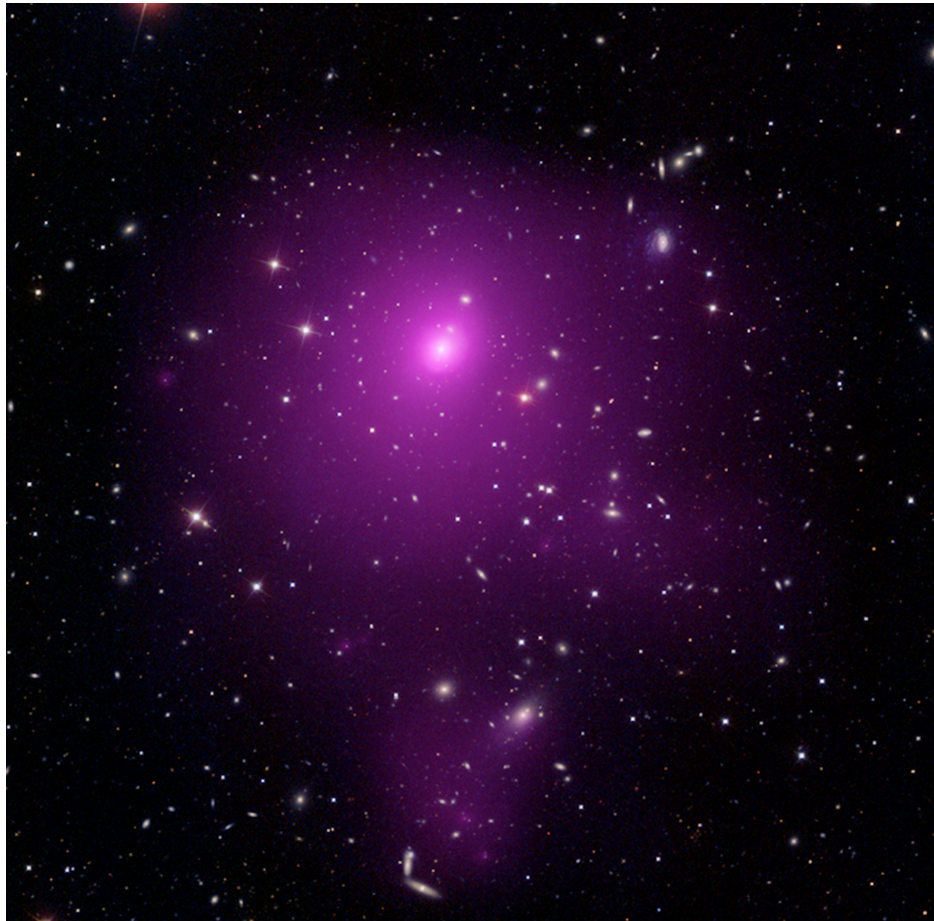


Figure 1.3: Composite image (purple: X-ray; white: optical) of the rich galaxy cluster Abell 85 (Credit: X-ray: NASA/CXC/SAO/A.Vikhlinin et al.; Optical: SDSS). The southern subcluster is thought to fall into the main cluster.

radiation), radiative recombination ("free-bound" radiation), and emission lines ("bound-bound" radiation).

1.3.1 The legacy of past X-ray missions

Luckily, the thermal emission of the ICM falls remarkably in the energy window accessible by the past and current X-ray telescopes ($\sim 0.3\text{--}10\text{ keV}$). When discovered by the first X-ray detectors aboard balloons and rock-

ets (Byram et al. 1966; Bradt et al. 1967), and eventually by the first X-ray satellite *Uhuru* (Cavaliere et al. 1971; Kellogg et al. 1972, 1973), whether this extended emission originated from thermal (e.g. bremsstrahlung) or non-thermal (e.g. inverse-Compton) processes was still unclear. A breakthrough came in the late 1970's, with the Ariel V and OSO-8 X-ray missions, whose improved spectral resolution allowed to detect for the first time an Fe-K emission feature around ~ 7 keV in the spectra of the Perseus, Virgo, and Coma clusters (Mitchell et al. 1976; Serlemitsos et al. 1977). This result was spectacular in two aspects: (i) it definitely confirmed the predominant thermal, collisional nature of the ICM; and (ii) it showed for the first time that the ICM is polluted by metals, providing evidence that chemical enrichment plays a role even at the largest scales of the Universe.

Since these pioneering studies, and all along the succession of several generations of X-ray observatories with improved technology and instruments, measurements of metals in the ICM (and their interpretation) considerably improved. Launched in 1978, the *Einstein* observatory allowed to detect line emission from other elements than Fe (Canizares et al. 1979; Mushotzky et al. 1981). Another valuable discovery made by the *Einstein* mission was that about half of the observed clusters show a sharp peak in the X-ray surface brightness. Converting this brightness into gas density¹ and estimating their gas temperature, it was found that the cooling time² at the centre of these clusters is shorter than the Hubble time (~ 14 Gyr) (Jones & Forman 1984; Stewart et al. 1984). In fact, these "cool-core" clusters (Molendi & Pizzolato 2001) are dynamically relaxed and usually exhibit a strong inverted temperature gradient in their cores. On the other hand, "non-cool-core" clusters show a more extended and disturbed X-ray surface brightness, and do not reveal a clear central ICM temperature drop.

A great step forward in chemical abundance studies of clusters occurred with the launch of *ASCA* in 1993. This Japanese mission provided for the first time a reasonable estimate of the abundances of O, Ne, Mg, Si, S, Ar, Ca, Fe, and Ni in the ICM (e.g. Mushotzky et al. 1996; Baumgartner et al. 2005). Furthermore, *ASCA* also allowed to study for the first time the spatial distribution of Fe within the ICM, and showed a clear increase in the abundance of this element toward the centre of the Centaurus clus-

¹The X-ray surface brightness of the ICM is proportional to the square of the gas density.

²In the case of an isobaric radiative cooling of a gas of density n_e and temperature T , the cooling time, t_{cool} , is calculated as $t_{\text{cool}} = 8.5 \times 10^{10} \text{ yr} \left(\frac{n_e}{10^{-3} \text{ cm}^{-3}} \right)^{-1} \left(\frac{T}{10^8 \text{ K}} \right)^{1/2}$ (Sarazin 1986).

ter (Allen & Fabian 1994; Fukazawa et al. 1994). Later on, the Italian-Dutch mission *BeppoSAX* (launched in 1996) established a clearer picture of the Fe distribution in clusters. In particular, De Grandi & Molendi (2001) showed that, while cool-core clusters host an excess of Fe in their core compared to the outskirts, non-cool-core clusters have a systematically flatter Fe radial profile.

1.3.2 The recent generation of X-ray missions

Among the recent generation of X-ray observatories, three missions should be mentioned: *Chandra* (launched on 23 July 1999, still active), *XMM-Newton* (launched on 10 December 1999, still active; see Fig. 1.4), and *Suzaku* (launched on 10 July 2005, ended on 2 September 2015). Each mission has its own benefits and is optimised for different purposes.

Chandra has a remarkable spatial resolution and is optimised to study in detail ICM substructures such as cavities and buoyant bubbles in cool-core clusters, probably created by the activity of the powerful active galactic nucleus in the central brightest cluster galaxy (BCG).

The European Photon Imaging Camera (EPIC) and Reflection Grating Spectrometer (RGS) instruments onboard *XMM-Newton*, on the other hand, have a larger effective area coupled to a better spectral resolution, which makes this mission the best suited one to measure abundances in the core of galaxy clusters and groups. The high resolution of RGS, covering and resolving the O-K, Ne-K, Mg-K and Fe-L lines, is particularly interesting for the study of systems showing a sharp peak in their X-ray surface brightness (Fig. 1.5 top). However, the RGS instruments are slitless, meaning that the emission lines in obtained spectra are broadened because of the spatial extent of the sources. The EPIC instruments (namely MOS 1, MOS 2, and pn) have a poorer spectral resolution but a more extended spectral window, accessing the Si-K, S-K, Ar-K, Ca-K, Fe-K and Ni-K lines, thereby allowing to study the spectrum of any extracted spatial region (Fig. 1.5 bottom). In this thesis, we use the *XMM-Newton* instruments to derive abundances in the ICM (see Sect. 1.5).

Finally, and despite its rather poor spatial resolution, the big advantage of *Suzaku* resides in its low instrumental background, allowing to probe regions of fainter emission, such as cluster outskirts. As explained in the next subsections, complementary studies performed by these three missions have completed the current picture we have about chemical enrichment of the ICM so far.



Figure 1.4: Artist impression of the *XMM-Newton* satellite in orbit around the Earth (Credit: ESA).

The new generation of X-ray missions includes *Hitomi* (launched in February 2016), *XARM* (expected launch in 2021), and *Athena* (expected launch in 2028). These three missions were/will be equipped with micro-calorimeter instruments, which allows a considerable improvement of the spectral resolution achieved so far. The expected contribution of this upcoming generation of satellites to cluster enrichment studies is discussed in detail in Chapter 7.

1.3.3 Constraining supernovae models by looking at the intra-cluster medium

As explained in Sect. 1.2, the yields that SNIa and SNcc release into their surroundings highly depend on several intrinsic physical assumptions such as the IMF and the average initial metallicity of the progenitor SNcc population, or the dominant explosion channel driving SNIa explosions. In principle, deriving the abundances in supernova remnants via their X-ray spectra would therefore help to constrain these assumptions and better understand the physics of supernovae and of their progenitors. In practice, however, this is very difficult for at least three good reasons:

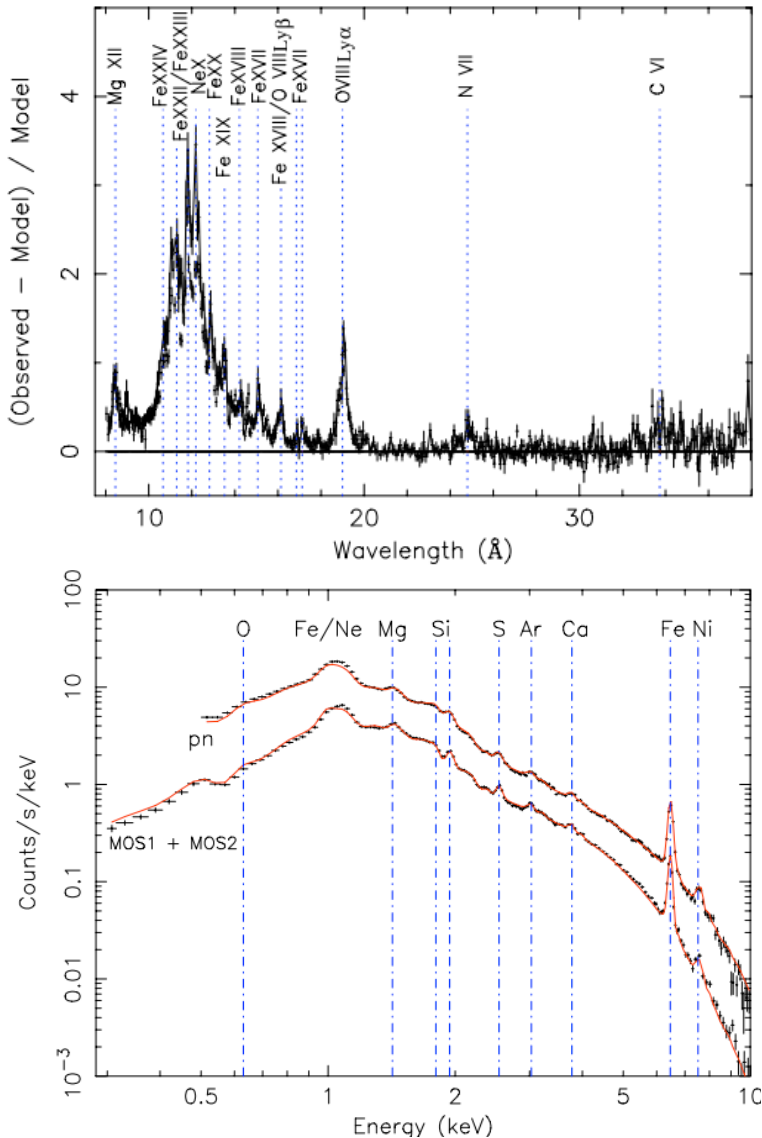


Figure 1.5: *Top:* XMM-Newton first-order RGS spectrum residuals of the core of the giant elliptical galaxy M87, where line emission has been set to zero in the model (Werner et al. 2006a). *Bottom:* XMM-Newton EPIC (including MOS1 + MOS2 and pn) spectra of the core of the cluster 2A 0335+096, together with their respective best-fit spectral models (Werner et al. 2006b). The metal emission lines from which the abundances can be measured are indicated by the blue dotted (RGS) and dash-dotted (EPIC) lines.

1. Only a few tens of supernova remnants can be studied in our Galaxy or in its very local neighbourhood, preventing a comprehensive study on large statistical samples;
2. The ionisation state and the thermal structure of the hot plasma in supernova remnants are often complicated, which makes difficult the conversion of relative spectral line emissivities into chemical abundances;
3. The yields produced by the supernova ejecta may easily mix with the metals that were already present in the surrounding interstellar medium, thus complicating even more the direct interpretation of the measurements.

Because all heavy elements in the Universe have been produced in stars and supernovae, metals present in the ICM are nothing else as than the integral yields of billions of SNIa and SNcc having continuously enriched galaxy clusters during and prior their evolution. In fact, clusters act as "closed-box" systems, as they are able to retain all the stellar products in their very large gravitational potential well. This implies that all supernovae exploding within the cluster remain locked either in their galactic hosts in the form of new stars or interstellar gas, or in the intra-cluster medium³ (see also Sect. 1.3.5). Moreover, and contrary to supernova remnants, the ICM is optically thin and in collisional ionisation equilibrium (CIE). This means that abundances can be robustly measured in the ICM, as they are directly proportional to the equivalent width⁴ of their X-ray emission lines. Consequently, the ICM provides a unique opportunity to constrain SNIa and SNcc models and to estimate the ratio of the number of SNIa/SNcc contributing by measuring the abundances of the elements they release in galaxy clusters and groups.

The pioneering study on this concept was done by Mushotzky et al. (1996) using ASCA observations. The authors concluded that their measured abundances in the ICM are consistent with a dominant SNcc contribution to the enrichment. Later on, Dupke & White (2000), based on

³This statement is more controversial in the case of low-mass systems (e.g. galaxy groups or giant ellipticals), where powerful galactic winds and active galactic nuclei outbursts might compete with the (somewhat) shallower gravitational potential well and uplift metals outside of the system.

⁴The equivalent width of a line is defined as the ratio of the line flux over the continuum flux at the position of the line.

ASCA observations of three clusters, favoured a dominant deflagration explosion channel for SNIa explosions. These two results, however, were challenged by more recent studies using the current generation of X-ray telescopes (e.g. Finoguenov et al. 2002; Böhringer et al. 2005; Werner et al. 2006b; de Plaa et al. 2006; Sato et al. 2007a). The most complete work has been done by de Plaa et al. (2007), who compiled the abundance measurements of 22 cool-core clusters observed by *XMM-Newton* and fitted their average abundance ratios with a combination of SNIa+SNcc models. They concluded that the measured abundance ratios: (i) favour the delayed-detonation channel for SNIa explosions; (ii) suggest that SNcc progenitors were previously enriched (i.e. have a positive initial metallicity); and (iii) show that Ca is overproduced with respect to the most common model predictions. Of course, such a study may now be further improved by compiling the abundance ratios of more (high- and low-mass) systems observed with deeper exposures, and by comparing these ratios with more recent supernova yield models, after carefully checking all the systematic uncertainties that may affect the results (see Chapters 3 and 4).

1.3.4 Stellar and intra-cluster phases of metals

As explained earlier, the baryonic content of galaxy clusters consists of two separate components: (i) the ICM and (ii) the stellar mass in (and between) galaxies. Whereas a significant fraction of the metals is somehow dispersed into the ICM (see also Sect. 1.3.5), the other part remains locked within the cluster galaxies, in particular in low- and intermediate-mass stars. In principle, such a fraction is simple to estimate on basis of the stellar luminosity (as a proxy of the stellar mass) and the assumed yields from SNIa and SNcc models. Several analytical works (Loewenstein 2013; Renzini & Andreon 2014, and references therein) estimate that there is at least as much Fe released into the ICM as there is still locked into stars. In massive clusters ($>10^{14} M_{\odot}$), this fraction seems to increase and may even pose a serious problem: there is 2 to 3 times too much Fe measured in the ICM compared to what could have been produced by all the stars in the cluster galaxies. A recent study based on semi-analytic simulations better conciliates the expected and measured Fe abundances in the ICM of the most massive clusters (Yates et al. 2017). However, a mismatch is still found in clusters of intermediate mass (too much metals compared to the predictions) and in groups (too few metals compared to the predictions). Clearly, the relation between absolute supernova yields and the metal content in groups and

clusters is far from being solved.

Do the intra-cluster abundances really reflect the nucleosynthesis of all the stars and supernovae in galaxy clusters? This question is not trivial at all, but the answer is probably no, essentially for two reasons. First, comparing directly the ICM abundances with supernova yields implicitly assumes that all stars and supernovae create and disperse their products instantaneously after their formation⁵. In reality, SNcc and SNIa require significant and different delays before they could effectively enrich the ICM (Matteucci & Chiappini 2005). Second, it is likely that SNIa and SNcc are not dispersed into the ICM with the same efficiency. It is currently believed that SNcc products are preferentially locked up in stars while SNIa products are more easily released in the ICM (e.g. Loewenstein 2013). Ignoring these enrichment delays may lead to some incorrect interpretations, for example about the true ratio of all supernovae having exploded in clusters.

Although the ICM abundances may not be fully representative of the chemical composition produced at first place, they can still be correctly interpreted in terms of SNIa and SNcc having actually contributed to the ICM enrichment. Keeping this difference in mind, the ICM abundances can still be used to constrain SNIa and SNcc models.

1.3.5 Where and when was the ICM chemically enriched?

Whereas it is clear that metals present in the ICM ultimately originate from SNIa and SNcc having occurred within the cluster gravitational potential well, three major questions still arise:

- From which astrophysical sources does the bulk of the enrichment originate? The central BCG, late-type satellite galaxies, or intra-cluster stars?
- By which dominant mechanism(s) does a fraction of the metals escape their galactic gravitational potential wells and pollute the intra-cluster gas?
- At which step(s) of the cosmic time and / or cluster evolution do metals enrich the ICM?

Clearly, these questions are not trivial and require a deep synergy between theory, simulations, and observations in order to be solved. Generally speaking, the bulk of the enrichment has probably occurred around the peak of

⁵This assumption is also known as the "instantaneous recycling approximation".

cosmic star formation $z \sim 2\text{--}3$ (for a review, see Madau & Dickinson 2014), i.e. when the ICM started to form. More precisely, the observed spatial distribution of metals in clusters (whether from real observations or from snapshots of chemo-dynamical simulations) may provide useful hints and further constraints (Fig. 1.6) to these three above questions.

Since the discovery of a systematic central Fe enhancement in cool-core clusters up to about one solar in the centre (Allen & Fabian 1994; Fukazawa et al. 1994; De Grandi & Molendi 2001, see also Sect. 1.3.1), several studies showed that the Fe mass of this excess has been likely produced by SNIa belonging to the central BCG (Böhringer et al. 2004a; De Grandi et al. 2004). On the other hand, recent observations by *Suzaku* showed a remarkably uniform level of Fe enrichment in the outskirts of the Perseus cluster (Werner et al. 2013). The latter result has also been extended to other elements as well. This includes SNcc-dominated products, like Mg, among other elements in the outskirts of the Virgo cluster (Simionescu et al. 2015). Put together, these findings converge toward the picture of two major stages of enrichment (at least for cool-core clusters):

1. An early ($z \gtrsim 2$) enrichment which took place essentially before the cluster was well assembled, when metals created by both SNIa and SNcc had been released and efficiently mixed in the still forming ICM from star-forming galaxies via powerful galactic winds (see also below);
2. A later enrichment, presumably coming from SNIa in the central BCG, responsible for the central Fe excess in cool-core clusters.

Observational hints toward this picture also seem to corroborate the most recent cosmological simulations that take the cluster enrichment aspect into account (e.g. Planelles et al. 2014; Biffi et al. 2017).

In parallel, several chemo-dynamical simulations investigated the relative role of the possible mechanisms that could be responsible for the galactic escape of metals into the ICM (for a review, see Schindler & Diaferio 2008). Among them, two dominant channels seem to be favoured: (i) ram-pressure stripping, occurring when an infalling galaxy gets its interstellar gas stripped by the pressure of the ambient ICM (Gunn & Gott 1972) and (ii) galactic winds or outflows provided by the total kinetic energy of the supernova explosions (De Young 1978). While ram-pressure stripping is more efficient in cluster cores, where the ICM pressure is more important and the gravitational potential more efficient to attract galaxies, galactic

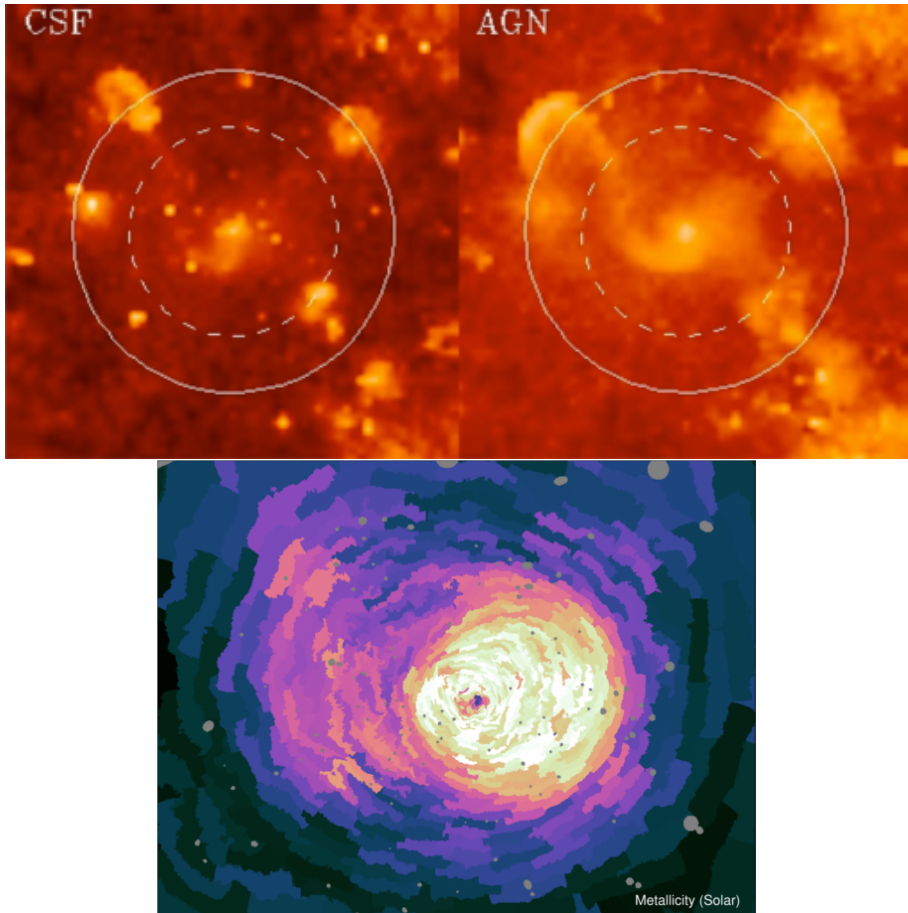


Figure 1.6: Top: Simulated maps of the (emission-weighted) Fe distribution in a massive cluster (Planelles et al. 2014). The "CSF" case (left panel) includes the effects of radiative cooling, star formation, and supernova feedback, while the "AGN" case (right panel) also accounts for AGN feedback. The typical radii r_{180} and r_{500} are indicated by the continuous and dashed white circles, respectively. The colour coding ranges between 0.02 solar (black) to 1.87 solar (light yellow). Bottom: Observed map of the (projected) Fe distribution in the Centaurus cluster (Sanders et al. 2016). The colour coding ranges between 0 solar (dark purple) to 1.7 solar (light yellow). The map extends to $\sim 0.07r_{500}$.

winds take a larger role in cluster outskirts (and presumably at earlier cosmic times), where there is less resistance of the ambient ICM to spread out the metals and when the star-forming activity in galaxies was more important than at present times (see also above). Note that other processes, such as galaxy-galaxy interaction, outflows from active galactic nuclei (AGN), or enrichment by the intra-cluster stars may also contribute to the ICM enrichment, although probably to a less significant extent (Schindler & Di-aferio 2008).

Despite all these significant progresses, many uncertainties on the full cluster enrichment picture still remain. For instance, due to their very low signal-to-noise obtained by the current generation of X-ray telescopes, cluster outskirts are left widely unexplored. For a recent review on cluster outskirts, see Reiprich et al. (2013). Moreover, the current instrumental limitations also prevent us from studying in detail the amount and spatial distributions of metals in high-redshift clusters ($z \gtrsim 0.5$). Last but not least, even in nearby clusters past and recent studies of individual objects or small samples did not converge toward a consistent radial distribution for SNcc products (O, Mg, Si, etc.; e.g. Werner et al. 2006a; Simionescu et al. 2009b; Lovisari et al. 2011), leaving questions on the role of SNcc in enriching the central parts of clusters and groups.

1.4 Spectral codes for a collisional ionisation equilibrium plasma

As mentioned in Sect. 1.3.3, the derivation of chemical abundances in the ICM from the equivalent widths of their corresponding emission lines is in principle straight forward. However, it clearly requires a good knowledge of all the subsequent emission processes responsible for both the line and the continuum spectral components. In other words, the use of proper spectral models with up-to-date atomic databases is crucial to correctly derive and interpret the ICM abundances.

Historically, the first atomic code reproducing X-ray spectra of hot, optically thin plasmas in CIE was calculated by Cox & Tucker (1969). After this pioneering work, and thanks to the increasing computing performance since the 1970's, essentially two atomic codes were built and then continuously updated up to now.

The first one was initially written by Mewe (1972), and after some updates (Mewe et al. 1985, 1986) became a reference for many years (abbrevi-

ated as the "Mewe-Gronenschild" code). The code was later updated first as the `meka` code (following its main contributors: Rolf Mewe and Jelle Kaastra), and then as the `meka1` code (Rolf Mewe, Jelle Kaastra, Duane Liedahl) in 1995. It was incorporated into the XSPEC fitting package⁶ (Arnaud 1996). Since 1995, the code (renamed `cie`) has been continuously updated as part of its own fitting package, SPEX⁷ (Kaastra et al. 1996), with two major updates, in 1996 and in 2016 (see Chapter 5). SPEX (and its available single- and multi-temperature CIE models) is the code that is used throughout this thesis.

The second one was initially written by Raymond & Smith (1977) and had been widely used by the X-ray community, together with the Mewe-Gronenschild code. Later on, the code was updated (Smith et al. 2001; Brickhouse & Smith 2005) and became part of the atomic database AtomDB⁸. This spectral model (and atomic database) is also known as the `apec` model as part of XSPEC, and is still regularly updated.

1.5 This thesis

As we have seen in the previous sections, despite considerable progress in the determination of abundances in the ICM and their interpretation as a chemical enrichment from SNIa and SNcc over the largest scales of the Universe, many intriguing questions on supernovae or on the chemical enrichment itself remain to be solved. Obviously, tackling all the aspects of the ICM enrichment would probably take several decades of future efforts. Nevertheless, in this thesis I focus on two particular questions, closely related to what has been discussed in Sect. 1.3.3 and 1.3.5:

1. What do the elemental abundances measured in the ICM cool cores tell us about the intrinsic physics and environmental conditions of the billions of supernovae that exploded and produced these elements?
2. What do the observed spatial distribution of elemental abundances in the cool-core ICM tell us about the main epoch(s) and production sites of the enrichment?

⁶<http://heasarc.gsfc.nasa.gov/docs/xanadu/xspec>

⁷<https://www.sron.nl/astrophysics-spx>

⁸<http://www.atomdb.org/index.php>

This thesis is essentially based on a large sample of *XMM-Newton* observations of 44 cool-core galaxy clusters, groups, and ellipticals (the CHEMi-
cal Enrichment Rgs Sample, or CHEERS), with a total net exposure of ~ 4.5 Ms (de Plaa et al. 2017). This is the first time that the ICM enrichment is studied over such a large sample and such a deep total exposure. The CHEERS sample combines new very deep observations of 11 systems with archival data of other clusters and groups. The selection of the objects of the sample are based on a $>5\sigma$ significance of the detection of the O VIII 1s–2p emission line at 19 Å with the RGS instrument. For further details on the CHEERS project, see de Plaa et al. (2017). In addition to ensuring optimal constraints on the SNcc enrichment, the instrumental detection of the O VIII line in the ICM is a good indicator of the reasonable detectability of the other main metal lines. Because line emissivities are larger in cooler plasmas and because cool-core clusters are more compact, hence produce higher resolution RGS spectra, all the objects in our sample are cool-core⁹.

The outline of this thesis is structured as follows.

Chapter 2 is devoted to the full *XMM-Newton* analysis of Abell 4059, a galaxy cluster which is part of the CHEERS sample. A careful treatment of the background is detailed, and is applied to the analysis of all the other objects in the next chapters. Abell 4059 is a textbook example that clear asymmetries can be found in the metal distribution of galaxy clusters, and that ram-pressure stripping might sometimes play a significant role in enriching the central regions of the ICM.

In **Chapter 3**, I present the individual abundances of all the CHEERS objects within a consistent radius, $0.05r_{500}$ ¹⁰, as well as within $0.2r_{500}$ when possible. I discuss extensively several systematic uncertainties that could be associated with our measurements. Then, I stack the individual measurements to build an average abundance pattern, representative of the enrichment in the ICM as a whole. Doing so, I also report constraints on the average Cr/Fe ratio and, for the very first time, the presence of Mn in the ICM.

Chapter 4 constitutes the immediate follow-up of Chapter 3, as well as a central point of this thesis. I interpret the previously derived ICM

⁹A similar study could be done on non-cool-core systems, although this would probably require even deeper exposures, and would be limited to less massive systems exhibiting reasonable central temperatures.

¹⁰Used as a common way to define astrophysically consistent sizes in galaxy clusters and groups, r_{500} defines the radius within which the cluster/group total density reaches 500 times the critical density of the Universe.

abundance pattern in terms of enrichment by SNIa and SNcc. By fitting the CHEERS data to various supernova yield models, I attempt to provide independent constraints on (i) the IMF and initial metallicity of the average population of the SNcc progenitors; (ii) the favoured channels driving SNIa explosions as well as the dominant nature of SNIa progenitors; and (iii) possible initial enrichment by metal poor (or Population III) stars, or hypernovae.

Chapter 5 is the updated version of Chapters 3 and 4, and corrects the previous results from a major update in the spectral models and atomic databases used to fit the X-ray spectra (SPEX). From a more global perspective, this chapter deals with the impact of atomic uncertainties on the interpretations of the ICM enrichment.

While Chapters 3, 4, and 5 essentially focus on the integrated supernova yields in the central cluster cool cores, in **Chapter 6** I use the CHEERS sample to establish radial abundance profiles in cool-core systems, and interpret them in term of enrichment sources and history.

Finally, **Chapter 7** concludes this thesis by discussing the current limitations in this field and the bright (although still somewhat far) future that the next generation of X-ray missions will offer.

Toeval is logisch.

Coincidence is logical.

– Johan Cruijff

2

Abundance and temperature distributions in the hot intra-cluster gas of Abell 4059

F. Mernier, J. de Plaa, L. Lovisari, C. Pinto, Y.-Y. Zhang, J. S. Kaastra,
N. Werner, and A. Simionescu

(Astronomy & Astrophysics, Volume 575, id.A37, 17 pp.)

Abstract

Using the EPIC and RGS data from a deep (200 ks) *XMM-Newton* observation, we investigate the temperature structure (kT and σ_T) and the abundances of nine elements (O, Ne, Mg, Si, S, Ar, Ca, Fe, and Ni) of the intra-cluster medium (ICM) in the nearby ($z=0.046$) cool-core galaxy cluster Abell 4059. Next to a deep analysis of the cluster core, a careful modelling of the EPIC background allows us to build radial profiles up to $12'$ (~ 650 kpc) from the core. Probably because of projection effects, the ICM temperature is not found to be in single phase, even in the outer parts of the cluster. The abundances of Ne, Si, S, Ar, Ca, and Fe, but also O are peaked towards the core. The elements Fe and O are still significantly detected in the outermost annuli, which suggests that the enrichment by both Type Ia and core-collapse SNe started in the early stages of the cluster formation. However, the particularly high Ca/Fe ratio that we find in the core is not well reproduced by the standard SNe yield models. Finally, 2-D maps of temperature and Fe abundance are presented and confirm the existence of a denser, colder, and Fe-rich ridge south-west of the core, previously observed by *Chandra*. The origin of this asymmetry in the hot gas of the cluster core is still unclear, but it might be explained by a past intense ram-pressure stripping event near the central cD galaxy.

2.1 Introduction

The deep gravitational potential of clusters of galaxies retains large amounts of hot ($\sim 10^7$ – 10^8 K) gas, mainly visible in X-rays, which accounts for no less than 80% of the total baryonic mass. This so-called intra-cluster medium (ICM) contains not only H and He ions, but also heavier metals. Iron (Fe) was discovered in the ICM with the first generation of X-ray satellites (Mitchell et al. 1976); then neon (Ne), magnesium (Mg), silicon (Si), sulfur (S), argon (Ar), and calcium (Ca) were measured with *ASCA* (e.g. Mushotzky et al. 1996). Precise abundance measurements of these elements have been made possible thanks to the good spectral resolution and the large effective area of the *XMM-Newton* (Jansen et al. 2001) instruments (e.g. Tamura et al. 2001). Nickel (Ni) abundance measurements and the detection of rare elements like chromium (Cr) have been reported as well (e.g. Werner et al. 2006b; Tamura et al. 2009). Finally, thanks to its low and stable instrumental background, *Suzaku* is capable of providing accurate abundance measurements in the cluster outskirts (e.g. Werner et al. 2013).

These metals clearly do not have a primordial origin; they are thought to be mostly produced by supernovae (SNe) within cluster galaxy members and have enriched the ICM mainly around $z \sim 2$ – 3 , i.e. during a peak of the star formation rate (Hopkins & Beacom 2006). However, the respective contributions of the different transport processes required to explain this enrichment are still under debate. Among them, galactic winds (De Young 1978; Baumgartner & Breitschwerdt 2009) are thought to play the most important role in the ICM enrichment itself. Ram-pressure stripping (Gunn & Gott 1972; Schindler et al. 2005), galaxy-galaxy interactions (Gnedin 1998; Kapferer et al. 2005), AGN outflows (Simionescu et al. 2008, 2009b), and perhaps gas sloshing (Simionescu et al. 2010) can also contribute to the redistribution of elements. Studying the metal distribution in the ICM is a crucial step in order to understand and quantify the role of these mechanisms in the chemical enrichment of clusters.

Another open question is the relative contribution of SNe types producing each chemical element. While O, Ne, and Mg are thought to be produced mainly by core-collapse SNe (SNcc, including types Ib, Ic, and II, e.g. Nomoto et al. 2006), heavier elements like Ar, Ca, Fe, and Ni are probably produced mainly by Type Ia SNe (SNIa, e.g. Iwamoto et al. 1999). The elements Si and S are produced by both types (see de Plaa 2013, for a review). The abundances of high-mass elements highly depend on SNIa

explosion mechanisms, while the abundances of the low-mass elements (e.g. nitrogen) are sensitive to the stellar initial mass function (IMF). Therefore, measuring accurate abundances in the ICM can help to constrain or even rule out some models and scenarios. Moreover, significant discrepancies exist between recent measurements and expectations from current favoured theoretical yields (e.g. de Plaa et al. 2007), and thus require further investigation.

The temperature distribution in the ICM is often complicated and its underlying physics is not yet fully understood. For instance, many relaxed cluster cores are radiatively cooling on short cosmic timescales, which was presumed to lead to so-called cooling flows (see Fabian 1994, for a review). However, the lack of cool gas (including the associated star formation) in the core revealed in particular by *XMM-Newton* (Peterson et al. 2001; Tamura et al. 2001; Kaastra et al. 2001) leads to the so-called cooling-flow problem and argues for substantial heating mechanisms, yet to be found and understood. For example, heating by AGN could explain the lack of cool gas (see e.g. Cattaneo & Teyssier 2007). Studying the spatial structure of the ICM temperature in galaxy clusters may help to solve it.

Abell 4059 is a good example of a nearby ($z=0.0460$, Reiprich & Böhringer 2002) cool-core cluster. Its central cD galaxy hosts the radio source PKS 2354-35 which exhibits two radio lobes along the galaxy major axis (Taylor et al. 1994). In addition to *ASCA* and *ROSAT* observations (Ohashi 1995; Huang & Sarazin 1998), previous *Chandra* studies (Heinz et al. 2002; Choi et al. 2004; Reynolds et al. 2008) show a ridge of additional X-ray emission located ~ 20 kpc south-west of the core, as well as two X-ray ghost cavities that only partly coincide with the radio lobes. Moreover, the south-west ridge has been found to be colder, denser, and with a higher metallicity than the rest of the ICM, suggesting a past merging history of the core prior to the triggering of the AGN activity.

In this paper we analyse in detail two deep *XMM-Newton* observations (~ 200 ks in total) of A 4059, obtained through the CHEERS¹ project (de Plaa et al., in prep.). The *XMM-Newton* European Photon Imaging Camera (EPIC) instruments allow us to derive the abundances of O, Ne, Mg, Si, S, Ar, Ca, Fe, and Ni not only in the core, but also up to ~ 650 kpc in the outer parts of the ICM. The *XMM-Newton* Reflection Grating Spectrometer (RGS) instruments are also used to measure N, O, Ne, Mg, Si, and Fe. This paper is structured as follows. The data reduction is described in Sect. 2.2.

¹CHEMical Evolution Rgs cluster Sample

We discuss our selected spectral models and our background estimation in Sect. 2.3. We then present our temperature and abundance measurements in the cluster core, as well as their systematic uncertainties (Sect. 2.4), measured radial profiles (Sect. 2.5), and temperature and Fe abundance maps (Sect. 2.6). We discuss and interpret our results in Sect. 2.7 and conclude in Sect. 2.8. Throughout this paper we assume $H_0 = 70 \text{ km s}^{-1} \text{ Mpc}^{-1}$, $\Omega_m = 0.3$, and $\Omega_\Lambda = 0.7$. At the redshift of 0.0460, 1 arcmin corresponds to $\sim 54 \text{ kpc}$. The whole EPIC field of view (FoV) covers $R \simeq 0.81 \text{ Mpc} \simeq 0.51r_{200}$ (Reiprich & Böhringer 2002, where r_{200} is the radius within which the density of cluster reaches 200 times the critical density of the Universe). All the abundances are given relative to the proto-solar values from Lodders et al. (2009). The error bars indicate 1σ uncertainties at a 68% confidence level. Unless mentioned otherwise, all our spectral analyses are done within 0.3–10 keV by using the Cash statistic (Cash 1979).

2.2 Observations and data reduction

Two deep observations (DO) of A 4059 were taken on 11 and 13 May 2013 with a gross exposure time of 96 ks and 95 ks respectively (hereafter DO 1 and DO 2). In addition to these deep observations, two shorter observations (SO; see also Zhang et al. 2011) are available from the *XMM-Newton* archive. The observations are summarised in Table 2.1. Both DO and SO datasets are used for the RGS analysis while for the EPIC analysis we only use the DO datasets. In fact, the SO observations account for $\sim 20\%$ of the total exposure time, and consequently the signal-to-noise ratio S/N would increase only by $\sqrt{1.20} \simeq 1.10$, while the risk of including extra systematic errors and unstable fits due to the EPIC background components (Sect. 2.3 and Appendix 2.B) is high. The RGS extraction region is small, has a high S/N, and its background modelling is simpler than using EPIC; therefore, combining the DO and SO remains safe.

The datasets are reduced using the *XMM-Newton* Science Analysis System (SAS) v13 and partly with the SPEX spectral fitting package (Kaastra et al. 1996) v2.04.

2.2.1 EPIC

In both DO datasets the MOS and pn instruments were operating in Full Frame mode and Extended Full Frame mode respectively. We reduce MOS 1,

Table 2.1: Summary of the observations of Abell 4059. We report the total exposure time together with the net exposure time remaining after screening of the flaring background.

ID	Obs. number	Date	Instrument	Total time (ks)	Net time (ks)
SO 1	0109950101	2000 11 24	RGS	29.3	20.0
SO 2	0109950201	2000 11 24	RGS	24.7	23.4
DO 1	0723800901	2013 05 11	EPIC MOS 1	96.4	71.0
			EPIC MOS 2	96.4	73.0
			EPIC pn	93.8	51.7
			RGS	97.1	77.1
DO 2	0723801001	2013 05 13	EPIC MOS 1	94.7	76.4
			EPIC MOS 2	94.7	77.5
			EPIC pn	92.9	66.4
			RGS	96.1	87.9

MOS 2 and pn data using the SAS tasks `emproc` and `epproc`. Next, we filter our data to exclude soft-proton (SP) flares by building appropriate good time intervals (GTI) files (Appendix 2.A.1) and we excise visible point sources to keep the ICM emission only (Appendix 2.A.2). We keep the single, double, triple, and quadruple events in MOS ($\text{pattern} \leq 12$). Owing to problems regarding charge transfer inefficiency for the double events in the pn detector², we keep only single events in pn ($\text{pattern}=0$). We remove out-of-time events from both images and spectra. After the screening process, the EPIC total net exposure time is ~ 150 ks (i.e. $\sim 80\%$ of the initial observing time). In addition to EPIC MOS 1 CCD3 and CCD6 which are no longer operational, CCD4 shows obvious signs of deterioration, so we discard its events from both datasets as well.

Figures 2.1 and 2.2 show an exposure map corrected combined EPIC image of our full filtered dataset (both detectors cover the full EPIC FoV). The peak of the X-ray emission is seen at $\sim 23^{\text{h}} 57^{\text{m}} 0.8^{\text{s}}$ RA, $-34^{\circ} 45' 34''$ DEC.

We extract the EPIC spectra of the cluster core from a circular region centred on the X-ray peak emission and with a radius of 3 arcmin (Fig. 2.2). Using the same centre we extract the spectra of eight concentric annuli, together covering the FoV within $R \leq 12$ arcmin (Fig. 2.1). The core region corresponds to the four innermost annuli. The RMFs and ARFs are

²See the *XMM-Newton* Current Calibration File Release Notes, XMM-CCF-REL-309 (Smith, Guainazzi & Saxton 2014).

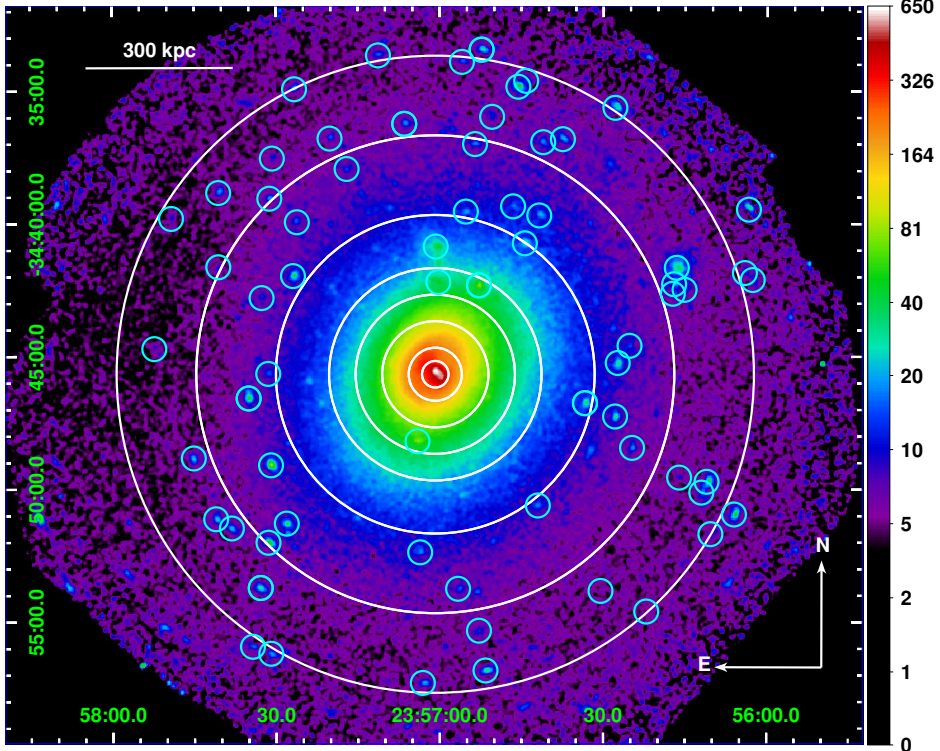


Figure 2.1: Exposure map corrected EPIC combined image of A 4059, in units of number of counts. The two datasets have been merged. The cyan circles show the detected resolved point sources that we excise from our analysis. For clarity of display the radii shown here are exaggerated (excision radius = $10''$, see Appendix 2.A.2). The white annuli show the extraction regions that are used for our radial studies (see text and Sect. 2.5).

processed using the SAS tasks `rmfgen` and `arfgen`, respectively. In order to look at possible substructures in temperature and metallicity, we also create EPIC maps. We divide our EPIC observations in spatial cells using the Weighted Voronoi Tesselations (WVT) adaptive binning algorithm (Diehl & Statler 2006). We restrict the size of our full maps to $R \leq 6$ arcmin. The cell sizes are defined in such a way that in every cell $S/N = 100$. The relative errors of the measured temperature and Fe abundance are then expected to be not higher than $\sim 5\%$ and $\sim 20\%$, respectively (see Appendix 2.C for more details). Because SAS does not allow RMFs and ARFs to be processed for complex geometry regions, we extract them on 10×10 square

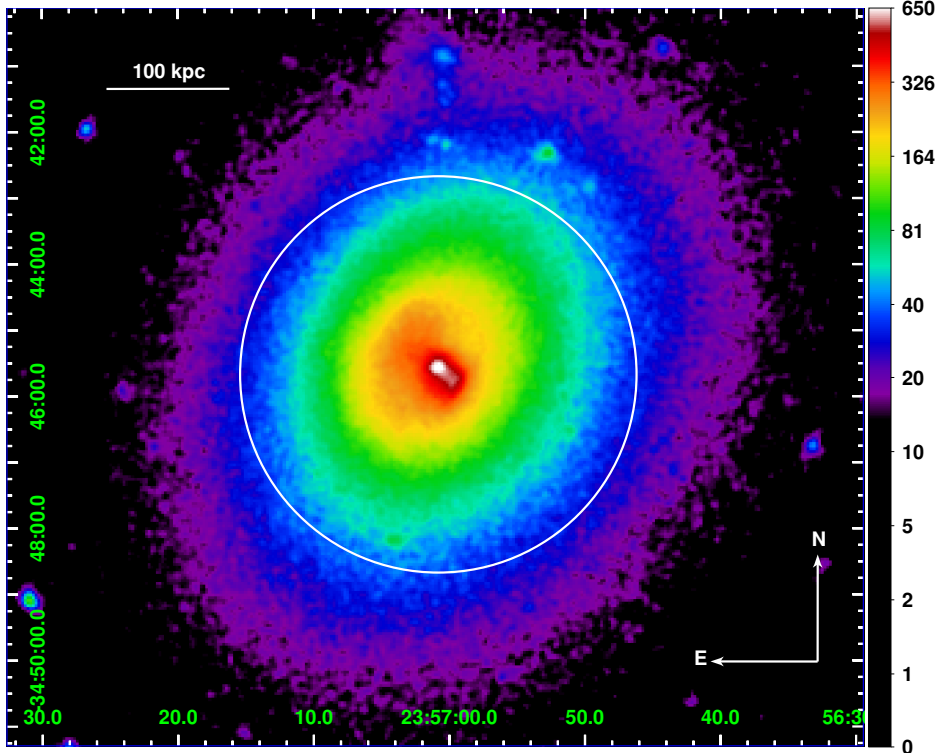


Figure 2.2: Close-up view from Fig. 2.1, centred on the cluster core. The white circle delimits the core region analysed in Sect. 2.4.

regions covering together our whole map and we attribute the raw spectra of each cell to the response files of its closest square region. The spectra and response files are converted into SPEX format using the auxiliary program *trafo*.

2.2.2 RGS

Reflection Grating Spectrometer data of all four observations are used (see Table 2.1 and also Pinto et al. 2015, for details). The RGS detector is centred on the cluster core and its dispersion direction extends from the north-east to the south-west. We process RGS data with the SAS task *rgsproc*. We correct for contamination from SP flares by using the data from CCD9, where hardly any emission from the source is expected. We build the GTI files

similarly to the EPIC analysis (Appendix 2.A.1) and we process the data again with `rgsproc` by filtering the events with these GTI files. The total RGS net exposure time is 208.4 ks. We extract response matrices and RGS spectra for the observations. The final net exposure times are given in Table 2.1.

We subtract a model background spectrum created by the standard RGS pipeline from the total spectrum. This is a template background file, based on the count rate in CCD9 of RGS.

We combine the RGS 1 and RGS 2 spectra, responses and background files of the four observations through the SAS task `rgscombine` obtaining one stacked spectrum for spectral order 1 and one for order 2. The two combined spectra are converted to SPEX format through `trafo`. Based on the MOS1 image, we correct the RGS spectra for instrumental broadening as described in Appendix 2.A.3. We include 95% of the cross-dispersion direction in the spectrum.

2.3 Spectral models

The spectral analysis is done using SPEX. Since there is an important offset in the pointing of the two observations, stacking the spectra and the response files of each of them may lead to bias in the fittings. Moreover, the remaining SP component is found to change from one observation to another (see Appendix 2.B). Therefore, the better option is to fit simultaneously the single spectra of every EPIC instrument and observation. This has been done using `trafo`.

2.3.1 The cie model

We assume that the ICM is in collisional ionisation equilibrium (CIE) and we use the `cie` model in our fits (see the SPEX manual³). Our emission models are corrected from the cosmological redshift and are absorbed by the interstellar medium of the Galaxy (for this pointing $N_H \simeq 1.26 \times 10^{20} \text{ cm}^{-2}$ as obtained with the method of Willingale et al. 2013). The free parameters in the fits are the emission measure $Y = \int n_e n_H dV$, the single-temperature kT , and O, Ne, Mg, Si, S, Ar, Ca, Fe, and Ni abundances. The other abundances with an atomic number $Z \geq 6$ are fixed to the Fe value.

³<http://www.sron.nl/spex>

2.3.2 The `gdem` model

Although `cie` single-temperature models (i.e. isothermal) fit the X-ray spectra from the ICM reasonably well, previous papers (see e.g. Peterson et al. 2003; Kaastra et al. 2004; Werner et al. 2006b; de Plaa et al. 2006; Simionescu et al. 2009b) have shown that employing a distribution of temperatures in the models provides significantly better fits, especially in the cluster cores. The strong temperature gradient in the case of cooling flows and the 2-D projection of the supposed spherical geometry of the ICM suggest that using multi-temperature models would be preferable. Apart from the `cie` model mentioned above, we also fit a Gaussian differential emission measure (`gdem`) model to our spectra. This model assumes that the emission measure Y follows a Gaussian temperature distribution centred on kT_{mean} and as defined by

$$Y(x) = \frac{Y_0}{\sigma_T \sqrt{2\pi}} \exp\left(\frac{(x - x_{\text{mean}})^2}{2\sigma_T^2}\right), \quad (2.1)$$

where $x = \log(kT)$ and $x_{\text{mean}} = \log(kT_{\text{mean}})$ (see de Plaa et al. 2006). Compared to the `cie` model, the additional free parameter from the `gdem` model is the width of the Gaussian emission measure profile σ_T . By definition $\sigma_T=0$ is the isothermal case.

2.3.3 Cluster emission and background modelling

We fit the spectra of the cluster emission with a `cde` and a `gdem` model successively, except for the EPIC radial profiles and maps, where only a `gdem` model is considered.

Since the EPIC cameras are highly sensitive to the particle background, a precise estimate of the local background is crucial in order to estimate ICM parameters beyond the core (i.e. where this background is comparable to the cluster emission). The emission of A 4059 entirely fills the EPIC FoV, making a direct measure of the local background impossible. Some efforts have been made in the past to deal with this problem (see e.g. Zhang et al. 2009, 2011; Snowden & Kuntz 2013), but a customised procedure based on full modelling is more convenient in our case. In fact, an incorrect subtraction of instrumental fluorescence lines might lead to incorrect abundance estimates.

For each extraction region, several background components are modelled in the EPIC spectra in addition to the cluster emission. This modelling

procedure and its application to our extracted regions are fully described in Appendix 2.B. We note that we do not explicitly model the cosmic X-ray background in RGS (although we did in EPIC) because any diffuse emission feature would be smeared out into a broad continuum-like component.

2.4 Cluster core

2.4.1 EPIC

Our deep exposure time allows us to get precise abundance measurements in the core, even using EPIC (Fig. 2.3 top). Moreover, the background is very limited since the cluster emission clearly dominates. Table 2.2 shows our results, both for the combined fits (MOS+pn) and independent fits (either MOS or pn only).

Using a multi-temperature model clearly improves the combined MOS +pn fit. Nevertheless, even by using a `gdem` model, the reduced C-stat value is still high because the excellent statistics of our data reveal anti-correlated residuals between MOS and pn, especially below ~ 1 keV (Fig. 2.3 bottom).

When we fit the EPIC instruments independently, the reduced C-stat number decreases from 1.87 to 1.40 and 1.78 in the MOS and pn fits, respectively. Visually, the models reproduce the spectra better as well. We also note that the temperature and abundances measurements in the core are different between the instruments (Table 2.2). While temperature discrepancies between MOS and pn have been already reported and investigated (Schellenberger et al. 2015), here we focus on the MOS-pn abundance discrepancies. Figure 2.4 (top) illustrates these values and shows the absolute abundance measurements obtained from our `gdem` models. Except for Ne, Ar, and Ca (all consistent within 2σ), we observe systematically higher values in MOS than in pn. Assuming (for convenience) that the systematic errors are roughly in a Gaussian distribution, we can estimate them for different abundance measurements Z_{MOS} and Z_{pn} , having their respective statistical errors σ_{MOS} and σ_{pn} ,

$$\sigma_{\text{sys}} = \sqrt{\sigma_{\text{tot}}^2 - \frac{\sigma_{\text{MOS}}^2 + \sigma_{\text{pn}}^2}{2}}, \quad (2.2)$$

where $\sigma_{\text{tot}} = \sqrt{((Z_{\text{MOS}} - \mu)^2 + (Z_{\text{pn}} - \mu)^2)/2}$ and $\mu = (Z_{\text{MOS}} + Z_{\text{pn}})/2$. We obtain absolute O, Si, S, and Fe systematic errors of $\pm 25\%$, $\pm 30\%$, $\pm 34\%$,

Table 2.2: Best-fit parameters measured in the cluster core (circular region, $R \sim 3$ arcmin). A single-temperature (cie) and a multi-temperature (gdem) model have been successively fitted.

Parameter	Model	MOS+pn	MOS only	pn only
C-stat / d.o.f.	cie	3719/1781	1904/1221	1109/546
	gdem	3331/1780	1703/1220	969/545
$Y (10^{70} \text{ m}^{-3})$	cie	806 ± 3	779.7 ± 1.8	827 ± 3
	gdem	821 ± 3	792 ± 3	845 ± 4
kT (keV)	cie	3.696 ± 0.012	3.837 ± 0.015	3.431 ± 0.18
kT_{mean} (keV)	gdem	3.838 ± 0.016	4.03 ± 0.02	3.58 ± 0.03
σ_T		0.261 ± 0.004	0.266 ± 0.007	0.251 ± 0.008
O	cie	0.49 ± 0.03	0.57 ± 0.04	0.34 ± 0.03
	gdem	0.46 ± 0.04	0.57 ± 0.04	0.33 ± 0.04
Ne	cie	1.08 ± 0.04	1.09 ± 0.04	1.05 ± 0.05
	gdem	0.33 ± 0.05	0.34 ± 0.06	0.36 ± 0.08
Mg	cie	0.45 ± 0.04	0.82 ± 0.05	< 0.04
	gdem	0.45 ± 0.03	0.78 ± 0.05	< 0.08
Si	cie	0.49 ± 0.02	0.64 ± 0.03	0.32 ± 0.03
	gdem	0.51 ± 0.02	0.66 ± 0.03	0.35 ± 0.03
S	cie	0.46 ± 0.03	0.61 ± 0.04	0.25 ± 0.05
	gdem	0.52 ± 0.03	0.66 ± 0.04	0.31 ± 0.05
Ar	cie	0.27 ± 0.07	0.17 ± 0.15	0.35 ± 0.14
	gdem	0.41 ± 0.08	0.30 ± 0.11	0.54 ± 0.15
Ca	cie	0.89 ± 0.09	0.91 ± 0.11	0.78 ± 0.15
	gdem	1.01 ± 0.10	0.98 ± 0.13	0.90 ± 0.15
Fe	cie	0.740 ± 0.008	0.851 ± 0.009	0.624 ± 0.009
	gdem	0.697 ± 0.006	0.803 ± 0.010	0.600 ± 0.010
Ni	cie	1.04 ± 0.08	1.86 ± 0.11	0.34 ± 0.11
	gdem	1.04 ± 0.07	1.83 ± 0.11	0.37 ± 0.10

2.4 Cluster core

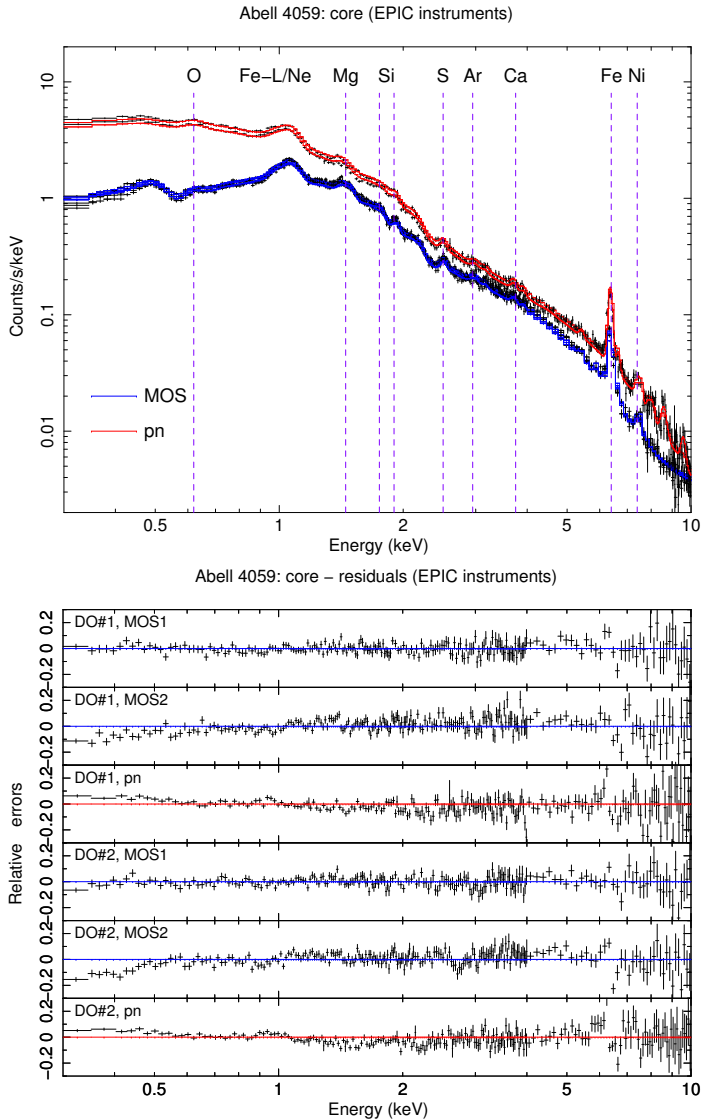


Figure 2.3: EPIC spectra (top) and residuals (bottom) of the core region ($0' - 3'$) of Abell 4059. The two observations are displayed and fitted simultaneously with a `gdem` model. For clarity of display the data are rebinned above 4 keV by a factor of 10 and 20 in MOS and pn spectra, respectively.

and $\pm 14\%$ respectively. The MOS-pn discrepancies in Mg and Ni are too big to be estimated as reasonable systematic errors (Fig. 2.4). No systematic errors are necessary for the absolute abundances of Ne, Ar, and Ca.

If we normalise the abundances relative to Fe in each instrument (Fig. 2.4 bottom), O/Fe is consistent within 2σ and Si/Fe and S/Fe within 3σ . Inversely, the discrepancies on Ar/Fe measurements slightly increase, but their statistical uncertainties are quite large because the main line (~ 3.1 keV) is weak. We note that the discrepancies in Mg and Ni measurements remain huge and almost unchanged. Based on the same method as above, we find that systematic errors of O/Fe, Si/Fe, and S/Fe are reduced to $\pm 8\%$, $\pm 15\%$, and $\pm 20\%$ while the systematic errors of Ar/Fe increase to $\pm 27\%$.

Equivalent widths

One way of determining the origin of the discrepancies in the fitted abundance from different instruments is to derive the abundances using a more robust approach. Instead of fitting the abundances using the gdem model directly, we model each main emission line/complex by a Gaussian and a local continuum (hereafter the Gauss method). The gdem model is still used to fit the local continuum; however, only the Fe abundance is kept to its best-fit value and the other abundances are set to zero⁴. We then check the consistency of this method by comparing it with the abundances reported above (hereafter the GDEM method) in terms of equivalent width (EW), which we define for each line as

$$\text{EW} = \frac{F_{\text{line}}}{F_{\text{c}}(E)}, \quad (2.3)$$

where F_{line} and $F_{\text{c}}(E)$ are the fluxes of the line and the continuum at the line energy E , respectively. Since the EW of a line is proportional to the abundance of its ion, in principle both methods should yield the same abundance. We compare them on the strongest lines of Mg, Si, S, Ca, Fe, and Ni in MOS and pn spectra (Table 2.3) and we convert the average MOS+pn EWs into abundance measurements (Fig. 2.4). While we find consistency between the Gauss and GDEM methods for Ca and Fe-K lines both in MOS and pn, the other elements need to be further discussed.

The EW of Mg obtained in pn using the Gauss method is, significantly, ~ 9 times higher than when using the GDEM method. In the latter case,

⁴When fitting the Fe-K line, the Fe abundance is also set to zero.

2.4 Cluster core

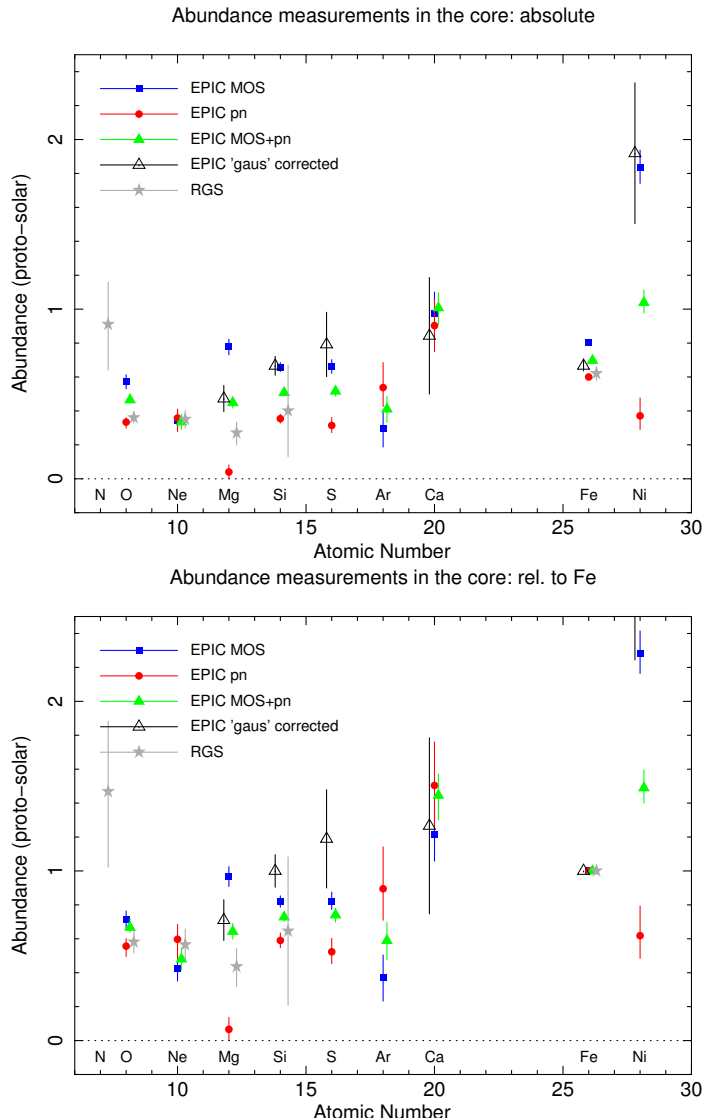


Figure 2.4: EPIC and RGS abundance measurements in the core of A 4059. *Top:* Absolute abundances. *Bottom:* Abundances relative to Fe. The black empty triangles show the mean MOS+pn abundances obtained by fitting Gaussian lines instead of the CIE models (the Gauss method; see text and Table 2.3). The numerical values are summarised in Table 2.4.

Table 2.3: Measured equivalent widths of K-shell lines in the core ($0' - 3'$) using the Gauss and GDEM methods independently for MOS and pn.

Elem.	Line E (keV)	MOS		pn	
		EW _{GDEM} (eV)	EW _{Gauss} (eV)	EW _{GDEM} (eV)	EW _{Gauss} (eV)
Mg	1.44	13.8 ± 0.9	10.1 ± 1.2	0.8 ± 0.8	7.5 ± 1.7
Si	2.00	36.8 ± 1.7	41 ± 3	24 ± 2	41 ± 4
S	2.62	39 ± 2	61 ± 12	23 ± 4	41 ± 13
Ca	3.89	30 ± 4	25 ± 11	33 ± 5	32 ± 12
Fe	6.65	820 ± 10	776 ± 34	684 ± 11	652 ± 32
Ni	7.78	127 ± 8	182 ± 33	28 ± 8	92 ± 26

the pn continuum of the model is largely overestimated around ~ 1.5 keV, making the Mg abundance underestimated. The elements Si and S also show significantly larger EWs in pn using the Gauss method. In terms of abundance measurements, they both agree with the MOS measurements (Fig. 2.4). We also note that beyond ~ 1.5 keV the MOS residuals ratio are known to be significantly higher than the pn ones (Read et al. 2014), and peak near the Si line. This might also partly explain the discrepancies found for S, Si, and maybe Mg.

When using the GDEM method for pn, the Ni-K line is poorly fitted. The large difference in EW obtained when fitting it using the Gauss method emphasises this effect. In fact, when fitting the pn spectra using a `cie` or `gdem` model, a low Ni abundance is computed by the model to compensate the issues in the calibration of the effective area around 1.0–1.5 keV (i.e. where most Ni-L lines are present). For this reason and because of large error bars for the Ni-K line, the fit in pn ignores it.

If we fit the spectra only between 2–10 keV, after freezing kT , σ_T , O, Mg, and Si obtained in our previous fits, we obtain Ni abundances of 1.61 ± 0.35 and 1.37 ± 0.26 for MOS and pn, respectively, making them consistent between each other. This clearly favours the Ni abundance measured with MOS in our previous fits. Interestingly, we also measure Fe abundances of 0.752 ± 0.019 and 0.676 ± 0.017 for MOS and pn, respectively; their discrepancies are then reduced, but still remain. Finally, we note that the pn data are shifted by ~ -20 eV compared to the model around the Fe-K line; this shift does not affect the abundance measurements though.

Our results on the abundance analysis in the core are summarised in Ta-

Table 2.4: Summary of the absolute abundances measured in the core (EPIC and RGS) using a `gdem` model. The mean MOS+pn abundances obtained by fitting Gaussian lines instead of the CIE models (the Gauss method; see text and Table 2.3) is also included. See also Fig. 2.4.

Elem.	EPIC			RGS	
	MOS	pn	MOS+pn	Gauss corr.	
N	—	—	—	—	0.9 ± 0.3
O	0.57 ± 0.04	0.33 ± 0.04	0.46 ± 0.04	—	0.36 ± 0.03
Ne	0.34 ± 0.06	0.36 ± 0.08	0.33 ± 0.05	—	0.35 ± 0.05
Mg	0.78 ± 0.05	< 0.08	0.45 ± 0.03	0.47 ± 0.08	0.27 ± 0.07
Si	0.66 ± 0.03	0.35 ± 0.03	0.51 ± 0.02	0.67 ± 0.06	0.4 ± 0.3
S	0.66 ± 0.04	0.31 ± 0.05	0.52 ± 0.03	0.79 ± 0.19	—
Ar	0.30 ± 0.11	0.54 ± 0.15	0.41 ± 0.08	—	—
Ca	0.98 ± 0.13	0.90 ± 0.15	1.01 ± 0.10	0.8 ± 0.3	—
Fe	0.803 ± 0.010	0.600 ± 0.010	0.697 ± 0.006	0.67 ± 0.03	0.62 ± 0.04
Ni	1.83 ± 0.11	0.37 ± 0.10	1.04 ± 0.07	1.9 ± 0.4	—

ble 2.4 and Fig. 2.4 and are briefly discussed in Sect. 2.7.1. Because their uncertainties are too large, we choose not to consider Mg and Ni abundances in the rest of the paper. Moreover, although the MOS-pn discrepancies are sometimes large and make some absolute abundance measurements quite uncertain, in the following sections we are more interested in their spatial variations. By comparing combined *MOS+pn* measurements only, the systematic errors we have shown here should not play an important role in this purpose.

2.4.2 RGS

Our RGS analysis of the core region focuses on the 7–28 Å (0.44–1.77 keV) first and second order spectra of the RGS detector; RGS stacked spectra are binned by a factor of 5. We test single-, two-temperature `cie` models, and a `gdem` model for comparison.

The models are redshifted and, to model the absorption, multiplied by a *hot* model (i.e. an absorption model where the gas is assumed to be in CIE) with a total $N_{\text{H}} = 1.26 \times 10^{20} \text{ cm}^{-2}$ (Willingale et al. 2013), $kT = 0.5$ eV, and proto-solar abundances.

In order to take into account the emission-line broadening due to the spatial extent of the source, we have convolved the emission components

Table 2.5: RGS spectral fits of Abell 4059.

Parameter	1T cie	2T cie	gdem
C-stat/d.o.f.	1274/887	1244/886	1268/885
$Y_1 (10^{70} \text{ m}^{-3})$	683 ± 4	662 ± 6	480 ± 8
$T_1 (\text{keV})$	2.74 ± 0.08	2.8 ± 0.1	
$Y_2 (10^{70} \text{ m}^{-3})$		4 ± 1	
$T_2 (\text{keV})$		0.80 ± 0.07	
$T_{\text{mean}} (\text{keV})$			3.4 ± 0.2
σ_T			0.26 ± 0.03
N	0.7 ± 0.2	0.9 ± 0.3	0.9 ± 0.3
O	0.32 ± 0.03	0.35 ± 0.03	0.36 ± 0.03
Ne	0.40 ± 0.05	0.43 ± 0.06	0.35 ± 0.05
Mg	0.26 ± 0.06	0.32 ± 0.07	0.27 ± 0.07
Si	0.6 ± 0.3	0.8 ± 0.3	0.4 ± 0.3
Fe	0.57 ± 0.03	0.63 ± 0.04	0.62 ± 0.04

by the *lpro* multiplicative model in SPEX (Tamura et al. 2004; Pinto et al. 2015).

The RGS order 1 and 2 stacked spectra have been fitted simultaneously (Fig. 2.5) and the results of the spectral fits are shown in Table 2.5 and Fig. 2.4. The 2T cie and gdem fits are comparable in terms of Cash statistics and the models are visually similar. Although there might be some residual emission at temperature below 1 keV that can be reproduced by the 2T cie model (Frank et al. 2013), using a gdem model is more realistic regarding the temperature distribution found in the core of most clusters. The abundances are in agreement between the different models because they depend on the relative strength of the lines.

2.5 EPIC radial profiles

We fit the EPIC spectra from each of the eight annular regions mentioned in Sect. 2.2 using a gdem model. We derive projected radial profiles of the temperature, temperature broadening, and abundances (Table 2.6). In our measurements, all the cluster parameters (Y , kT , σ_T , and abundances) are coupled between the three instruments and the two datasets. Since we ig-

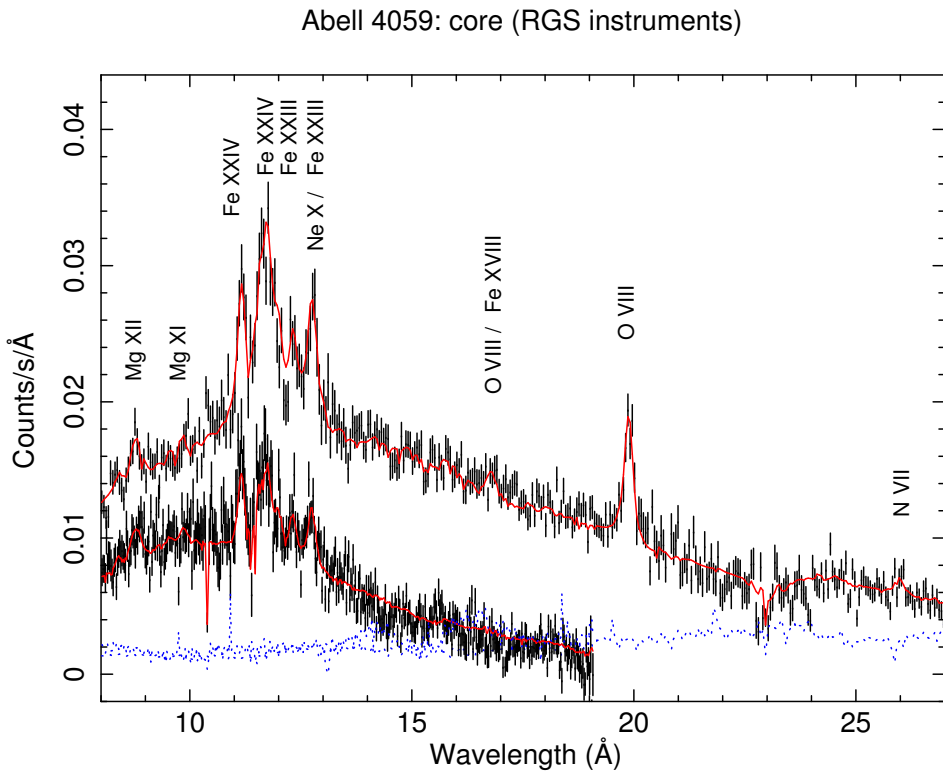


Figure 2.5: RGS first and second order spectra of A 4059 (see also Table 2.5). The spectra are fitted with a 2T cie model. The subtracted backgrounds are shown in blue dotted lines. The main resolved emission lines are also indicated.

more the channels below 0.4 keV (MOS) and 0.6 keV (pn) in the outermost annulus to avoid background contamination (Appendix 2.B), we restrict our O radial profile within 9'. For the same reason, the O abundance measurement between 6'-9' might be biased up to $\sim 25\%$ (i.e. our presumed MOS-pn systematic uncertainty for the O measurement).

Table 2.6: Best-fit parameters measured in eight concentric annuli (covering a total of ~ 12 arcmin of FoV). The spectra of all the annuli have been fitted using a gdem model and adapted from our background procedure.

Parameter	0' – 0.5'	0.5' – 1'	1' – 2'	2' – 3'	3' – 4'	4' – 6'	6' – 9'	9' – 12'
C-stat/d.o.f.	2440/1482	2302/1575	2641/1670	2182/1658	1967/1627	2061/1703	2129/1686	2223/1671
$Y (10^{70} \text{ m}^{-3})$	82.5 ± 0.9	155.9 ± 1.2	314.0 ± 1.6	240.5 ± 1.5	176.1 ± 1.1	256.7 ± 1.9	240 ± 3	150 ± 3
$kT_{\text{mean}} (\text{keV})$	2.84 ± 0.03	3.39 ± 0.03	3.69 ± 0.02	4.06 ± 0.03	4.16 ± 0.05	4.17 ± 0.06	4.21 ± 0.10	3.98 ± 0.20
σ_T	0.222 ± 0.008	0.231 ± 0.010	0.224 ± 0.012	0.23 ± 0.02	0.27 ± 0.02	0.280 ± 0.014	0.33 ± 0.02	0.33 ± 0.04
O	0.53 ± 0.08	0.54 ± 0.06	0.43 ± 0.04	0.38 ± 0.06	0.32 ± 0.07	0.29 ± 0.06	0.39 ± 0.08	–
Ne	0.63 ± 0.13	0.36 ± 0.11	0.41 ± 0.08	0.14 ± 0.09	0.11 ± 0.09	< 0.04	< 0.04	< 0.29
Mg	0.51 ± 0.09	0.51 ± 0.07	0.44 ± 0.05	0.42 ± 0.07	0.45 ± 0.09	0.23 ± 0.08	0.18 ± 0.10	< 0.34
Si	0.78 ± 0.05	0.59 ± 0.04	0.50 ± 0.03	0.32 ± 0.04	0.32 ± 0.05	0.08 ± 0.05	0.07 ± 0.05	< 0.03
S	0.69 ± 0.08	0.55 ± 0.06	0.57 ± 0.05	0.36 ± 0.06	0.29 ± 0.07	0.09 ± 0.07	< 0.13	0.41 ± 0.17
Ar	0.8 ± 0.2	0.65 ± 0.16	0.40 ± 0.13	0.40 ± 0.16	< 0.42	0.2 ± 0.2	< 0.07	0.8 ± 0.5
Ca	1.8 ± 0.3	1.2 ± 0.2	1.12 ± 0.15	0.77 ± 0.19	0.5 ± 0.3	0.7 ± 0.2	0.41 ± 0.36	< 1.34
Fe	0.88 ± 0.03	0.75 ± 0.02	0.653 ± 0.013	0.46 ± 0.02	0.38 ± 0.02	0.31 ± 0.02	0.20 ± 0.02	0.17 ± 0.04
Ni	1.11 ± 0.17	1.28 ± 0.14	0.97 ± 0.12	0.72 ± 0.15	0.68 ± 0.18	0.27 ± 0.18	< 0.25	< 0.07

2.5 EPIC radial profiles

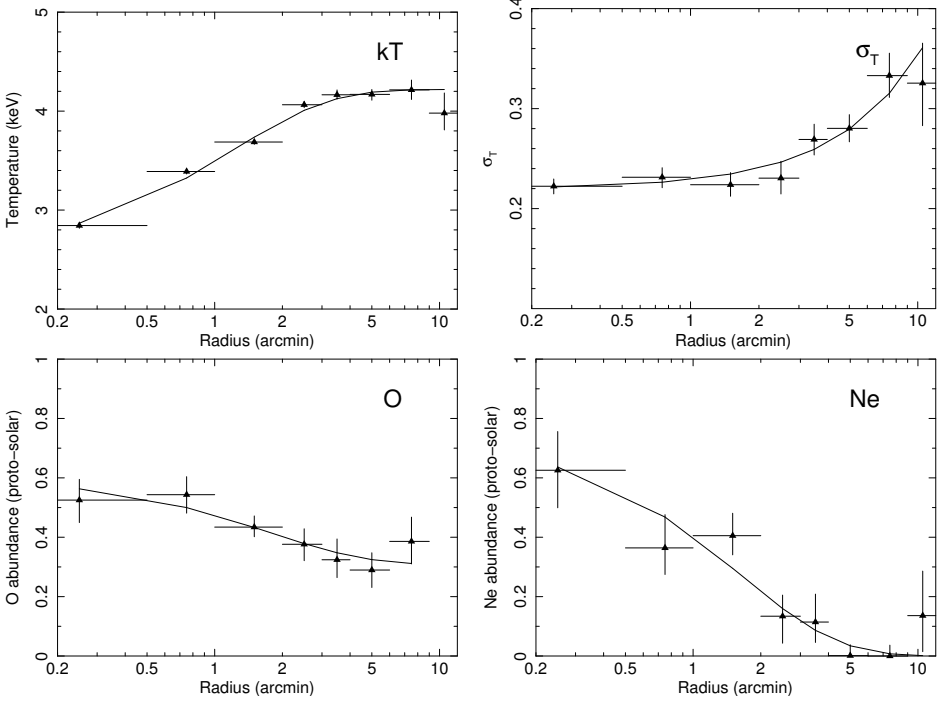


Figure 2.6: EPIC radial profiles of Abell 4059. The datapoints show our best-fit measurements (Table 2.6). The solid lines show our best-fit empirical distributions (Table 2.7). The spectra of all the annuli have been fitted using a gdem model and adapted from our background modelling. We note the change of abundance scale for Ar and Ca.

In order to quantify the trends that appear in our profiles, we fit them with simple empirical distributions. For temperature and abundance profiles,

$$kT(r) = D_\infty + \alpha \exp(-r/r_0) \quad (2.4)$$

$$Z(r) = D_\infty + \alpha \exp(-r/r_0) \quad (2.5)$$

and for σ_T radial profile,

$$\sigma_T(r) = D_\infty + \alpha r^\gamma. \quad (2.6)$$

Table 2.7 shows the results of our fitted trends. Figure 2.6 shows the radial profiles and their respective best-fit distributions.

The temperature profile reveals a significant drop from $\sim 2.5'$ to the innermost annuli, confirming the presence of a cool-core. Beyond $\sim 2.5'$, the

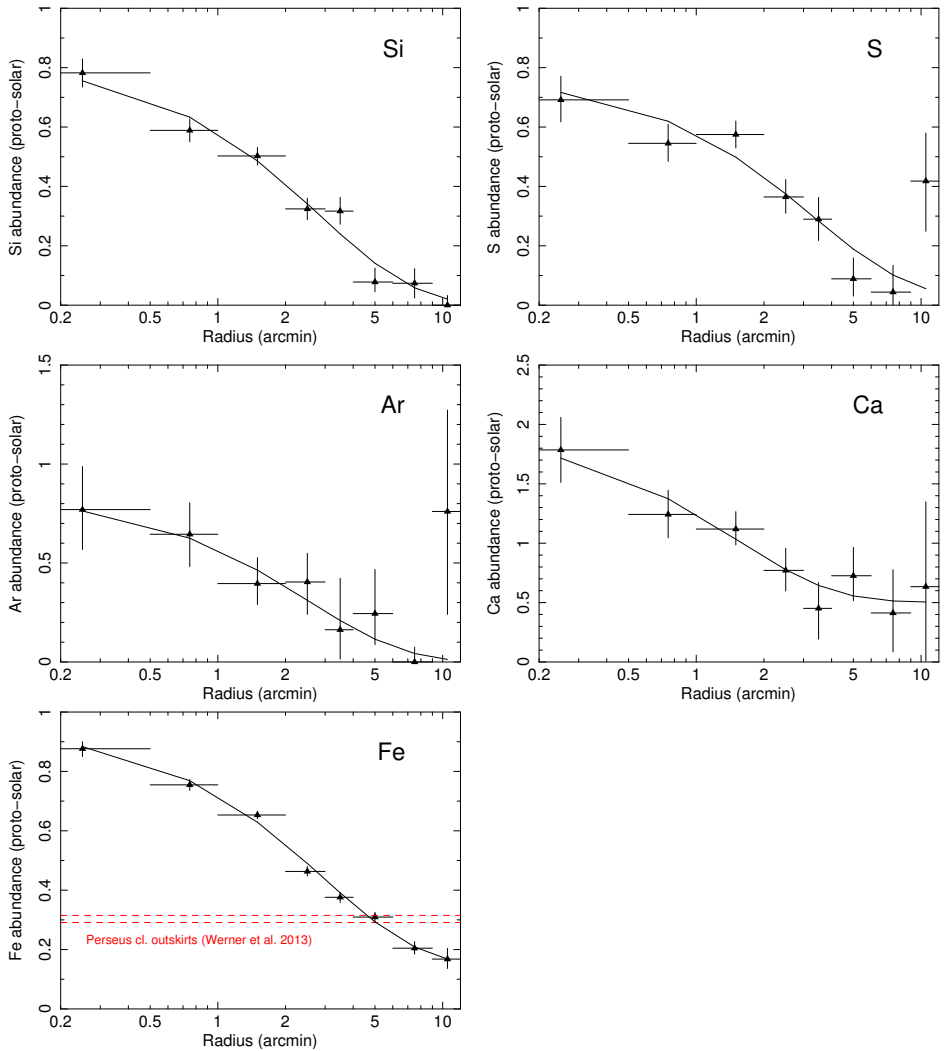


Figure 2.6 (Continued)

Table 2.7: Best-fit parameters of empirical models for our radial profiles. For the meaning of α , r_0 , γ , and D_∞ , see Eqs. 2.4, 2.5, and 2.6 in the text. Unless mentioned (^{c_{ie}}), the empirical models follow the gdem measurements of Table 2.6.

Param.	α	r_0	γ	D_∞	$\chi^2/\text{d.o.f.}$
kT_{mean}	-1.66 ± 0.04	1.21 ± 0.08	—	4.22 ± 0.04	17.28/4
σ_T	0.009 ± 0.010	—	1.2 ± 0.3	0.220 ± 0.016	3.79/4
$kT^{\text{cie$	-1.61 ± 0.04	1.04 ± 0.07	—	4.05 ± 0.03	22.11/4
O	0.29 ± 0.07	$1.76^{+1.1}_{-0.4}$	—	0.31 ± 0.03	7.75/3
O	—	—	—	0.41 ± 0.02	14.22/5
Ne	0.74 ± 0.12	1.63 ± 0.3	—	< 0.019	4.88/4
Si	0.83 ± 0.03	2.83 ± 0.2	—	< 0.02	7.28/4
S	0.75 ± 0.06	3.3 ± 0.6	—	< 0.02	11.72/4
Ar	0.84 ± 0.18	$2.5^{+1.0}_{-0.6}$	—	< 0.07	3.52/4
Ar	—	—	—	0.25 ± 0.04	26.52/6
Ca	1.43 ± 0.3	$1.5^{+1.6}_{-0.4}$	—	< 0.64	2.24/4
Ca	—	—	—	0.96 ± 0.13	22.12/6
Fe	0.80 ± 0.02	2.96 ± 0.3	—	0.14 ± 0.03	9.01/4
Fe ^{c_{ie}}	0.82 ± 0.03	3.06 ± 0.3	—	0.18 ± 0.03	11.39/4

temperature stabilises around $kT \sim 4.2$ keV. More surprisingly, after a plateau around 0.22 from the core to $\sim 2.5'$, σ_T increases up to 0.33 ± 0.04 in the outermost annulus. This increase is significant in our best-fit distribution. In this outer region, we show that kT and σ_T are slightly correlated (Fig. 2.7); however, the radial profiles of kT and σ_T show different trends. Moreover, constraining $\sigma_T=0$ in the outermost annulus clearly deteriorates the goodness of the fit (Fig. 2.7), meaning that the σ_T increase is probably genuine.

Our analysis reveals a slightly decreasing O radial profile. Even if fully excluding a flat trend is hard based on our data, the exponential model (Eq. 2.5) gives a better fit than a constant model $Z(r) = D_\infty$ (Table 2.7). A decrease from 0.54 ± 0.06 to 0.29 ± 0.06 is observed between $0.5'-6'$ as well. Finally, O is still strongly detected in the outermost annuli. We note, however, that additional uncertainties should be taken into account (see above). In fact, the O measurement near the edge of the FoV may also be slightly affected by the modelling of the Local Hot Bubble (Appendix 2.B) through its flux and its assumed O abundance.

As mentioned earlier, Ne is hard to constrain, but is detected. Its abun-

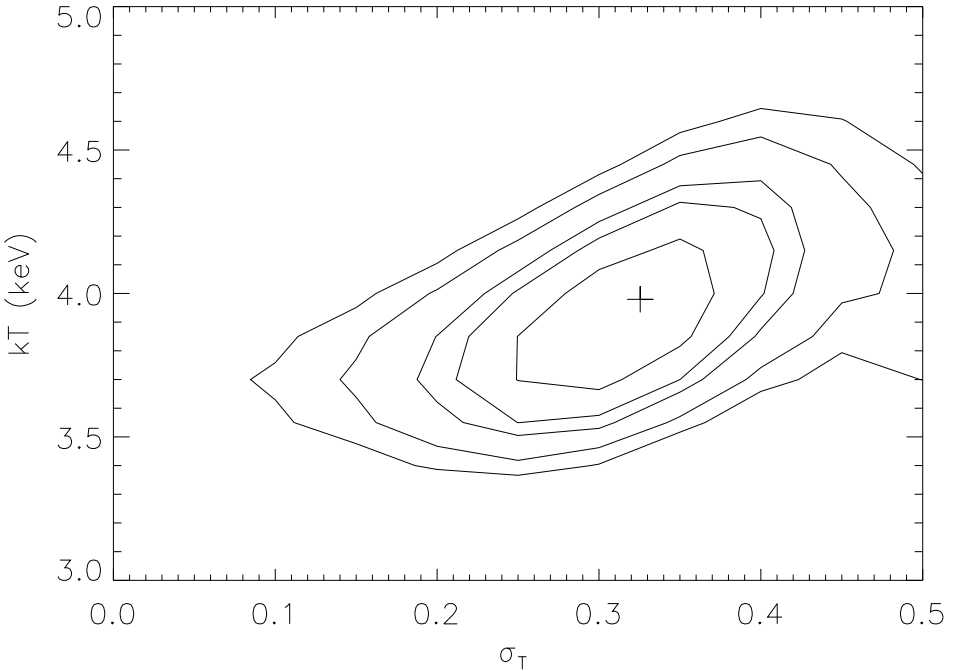


Figure 2.7: Error ellipses comparing the temperature kT with the broadening of the temperature distribution σ_T in the $9'-12'$ annulus spectra. Contours are drawn for 1, 2, 3, 4, and 5σ . The "+" sign shows the best-fit value.

dance drops to zero outside the core while it is found to be more than half its proto-solar value within 0.5 arcmin. Profiles of Si and S abundances also decrease, typically from ~ 0.8 to very low values in the outermost annuli. In every annulus the Si and S measurements are quite similar; this is also confirmed by the best-fit trends which exhibit consistent parameters between the two profiles. The Ar radial profile is harder to interpret because of its large uncertainties, but the trend suggests the same decreasing profile as observed for Si and S.

The Ca radial profile shows particularly high abundances in general, significantly peaked toward the core where it reaches 1.8 ± 0.3 times the proto-solar value and 2.0 ± 0.3 times the local Fe abundance. Finally, we show that Fe abundance is also significantly peaked within the core and decreases toward the outskirts, where our fitted model suggests a flatten-

ing to 0.14 ± 0.03 .

We note that our radial analysis focuses on the projected profiles only. Although deprojection can give a rough idea about the 3-D behaviour of the radial profiles, they are based on the assumption of a spherical symmetry, which is far from being the case in the innermost parts of A 4059 (Sect. 2.6). Moreover, the deprojected abundance radial profiles are not thought to deviate significantly from the projected ones (see e.g. Werner et al. 2006b). Based on the analysis of Kaastra et al. (2004), we estimate that the contamination of photons into incorrect annuli as a result of the EPIC point-spread function (PSF) changes our Fe abundance measurements by $\sim 2\%$ and $\sim 4\%$ in the first and second innermost annuli, respectively, which is not significant regarding our 1σ error bars. The choice of a `gdem` model should take into account both the multi-temperature features due to projection effects and the possible PSF contamination in the kT radial profile.

2.6 Temperature, σ_T , and Fe abundance maps

Using a `gdem` model, we derive temperature and abundance maps from the EPIC data of our two deep observations. The long net exposure time (~ 140 ks) for A 4059 allows the distribution of kT , σ_T , and Fe abundance to be mapped within $6'$. As in the radial analysis, all the EPIC instruments and the two datasets are fitted simultaneously.

In order to emphasise the impact of the statistical errors on the maps and to possibly reveal substructures, we create so-called residuals maps following the method of Lovisari et al. (2011). In each cell, we subtract from each measured parameter the respective value estimated from our modelled radial profile (Fig. 2.6) at the distance r of the geometric centre of the cell. The significance index is defined as being this difference divided by the error on the measured parameter. The kT , σ_T , and Fe abundance maps and their respective error and residuals maps are shown in Fig. 2.8.

The kT map reveals the cool core of the cluster in detail. It appears to be asymmetric and to have a roughly conic shape extending from the north to the east and pointing toward the south-west. Along this axis, the temperature gradient is steeper to the south-west than to the north-east of the core. Most of the relative errors obtained with the `cie` model (not shown here) are within 2–5%, which is in agreement with our expectations (Appendix 2.C); however, they slightly increase with radius. This trend is stronger when using the `gdem` model, and the errors are somewhat larger.

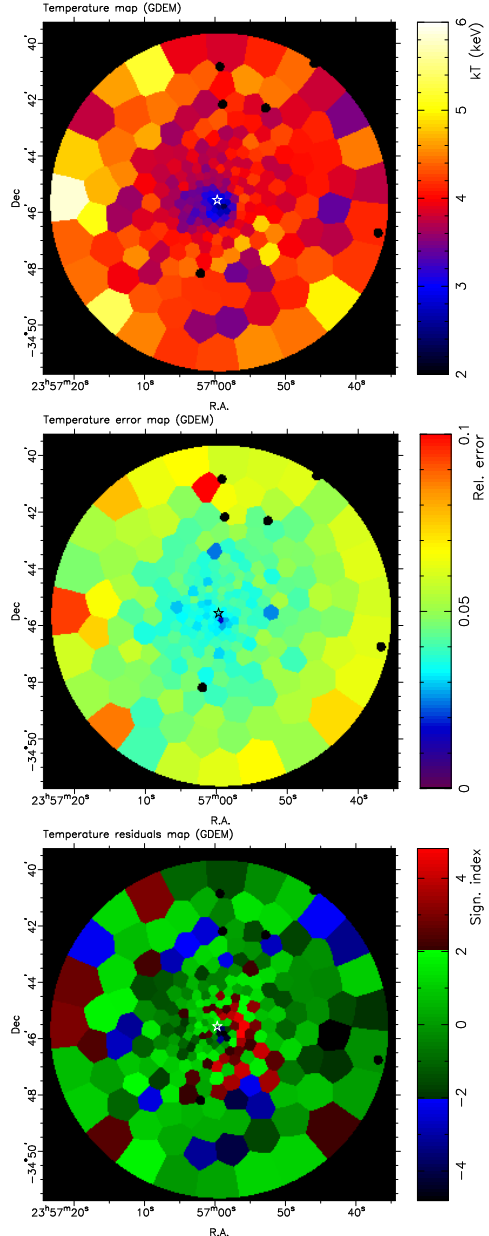


Figure 2.8: From left to right pages: kT , σ_T and Fe abundance maps of A 4059. The top panels show the basic maps (using a gdem model). The middle panels show their corresponding absolute ($\Delta\sigma_T$) or relative ($\Delta T/T$; $\Delta \text{Fe}/\text{Fe}$) errors. The bottom panels show their corresponding residuals (see text). In the centre of each map, the (black or white) star shows the peak of X-ray emission. All the maps cover $R \leq 6$ arcmin of FoV.

2.6 Temperature, σ_T , and Fe abundance maps

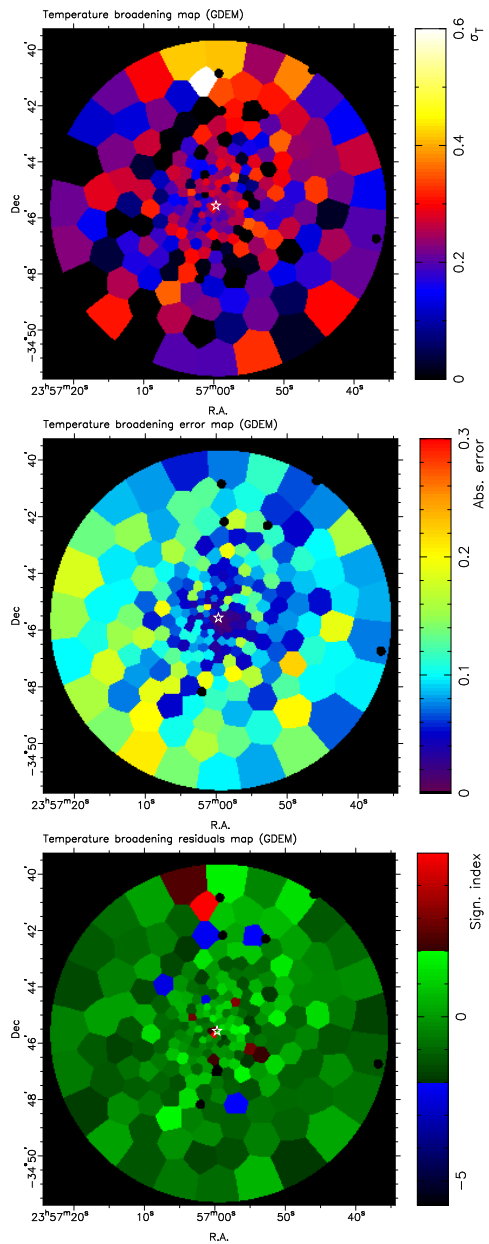


Figure 2.8 (Continued)

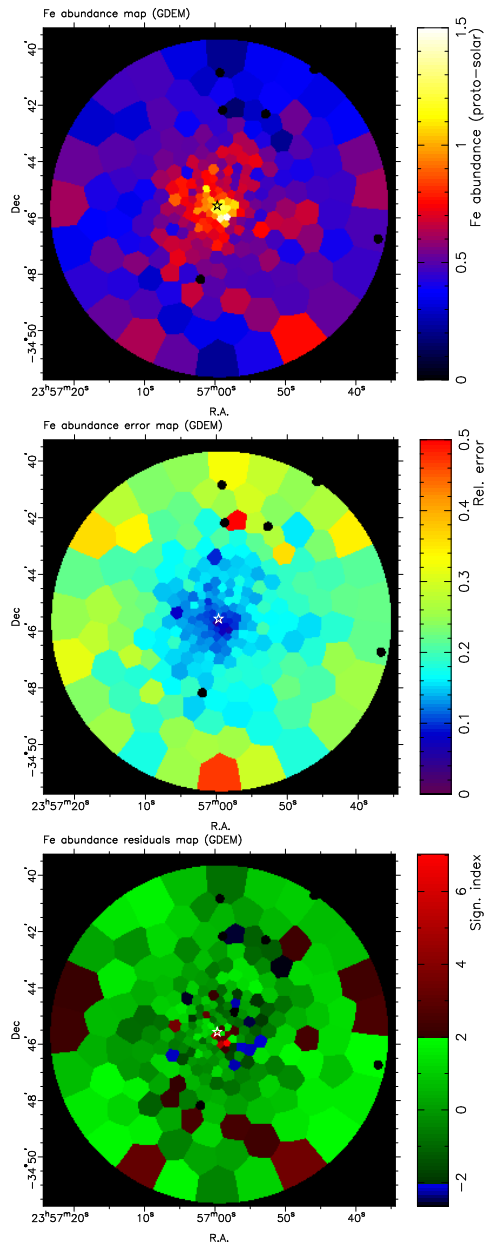


Figure 2.8 (Continued)

2.7 Discussion

A very local part (~ 5 cells) of the core is up to 8σ cooler than our modelled temperature profile. This coldest part is offset $\sim 25''$ SW from the X-ray peak emission. This contrasts with the western part of the core, which shows a significantly hotter bow than the average $\sim 55''$ away from the X-ray peak emission. We also note that some outer cells are found significantly ($>2\sigma$) colder or hotter than the radial trend.

The σ_T map confirms the positive σ_T measurements in most of the cells outside the core, typically within 0.1–0.4. Globally, σ_T is consistent with that measured from the σ_T radial profile. We note that outside the core the errors are inhomogeneous and are sometimes hard to estimate precisely.

The Fe map also shows that the core is asymmetric. As it is in the kT map, the abundance gradient from the core toward the south-west is steeper than toward the north-east. The highest Fe emitting region is found to be $\sim 25''$ SW offset from the X-ray peak emission and coincides with the coldest region. In this offset SW region, Fe is measured to be more than 7σ over-abundant.

We note that the smallest cells ($\sim 12''$) have a size comparable to the EPIC PSF ($\sim 6''$ FWHM); a contamination from leaking photons between adjacent cells might thus slightly affect our mapping analysis. However, the PSF has a smoothing effect on the spatial distributions, and gradients may be only stronger than they actually show in the map. This does not affect our conclusion of important asymmetries of temperature and Fe abundance in the core of A 4059.

2.7 Discussion

We determined the temperature distribution and the elemental abundances of O, Ne, Si, S, Ar, Ca, and Fe in the core region ($\leq 3'$) of A 4059 and in eight concentric annuli centred on the core. In addition, we built 2-D maps of the mean temperature (kT), the temperature broadening (σ_T), and the Fe abundance. Because of the large cross-calibration uncertainties, Mg and Ni abundances are not reliable in these datasets using EPIC, and we prefer to measure the Mg abundance using RGS instead.

2.7.1 Abundance uncertainties and SNe yields

As shown in Table 2.2, the Ne abundance measured using EPIC depends strongly on the choice of the modelled temperature distribution. The main

Ne lines are hidden in the Fe-L complex, around ~ 1 keV. This complex contains many strong Fe lines and is extremely sensitive to temperature. A slight change in the temperature distribution will thus significantly affect the Ne abundance measurement, making it not very reliable using EPIC (see also Werner et al. 2006b). For the same reason, Fe abundances of single- and multi-temperature models might change slightly but already cause a significant difference between both models.

Most of the discrepancies in the abundance determination between the EPIC instruments come from an incorrect estimation of the lines and/or the continuum in pn (Sect. 2.4.1). Cross-calibration issues between MOS and pn have been already reported (see e.g. de Plaa et al. 2007; Schellenberger et al. 2015), but their deterioration has probably increased over time despite current calibration efforts (Read et al. 2014). Our analysis using the Gauss method (Table 2.3 and Fig. 2.4) suggests that in general MOS is more reliable than pn in our case, even though MOS might slightly overestimate some elements as well (e.g. Mg, S, or even Fe). In all cases, this latest method is the most robust one with which to estimate the abundances in the core using EPIC.

Another interesting result is our detection of very high Ca/Fe abundances in the core. This trend has been already reported by de Plaa et al. (2006) in Sérsic 159-03 (see also de Plaa et al. 2007). Within $0.5'$ the combined EPIC measurements give a Ca/Fe ratio of 2.0 ± 0.3 . This is even higher than measured within $3'$ ($\text{Ca}/\text{Fe} = 1.45 \pm 0.14$). Following the approach of de Plaa et al. (2007) and assuming a Salpeter IMF (Salpeter 1955), we select different SNIa models (soft deflagration versus delayed-detonation, Iwamoto et al. 1999) as well as different initial metallicities affecting the yields from SNcc population (Nomoto et al. 2006). We fit the constructed SNe models to our measured abundances in the core (O, Ne, Mg, and Si from RGS; Ar and Ca from EPIC; Fe from the Gauss method). We find that a WDD2 model, taken with $Z=0.02$ and a Salpeter IMF, reproduce our measurements best, with $(\chi^2/\text{d.o.f.})_{\text{WDD2}} = 4.28/6$ (Fig. 2.9). Although the fit is reasonable in terms of reduced χ^2 , it is unable to explain the high Ca/Fe value that we found. Based again on de Plaa et al. (2007), we also considered a delayed-detonation model that fitted the Tycho SNIa remnant best (Badenes et al. 2006). The fit is improved $((\chi^2/\text{d.o.f.})_{\text{Tycho}} = 1.77/5)$, but the model barely reaches the lower error bar of our measured Ca/Fe. Assuming that the problem is not fully solved even by using the latest model, we can raise two further hypotheses that might explain it:

2.7 Discussion

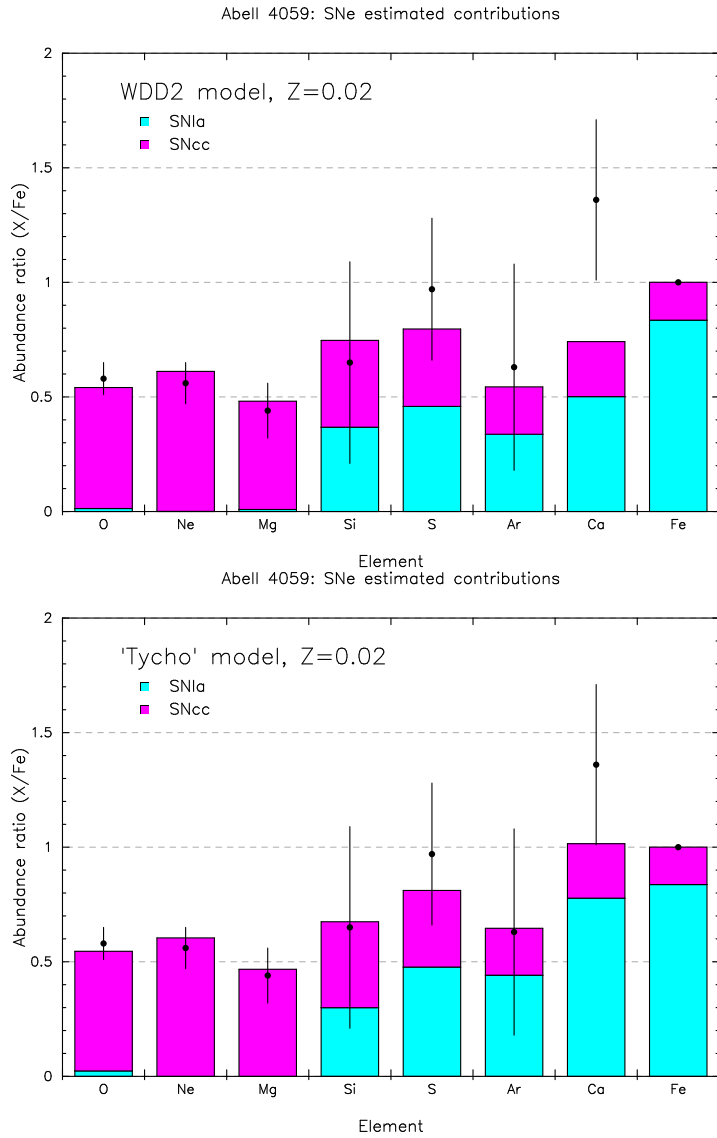


Figure 2.9: Comparison of our EPIC abundance measurements with standard SNe yield models. *Top:* WDD2 delayed-detonation SNIa model (Iwamoto et al. 1999). *Bottom:* Empirically modified delayed detonation SNIa model from the yields of the Tycho supernova (Badenes et al. 2006). The two models are computed with a Salpeter IMF and an initial metallicity of $Z = 0.02$ (Nomoto et al. 2006).

1. Calcium abundance measurements might suffer from additional systematic uncertainties. Our analysis (Sects. 2.4.1 and 2.5) shows, however, that MOS and pn Ca/Fe measurements are consistent within the entire core ($3'$). Moreover, the continuum and EW of Ca lines (~ 3.9 keV) are correctly estimated by our cie models. Because of current efforts to limit them, uncertainties in the atomic database can contribute only partly. Finally the effective area at the position of this line is smooth and no instrumental-line feature is known around ~ 3.9 keV.
2. Some SNe subclasses, so far ignored, might contribute to the metal enrichment in the ICM. For example, the so-called calcium-rich gap transients as a possible subclass of SNIa, are expected to produce a large amount of Ca even outside galaxies, making the transportation of Ca in the ICM much easier (Mulchaey et al. 2014).

2.7.2 Abundance radial profiles

All the abundance radial profiles decrease with radius. Interestingly, O shows a slight decrease (confirmed by our empirical fitted distribution), even though a flat profile cannot be fully excluded. This decreasing trend has been observed in other clusters, such as Hydra A (Simionescu et al. 2009a), A2029, and Centaurus (Lovicari et al. 2011). However, the observations of A 496 (Lovicari et al. 2011) and A 1060 (Sato et al. 2007b) suggest a flatter profile. The O distribution is less clear in Sérsic 159-03 (de Plaa et al. 2006; Lovicari et al. 2011).

Moreover, only O and Fe profiles show abundances significantly higher than zero in the outermost annuli. The Fe profile is clearly peaked to the core, and agrees with typical slopes found in many other clusters (e.g. Simionescu et al. 2009a; Lovicari et al. 2011). Moreover, its apparent plateau in the outer regions may suggest a constant Fe abundance in the ICM even outside r_{500} , as recently observed by *Suzaku* in Perseus (Werner et al. 2013) and other clusters (e.g. Leccardi & Molendi 2008; Matsushita 2011). As seen in Fig. 2.6, the Fe abundance found in the outskirts of Perseus (0.303 ± 0.012 , in proto-solar abundance units) is higher than what we find for A 4059, even when accounting for the systematic uncertainties estimated from the core in Sect. 2.4.1. This constant Fe abundance found in other cluster outskirts and this work suggest that the bulk of the enrichment at least by SNIa started in the early stages of the cluster formation.

In the previous cluster analyses where O appeared to be flat, the increase of O/Fe with radius is usually justified by arguing a very early population of SNIa and SNcc, starting after an intense star formation around $z \sim 2\text{--}3$ (Hopkins & Beacom 2006) and undergoing a very efficient mixing all over the potential well, followed by a delayed population of SNIa responsible for the Fe peaked profile, and produced preferably in the central galaxy members in which a strong ram-pressure stripping is assumed (see also discussion for Sérsic 159-03 from de Plaa et al. 2006). It has also been suggested that ram-pressure stripping could shape the Fe peak profile between $z = 1$ and $z = 0$ (Schindler et al. 2005). However, De Grandi et al. (2014) suggest that the bulk of the Fe peak was already in place before $z = 1$ in most clusters, meaning that at least SNIa type products started to get a centrally peaked distribution early on in the cluster formation. In fact, Fe seems to follow the near-infrared light profile of the central cD galaxies much better at $z = 1$ than at $z = 0$, suggesting that most of the current mixing mechanisms tend to spread out the metals in the ICM.

The decreasing O radial profile measured in this work suggests that the same kind of scenario is likely for SNcc type products. Although its best-fit slope of the profile appears to be flatter than the slope of the Fe radial profile (Table 2.7), the O/Fe radial values are still compatible with a constant distribution (except possibly for the 6'-9' annulus, where systematics might affect the O measurements). Consequently, it is not necessary to invoke a delayed population of SNIa and / or SNcc occurring after $z = 1$, although it might contribute to a minor part of the metals found in the core. At $z \sim 2\text{--}3$ the central cD galaxy and its surrounding galaxy members were already actively star-forming and could have produced the bulk of all metals observed in the core, probably injected into the ICM through galactic winds. More recently, ram-pressure stripping could have also played a minor role in the enrichment of the core, for example to explain the asymmetry found on the maps (see below).

Assuming a flat and positive distribution of Fe and O beyond the FoV, the mixing of the metals is likely very efficient in the outskirts, where the entropy is high. In the core however, the entropy was already very stratified early on without any major mergers to disturb it, and the mixing mechanisms could be less efficient there.

While O and Fe are detected far from the core and this favours an early initial enrichment from SNIa and SNcc types, puzzlingly we do not detect significant abundances of Ne and Si in the outermost annuli. This result

is less striking in the S and Ar radial measurements, even though our fitted trends give small upper limits for D_∞ . Nevertheless, abundance measurements in the outer parts of the FoV can also suffer from additional systematic uncertainties related to the background contribution. These uncertainties may explain our lack of clear detection of Ne, Si, S, and Ar in the outermost annuli. Finally, we note the similarity between the Si and S profiles, already reported in the cD galaxy M 87 by Million et al. (2011).

In addition to these radial trends, our maps show local regions of anomalously rich Fe abundance in the core. This is particularly striking in the south-west ridge, where the Fe abundance is $>7\sigma$ higher than the average trend from its corresponding radial profile. Since no galaxy can be associated with this particular region, it is hard to explain its enrichment with galactic winds. As previously reported and discussed by Reynolds et al. (2008), it is possible that an important part of the metals in the core comes from one early starburst galaxy that passed very close to the cD central galaxy before the onset of the central AGN. In this case ram-pressure stripping could probably have played a dominant role in the enrichment within ~ 0.5 arcmin after the initial enrichment seen through the radial profiles. This possible scenario is also discussed in the next section.

2.7.3 Temperature structures and asymmetries

Although the ICM appears homogeneous and symmetric at large scale, the inner part appears to be more asymmetric (Fig. 2.2). As already observed in the past by *Chandra* (Heinz et al. 2002; Reynolds et al. 2008), the south-west ridge is clearly visible as an additional peaked X-ray emission near the core, and a diffuse tail from the core toward the north-east can also be detected.

Evidence of asymmetries are also found in our spectral analyses. Although our radial kT profile looks similar to other cool-core clusters, our kT and Fe abundance maps show clear inhomogeneities in the ICM structure of A 4059. Compared to the 2-D maps previously measured using *Chandra* (Reynolds et al. 2008), the S/N of the cells in our EPIC maps are ~ 3.3 and ~ 2.5 times greater for kT and the Fe abundance, respectively, allowing us to confirm these substructures with a higher precision and over a larger FoV.

First, like the Fe abundance, the temperature gradient is steeper within the south-west ridge than north-east of the core. The central core (including the south-west ridge) is also significantly colder (~ 2.3 keV) and the south-

west ridge has a higher Fe abundance (~ 1.5) than the rest of the core within $0.5'$. These results confirm the previous study by Reynolds et al. (2008) who also found strong asymmetry in the core of A 4059 using *Chandra*. Their pressure map shows neither asymmetry nor discontinuity in the core, even around the south-west ridge. From both *Chandra* and *XMM-Newton* studies, it is clear that this ridge plays a role in the metal enrichment of the core (see also Sect. 2.7.2) and must be closely linked to the history of the cluster (Reynolds et al. 2008). The hotter bow region found W of the core is likely related to it. Based on the *Chandra* images (Reynolds et al. 2008), sloshing seems an unlikely explanation for the origin of the ridge. Indeed, it appears to be a second brightness peak separated from the core, and its particular morphology is very different from the typical spiral regular pattern of sloshing fronts (see e.g. Paterno-Mahler et al. 2013; Ichinohe et al. 2015). Another scenario is that this local cool, dense, and Fe-rich asymmetry was already present before the triggering of central AGN radio-activity; it was formed by a gas-rich late-type galaxy that plunged very close to the central cD galaxy. An intense starburst caused by its interactions with the dense local ICM occurred and it lost an important part of its metals as a result of the strong gravitational interaction coupled with intense ram-pressure stripping.

Reynolds et al. (2008) estimated that such a galaxy should be within $300v_3$ kpc of the cluster core. They suggested the bright spiral galaxy ESO 349-G009 as being a good candidate, although they were not sure whether this object belongs to A 4059. Looking at the caustic taken from Zhang et al. (2011, see individual galaxy redshifts in the references therein, e.g. Andernach et al. 2005), we can confirm that this is indeed the case (Fig. 2.10). The galaxy is located in the front part of the cluster and moves with a high radial velocity compared to the cD galaxy ($\Delta v \simeq 1800$ km/s). Assuming that this scenario is correct and that the movement of this galaxy near the central cD galaxy was essentially along the line of sight, the absence of an obvious metal tail from ram-pressure stripping on the plane of the FoV is naturally explained. Moreover, the X-ray isophotes joining ESO 349-G009 and the cluster ICM (Fig. 2.11) show an interaction between them and might suggest that the galaxy is escaping from the core. The UV light detected in its arms using the *XMM-Newton* OM instrument (e.g. UVM2 filter) reveals that the galaxy still has a high star formation rate. The gas mass of the ridge ($5 \times 10^9 M_\odot$) is a small percentage of the total stellar mass of ESO 349-G009 (Reynolds et al. 2008).

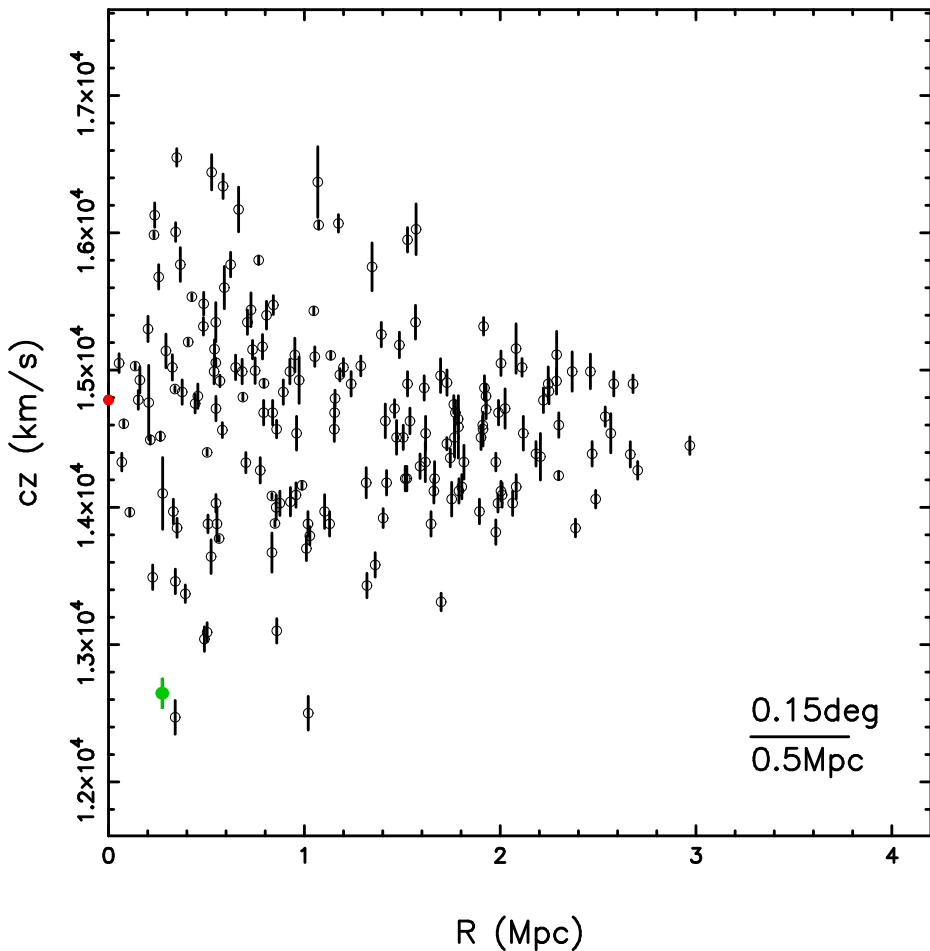


Figure 2.10: Line-of-sight velocity versus projected distance from the central cD galaxy for the member galaxies with optical spectroscopic redshifts in A 4059 taken from Zhang et al. (2011). The central cD galaxy is shown in red. The location of spiral galaxy ESO 349-G009 (green) in the caustic indicates that it belongs to the cluster.

2.8 Conclusions

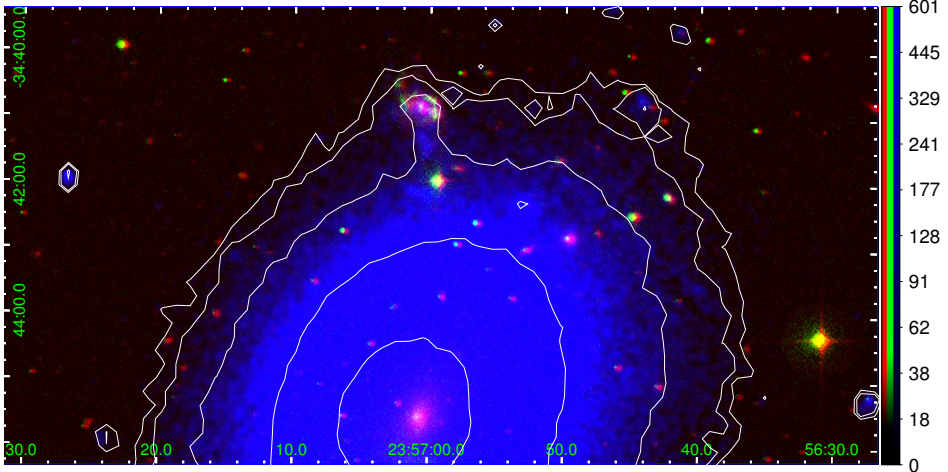


Figure 2.11: RGB mosaic of the central-north part of A 4059. Red: optical filter (UK Schmidt telescope, public data). Green: UVM2 filter (OM instrument). Blue and contours: X-rays (EPIC MOS2+pn). The spiral galaxy ESO 349-G009 and the central cD galaxy are in the top and the bottom of the image respectively.

Finally, both the radial profile and map reveal a constant or increasing trend of σ_T with radius. This is likely explained by projection effects such as the increased effective length along our line of sight. For cooling core clusters, this effective length increases as a function of radius, and a longer effective length will mix more temperatures along the line of sight. A still broad range of temperatures in the local ICM beyond the core cannot be fully excluded, but seems more unlikely. Indeed, although the few outer local colder or hotter cells found in the kT residuals map (Fig. 2.8 bottom) might argue in favour of this second explanation, the temperature (and thus σ_T) measurements in the outer map cells are very sensitive to the background modelling, and are thus affected by these additional systematic uncertainties.

2.8 Conclusions

In this paper we have studied a very deep *XMM-Newton* observation (~ 140 ks of net exposure time) of the nearby cool-core cluster A 4059. Several temperature and abundance parameters have been derived from the spectra both in the core and in eight concentric annuli; moreover, we were able to

derive kT , σ_T , and Fe abundance maps. We conclude the following:

- The temperature structure shows the cool-core and in addition increasing deviations from apparent isothermality in and out of the core.
- The abundances of O, Ne, Si, S, Ar, Ca, and Fe all are peaked toward the core, and we report the presence of Fe and O beyond ~ 0.3 Mpc from the core. This suggests that the enrichment from SNIa and SNcc started early on in the cluster formation, probably through galactic winds in the young galaxy members.
- The EPIC image as well as the temperature and Fe abundance maps reveal strong asymmetries in the cluster core. We confirm a colder and Fe-richer ridge south-west of the core, previously found by *Chandra*, perhaps due to an intense ram-pressure stripping event. Therefore, in addition to an early enrichment through galactic winds, ram-pressure stripping might have greatly contributed to a more recent enrichment of the inner core.
- The Ca/Fe abundance ratio in the core is particularly high (1.45 ± 0.14 using a combined EPIC fit), even accounting for systematic uncertainties. If we assume the Ca/Fe abundance of the entire core to be genuine, it is unlikely explained by current standard SNe yield models. Recently proposed calcium-rich gap transient SNIa might be an interesting alternative with which to explain the high Ca abundance generally found in the ICM.
- Because of cross-calibration issues, the EPIC MOS and pn detectors measure significantly different values of temperature and most abundances. Although this leads to systematic uncertainties on their absolute values, the discrepancies are generally smaller when considering abundances relative to Fe. Moreover, it should not affect relative differences between spectra from different regions if the same instrument(s) are used. Fitting a Gaussian line and a local continuum instead of CIE models is a robust method to measure more reliable abundances.

Acknowledgements

This work is a part of the CHEERS (CHEmical Evolution Rgs cluster Sample) collaboration. We would like to thank its members and the anonymous referee for their feedback and discussions. F.M. thanks Huub Röttgering and Darko Donevski for useful discussions. L.L. acknowledges support by the DFG through grant LO 2009/1-1. Y.Y.Z. acknowledges support by the German BMWi through the Verbundforschung under grant 50 OR 1304. This work is based on observations obtained with *XMM-Newton*, an ESA science mission with instruments and contributions directly funded by ESA member states and the USA (NASA). The SRON Netherlands Institute for Space Research is supported financially by NWO, the Netherlands Organisation for Scientific Research.

2.A Detailed data reduction

2.A.1 GTI filtering

In order to reduce the soft-proton (SP) background, we build good time intervals (GTI) using the light curves in the 10–12 keV band for MOS and 12–14 keV band for pn. We fit the count-rate histograms from the light curves of each instrument, binned in 100 s intervals, with a Poissonian function and we reject all time bins for which the number of counts lies outside the interval $\mu \pm 2\sigma$ (i.e. $\mu \pm 2\sqrt{\mu}$), where μ is the fitted average of the distribution. We repeat the same screening procedure and threshold (so-called 2σ -clipping) for 10 s binned histograms in the 0.3–10 keV band because De Luca & Molendi (2004) reported episodes of particularly soft background flares. In order to get a qualitative estimation of the residual SP flare contamination, we use the `Fin_over_Fout` algorithm which compares the count rates in and out of the FoV of each detector (De Luca & Molendi 2004). We found that in both observations MOS 1 displays a $F_{\text{in}}/F_{\text{out}}$ ratio higher than 1.3, meaning that the observations have been significantly contaminated by SP events. This value is still reasonable though, and a look at the filtered light curve lead us to keep the MOS 1 datasets. Furthermore, a careful modelling of convenient SP spectral components are used in our spectral fittings as well (see Appendix 2.B).

2.A.2 Resolved point sources excision

The point sources in our FoV contribute to the total flux and may bias the astrophysical results that we aim to derive from the cluster emission. Therefore, they should be discarded. We detect all the resolved point sources (RPS) with the SAS task `edetect_chain` and we proceed with a second check by eye in order to discard erroneous detections and possibly include a few missing candidates. It is common practice in extended source analysis to excise bright point sources from the EPIC data. We note, however, that many sources have fluxes below the detection limit S_{cut} and an unresolved component might remain (Appendix 2.B.2).

A remaining problem is how to choose the excision radius in the best way. A very small excision radius may leave residual flux from the excised point sources while a very large radius may cut out a significant fraction of the cluster emission leading to decreased S/N. We define A_{eff} as the extraction region area for the cluster emission when the point sources are

excised with a radius r_s ,

$$A_{\text{eff}} = A \left(1 - \pi r_s^2 \int_{S_{\text{cut}}}^{\infty} \left(\frac{dN}{dS} \right) dS \right), \quad (2.7)$$

where N is the number of sources, S is the flux, and A is the full detection area.

Since we are dealing with a Poissonian process, S/N can be estimated as $\text{S/N} = \frac{C}{\sqrt{C+B}}$, where C and B are the number of counts of the cluster emission and the total background, respectively. The value of C depends on the extraction area and can thus be written $C = C^* A_{\text{eff}}$, where C^* is the local surface brightness of the cluster (counts/"), and B can be divided into the instrumental or hard particle (HP) background I , an unresolved point sources (UPS) component, and the remaining excised point source flux outside the excision region. The total background can be thus written as

$$B = I + \int_0^{S_{\text{cut}}} S \left(\frac{dN}{dS} \right) dS + (1 - EEF(r_s)) \int_{S_{\text{cut}}}^{\infty} S \left(\frac{dN}{dS} \right) dS, \quad (2.8)$$

where $EEF(r_s)$ is the encircled energy fraction of the PSF as a function of radius. We can finally write the total S/N as

$$\text{S/N} = \frac{C^* \sqrt{A \left(1 - \pi r_s^2 \int_{S_{\text{cut}}}^{\infty} \left(\frac{dN}{dS} \right) dS \right)}}{\sqrt{C^* + I + \int_0^{S_{\text{cut}}} S \left(\frac{dN}{dS} \right) dS + (1 - EEF(r_s)) \int_{S_{\text{cut}}}^{\infty} S \left(\frac{dN}{dS} \right) dS}}. \quad (2.9)$$

The optimum S/N can be then computed as a function of r_s and S_{cut} (Eq. 2.9). In Appendix 2.B.2 we discuss the origin of dN/dS . We find and adopt an optimised radius for RPS excision in our dataset of $\sim 10''$.

2.A.3 RGS spectral broadening correction from MOS 1 image

Because the RGS spectrometers are slitless and the source is spatially extended in the dispersion direction, the RGS spectra are broadened. The effect of the broadening of a spectrum by the spatial extent of the source is given by

$$\Delta\lambda = \frac{0.138}{m} \Delta\theta, \quad (2.10)$$

where m is the spectral order and θ is the offset angle in arcmin (see the *XMM-Newton* Users Handbook).

The MOS 1 DET Y direction is parallel to the RGS dispersion direction. Therefore, we extract the brightness profile of the source in the dispersion direction from the MOS 1 image and use this to account for the broadening following the method described by Tamura et al. (2004). This method is implemented through the `Rgsvprof` task in SPEX. As an input of this task, we choose a width of $10'$ around the core and along the dispersion axis, in which the cumulative brightness profile is estimated. In order to correct for continuum and background, we use a MOS 1 image extracted within 0.5–1.8 keV (i.e. the RGS energy band). This procedure is applied to both observations and we average the two spatial profiles obtaining a single profile that will be used for the stacked RGS spectrum.

2.B EPIC background modelling

We split the total EPIC background into two categories, divided further into several components:

1. Astrophysical X-ray background (AXB), from the emission of astrophysical sources and thus folded by the response files. The AXB includes the Local Hot Bubble (LHB), the galactic thermal emission (GTE), and the UPS.
2. Non-X-ray background (NXB), consisting of soft or hard particles hitting the CCD chips and considered as photon events. For this reason, they are not folded by the response files. The NXB contains the SP and the HP backgrounds.

In total, five components are thus carefully modelled.

2.B.1 Hard particle background

High energy particles are able to reach the EPIC detectors from every direction, even when the filter wheel is closed. Besides continuum emission, they also produce instrumental fluorescence lines which should be carefully modelled. Moreover, for low S/N areas, we observe a soft tail in the spectra due to the intrinsic noise of the detector chips. A good estimate of the HP background can be obtained by using Filter Wheel Closed (FWC)

Table 2.8: Best-fit parameters of the HP component, estimated from the full FoV of FWC observations. An equal sign (=) means that the MOS 2 value is coupled with the MOS 1 value.

Parameters	MOS 1	MOS 2	pn
$Y (10^{46} \text{ ph/s/keV})$	87.3 ± 1.2	133.6 ± 1.6	478 ± 117
Γ	0.33 ± 0.01	=	1.37 ± 0.70
$\Delta\Gamma$	-0.18 ± 0.02	=	-1.08 ± 0.25
$E_{\text{break}} (\text{keV})$	3.49 ± 0.25	=	1.05 ± 0.53
b	≤ 0.01	=	0.39 ± 0.17

data which are publicly available on the XMM-Newton SOC webpage⁵. We select FWC data that were taken on 1 October 2011 and 28 April 2011 with an exposure time of 53.7 ks and 35.5 ks for MOS and pn, respectively. We removed the MOS 1 events from CCD3, CCD4, and CCD6 to be consistent with our current dataset.

Instead of subtracting directly the FWC events from our observed spectra, modelling the HP background directly allows a much more precise estimate of the instrumental lines fluxes, which are known to vary across the detector (Snowden & Kuntz 2013).

We fit the individual FWC MOS and pn continuum spectra with a broken power law $F(E) = YE^{-\Gamma}e^{\eta(E)}$ where $\eta(E)$ is given by

$$\eta(E) = \frac{r\xi + \sqrt{r^2\xi^2 + b^2(1 - r^2)}}{1 - r^2} \quad (2.11)$$

with $\xi = \ln(E/E_0)$ and $r = \frac{\sqrt{1+(\Delta\Gamma)^2}-1}{|\Delta\Gamma|}$ (see SPEX manual). In this model, the independent parameters are A , Γ (spectra index), $\Delta\Gamma$ (spectral index break), E_0 (break energy), and b (break strength). Unlike the instrumental lines, this continuum does not vary strongly across the detector. Tables 2.8 and 2.9 show the best-fit parameters that we found for the entire FoV extraction area and the modelled instrumental lines, respectively. In addition to the broken power-law, each instrumental line is modelled with a narrow (FWHM ≤ 0.3) Gaussian function. Although a delta function is more realistic, in this case allowing a slight broadening optimises the correction for the energy redistribution on the instrumental lines.

⁵<http://xmm.esac.esa.int>

Table 2.9: Fluorescent instrumental lines produced by the hard particles. The centroid energies are adapted from Snowden & Kuntz (2013) and Iakubovskiy (2013) (MOS except Si K α) and from our best-fit model (pn + MOS Si K α).

MOS		pn	
Energy (keV)	Line	Energy (keV)	Line
1.49	Al K α	1.48	Al K α
1.75	Si K α	4.51	Ti K α
5.41	Cr K α	5.42	Cr K α
5.90	Mn K α	6.35	Fe K α
6.40	Fe K α	7.47	Ni K α
7.48	Ni K α	8.04	Cu K α
8.64	Zn K α	8.60	Zn K α
9.71	Au L α	8.90	Cu K β
		9.57	Zn K β

2.B.2 Unresolved point sources

An important component of the EPIC background is the contribution of UPS to the total X-ray background. Its flux can be estimated using the so called log N -log S curve derived from blank field data. This curve describes how many sources are expected at a certain flux level. The source function has the form of a derivative (dN/dS) and can be integrated to estimate the number of sources in a certain flux range,

$$N(< S) = \int_S^\infty \left(\frac{dN'}{dS'} dS' \right), \quad (2.12)$$

where N is the number of sources and S is the low-flux limit.

The most common bright UPS are AGNs, but galaxies and hot stars contribute as well. Based on the *Chandra* deep field, Lehmer et al. (2012) find that AGNs are the most dominant in terms of number counts, but in the 0.5–2 keV band the galaxy counts become higher than the AGN counts below a few times $10^{-28} \text{ W m}^{-2} \text{ deg}^{-2}$. The assumed spectral model of this component is a power-law with a photon index of $\Gamma=1.41$ (see e.g. Moretti et al. 2003; De Luca & Molendi 2004). In reality, the power-law index may vary slightly between 1.4–1.5, given the uncertainties in the different surveys and estimations (Moretti et al. 2009). Based on the *Chandra* Deep Field

2.B EPIC background modelling

South (CDF-S) data, Lehmer et al. (2012) define the (dN/dS) relations for each source category as follows:

$$\frac{dN}{dS}^{\text{AGN}} = \begin{cases} K^{\text{AGN}}(S/S_{\text{ref}})^{-\beta_1^{\text{AGN}}} & (S \leq f_b^{\text{AGN}}) \\ K^{\text{AGN}}(f_b/S_{\text{ref}})^{\beta_2^{\text{AGN}}-\beta_1^{\text{AGN}}}(S/S_{\text{ref}})^{-\beta_2^{\text{AGN}}} & (S > f_b^{\text{AGN}}) \end{cases}, \quad (2.13)$$

$$\frac{dN}{dS}^{\text{gal}} = K^{\text{gal}}(S/S_{\text{ref}})^{-\beta^{\text{gal}}}, \quad (2.14)$$

$$\frac{dN}{dS}^{\text{star}} = K^{\text{star}}(S/S_{\text{ref}})^{-\beta^{\text{star}}}. \quad (2.15)$$

Each relation describes a power law with a normalisation constant K and a slope β . Since the (dN/dS) relation of AGNs shows a break, there is an additional β_2 parameter and a break flux f_b . The reference flux is defined as $S_{\text{ref}} \equiv 10^{-14} \text{ erg cm}^{-2} \text{ s}^{-1}$. The best-fit parameters for the studied energy bands are listed in Table 1 of Lehmer et al. (2012).

The relations above can be used to estimate the flux from sources that are not detected in our EPIC observations. The UPS component also holds for the deepest *Chandra* observations. Hickox & Markevitch (2006) found a detection limit of 1.4×10^{-16} in a 1 Ms CDF-S observation and estimated the unresolved flux to be $(3.4 \pm 1.7) \times 10^{-12} \text{ erg cm}^{-2} \text{ s}^{-1} \text{ deg}^{-2}$ in the 2–8 keV band. Since *Chandra* has a much lower confusion limit and a narrower PSF, we do not expect EPIC to reach this detection limit even in a deep cluster observation. It is therefore not necessary to know the log N –log S curve below this flux limit to obtain a reasonable estimate for the unresolved flux.

In the flux range from 1.4×10^{-16} up to the EPIC flux limit, we can calculate the flux using the log N –log S relation. The total unresolved flux Ω_{UPS} for the 2–8 keV band is then calculated using

$$\Omega_{\text{UPS}} = 3.4 \times 10^{-12} + \int_{1.4 \times 10^{-16}}^{S_{\text{cut}}} S' \left(\frac{dN}{dS'} \right) dS' \text{ erg cm}^{-2} \text{ s}^{-1} \text{ deg}^{-2}. \quad (2.16)$$

Using the Eqs. 2.13, 2.14, and 2.15 for $\frac{dN}{dS'}$ in the integral above, the unresolved flux calculation is straightforward. Given the detection limit of our observations $S_{\text{cut}} = 3.83 \times 10^{-15} \text{ W m}^{-2}$, we find a total UPS flux of $8.07 \times 10^{-15} \text{ W m}^{-2} \text{ deg}^{-2}$. This value can be used to constrain the normalisation of the power-law component describing the AXB background in cluster spectral fits. We note that this method does not take the cosmic variance into account (see e.g. Miyaji et al. 2003), which means that the normalisation may still be slightly biased.

2.B.3 Local Hot Bubble and Galactic thermal emission

The LHB component is thought to originate from a shock region between the solar wind and our local interstellar medium (Kuntz & Snowden 2008), while the GTE is the X-ray thermal emission from the Milky Way halo. At soft energies (below ~ 1 keV), the flux of these two foreground components is significant. They are both known to vary spatially across the sky, but we assume that they do not change significantly within the EPIC FoV. Both components are modelled with a `cie` component where we assume the abundances to be proto-solar. Both temperatures are left free, but are expected to be within 0.1–0.7 keV. The GTE component is absorbed by a gas with hydrogen column density ($N_H = 1.26 \times 10^{20} \text{ cm}^{-2}$), while the LHB component is not.

2.B.4 Residual soft-proton component

Even after filtering soft flare events from our raw datasets, a quiescent level of SP remains that might affect the spectra, especially at low S/N and above ~ 1 keV. It is extremely hard to precisely estimate the normalisation and the shape of its spectrum since SP quiescent events strongly vary with detector position and time (Snowden & Kuntz 2013). They may also depend on the attitude of the satellite. For these reasons, blank sky *XMM-Newton* observations are not good enough for our deep exposures. The safest way to deal with this issue is to model the spectrum by a single power law (Snowden & Kuntz 2013). Using a broken power law might be slightly more realistic, but the number of free parameters is then too high to make the fits stable. Although the spectral index Γ of the power law is unfortunately unpredictable and may be different for MOS and pn instruments and between different observations. Since Snowden & Kuntz (2013) reported spectral indices between ~ 0.1 –1.4, we allow the Γ parameter in our fits to vary within this range.

2.B.5 Application to our datasets

We apply the procedure described above for each component on our two observations of A 4059. We extract an annular region with inner and outer radii of 6' and 12', respectively, and centred on the cluster core (Fig. 2.1, the outer two annuli), assuming that all the background components described above contribute to the detected events covered by this area. In order to get

2.B EPIC background modelling

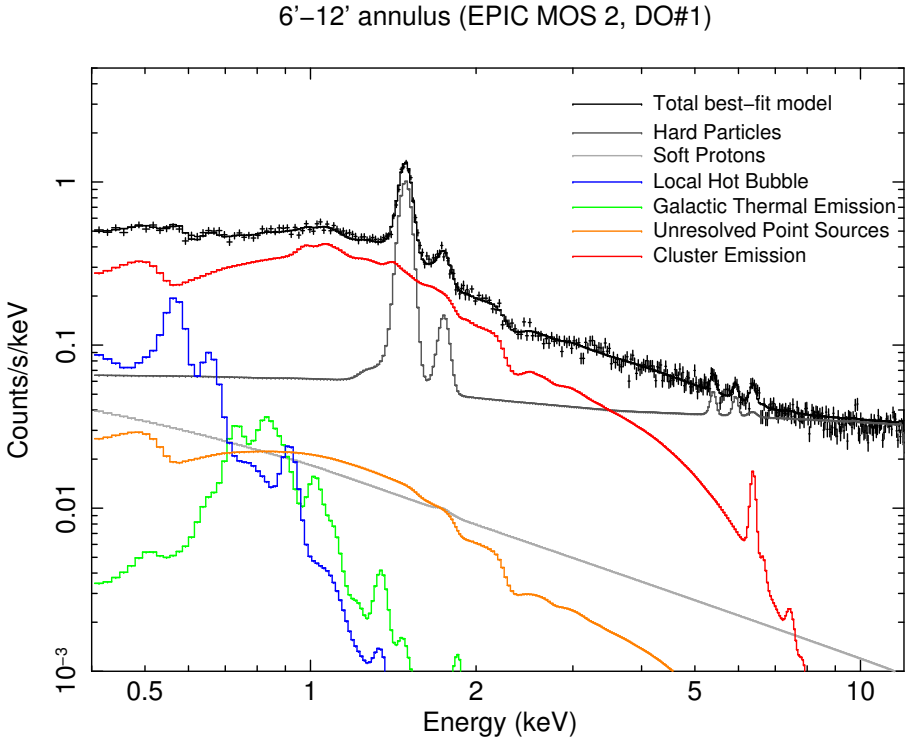


Figure 2.12: EPIC MOS2 spectrum of the 6'-12' annular region around the core (see text). The solid black line represents the total best-fit model. Its individual modelled components (background and cluster emission, solid coloured lines) are also shown.

a better estimation of the foreground thermal emission (GTE and LHB), we fit a *ROSAT* PSPC spectrum from Zhang et al. (2011) simultaneously with our EPIC spectra. This additional observation covers an annulus centred to the core and with inner and outer radii of 28' ($\sim r_{200}$) and 40' ($\sim r_{200} + 12'$), respectively, avoiding instrumental features and visible sources. We note that in this fit we also take the UPS contribution into account. Depending on the extraction area, all the normalisations (except for the UPS component, Appendix 2.B.2) are left free, but are properly coupled between each observation and instrument.

Table 2.10 shows the different background values that we found for the extracted annulus. Figure 2.12 shows the result for the MOS 2 spectrum at the first observation, its best-fit model, and the contribution of every modelled component. As expected, the NXB contribution is more important at

Table 2.10: Best-fit parameter values of the total background estimated in the 6'–12' annular region around the core (see text). A simple asterisk (*) means that the value reaches the upper or lower fixed range. An equal sign (=) means that the corresponding parameters from DO 1 and DO 2 are coupled together.

Bkg comp.	Parameter	Instrument	DO 1	DO 2
SP	Norm. (10^{46} ph/s/keV)	MOS 1	46 \pm 10	30.3 ± 4.5
		MOS 2	18.1 ± 9.4	14.5 ± 3.4
		pn	22.8 ± 4.2	15.70 ± 1.07
	Γ	MOS	1.18 ± 0.08	1.63 ± 0.11
		pn	0.29 ± 0.09	0.10 ± 0.02 0.00^*
		MOS+pn	26.4 ± 4.7	=
GTE	$Y (10^{69} \text{ m}^{-3})$			
	kT (keV)		0.54 ± 0.08	=
LHB	$Y (10^{69} \text{ m}^{-3})$	MOS+pn	311.8 ± 5.1	=
	kT (keV)		0.168 ± 0.002	=
UPS	Norm. (10^{49} ph/s/keV)	MOS+pn	58.29 (fixed)	=
	Γ		1.41 (fixed)	=

high energies. Above \sim 5 keV, the cluster emission is much smaller than the HP background. Consequently and as already reported, the temperature and abundances measured by EPIC are harder to estimate in the outer parts of the FoV.

Finally, we apply and adapt our best background model to the core region (Sect. 2.4) and the eight concentric annuli (Sect. 2.5). The normalisation of every background component has been scaled and corrected for vignetting if necessary. From the background parameters, only the normalisations of the HP component (initially evaluated from the 10–12 keV band, where negligible cluster emission is expected), as well as those of the instrumental fluorescent lines, are kept free for all the spectra. In the outermost annulus (9'–12') we ignore the channels below 0.4 keV (MOS) and 0.6 keV (pn) to avoid low energy instrumental noise. For the same reason we ignore the channels below 0.4 keV (MOS) and 0.5 keV (pn) in the second outermost annulus (6'–9'). The background is also applied to and adapted for the analysis of the spectra of each map cell (Sect. 2.6).

2.C S/N requirement for the maps

Despite their good statistics, we want to optimise the use of our data and find the best compromise between the required spatial resolution of our maps (Sect. 2.6) and S/N. The former is necessary when searching for inhomogeneities and kT /metal clumps (i.e. the smaller the better), the latter to ensure that the associate error bars are small enough to make our measurement significant. Clearly, these variables depend on the properties of the cluster and on the exposure time of our observations.

We perform a set of simulations to determine what the best combination of S/N and spatial resolution is for the case of A 4059. For every annulus (i.e. the ones determined in Sect. 2.5) we simulate a spectrum with input parameters (i.e. kT , O, Ne, Mg, Si, S, Ca, Fe, Ni, and the normalisation) corresponding to the ones determined in the radial profiles analysis. The AXB and the HP background are added to the total spectrum by using the properties derived in Appendix 2.B. We allow their respective normalisations to vary within $\pm 3\%$ in order to take into account spatial variations on the FoV. Starting from the value we derived for the radial profile, we rescale the normalisation of the simulated spectrum to the particular spatial resolutions we are interested in (here we test $15'', 20'', 25'', 30'', 40'', 50'',$ and $60''$). We then fit the spectrum as done for the real data and for all the annuli and spatial resolutions we calculate the relative errors on the temperature and Fe abundance as a function of S/N. The median values of 300 realisations are shown in Fig. 2.13 with their 1σ errors.

A S/N of 100 is required to measure the abundance with a relative error lower than $\sim 20\%$. With this choice the temperature will be also determined with a very good accuracy, i.e. relative errors always lower than $\sim 5\%$.

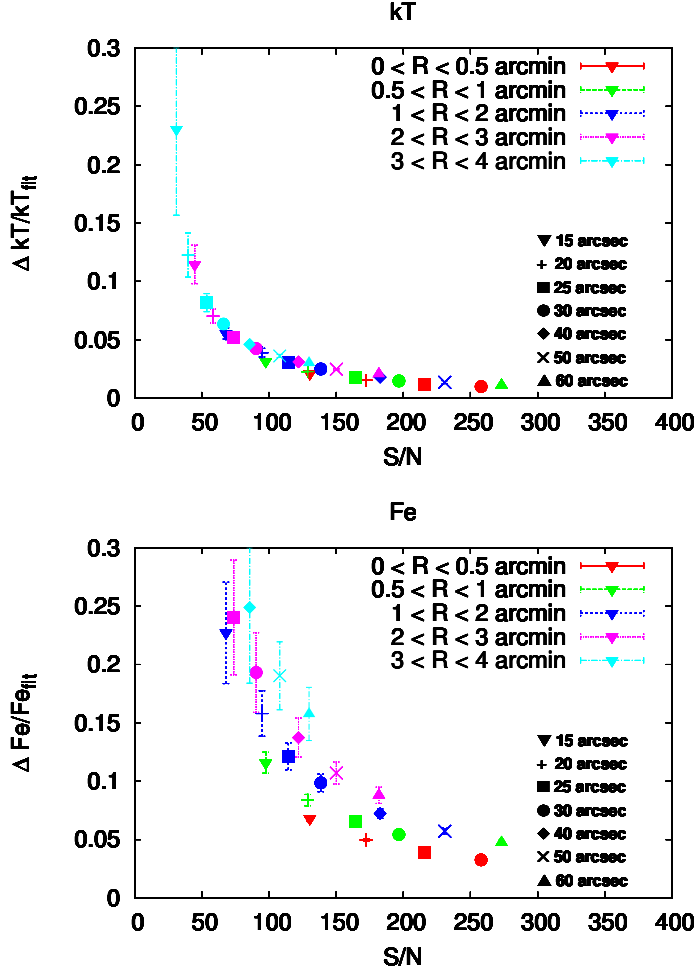


Figure 2.13: Expected relative errors on the temperatures (top) and abundances (bottom). Different cell sizes (symbols) are simulated within the inner five annuli (colours).

*The world is noisy and messy.
You need to deal with the noise and uncertainty.*

– Daphne Koller

3

Origin of central abundances in the hot intra-cluster medium I. Individual and average abundance ratios from **XMM-Newton EPIC**

F. Mernier, J. de Plaa, C. Pinto, J. S. Kaastra, P. Kosec, Y.-Y. Zhang, J. Mao,
and N. Werner

(Astronomy & Astrophysics, Volume 592, id.A157, 18 pp.)

Abstract

The hot intra-cluster medium (ICM) is rich in metals, which are synthesised by supernovae (SNe) explosions and accumulate over time into the deep gravitational potential well of clusters of galaxies. Since most of the elements visible in X-rays are formed by Type Ia (SNIa) and / or core-collapse (SNcc) supernovae, measuring their abundances gives us direct information on the nucleosynthesis products of billions of SNe since the epoch of the star formation peak ($z \sim 2\text{--}3$). In this study, we use the EPIC and RGS instruments on board *XMM-Newton* to measure the abundances of nine elements (O, Ne, Mg, Si, S, Ar, Ca, Fe, and Ni) from a sample of 44 nearby cool-core galaxy clusters, groups, and elliptical galaxies. We find that the Fe abundance shows a large scatter ($\sim 20\text{--}40\%$) over the sample, within $0.2r_{500}$ and especially $0.05r_{500}$. Unlike the absolute Fe abundance, the abundance ratios (X/Fe) are uniform over the considered temperature range ($\sim 0.6\text{--}8 \text{ keV}$) and with a limited scatter. In addition to an unprecedented treatment of systematic uncertainties, we provide the most accurate abundance ratios measured so far in the ICM, including Cr/Fe and Mn/Fe which we firmly detected ($>4\sigma$ with MOS and pn independently). We find that Cr/Fe, Mn/Fe, and Ni/Fe differ significantly from the proto-solar values. However, the large uncertainties in the proto-solar abundances prevent us from making a robust comparison between the local and

the intra-cluster chemical enrichments. We also note that, interestingly, and despite the large net exposure time (~ 4.5 Ms) of our dataset, no line emission feature is seen around ~ 3.5 keV.

3.1 Introduction

About 80–90% of the baryonic matter in the Universe is in the form of a hot and diffuse intergalactic gas, which has mostly a very low density and, therefore, is hard to observe. However, in the largest gravitationally bound regions of the Universe, which are clusters of galaxies, the density and temperature of this hot gas, or intra-cluster medium (ICM), becomes high enough for it to glow in X-rays. This ICM, which has been extensively studied by X-ray observatories over the past decades (for a review, see Böhringer & Werner 2010), is particularly rich in metals (e.g. Mitchell et al. 1976; Mushotzky et al. 1996). Since the baryonic content of the Universe just after the Big Bang consists exclusively of hydrogen and helium (and traces of lithium), these heavy elements – typically from oxygen to nickel – must have been synthesised by stars and supernovae (SNe) in the galaxy members and then ejected into the ICM (for a review, see Werner et al. 2008; de Plaa 2013).

Although the general picture of this chemical enrichment is now well established, many aspects are still poorly understood. In addition to the question of the transport mechanisms that drive the enrichment, a major uncertainty resides in the metal yields produced by Type Ia (SNIa) and core-collapse (SNcc) supernovae. In fact, the nature of the SNIa progenitors and the SNIa explosion mechanisms are still under debate, while the global nucleosynthesis of SNcc highly depends on the initial mass function (IMF) and the initial metallicity of the considered stellar population. Moreover, in addition to SNe, AGB stars can also play a role in releasing lighter metals (e.g. nitrogen) or even heavy metals (via the *s*-process). Taken together, these unsolved questions lead to large uncertainties in predicting the global abundance ratios that are finally released by the SNe and AGB stars into the ICM.

In contrast to the remaining uncertainties in the theoretical yields from the SNe/AGB models, the current generation of X-ray observatories measures the chemical abundances in the ICM with remarkable accuracy since most transitions of H- and He-like elements from $Z=7$ to $Z=28$ fall within 0.2–12 keV. Thanks to the large effective area and the good spectral reso-

lution of its European Photon Imaging Camera (EPIC, Strüder et al. 2001; Turner et al. 2001) and Reflection Grating Spectrometer (RGS, den Herder et al. 2001), *XMM-Newton* is particularly suitable for measuring abundances of elements like oxygen (O), neon (Ne), magnesium (Mg), silicon (S), sulfur (S), argon (Ar), calcium (Ca), iron (Fe), and nickel (Ni), especially in cool-core objects¹ which exhibit a high surface brightness in X-ray and where the most prominent K-shell emission lines of these elements are clearly detected. Consequently, the accuracy of these measurements can, in principle, bring new constraints on the SNe (and AGB) models, and can lead to a deeper understanding of the chemical enrichment processes beyond galactic scales.

Several authors have reported such analyses by measuring the abundances in the ICM of nearby clusters and groups. For instance, de Plaa et al. (2007) has compiled a sample of 22 cool-core clusters and found that the standard SNIa models fail to reproduce the Ar/Ca and Ca/Fe abundance ratios. They also show that the number of SNIa over the total number of SNe highly depends on the considered models. De Grandi & Molendi (2009) have shown that Si/Fe abundance ratios are remarkably uniform over a sample of 26 cool-core clusters observed with *XMM-Newton*, arguing for a similar enrichment process within cluster cores. However they suggest that systematic uncertainties are too large to precisely estimate the relative contribution of SNIa and SNcc. Finally, many abundance studies have also been performed on individual objects (e.g. Werner et al. 2006b; de Plaa et al. 2006; Sato et al. 2007a; Simionescu et al. 2009b, Chapter 2). From these studies, and considering the actual instrumental performances of current X-ray observatories, it appears that higher quality data (i.e. with longer exposure time) spread over larger samples are needed to clarify the actual picture of the precise origin of metals in the ICM.

In this work, we use new and archival *XMM-Newton* EPIC observations to measure the chemical abundances of nine elements (O, Ne, Mg, Si, S, Ar, Ca, Fe, and Ni) in the core of a sample of nearby cool-core galaxy clusters, groups, and elliptical galaxies. These EPIC observations are then combined with the RGS abundance measurements adapted from de Plaa et al. (2017) in order to derive average X/Fe abundance ratios representative of the nearby ICM. Taking into account as many systematic uncer-

¹A cluster, or group, is defined as “cool-core” when the ICM in its core is sufficiently dense that its cooling time, typically of the order of $\sim \sqrt{T_X/n_e}$, is shorter than the Hubble time.

tainties as possible, we discuss the robustness of these measurements and compare them to the proto-solar abundances. In Chapter 4, we discuss in detail the astrophysical implications of our results, and compare our average abundance pattern presented here with predictions from theoretical SNIa and SNcc yield models.

This paper is structured as follows. In Sect. 3.2, we present the sample and the data reduction pipeline. In Sect. 3.3 we describe the spectral analysis procedure applied to our EPIC observations. Our results are presented in Sect. 3.4, briefly discussed in Sect. 3.5, and summarised in Sect. 3.6. Throughout this paper we assume cosmological parameters of $H_0 = 70 \text{ km s}^{-1} \text{ Mpc}^{-1}$, $\Omega_m = 0.3$, and $\Omega_\Lambda = 0.7$. All the error bars are given at a 68% confidence level.

3.2 Observations and data preparation

Our sample consists of the CHEERS² catalogue (de Plaa et al. 2017), and is detailed in Table 3.1 (see also Pinto et al. 2015; de Plaa et al. 2017). It includes 44 nearby ($z < 0.1$) cool-core clusters, groups, and elliptical galaxies for which the OVIII 1s–2p line at 19 Å is detected by the RGS instrument with $>5\sigma$. More information on the intrinsic properties of these objects (e.g. fluxes) can be found in various available cluster catalogues, such as the HIGFLUGCS (Reiprich & Böhringer 2002), the REFLEX (Böhringer et al. 2004b), and the ACCEPT (Cavagnolo et al. 2009) catalogues. In our sample, recent *XMM-Newton* observations (AO-12, PI: de Plaa) have been combined with archival data. We only select the pointings for which the combined EPIC observations (MOS 1, MOS 2, and pn) gather at least 15 ks of net exposure time. The observations that suffer from high soft flare events or calibration problems are also excluded.

3.2.1 Data reduction

All the data are reduced with the *XMM-Newton* Science Analysis System (SAS) v14.0.0 and by using the calibration files dated by March 2015. The RGS data are the same as used in Pinto et al. (2015, see their Table 1), and are reduced the same way. We reduce the EPIC data by using the standard pipeline command `emproc` and `epproc`, and, following the standard recommendations, we keep the single to quadruple pixel MOS events

²CHEmical Enrichment Rgs Sample

Table 3.1: *XMM-Newton*/EPIC observations used in this paper (see Pinto et al. 2015, for details on RGS observations). The new observations from the CHEERS proposal are shown in boldface.

Source	ObsID	Net exposure time ^(a)			z ^(b)	r_{500} ^(c)	Type ^(d)
		MOS 1 (ks)	MOS 2 (ks)	pn (ks)			
2A 0335+096	0109870101 0147800201	85.7	86.6	81.4	0.0349	1.05	h
A 85	0723802101/2201	191.1	193.6	158.2	0.0556	1.21	h
A 133	0144310101 0723801301/2001	134.3	137.4	95.8	0.0569	0.94	h
A 189	0109860101	35.7	36.8	33.3	0.0318	0.50	c
A 262	0109980101 0504780201	53.4	54.7	43.2	0.0161	0.74	h
A 496	0135120201 0506260301/0401	131.4	138.2	103.3	0.0328	1.00	h
A 1795	0097820101	38.1	37.0	25.4	0.0616	1.22	h
A 1991	0145020101	29.2	29.3	20.5	0.0587	0.82	h
A 2029	0111270201 0551780201/0301/0401/0501	147.5	154.4	107.7	0.0767	1.33	h
A 2052	0109920101 0401520501/0801 0401520901/1101/1201/1601	93.0	92.7	53.7	0.0348	0.95	h
A 2199	0008030201/0301/0601 0723801101/1201	130.2	129.7	114.1	0.0302	1.00	h
A 2597	0147330101 0723801701	110.7	112.0	85.3	0.0852	1.11	h
A 2626	0083150201 0148310101	50.1	50.6	41.8	0.0573	0.84	h
A 3112	0105660101 0603050101/0201	186.6	190.8	153.6	0.0750	1.13	h
A 3526 / Centaurus	0046340101 0406200101	151.8	153.1	128.8	0.0103	0.83	h
A 3581	0205990101 0504780301/0401	113.0	117.8	84.1	0.0214	0.72	c
A 4038 / Klemola 44	0204460101 0723800801	78.7	79.6	71.4	0.0283	0.89	h
A 4059	0109950101/0201 0723800901/1001	194.9	198.5	153.9	0.0460	0.96	h
AS 1101 / Sérsic 159-03	0123900101 0147800101	121.0	122.9	108.8	0.0580	0.98	h
AWM 7	0135950101 0605510101	148.7	149.6	153.9	0.0172	0.86	h
EXO 0422	0300210401	39.5	38.9	34.9	0.0390	0.89	h
Fornax / NGC 1399	0012830101 0400620101	106.2	114.2	75.1	0.0046	0.40	c
HCG 62	0504780501/0601	121.8	126.7	101.6	0.0146	0.46	c
Hydra A	0109980301 0504260101	96.3	101.5	74.7	0.0538	1.07	h
M 49 / NGC 4472	0112550601 0200130101	93.1	94.8	86.3	0.0044	0.53	c
M 60 / NGC 4649	0021540201 0502160101	118.4	119.1	108.0	0.0037	0.53	c
M 84 / NGC 4374	0673310101	32.0	34.0	30.5	0.0034	0.46	c
M 86 / NGC 4406	0108260201	68.4	70.4	47.0	-0.0009	0.49	c
M 87 / NGC 4486	0114120101 0200920101	113.9	114.5	96.8	0.0044	0.75	c
M 89 / NGC 4552	0141570101	23.2	24.4	18.3	0.0010	0.44	c
MKW 3s	0109930101 0723801501	147.7	148.9	126.9	0.0450	0.95	h
MKW 4	0093060101 0723800701	75.5	74.9	56.9	0.0200	0.62	h
NGC 507	0080540101 0723800301	124.4	124.8	103.7	0.0165	0.60	c
NGC 1316 / Fornax A	0302780101 0502070201	123.7	127.2	75.2	0.0059	0.46	c
NGC 1404	0304940101	26.8	14.8	21.0	0.0064	0.61	c
NGC 1550	0152150101 0723800401/0501	166.3	167.0	128.2	0.0123	0.62	c
NGC 3411	0146510301	21.4	21.6	19.8	0.0155	0.47	c
NGC 4261	0056340101 0502120101	108.6	109.8	85.8	0.0074	0.45	c
NGC 4325	0108860101	20.2	19.0	16.3	0.0258	0.58	c
NGC 4636	0111190701	56.1	56.3	54.5	0.0037	0.35	c
NGC 5044	0037950101 0554680101	119.0	121.8	100.4	0.0090	0.56	c
NGC 5813	0302460101 0554680201/0301	138.2	143.2	106.8	0.0064	0.44	c
NGC 5846	0021540501 0723800101/0201	171.0	173.9	147.9	0.0061	0.36	c
Perseus	0085110101 0305780101	155.5	156.6	132.1	0.0183	1.29	h
Total		4 492.3	4 563.6	3 666.9			

^(a) Total exposure time after cleaning the data from soft flares (see text). ^(b) Redshifts were taken from Reiprich & Böhringer (2002), except for A 189 (Hudson et al. 2001); A 1991, A 2626, HCG 62, and M 87 (ACCEPT catalog – Cavagnolo et al. 2009); M 89 (Mahdavi & Geller 2001); NGC 1316 (Pinto et al. 2014); NGC 1404 (Morris et al. 2007); M 84, M 86, NGC 4261, and NGC 4649 (Smith et al. 2000).

^(c) Values of r_{500} were taken from Pinto et al. (2015, and references therein). ^(d) Classification of the objects. The letter h stands for the “hot” clusters (>1.7 keV), while the letter c stands for the “cool” groups/ellipticals (<1.7 keV). M 87 is an exception, and is classified as cool even though its central temperature is about ~ 2 keV (see text).

(PATTERN \leqslant 12), and only the single pixel pn events (PATTERN==0). Moreover, only the highest quality MOS and pn events (FLAG==0) are taken into account. We filter our observations from soft-proton flares by building good time interval (GTI) files following the method described in Chapter 2. We extract light curves within the 10–12 keV (MOS) and the 12–14 keV (pn) bands in 100 s bins, we calculate the mean count rate μ and the standard deviation σ , and we apply a threshold of $\mu \pm 2\sigma$ to the fitted distribution. For safety (Lumb et al. 2002), we repeat the procedure for the 0.3–10 keV band in 10 s bins. The average fraction of “good” time accepted after such a filtering is \sim 77%, \sim 78%, and \sim 66% for MOS 1, MOS 2, and pn, respectively, although this fraction varies widely from pointing to pointing. For each object, the net exposure times of the EPIC instruments are indicated in Table 3.1. Combining our whole dataset, we obtain total EPIC and RGS net exposure times of \sim 4.5 Ms and \sim 5.1 Ms, respectively.

Finally, point-like sources might pollute our spectra; therefore, we need to discard all of them from the rest of our analysis. We first detect the point sources of every dataset within four spectral bands (0.3–2 keV, 2–4.5 keV, 4.5–7.5 keV, and 7.5–12 keV) using the SAS task edetect_chain. After a second check by eye, we excise circular regions with $10''$ of radius around the point sources (except in some specific situations where a larger excision radius is required to remove scattered photons from bright foreground sources). This radius size is estimated to be a good compromise between discarding the polluting flux of the point sources and keeping a maximum of cluster emission in their neighbourhood (Chapter 2). Depending on the target, the typical fraction of removed flux after discarding the point sources varies between \sim 0.3% and \sim 4%.

3.2.2 Spectra extraction

The sources of our sample span a wide range of sizes, masses, and temperatures, and studying their elemental abundances with EPIC over one common astrophysical scale r_{core} is difficult in practice. A definition of r_{core} as $0.2r_{500}$ ³ for the farther (and, by selection, hotter) clusters is commonly found in the literature (e.g. de Plaa et al. 2007); however, most of the nearest galaxy groups from our sample are seen at this radius with an angular size $\theta > 15$ arcmin, i.e. beyond the EPIC field of view (FoV). Moreover,

³ r_{500} is defined as the radius within which the gas density is 500 times the critical density of the Universe.

extracting spectra over a large θ for these cooler and more compact objects will include a lot of background, which may dominate beyond $\sim 2\text{--}3$ keV and entirely flood the K-shell lines of crucial elements such as S, Ar, Ca, or Ni. Therefore, we choose to split our sample into two subsamples:

1. The “hot” galaxy clusters ($kT \geq 1.7$ keV, 23 objects),
2. The “cool” galaxy groups and ellipticals ($kT < 1.7$ keV, 21 objects).

Using the SAS task `evselect`, we extract the EPIC spectra of every source within a circular region, centred on the peak of the cluster X-ray emission and within a radius of $0.05r_{500}$. Since in the hot clusters a radius of $0.2r_{500}$ can also be reached and provides better signal-to-noise ratio (S/N), we extract these spectra as well.

Table 3.1 classifies each object in one of these two subsamples. Only M87 deviates from the rule. Indeed, although its main central temperature is about ~ 2 keV (and is thus considered a hot object), its $0.2r_{500}$ limit is beyond the EPIC FoV, and only the spectra within $0.05r_{500}$ could be extracted.

We extract the RGS spectra as described in Pinto et al. (2015) and in de Plaa et al. (2017). Since the dispersion direction of RGS extends along the whole EPIC FoV, its extraction region will be always different from our circular EPIC extraction regions. Therefore, we extract all the RGS spectra using a cross-dispersion width of $0.8'$ from the EPIC FoV, which still focuses on the ICM core. In Sect. 3.4.3 we show that this choice does not affect our results.

The redistribution matrix file (RMF), which gives the channel probability distribution for a photon of given energy, is built using the task `rmfgen`. The ancillary response file (ARF), which provides the effective area curve as a function of the energy and the position on the detectors, is built using the task `arfgen`. Both the RMF and the ARF contain all the information relative to the response of the instruments, and need to be further applied for each observation to the spectral modelling⁴.

3.3 EPIC spectral analysis

We use the SPEX fitting package (Kaastra et al. 1996) v2.05 to perform the spectral analysis of our sample. We fit all our spectra using the C-

⁴See the “Users Guide to the XMM-Newton Science Analysis System”, Issue 11.0, 2014 (ESA: XMM-Newton SOC).

statistics (i.e. a modified Cash statistics; Cash 1979), which is appropriate for Poisson-noise dominated data (see the SPEX manual).

Making the reasonable assumption that the hot ICM is in a collisional ionisation equilibrium (CIE) state, throughout this paper we describe its emission using a `cie` model (based on an updated version of the `mekal` plasma code, Mewe et al. 1985). This model includes processes such as collisional ionisation and excitation-autoionisation, as well as radiative and dielectronic recombination (for further details, we refer the reader to the SPEX manual⁵). We adopt the updated ionisation balance calculations of Bryans et al. (2009). The abundances are calculated from all the transitions and ions of a given element, and are scaled to the proto-solar values⁶ of Lodders et al. (2009).

We fit the cluster emission component in EPIC with a multi-temperature `cie` model, the Gaussian Differential Emission Measure (`gdem`) model, which reproduces a Gaussian temperature distribution in the form

$$Y(x) = \frac{Y_0}{\sigma_T \sqrt{2\pi}} \exp\left(\frac{(x - x_{\text{mean}})^2}{2\sigma_T^2}\right), \quad (3.1)$$

where $x = \log(kT)$ and $x_{\text{mean}} = \log(kT_{\text{mean}})$, kT_{mean} is the peak temperature of the distribution, and σ_T is the full width at half maximum of the distribution (see de Plaa et al. 2006). By definition, $\sigma_T=0$ provides a single-temperature `cie` model (1T).

The use of a multi-temperature model for such a study is crucial since most of the clusters and groups have a complicated thermal structure in their cores where the cooling rate and temperature gradient are quite important. Therefore, assuming the plasma to be isothermal in general may lead to the so-called Fe bias, i.e. an underestimate of the Fe abundance (see e.g. Buote & Canizares 1994; Buote & Fabian 1998; Buote 2000). The effects of different thermal models on the abundances and a comparison between EPIC and RGS measurements are discussed below (Sect. 3.4.3).

For both EPIC and RGS abundances, we also correct the O and Ne estimates from updated calculations of the radiative recombination contribution to the cluster emission as a function of its mean temperature. We do so by multiplying the O and Ne best-fit measurements of each object by the

⁵<https://www.sron.nl/astrophysics-spex>

⁶The proto-solar abundances used in this paper (Lodders et al. 2009) are the most up-to-date representative abundances of the solar system at its formation, as they are based on meteoritic compositions.

factors of the corrected O VIII and Ne X Lyman α fluxes, as described in Appendix 3.B. On average, these corrections increase the O and Ne abundances by $\sim 20\%$ and $\sim 6\%$, respectively.

The Galactic absorption that we apply to our fitted thermal models is modelled by the transmission of a neutral plasma (hot model, for which $kT=0.5$ eV). In EPIC, the hydrogen column density N_{H} has been estimated from a grid search of (fixed) values within

$$N_{\text{HI}} - 5 \times 10^{19} \text{ cm}^{-2} \leq N_{\text{H}} \leq N_{\text{H,tot}} + 1 \times 10^{20} \text{ cm}^{-2}, \quad (3.2)$$

where N_{HI} and $N_{\text{H,tot}}$ are respectively the neutral (Kalberla et al. 2005) and total (neutral and molecular) hydrogen column densities estimated using the method of Willingale et al. (2013). More details on the reasons for this approach are given in Appendix 3.A.

Details on the RGS spectral analysis (including models, free parameters, and background treatment) can be found in de Plaa et al. (2017), and in Pinto et al. (2015).

3.3.1 Background modelling

Although the clusters considered in this work are usually bright and display a high S/N within their core, in most of them the EPIC background can still play a significant role, especially in the hard spectral bands (i.e. $\gtrsim 2$ keV) where less thermal emission is expected. Because a slightly incorrect scaling in the subtraction of background data (taken from either filter closed wheel data or blank sky observations) can significantly affect the temperature estimates and thus bias the spectral analyses (de Plaa et al. 2006), we choose here to model the background directly in our spectra. The method we use is extensively described in Chapter 2. In summary, we model five separate background components:

- The local hot bubble, modelled by a non-absorbed isothermal `cie` component, whose abundances are kept proto-solar;
- The galactic thermal emission, modelled by an absorbed isothermal `cie` component, whose abundances are also kept proto-solar;
- The unresolved point sources, modelled by an absorbed power law with a photon index fixed to 1.41 (De Luca & Molendi 2004);

- The hard particle background, modelled by a broken power law (unfolded by the effective area) and several instrumental Gaussian profiles. The parameters are taken from Chapter 2, except for all the normalisations, which are left free;
- The soft-proton background, modelled by a power law (unfolded by the effective area). The parameters are estimated using EPIC spectra covering the total FoV (where the parameters of the g_{dem} component from the ICM are also left free; see Sect. 3.3.2). From such spectra, the ICM emission can be easily constrained in the soft band ($\lesssim 2$ keV), while the particle backgrounds clearly dominate the harder bands, making the soft-proton background contribution easier to estimate.

The fluxes and the temperatures of the local hot bubble and galactic thermal emission components, as well as the flux of the unresolved point sources, are estimated from *ROSAT* PSPC spectra extracted from the region beyond r_{200} of each object (Zhang et al. 2009).

Finally, all these background components are fixed and rescaled to the sky area of our EPIC core spectra (except the normalisation of the hard particle background, which we always left free in order to avoid incorrect scalings and temperature biases, see above).

In addition to the background described above, M 87, M 89, NGC 4261, NGC 4636, and NGC 5813 host a powerful active galactic nucleus (AGN), which can generate cavities in the hot gas (e.g. Russell et al. 2013), but can also pollute the total X-ray emission. For each of these observations, we start by extracting a circular region of $30''$ centred on the AGN, and we fit its EPIC spectra with an absorbed power law (in addition to the cluster emission and the background components described above). We then extrapolate this additional component to the EPIC core spectra, fixing its column density and photon index values derived from the $30''$ aperture region, and rescaling its normalisation to the area ratio of these two extracted regions. We note that in the EPIC core spectra the 0.5–10 keV flux of the AGN component is never larger than $\sim 15\text{--}20\%$ of the cluster emission. This justifies a posteriori our choice of fitting the AGN contribution rather than excising the AGN, i.e. where the peak of the cluster emission is.

3.3.2 Global fits

In addition to the normalisation of the hard particle background, the only parameters that are left free when fitting our spectral components to the EPIC spectra of the core regions are the normalisation (or emission measure, $Y = \int n_e n_H dV$) of the gdem model; its mean temperature (kT_{mean}); σ_T ; and the abundances of O, Ne, Mg, Si, S, Ar, Ca, Fe, and Ni. The other $Z \geq 6$ abundance parameters are coupled to the value of the Fe abundance parameter, and are thus not free. The MOS and pn spectra of every pointing are fitted simultaneously. Since the large number of total parameters prevents us from fitting simultaneously three observations or more, for each object we form pairs of two pointings that we fit simultaneously. For objects including ≥ 3 pointings, we then combine the results of the fitted pairs using a weighting factor of $1/\sigma_i^2$, where σ_i is the statistical error on the considered parameter.

An important variable that might affect our EPIC results is the spectral ranges of our fits. In particular, significant cross-calibration issues between MOS and pn have been reported in the soft bands (Read et al. 2014; Schellenberger et al. 2015). Similarly, we observe a sharp and extremely variable soft tail in the EPIC filter wheel closed events⁷ that might considerably affect the spectra below 0.5 keV. On the other hand, we would like to keep our spectral range as large as possible, for instance to estimate the abundance measurements of O and the temperature structure in the Fe-L complex. A good compromise is found by using the 0.5–10 keV and 0.6–10 keV bands for MOS and pn, respectively.

3.3.3 Local fits

In the case of a plasma in CIE, the abundances of a given element showing prominent and well-resolved emission lines are easy to derive as they are proportional to the ratio between the line flux and the continuum flux, namely the equivalent width (EW). However, as a consequence of the imperfections of the EPIC instruments effective areas, when fitting the EPIC spectra over a large range (0.5/0.6–10 keV in the previous subsection, hereafter the “global” fits), the modelled continuum emission may be slightly over- or underestimated in some specific energy bands. Consequently, the modelled line fluxes tend to compensate the continuum discrepancies in

⁷See also the XMM-Newton Calibration Technical Note, XMM-SOC-CAL-TN-0018 (Ed: Guainazzi, 2014).

3.4 Results

the global fits, by, in turn, slightly under- or overestimating the value of the abundance parameters.

This effect, already discussed in Chapter 2, can be easily corrected by fitting the EPIC spectra locally, in order to allow the modelled continuum to be fitted to its correct (local) level. Therefore, we re-fit the EPIC spectra within local bands successively centred around the strongest K-shell lines of each element (except Ne, whose strongest lines reside in the Fe-L complex and are not resolved by the EPIC instruments). The temperature parameters kT_{mean} and σ_T are frozen to their EPIC global best-fit values, in such a way that in every local fit, the free parameters are only the (local) normalisation Y and the abundance of the considered element. We compare these abundances estimated locally in MOS (MOS 1 and MOS 2 are fitted simultaneously) and in pn individually. If the MOS and pn abundances agree within 1σ , we combine the measurements using a weighting factor of $1/\sigma_i^2$ (see also Sect. 3.3.2). Otherwise, we compute the weighted average and artificially increase the combined uncertainties until they fully cover the extreme MOS and pn 1σ values. By applying such a conservative method to each object, we cover individual systematic uncertainties related to the EPIC cross-calibration issues (see also Sect. 3.4.3), and ensure getting fully reliable abundance measurements.

Hereafter, all the EPIC abundances are locally corrected, unless otherwise stated. We note, however, that the EPIC Fe abundances reported in this paper are obtained using global fits because they are more accurately determined using both the Fe-K and Fe-L complexes. Except A 3526 (for which we estimate Fe using local fits), all the other objects show ($<2\sigma$) consistent EPIC Fe abundances when using successively local and global fits, so this choice does not affect our results.

3.4 Results

The final abundance estimates for EPIC (within $0.2r_{500}$ and $0.05r_{500}$) and RGS of all the objects in the sample are presented in Fig. 3.1 (Fe abundance) and Fig. 3.2 (other relative-to-Fe abundance ratios), spread over their EPIC mean temperatures.

As can be seen in Fig. 3.1, some sources show a significant discrepancy between their EPIC and RGS measured Fe abundances. This is not surprising, since the RGS extraction regions always have the same angular size ($\sim 30' \times 0.8'$), while the radius of the circular EPIC extraction regions

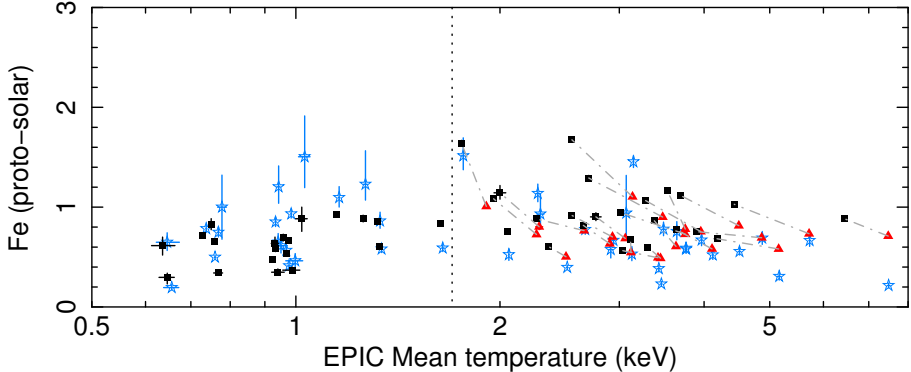


Figure 3.1: Mean temperature (EPIC) versus absolute Fe abundance for the full sample. The black squares and the red triangles show the EPIC measurements within $0.05r_{500}$ and $0.2r_{500}$, respectively. Each pair of measurements ($0.05r_{500}, 0.2r_{500}$) that belong to the same hot cluster is connected by a grey dash-dotted line. The blue stars show the RGS measurements (adapted from de Plaa et al. 2017), scaled on their respective EPIC mean temperature within $0.2r_{500}$. The vertical black dotted line separates the cool groups/ellipticals from the hot clusters (see text).

is different for each object (Sect. 3.2.2). Moreover, owing to its poorly constrained continuum level and its limited spectral range (in particular with no access to the Fe-K lines), RGS is not very suitable for deriving absolute Fe abundances. In the case of very extended sources, the instrumental line broadening makes Fe even more difficult to derive with RGS, leading to larger uncertainties. Nevertheless, the relative abundance ratios O/Fe, Ne/Fe, and Mg/Fe measured with RGS do not depend on the continuum and are easier to constrain (Sect. 3.4.1).

Within $0.2r_{500}$ (red triangles), the Fe abundance of the hot clusters are somewhat dispersed, with a mean value of 0.71. Within $0.05r_{500}$ (black squares), the mean Fe abundance in the cool groups/ellipticals is 0.64, while in the hot clusters it is 0.78 (see also Fig. 3.3). We estimate the intrinsic scatter in our subsamples, and its upper and lower 1σ limits by following the method described in de Plaa et al. (2007). Knowing the statistical errors σ_{stat} of our measurements, we determine the intrinsic scatter σ_{int} using fits to our data with a constant model and with total uncertainties $\sqrt{\sigma_{\text{stat}}^2 + \sigma_{\text{int}}^2}$ that have $\chi^2 = k \pm \sqrt{2k}$ (where k is the number of degrees of freedom). For the hot clusters we find an intrinsic scatter of $(21 \pm 4)\%$ within $0.2r_{500}$, and $(33 \pm 7)\%$ within $0.05r_{500}$. The intrinsic scatter in the cool groups ($0.05r_{500}$)

3.4 Results

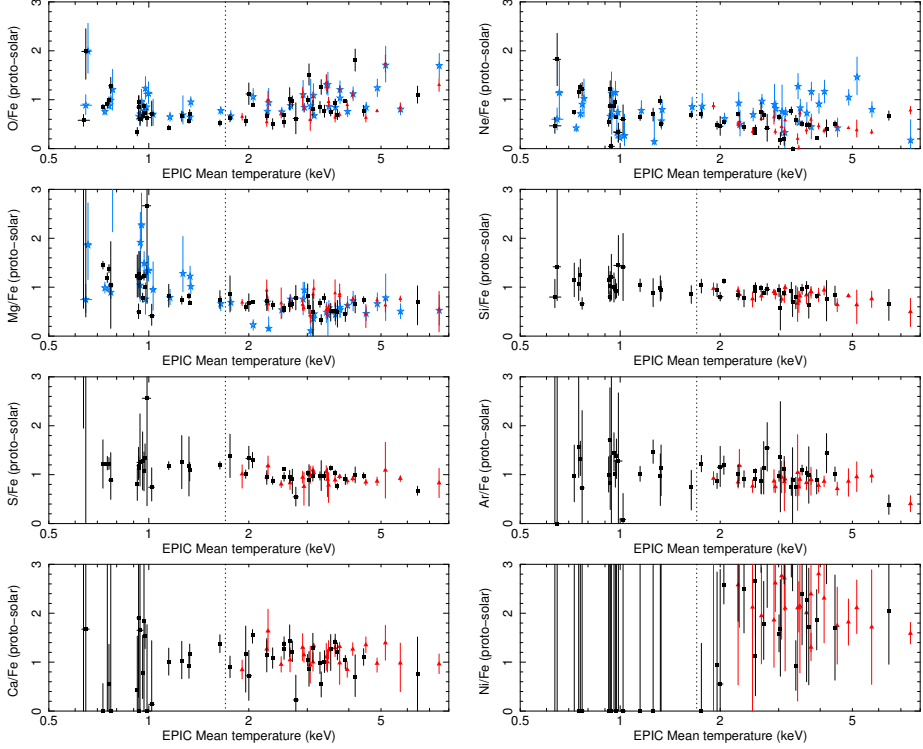


Figure 3.2: Same as Fig. 3.1 for the other (relative-to-Fe) abundance ratios. For clarity, the $(0.05r_{500}, 0.2r_{500})$ pairs are not shown explicitly.

is $(31 \pm 5)\%$, which is comparable to the value found in hot clusters within the same core radius. Finally, we note an interesting trend regarding the pair of measurements $(0.05r_{500}, 0.2r_{500})$ for each hot cluster (blue dotted lines). When the cluster mean temperature increases, the temperature gradient seems to increase, while on the contrary, the Fe gradient seems to flatten.

All the abundance ratios shown in Fig. 3.2 are consistent with being uniform over the considered temperatures range, even when considering the two different EPIC extraction regions. This is particularly striking for Si/Fe (although a slightly decreasing trend cannot be excluded) and S/Fe. This trend is investigated more quantitatively in Sect. 3.4.3 where we compare the average abundance ratios of the hot and the cool objects. Moreover, we note that both EPIC and RGS measurements are consistent; the exception is

Ne/Fe , for which the RGS measurements remain uniform while the EPIC values suggest a decrease with temperature (see discussion in Sect. 3.4.1, and a further inspection in Sect. 3.4.3). Finally, although their uncertainties are large and deriving any trend is very difficult, we note that the Ni/Fe abundance ratios are all consistent with being larger than the proto-solar value.

3.4.1 Estimating reliable average abundances

Assuming that all these relative-to-Fe abundance ratios are indeed uniform over clusters and do not depend (much) on their histories, we can combine our individual measurements and estimate for each element one average abundance ratio representative of the nearby cool-core ICM as a whole. We estimate the average relative-to-Fe abundance of a given element “X” by using the weighting factors $1/\sigma(\text{X}/\text{Fe})_i^2$, where $\sigma(\text{X}/\text{Fe})_i$ is the uncertainty on the X/Fe abundance in the i th observation. In the case of asymmetric X/Fe uncertainties in some observations, we systematically choose the larger one (in absolute value).

In addition to studying the subsamples of the hot clusters (within either $0.2r_{500}$ or $0.05r_{500}$), we can also combine the hot subsample (within $0.2r_{500}$) with the cool subsample (within $0.05r_{500}$), in order to get a “full” sample, named hereafter $(0.05 + 0.2)r_{500}$, which contains the highest statistics. A complete comparison of this full sample with the three subsamples mentioned above is discussed in Sect. 3.4.3.

As mentioned earlier, RGS measures the absolute Fe abundance with a high degree of uncertainty. However, it is quite reliable in measuring the abundance ratios of O/Fe , Ne/Fe , and sometimes Mg/Fe (assuming a low redshift and a high S/N, which is the case for our sample). Unlike RGS, EPIC is not very suitable for measuring O/Fe abundance ratios (whose main emission lines reside at ~ 0.6 keV near the O absorption edge and where the calibration is somewhat uncertain) and Ne/Fe abundance ratios (whose K-shell transitions are within the Fe-L complex, which depends on the temperature structure and is not resolved by the EPIC instruments), but can in principle make reliable measurements of all the other considered ones. Moreover, EPIC observes both the Fe-L and Fe-K complexes, as well as the continuum emission, and thus provides more trustworthy absolute Fe abundances and temperatures. We note that we find large positive residuals around 1.2 keV in the EPIC spectra of NGC 5813 and NGC 5846, which prevents us from estimating reasonable Mg abundances, even by perform-

3.4 Results

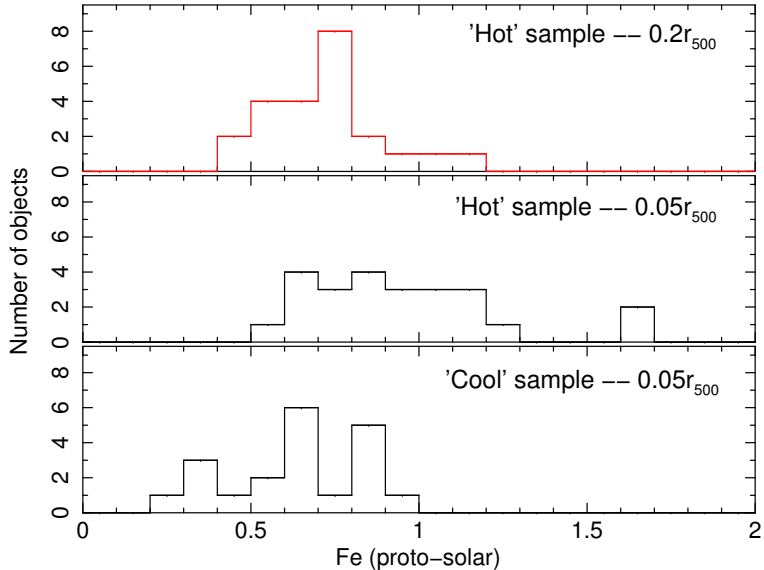


Figure 3.3: Distributions of the EPIC absolute Fe abundances for all the objects in our sample. Three subsamples (hot clusters within $0.2r_{500}$ and $0.05r_{500}$, and cool groups within $0.05r_{500}$) are considered separately (see also Fig. 3.1).

ing local fits. For these two groups, the Mg/Fe ratios inferred from RGS are undoubtedly more reliable.

Taking these instrumental characteristics into account, in the following we use the O/Fe and Ne/Fe abundances from RGS. We use EPIC for the Mg/Fe (except in NGC 5813 and NGC 5846), Si/Fe, S/Fe, Ar/Fe, Ca/Fe, Fe, and Ni/Fe abundances. We discuss more extensively the robustness of this choice in Sect. 3.4.3. Table 3.4 shows the best estimated temperature and selected abundance measurements for all the objects in our samples. The average abundance ratios and their statistical uncertainties σ_{stat} are indicated in the second and third columns of Table 3.2. We note again that O/Fe and Ne/Fe have been corrected from updated radiative recombination calculations (Appendix 3.B).

3.4.2 EPIC stacked residuals

The large net exposure time allows us to stack the residuals of the previously fitted global EPIC spectra. The residuals of each observation are obtained after fitting the three instruments simultaneously for each point-

ing (Sect. 3.3.2), and are corrected from their respective redshift before the stacking process. The residuals are summed over observations following

$$\sum_{i=1}^N \sum_{k=1}^M w_{i,k} (\text{data}(k)_i / \text{model}(k)_i - 1), \quad (3.3)$$

where $\text{data}(k)_i$ and $\text{model}(k)_i$ are respectively the measured and modelled count rates of the i th observation at its k th spectral bin, N is the total number of observations, M is the number of spectral bins (in the considered spectrum), and $w_{i,k}$ is the weight used to stack the results. This weight, which depends on both the observation and the spectral bin considered, is the product of two values: the inverse square of the statistical error of $\text{data}(k)_i$ and a factor, between 0 and 1, corresponding to the overlapping fraction between a bin from a reference spectrum, and a bin from a spectrum to be stacked to the reference one (e.g. if the “reference spectrum” and “stacking spectrum” bins do not overlap, the overlapping fraction is 0, if they fully overlap, the fraction is 1; see also Leccardi & Molendi 2008). This second factor is necessary because the spectra (or spectral residuals) from different observations have different offsets in their rest frame binning owing to their different redshift corrections. Figure 3.4 (top three panels) shows the stacked MOS 1, MOS 2, and pn residuals.

Although the deviations are not larger than a few per cent, remaining cross-calibration issues between MOS and pn effective areas clearly appear, and positive residuals in one instrument are often compensated by negative residuals in the other, especially around the Fe-L complex (and more generally below 2 keV). In the 4–6 keV band, the model underestimates the spectra, while above 7 keV, the opposite situation occurs. It is also worth mentioning the apparent slightly overestimated broadening of the modelled Fe-K line complex, in particular in MOS (seen through the characteristic dips on both sides of the peak), which is likely due to imperfections of the RMF. The pn stacked residuals also suggest a small offset due to incorrect energy calibration. Although the last two points should not significantly affect our results, the overall shape of the stacked residuals clearly illustrates that, despite past and recent efforts to cross-calibrate the EPIC instruments, imperfections are still present and bring additional uncertainties in the parameter determination (see also Schellenberger et al. 2015). In particular, the biased determination of the continuum, especially beyond 4 keV, emphasises the importance of using a local fitting method to derive reliable abundances (Sect. 3.3.3).

3.4 Results

We do the same exercise, this time by fitting the instruments independently (to minimise the cross-calibration residuals discussed above), and by setting all the line emission to zero in the `gdem` model after having fitted the spectra. We calculate the residuals relative to this “continuum only” model for each observation, and we sum the residuals as described above. The stacked result is shown in the lower panel of Fig. 3.4, and reveals all the emission lines/complexes that the EPIC instruments are able to resolve. The small stacked error bars on the residuals allow us to detect the main emission lines of chromium (Cr) and manganese (Mn) around ~ 5.7 keV and ~ 6.2 keV respectively. Following the Gauss method described in Chapter 2, we re-fit locally the EPIC spectra of every pointing with a local continuum and an additional Gaussian centred successively on these two energies. From this we get the EWs of the two lines, which we can convert into Cr and Mn abundances. After stacking these measurements over the whole sample, the MOS and pn instruments find a positive detection of Cr/Fe with $>7\sigma$ and $>4\sigma$ significances, respectively. For Mn/Fe, the positive detection is $>5\sigma$ in both MOS and pn. Combining the MOS and pn instruments, we obtain average Cr/Fe and Mn/Fe abundances of 1.56 ± 0.19 and 1.70 ± 0.22 , respectively. These abundances are not so different from the Fe values assumed for Cr and Mn in the previously discussed fits (Sect. 3.3.2), and consequently, their residuals did not bias our fits much, if at all. We also note that because the error bars of these abundances in individual pointings are often 1σ consistent with zero, we must ensure that negative abundances are allowed in order to avoid statistical biases when averaging over the whole sample (Leccardi & Molendi 2008).

The stacking process described above can also be performed separately in the hot and cool subsamples, respectively within $0.2r_{500}$ and $0.05r_{500}$. This comparison is shown in Fig. 3.5. Unsurprisingly, most of the emission lines, including the Fe-L complex, are clearly enhanced in the cool subsample (grey curve), while the Fe-K and Ni-K lines are more prominent in the hot subsample (black). Beyond ~ 6 keV, the overestimate of the continuum (discussed above and in Sect 3.3.3) also seems more important in the cool subsample.

3.4.3 Systematic uncertainties

A crucial point when averaging the abundances over a large sample is that the stacked statistical uncertainties become very small. Therefore, the systematic uncertainties may clearly dominate, and care must be taken to eval-

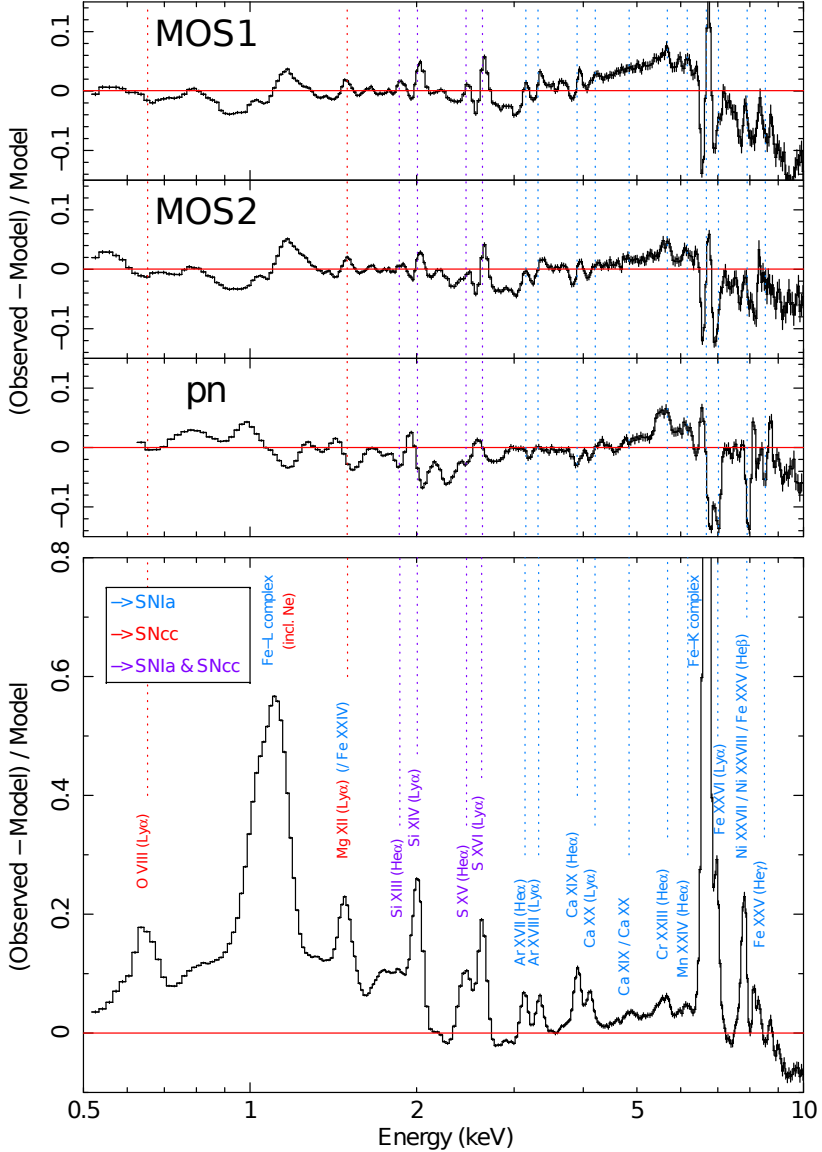


Figure 3.4: Top: EPIC MOS 1, MOS 2, and pn stacked and redshift-corrected residuals of the $(0.05 + 0.2)r_{500}$ sample (using a `gdem` model). Before stacking, the MOS and pn spectra of every pointing were fitted simultaneously with coupled parameters. The vertical dotted lines indicate the position of the detected line emissions in the EPIC spectra (see lower panel). Bottom: EPIC stacked and redshift-corrected residuals of the $(0.05 + 0.2)r_{500}$ sample (using a `gdem` model, all instruments combined). Before stacking, the MOS and pn spectra of every pointing were fitted independently and the line emission was set to zero in the model. The height of the peak of the Fe-K complex is ~ 1.95 .

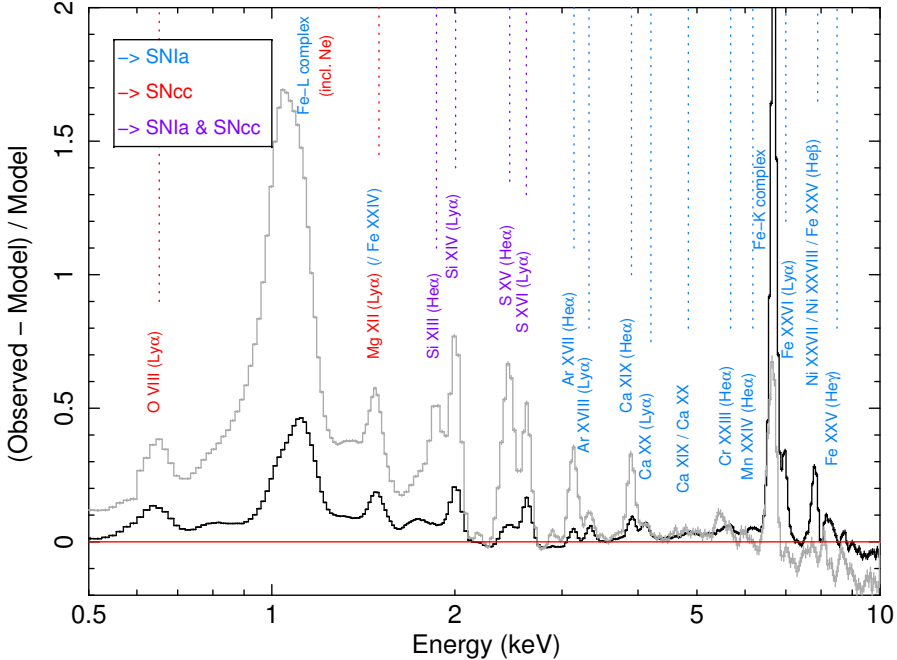


Figure 3.5: Same as Fig. 3.4 (bottom), this time comparing the $0.05r_{500}$ cool (grey curve) and the $0.2r_{500}$ hot (black curve) subsamples. The height of the peak of the Fe-K complex in the $0.2r_{500}$ hot sample is ~ 2.23 .

uate them properly. The average abundance ratios and all their uncertainties discussed below are summarised in Table 3.2.

First, because of their different chemical histories, it seems reasonable to assume that some clusters intrinsically deviate from the average estimated abundances. Such an intrinsic scatter σ_{int} has been already introduced, and has been estimated (as well as their 1σ uncertainties) for all the available abundance ratios (Table 3.2). Except for O/Fe ($\sim 16\%$) and Mg/Fe ($\sim 29\%$), the intrinsic scatter of the other elements are of the order of a few percent. In order to remain as conservative as possible in determining our final abundance ratios, we choose to consider the most extreme case where the true intrinsic scatters would actually correspond to the (1σ) upper limits of σ_{int} . In the following, the systematic uncertainties we associate with the intrinsic scatters are, therefore, $\sigma_{\text{int}} + 1\sigma$. Owing to their still large statistical error bars, no intrinsic scatter was needed for Ar/Fe, Cr/Fe, Mn/Fe, and Ni/Fe.

Second, we investigate whether the average abundance ratios change significantly when considering different EPIC extraction regions and/or subsamples. The comparison of these ratios over the four (sub-)samples described in Sect. 3.4.1 is shown in Fig. 3.6 (top). The abundance ratios of all the elements are consistent, except for S/Fe and Ar/Fe, which we discuss more extensively in Sect. 3.5.1. For these two elements, we determine the systematic uncertainty σ_{region} by artificially increasing their combined uncertainties $\sqrt{\sigma_{\text{stat}}^2 + (\sigma_{\text{int}} + 1\sigma)^2 + \sigma_{\text{region}}^2}$, until they cover the discrepancies between the (sub-)samples, and make them all $\leq 1\sigma$ consistent.

Third, after correction for σ_{int} and σ_{region} , we look for possible cross-calibration biases by comparing the average abundances estimated from the separate *XMM-Newton* instruments (Fig. 3.6 top). Three elements have MOS and pn abundance ratios that differ with more than 1σ significance, and need an additional systematic uncertainty ($\sigma_{\text{cross-cal}}$ defined similarly to σ_{region}): Si/Fe, Ar/Fe, and Ni/Fe. The last two are the most striking: pn estimates the Ar/Fe and Ni/Fe ratios on average respectively $\sim 25\%$ lower and $\sim 52\%$ higher than MOS. A further discussion on the discrepancies found in these two ratios will be addressed in Sect. 3.5.1.

Fourth, since the conversion from the EW of a considered line to the abundance of its element strongly depends on the plasma temperature, a multi-temperature structure deviating from the *gdem* distribution may affect the abundance ratios. We investigate this dependency for the best EPIC observations of Perseus and M 87 in Appendix 3.C. Among the two continuous temperature distributions tested here (which are thought to be the most reasonable to describe the thermal structure of the ICM; e.g. de Plaa et al. 2006), we find that the deviations in the EPIC abundance ratios are marginal, well below the range of the other systematic uncertainties discussed above. Therefore, we do not consider this effect in the rest of this paper.

Assuming the systematic errors mentioned above to be roughly symmetric, we add them in quadrature to obtain the total uncertainties:

$$\sigma_{\text{tot}}^2 = \sigma_{\text{stat}}^2 + (\sigma_{\text{int}} + 1\sigma)^2 + \sigma_{\text{region}}^2 + \sigma_{\text{cross-cal}}^2. \quad (3.4)$$

Finally, we must note that further systematic uncertainties might still play a role. For example, we show in Appendix 3.B that too simple approximations in the calculation of the emission processes might alter the

Table 3.2: Average abundance ratios estimated from the $(0.05 + 0.2)r_{500}$ sample, as well as their statistical, systematic, and total uncertainties. An absence of value (–) means that no further uncertainty was required (see text).

Element	Mean value	σ_{stat}	σ_{int}	σ_{region}	$\sigma_{\text{cross-cal}}$	σ_{tot}
O/Fe	0.817	0.018	0.116 ± 0.035	–	–	0.152
Ne/Fe	0.724	0.028	0.103 ± 0.054	–	–	0.159
Mg/Fe	0.743	0.010	0.145 ± 0.029	–	–	0.174
Si/Fe	0.871	0.012	0.031 ± 0.022	–	0.018	0.057
S/Fe	0.984	0.014	0.042 ± 0.026	0.076	–	0.103
Ar/Fe	0.88	0.03	–	0.11	0.09	0.15
Ca/Fe	1.218	0.031	(< 0.091)	–	–	0.096
Cr/Fe	1.56	0.19	–	–	–	0.19
Mn/Fe	1.70	0.22	–	–	–	0.22
Ni/Fe	1.93	0.12	–	–	0.38	0.40

line emissivities, and thus the abundances we measure. Therefore, we cannot exclude that future improvements in the currently used spectral fitting codes could still slightly affect the measurements we report here (see also Chapter 5). Moreover, from some aspects (e.g. Fe XVII line ratios; see de Plaa et al. 2012), small deviations have been reported in the spectral modelling of CIE plasmas using either the SPEX code, or the apec model (based on the AtomDB code). In terms of abundances, the discrepancies between the two codes may bring further uncertainties, at least for RGS measurements (de Plaa et al. 2017); however, apec is a single-temperature model, which should be avoided in this kind of analysis (Sect. 3.3). Moreover, this lack of multi-temperature distribution for apec makes a direct comparison between the two codes difficult.

3.5 Discussion

In this work, we have derived the abundances in the cores of 44 galaxy clusters, groups, and ellipticals (CHEERS), using both the EPIC and RGS instruments. We have shown (Fig. 3.2) that the abundance ratios of O/Fe, Ne/Fe, Mg/Fe, Si/Fe, S/Fe, Ar/Fe, Ca/Fe, and Ni/Fe are quite uniform over the considered ranges of temperatures in the sample (0.6–8 keV). These

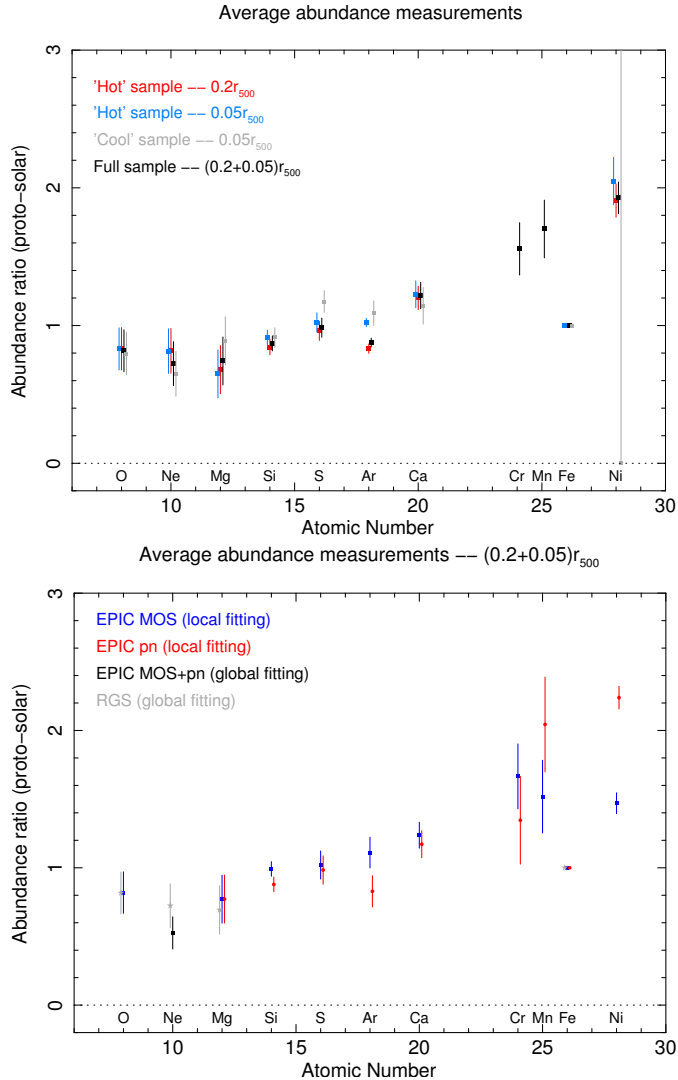


Figure 3.6: Top: Average abundance ratios considering different (sub-)samples and/or different EPIC extraction regions. The O/Fe and Ne/Fe ratios are measured using RGS (cross-dispersion width of $0.8'$). For these two ratios there is thus no distinction between the two hot samples or between the two full samples. The error bars incorporate the statistical errors (σ_{stat}) and the intrinsic scatters ($\sigma_{\text{int}} + 1\sigma$). Bottom: Average abundance ratios estimated from the $(0.05 + 0.2)r_{500}$ sample, measured independently by different combinations of instruments. The error bars incorporate the statistical errors (σ_{stat}), the intrinsic scatters ($\sigma_{\text{int}} + 1\sigma$), and the uncertainties derived from the different EPIC extraction regions and/or subsamples (σ_{region} , see upper panel).

results corroborate the study of De Grandi & Molendi (2009), who also found flat trends for Si/Fe and Ni/Fe independently of the considered clusters. This strongly suggests that regardless of their precise nature and of their different spatial scales, the physical processes that are responsible for the enrichment of the ICM must be the same for ellipticals, galaxy groups, and galaxy clusters.

Unlike these ratios, the absolute Fe abundance is far from being uniform, and seems much more dependent on cluster history (Fig. 3.1). The scatter is more important in the inner regions ($0.05r_{500}$) of the core. A less scattered Fe abundance within $0.2r_{500}$ could suggest a flatter abundance distribution as we look away from the centre with a similar level of enrichment outside the core of most objects. This is in agreement with the hypothesis of an early (pre-)enrichment, supported by recent *Suzaku* observations of outskirts of clusters/groups (Werner et al. 2013; Simionescu et al. 2015).

The cool groups/ellipticals appear on average to be less Fe-rich than the hot clusters. In particular, it is interesting to note that nine hot clusters have an Fe abundance that is higher than proto-solar within $0.05r_{500}$, while, at the same scale, no cool group/elliptical has a similar feature (Fig. 3.3). This trend has been already reported observationally (Rasmussen & Ponman 2009) and in simulations (Liang et al. 2016). It might be explained by several scenarios:

- More massive objects are more efficient in retaining metals within their core (owing to their larger gravitational well or a less powerful AGN activity);
- The more massive clusters are somewhat more efficient in injecting synthesised metals into the ICM;
- The galaxies of the more massive clusters are somewhat more efficient in producing stars, and hence, SNe;
- A more efficient cooling in group cores removes the enriched gas observed in X-ray.

While Liang et al. (2016) propose that the last scenario explains the lack of metal-rich gas in lower-mass (hence, lower-temperature) objects, Rasmussen & Ponman (2009) explored the four possibilities, and argue that the two first are the most likely. In particular, the galactic outflows could

be less efficient in releasing metals in the ICM of cooler groups or, alternatively, the AGN activity of the BCG could have helped to remove metals from their core (see also Yates et al. 2017). However, we must emphasise that several of these mechanisms might co-exist, and that the list above is not necessarily exhaustive. For instance, Elkholy et al. (2015) recently found a hint of a positive correlation between the metallicity in low-mass clusters, and the morphological disturbance of their ICM (likely related to the dynamical activity of their galaxy members). Alternatively, cooler ICM might be more efficient in depleting ionic Fe (and probably other metals) into grains close to the brightest central galaxy, although Panagoulia et al. (2015) found hints of Fe depletion in the cores of more massive clusters as well.

We must warn, however, that the large intrinsic scatters mentioned above prevent us from claiming any clear and significant trend on the absolute Fe abundances. Moreover, a more complicated thermal structure in groups/ellipticals than in more massive clusters cannot be excluded, and could lead to a slight but significant Fe bias, which would affect in priority the cooler objects in our sample.

We have also found an apparent variation in the Fe abundance and temperature gradients (i.e. between $0.05r_{500}$ and $0.2r_{500}$) in the hot clusters. These differences could be related to the individual cluster enrichment histories or to other parameters, such as the cooling rate. Linking the history of each cluster/group to its Fe budget requires a more careful spatial study of the Fe distribution. Establishing radial profiles for the entire sample is beyond the scope of this work, but are addressed in Chapter 6.

From the stacked results of our $(0.05 + 0.2)r_{500}$ sample, we have estimated the average abundance ratios and their respective total uncertainties (statistical and systematic). This also includes Cr/Fe and Mn/Fe, which we have detected within $>4\sigma$ significance with MOS and pn independently. To our knowledge, this is the first time that Mn has been firmly detected in the ICM. For comparison, Werner et al. (2006b) already detected Cr in 2A 0335+096 within 2σ (but were unable to detect Mn), while Cr and Mn have been detected in Perseus within 5σ and 1σ , respectively (Tamura et al. 2009). It is also striking to note that we do not see any emission line feature around ~ 3.5 keV in the stacked EPIC spectra (Fig. 3.4 bottom, Fig. 3.5) contrary to several claims from recent studies, in particular Bulbul et al. (2014) and Boyarsky et al. (2014), whose total EPIC net exposure times are ~ 3 Ms and ~ 1.5 Ms, respectively (i.e. less than in this work). Such an apparent

non-detection is thus very interesting to report, since it might challenge the hypothesis of decaying sterile neutrinos, known as a dark matter candidate, being observed in the ICM. We note that the dark matter interpretation is far from being the only possible explanation of an emission line at ~ 3.5 keV (e.g. Gu et al. 2015), and our non-detection could also be explored in the context of these other possibilities. However, this question is not the initial purpose of this present study, and a more detailed investigation of our stacked spectra around ~ 3.5 keV, and consequent discussions, are left to a future paper.

3.5.1 Discrepancies in the S/Fe, Ar/Fe and Ni/Fe ratios

The average S/Fe ratio shows a slight but significant enhancement in the cool objects within $0.05r_{500}$ compared to the hot objects within $0.2r_{500}$ (Fig. 3.6). From Fig. 3.2 (left, third panel), it is clear that M49 ($kT_{\text{mean}} \sim 1.148$ keV) and A3581 ($kT_{\text{mean}} \sim 1.637$ keV) largely contribute to this higher S/Fe ratio measured in the cool subsample because their statistical errors are small compared to the other cool objects. Moreover, the $>1\sigma$ discrepancy between the cool and hot measured S/Fe ratios disappears when considering the same radius ($0.05r_{500}$) for all the objects.

The Ar/Fe discrepancy observed in Fig. 3.6 (top) is more intriguing, since a larger aperture seems to lower its measurement. This trend is difficult to interpret. A change in the relative Ar to Fe radial distribution in the ICM cannot be excluded, although we would then expect it for other elements as well. A full study of the abundance radial profiles of the sample are performed in Chapter 6. Furthermore, it also appears from Fig. 3.6 (bottom) that MOS and pn measure significantly different Ar/Fe values, even after taking account of the uncertainty described above (i.e. σ_{region}). The reason for this second Ar/Fe discrepancy is again challenging to clearly identify, but it is very likely due to imperfections in the calibration of the EPIC instruments.

As seen in Fig. 3.6 (bottom), the large MOS-pn discrepancy in the Ni/Fe abundance ratio prevents us from deriving a precise measurement. This discrepancy is worrying, but can be explained by imperfections in the cross-calibration of the two instruments. Alternatively, and perhaps more likely, the high energy band around the Ni-K transitions is significantly affected by the instrumental background (as the flux of the cluster emission sharply decreases at high energies). This hard particle background (already mentioned in Sect. 3.3.1) has a different spectral shape in MOS and pn, which

might even vary with time, thus between observations. In particular, an instrumental line ($\text{Cu K}\alpha$) is known to affect pn at a rest-frame energy of ~ 8 keV (Chapter 2). Despite our efforts to carefully estimate the background, that line might interfere with the Ni-K line in several observations, making a proper modelling of the Ni-K line impossible, and hence, boosting the Ni absolute abundance in pn. In this context, it can be instructive to compare our Ni/Fe measurements with those of *Suzaku*, which has a lower relative hard particle background. Sato et al. (2007b) (A 1060) and Tamura et al. (2009) (Perseus) reported ratios of $\sim 1.3 \pm 0.4$ and $\sim 1.11 \pm 0.19$, respectively (after rescaling to the proto-solar values). Although these measurements might be also be affected by further uncertainties (e.g. the choice of the spectral modelling, Sect. 3.4.3), they appear to be consistent with the Ni/Fe average ratio measured with MOS in this work, favouring our above supposition that MOS is more trustworthy than pn for measuring Ni/Fe. However, in order to be conservative, we prefer to retain the pn value as a possible result and, therefore, we keep large systematic uncertainties for Ni/Fe. We finally note that, unsurprisingly, Ni/Fe cannot be constrained in the cool objects (Fig. 3.6 top) because the gas temperature is too low to excite Ni-K transitions.

3.5.2 Comparison with the proto-solar abundance ratios

In Fig. 3.7 (black squares), we report our final X/Fe abundance pattern measured in the $(0.05 + 0.2)r_{500}$ sample, accounting for all the systematic uncertainties discussed earlier in this paper. At first glance, most of the abundance ratios measured in the ICM look significantly different from the proto-solar abundance ratios. Indeed, if we fit a constant to our abundance pattern (dashed grey line), we obtain a χ^2 of 43.1 for 10 degrees of freedom, in poor agreement with the abundance ratios in the ICM. However, as shown by the red dash-dotted lines (adapted from Lodders et al. 2009), the solar abundance ratios also suffer from large uncertainties, typically about 20–25%. When comparing the two sets of abundance ratios taken with their respective uncertainties, we find that the O/Fe, Ne/Fe, Mg/Fe, Si/Fe, S/Fe, Ar/Fe, and Ca/Fe ratios measured in the ICM are consistent within 1σ with the proto-solar values ($\pm 1\sigma$). The Cr/Fe abundance ratios measured in the ICM are consistent within 2σ with the proto-solar values ($\pm 1\sigma$), and the Mn/Fe and Ni/Fe abundance ratios are consistent within 3σ .

Given these considerations, whether the chemical enrichment in the

ICM is similar to the chemical enrichment of the solar neighbourhood is not a trivial question to solve. As mentioned above, while most of the relative abundances appear to be consistent with being proto-solar, Ni/Fe, Mn/Fe, and perhaps Cr/Fe seem to be significantly enhanced. This result might be of interest since significant different abundance ratios in the ICM means that the fraction of SNIa (or conversely SNcc) responsible for the ICM enrichment differs from that of the Galactic enrichment. We will address this discussion in greater detail in Chapter 4. We recall, however, that the abundances of interest in this context (Cr, Mn, and Ni) are not well constrained in X-ray, given the current instrument capabilities. Moreover, as specified in Sect. 3.4.3, we do not exclude that differences in current atomic codes might bring further systematic uncertainties to the measurements reported in this work. Therefore, whether our abundance ratios are significantly more accurate than the proto-solar estimates should still be considered an open question.

3.5.3 Current limitations and future prospects

As we have shown throughout this paper, our excellent data quality (~ 4.5 Ms and ~ 3.7 Ms of total net exposure time for EPIC MOS and pn, respectively) provides very accurate abundance measurements in the ICM of cool-core galaxy clusters and groups. Therefore, these data should be a legacy for any future work directly or indirectly related to the chemical enrichment in the ICM. However, our study clearly reveals that the abundance ratios of some elements of interest are still poorly constrained. In particular, the Cr/Fe, Mn/Fe, and Ni/Fe ratios in our study appear higher than the solar neighbourhood and are thus crucial to study in detail, which is currently challenging given the limited spectral resolution of CCDs and the large cross-calibration uncertainties (at least for Ni/Fe) that we emphasise here.

In this work we probably reach the instrumental limitations of *XMM-Newton* in terms of abundance determination, and thus stacking more data will have very little impact on the current accuracy of our already existing measurements. Indeed, in our sample, the statistical uncertainties are already marginal compared to the systematic ones. In addition to further efforts in calibrating the instruments and improving the atomic databases, it is clear that a sensibly higher X-ray spectral resolution is now needed.

Such an improvement can be reached with micro-calorimeter spectrometers, which should be on board the next generation of X-ray observato-

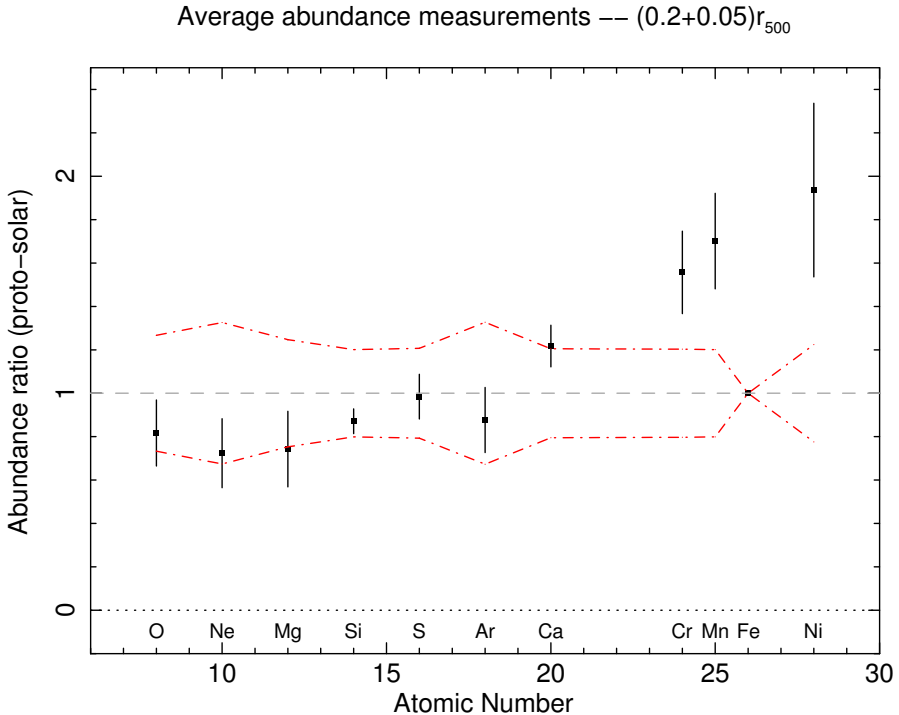


Figure 3.7: Average abundance ratios in our $(0.05 + 0.2)r_{500}$ sample (black squares) versus proto-solar abundances (grey dashed line) and their 1σ uncertainties (red dash-dotted lines, adapted from Lodders et al. 2009).

ries. In particular, the Japanese X-ray observatory *Hitomi* (formerly named *ASTRO-H*; Takahashi et al. 2014) has been able to resolve, for instance, K-shell and also L-shell Ni lines with a limited instrumental background, and should thus reduce the Ni/Fe uncertainties to a few per cent. Unfortunately, owing to a loss of contact a few weeks after launch, the fate of the mission is now unclear. Alternatively, the X-IFU instrument, which will be on board the *Athena* observatory (Nandra et al. 2013), will greatly improve the spectral resolution currently achieved with *XMM-Newton* to ~ 2.5 eV. Undoubtedly, this upcoming mission will allow a significant step forward in such an analysis, especially if improvements in atomic data are also carried out.

3.6 Conclusions

In this paper, we have used the *XMM-Newton* EPIC and RGS instruments to investigate the Fe abundance and abundance ratios of O/Fe, Ne/Fe, Mg/Fe, Si/Fe, S/Fe, Ar/Fe, Ca/Fe, Cr/Fe, Mn/Fe, and Ni/Fe in the central regions of 44 cool-core galaxy clusters, groups, and elliptical galaxies (CHEERS). Our main results can be summarised as follows.

- The X/Fe abundance ratios appear quite uniform over the mean temperature range of our sample. This confirms previous results, and indicates that no matter what the physical mechanisms responsible for the enrichment are, they must be very similar in enriching the ICM of ellipticals, groups, and clusters of galaxies.
- By stacking all the EPIC spectra of our sample (within $0.2r_{500}$ when possible, within $0.05r_{500}$ otherwise), we were able to derive abundances of Cr/Fe and Mn/Fe independently with MOS and pn, with $>4\sigma$ significance. While Cr had been already detected in the past, this is the first time that a firm detection of Mn in the hot ICM has been reported.
- Contrary to recent claims, and despite the large net exposure time (~ 4.5 Ms) of our combined data, we do not see any emission line at ~ 3.5 keV. Although a deeper investigation will be addressed in a future paper, this might challenge the possibility of decaying sterile neutrinos, a dark matter candidate, being observed in the ICM.
- The Fe abundance varies between 0.2–2 times the proto-solar values, and shows an important scatter, especially within a radius of $0.05r_{500}$ (~ 30 –40%). Looking at smaller ($0.05r_{500}$) and larger ($0.2r_{500}$) central regions in a subsample of hot clusters, it appears that the Fe peak sharpens and the temperature drop flattens as the mean cluster temperature decreases. Clearly, these various Fe abundances must depend on individual clusters histories, and complete abundance radial profiles are investigated in greater detail in Chapter 6.
- Having benefited from a large total net exposure time (~ 4.5 Ms) and having processed a very careful estimation of the systematic effects that could affect our measurements, we have shown that the systematic uncertainties clearly dominate over the statistical ones. Taking

these systematic uncertainties into account, most of the ICM abundance ratios measured in this work are consistent with the proto-solar abundance ratios. Notable exceptions are Mn/Fe, Ni/Fe, and perhaps Cr/Fe, which are found to be significantly higher in the ICM than in the solar neighbourhood.

- Overall, our careful analysis demonstrates that stacking more observations would not further improve the accuracy of our results, and, more generally, that we have probably reached the limits of the current X-ray capabilities (in particular *XMM-Newton*) for this science case. Therefore, our data constitute the most accurate abundance ratios ever measured in the ICM, and should be a legacy for future work. Using the results presented in this paper, a full discussion on the role of the SNIa and SNcc in the context of both the proto-solar and the ICM enrichments is addressed in Chapter 4. However, a more accurate comparison between the local Galactic enrichment and the ICM enrichment in the local Universe will require improvements in atomic data, as well as better calibration of the instruments. In parallel to these needs for improvements, the upcoming X-ray observatories should further improve the accuracy of the abundance measurements, and thus help to solve the puzzle of the chemical enrichment in the hot ICM.

Acknowledgements

The authors would like to thank the referee Marten van Kerkwijk for his helpful comments and suggestions. This work is partly based on the *XMM-Newton* AO-12 proposal “*The XMM-Newton view of chemical enrichment in bright galaxy clusters and groups*” (PI: de Plaa), and is a part of the CHEERS (CHEmical Evolution Rgs cluster Sample) collaboration. The authors thank its members, as well as Liyi Gu and Craig Sarazin for helpful discussions. P.K. thanks Steve Allen and Ondrej Urban for support and hospitality at Stanford University. Y.Y.Z. acknowledges support by the German BMWI through the Verbundforschung under grant 50 OR 1506. This work is based on observations obtained with *XMM-Newton*, an ESA science mission with instruments and contributions directly funded by ESA member states and the USA (NASA). The SRON Netherlands Institute for Space Research is supported financially by NWO, the Netherlands Organisation for Scientific

| 3.6 *Conclusions*

Research.

3.A EPIC absorption column densities

In the hot model used in this work to mimic absorption of X-rays through interstellar material (Sect. 3.3), we initially fixed the hydrogen column density N_{H} to the weighted value $N_{\text{H,tot}}$ of both the neutral (N_{HI} , Kalberla et al. 2005) and the molecular (N_{H_2} , Schlegel et al. 1998) materials, calculated using the method of Willingale et al. (2013)⁸. However, this approach often gives poor fits in the soft band of our EPIC spectral modelling, by significantly under- or overestimating the flux of its continuum. In order to compensate this effect, the O abundance is often biased consequently by the fits. Fig. 3.8 (red data points) clearly illustrates that some objects have their EPIC O/Fe ratio significantly offset from the corresponding RGS values.

The EPIC-RGS correlation for the O/Fe ratio is clearly improved if we free the N_{H} (Fig. 3.8, black data points). Similarly, most of the fits are improved in terms of C-stat/d.o.f. However, keeping N_{H} as a free parameter without any further constraint is quite dangerous, and might lead to unphysical results. In order to remain reasonably consistent with the estimated values of N_{HI} and $N_{\text{H,tot}}$ mentioned above, we allow N_{H} to take values within the following arbitrary limits:

$$N_{\text{HI}} - 5 \times 10^{19} \text{ cm}^{-2} \leq N_{\text{H}} \leq N_{\text{H,tot}} + 1 \times 10^{20} \text{ cm}^{-2}. \quad (3.5)$$

These upper and lower ranges allow limited deviations also around N_{HI} and $N_{\text{H,tot}}$. Since constraining a free parameter within a narrow range can lead to problems in evaluating the statistical errors, we perform a grid search of fixed N_{H} values (taken within the limits mentioned above), and select the one that gives the lowest C-stat/d.o.f. to the fits. Despite all these precautions, it should also be kept in mind that the O abundance measured in clusters with EPIC is also affected by the oxygen absorption in the interstellar medium, which in turn depends on N_{H} (e.g. de Plaa et al. 2004). Similarly, the measured O abundance in the ICM may be also affected by the foreground thermal X-ray emission.

3.B Radiative recombination corrections

The version of SPEX that is used in this work calculates the line emissivities assuming that the radiative recombination (RR) rates of the cluster emission can be expressed as a power law of the electron temperature (Mewe

⁸<http://www.swift.ac.uk/analysis/nhtot/index.php>

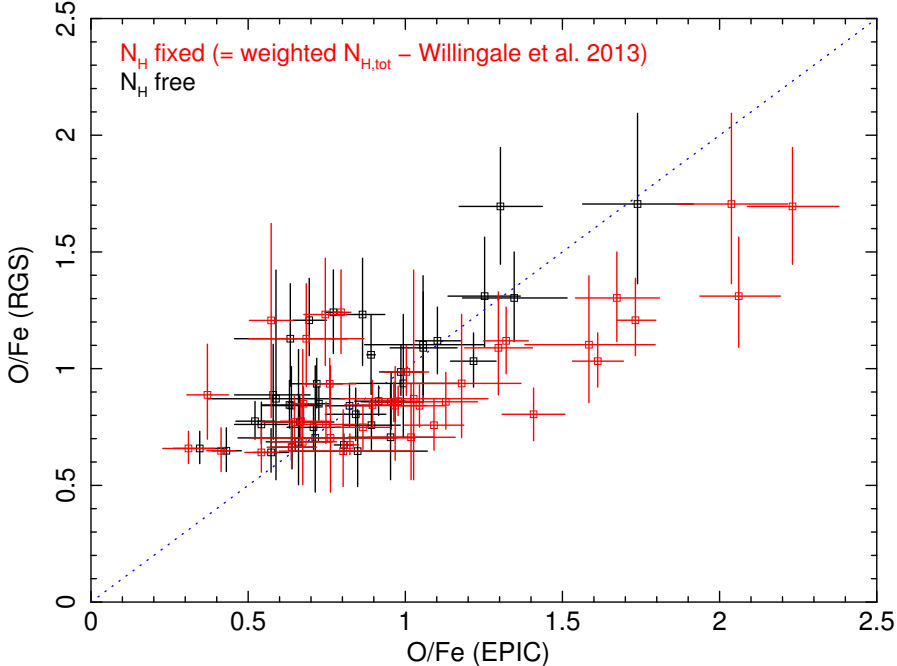


Figure 3.8: Comparison between the EPIC and RGS measurements of the O/Fe abundance ratio in most objects of our $(0.05 + 0.2)r_{500}$ sample. The blue dotted line shows the one-to-one EPIC-RGS correspondence. In our fits we alternatively fix the N_{H} to the weighted neutral+molecular values calculated from Willingale et al. (2013), and leave it free within the ranges given by Eq. (3.5). The two approaches are shown in red and black, respectively.

& Gronenschild 1981; Mewe et al. 1985). However, this approximation has turned out to be too simplified at high temperature. A more accurate calculation of the RR rate coefficients has been done by Badnell (2006), and parametrised by Mao & Kaastra (2016) as a function of the temperature T in the form

$$R(T) \propto T^{-b_0 - c_0 \ln T} \left(\frac{1 + a_2 T^{-b_2}}{1 + a_1 T^{-b_1}} \right), \quad (3.6)$$

where a_0 , b_0 , c_0 , a_1 , a_2 , b_1 , and b_2 are constant (fitted) parameters.

Since the RR rates directly affect the line emissivities, which in turn affect our estimated abundances, the RR updated model of Mao & Kaastra (2016) must be taken into account in our analysis, even though its implementation into SPEX is yet to come. Knowing that the O and Ne emission lines seen in clusters spectra are dominated by H-like Lyman α transitions,

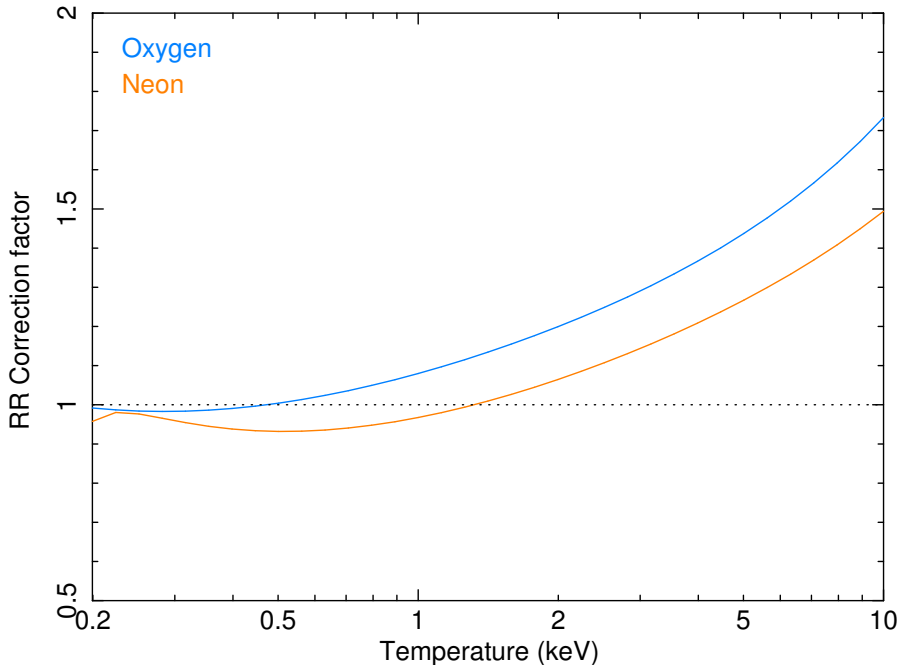


Figure 3.9: Calculated radiative recombination correction factors of H-like Lyman α lines of O and Ne as a function of the cluster (mean) temperature (adapted from the results of Mao & Kaastra 2016).

and that these two elements are the most affected by changing RR rates, we correct their abundances by computing the change in flux of their H-like Lyman α lines from the old RR calculations (i.e. used in the current SPEX version) to the new ones. This RR correction factor is shown (again, for O and Ne) in Fig. 3.9 as a function of the plasma temperature, and is to be multiplied by the measured O and Ne abundances of each object in our sample.

Figure 3.9 clearly shows that better calculations of the RR rates can lead to significant increases of the estimated O and Ne abundances in hot clusters. After applying this RR correction factor for each source, we find that, on average, the O/Fe and Ne/Fe abundance ratios increase by $\sim 20\%$ and $\sim 9\%$, respectively. We note, however, that reprocessing the whole analysis presented in this paper by using the uncorrected O and Ne abundance values does not affect our main conclusions, since we keep large systematic uncertainties in the final abundance ratios.

3.C Effects of the temperature distribution on the abundance ratios

As already specified in Sect. 3.3, the measured absolute abundances (in particular Fe) are in principle sensitive to the choice of the thermal model used in the fits (single- vs. multi-temperature). Among multi-temperature models, the assumed temperature distribution might also affect the measured (X/Fe) abundances. We explore this possibility by successively fitting the best-quality observations of Perseus and M 87 (which both have excellent statistics but rather different mean temperatures) with a 1T (i.e. `cie`), a 2T (i.e. `cie+cie`), and a power-law differential emission measure model⁹ (`wdem`; see e.g. Kaastra et al. 2004). The results are shown in Fig. 3.10 and Table 3.3. From Fig. 3.10, it clearly appears that the abundance pattern depends on the considered thermal model. In particular, Ne/Fe varies a lot (i.e. by more than a factor of 6 for Perseus and by almost a factor of 3 for M 87) because the Ne abundance parameter from the models is used by the fits to compensate the EPIC residuals in the Fe-L complex (e.g. de Plaa et al. 2006). This illustrates that the EPIC estimate of Ne/Fe cannot be interpreted as a reliable Ne abundance (Sect. 3.4.1). Striking differences in the Ca/Fe and Ni/Fe ratios considering the four different models should also be noted; for instance, a considerably high Ca/Fe ratio is measured by the 1T and/or 2T model(s).

⁹This model is thought to reproduce quite well the temperature structure in the ICM of most cool-core objects, but has not been used in this work owing to computing time.

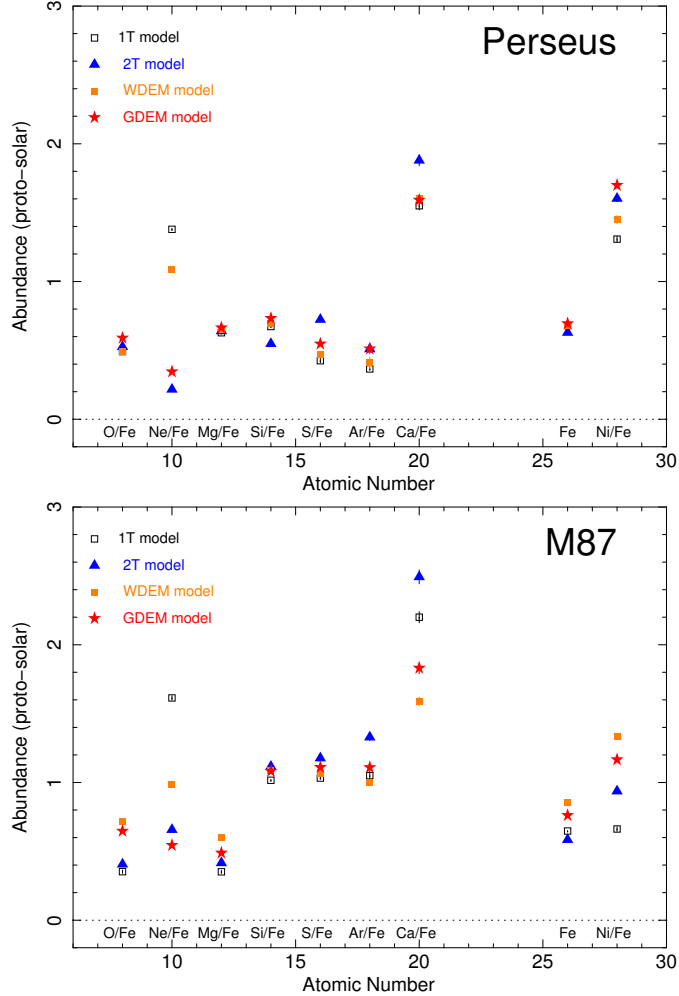


Figure 3.10: EPIC abundance measurements in the two best-quality observations of our sample, based on global fittings (see also Table 3.3). Four thermal models are successively considered: 1T (black empty squares), 2T (blue filled squares), wDEM (orange filled squares), and gDEM (red filled squares). The Fe abundance is given in absolute values, while the other abundances are given relative to Fe. *Top:* Perseus ($0.2r_{500}$). *Bottom:* M 87 ($0.05r_{500}$).

3.C Effects of the temperature distribution on the abundance ratios

Table 3.3: Comparison of the abundance results obtained by performing global fittings to the best-quality EPIC spectra of Perseus ($0.2r_{500}$) and M 87 ($0.05r_{500}$). Four different temperature distributions of the CIE model are successively considered ($1T$, $2T$, w_{dem} , and g_{dem} ; see also Fig. 3.10).

Element	1T	2T	Perseus	w_{dem}	g_{dem}
O/Fe	0.491 ± 0.006	0.526 ± 0.007	0.491 ± 0.007	0.589 ± 0.006	
Ne/Fe	1.379 ± 0.008	0.217 ± 0.012	1.090 ± 0.009	0.344 ± 0.008	
Mg/Fe	0.628 ± 0.010	0.641 ± 0.012	0.651 ± 0.010	0.663 ± 0.010	
Si/Fe	0.673 ± 0.006	0.548 ± 0.011	0.693 ± 0.006	0.732 ± 0.005	
S/Fe	0.425 ± 0.016	0.724 ± 0.005	0.470 ± 0.010	0.546 ± 0.008	
Ar/Fe	0.365 ± 0.010	0.51 ± 0.03	0.41 ± 0.04	0.51 ± 0.03	
Ca/Fe	1.55 ± 0.03	1.88 ± 0.04	1.60 ± 0.03	1.59 ± 0.03	
Fe	0.6802 ± 0.0011	0.6296 ± 0.0012	0.6808 ± 0.0015	0.6934 ± 0.0012	
Ni/Fe	1.308 ± 0.022	1.603 ± 0.024	1.45 ± 0.03	1.698 ± 0.022	
C-stat / d.o.f.	$39\,168 / 1963$	$25\,669 / 1961$	$25\,124 / 1962$	$32\,481 / 1962$	
M 87					
O/Fe	0.352 ± 0.012	0.406 ± 0.007	0.713 ± 0.008	0.646 ± 0.009	
Ne/Fe	1.614 ± 0.016	0.657 ± 0.015	0.987 ± 0.013	0.543 ± 0.011	
Mg/Fe	0.351 ± 0.011	0.416 ± 0.010	0.597 ± 0.009	0.487 ± 0.009	
Si/Fe	1.016 ± 0.006	1.116 ± 0.006	1.084 ± 0.006	1.081 ± 0.007	
S/Fe	1.032 ± 0.009	1.177 ± 0.009	1.065 ± 0.008	1.109 ± 0.009	
Ar/Fe	1.05 ± 0.03	1.329 ± 0.025	1.002 ± 0.021	1.108 ± 0.023	
Ca/Fe	2.20 ± 0.04	2.493 ± 0.05	1.59 ± 0.03	1.83 ± 0.04	
Fe	0.6472 ± 0.0020	0.5847 ± 0.0016	0.8532 ± 0.0020	0.7601 ± 0.0017	
Ni/Fe	0.662 ± 0.017	0.937 ± 0.014	1.334 ± 0.015	1.165 ± 0.016	
C-stat / d.o.f.	$19\,034 / 914$	$13\,602 / 912$	$9\,474 / 913$	$8\,680 / 913$	

Despite these considerations, and the fact that the real temperature distributions in the ICM is unknown, considering a continuous distribution is clearly more realistic than only one or two unique temperatures. By comparing only the `gdem` and `wdem` models, we note that they give very similar abundance ratios for both Perseus and M87. Except for Ne/Fe, the largest difference is found for Ni/Fe, and is clearly smaller than the range of systematic uncertainties affecting the measurements. Therefore, using a `wdem` model instead of a `gdem` model should have a limited impact on our EPIC final results. For comparison, de Plaa et al. (2017) find that such an effect on the O/Fe ratio derived from RGS is always smaller than 20%. Therefore, considering further uncertainties related to the thermal models is not necessary for the purpose of this work.

3.D Best-fit temperature and abundances

In Table 3.4 we present the full results of our best-fit parameters (kT , σ_T , the absolute Fe abundance, and the abundance ratios of O/Fe, Ne/Fe, Mg/Fe, Si/Fe, S/Fe, Ar/Fe, Ca/Fe, and Ni/Fe) for each object of the CHEERS sample, within a radius of $0.05r_{500}$. When possible (hot clusters), we indicate the parameters extracted from $0.2r_{500}$ as well. The O/Fe and Ne/Fe abundances have been corrected from updated RR calculations, as described in Appendix 3.B.

3.D Best-fit temperature and abundances

Table 3.4: Summary of the best-fit temperatures, σ_T and abundances for all the clusters/groups/ellipticals of the CHEERS sample. The kT , σ_T parameters and the Fe absolute abundance are measured with EPIC, based on global fittings, as described in Sect. 3.3.2. The Mg/Fe, Si/Fe, S/Fe, Ar/Fe, Ca/Fe and Ni/Fe abundance ratios as well as their error bars are measured using EPIC, based on local fittings, as described in Sect. 3.3.3. The O/Fe and Ne/Fe abundance ratios are measured using RGS, and do not depend on the considered EPIC extraction region ($=$). When parameters are unrealistic or fully uncertain, we do not report any measurement ($-$).

Source	Region	kT (r_{500} , keV)	σ_T	O/Fe	Ne/Fe	Mg/Fe	Si/Fe	S/Fe	Ar/Fe	Ca/Fe	Fe	Ni/Fe
2A 0335	0.2	2.661 \pm 0.004	0.2433 \pm 0.0013	0.88 \pm 0.09	0.97 \pm $=$	0.69 \pm 0.15	0.82 \pm 0.10	0.83 \pm 0.14	0.87 \pm 0.27	1.04 \pm 0.25	0.765 \pm 1.1	2.0 \pm 1.0
	0.05	2.265 \pm 0.005	0.2116 \pm 0.0014	$=$	0.72 \pm 0.20	0.83 \pm 0.10	0.96 \pm 0.15	1.01 \pm 0.26	1.1 \pm 0.3	0.882 \pm 0.007	3.4 \pm 1.6	
A 85	0.2	5.715 \pm 0.018	0.354 \pm 0.003	0.80 \pm 0.11	0.80 \pm $=$	0.76 \pm 0.06	0.76 \pm 0.18	0.92 \pm 0.06	0.98 \pm 0.13	1.0 \pm 0.6	0.733 \pm 0.006	1.7 \pm 1.2
	0.05	4.432 \pm 0.020	0.300 \pm 0.004	$=$	0.74 \pm 0.07	0.84 \pm 0.20	0.98 \pm 0.15	1.01 \pm 0.15	1.10 \pm 0.17	1.028 \pm 0.011	1.7 \pm 1.1	
A 133	0.2	3.476 \pm 0.021	0.269 \pm 0.004	0.86 \pm 0.13	0.83 \pm 0.18	0.57 \pm 0.07	0.82 \pm 0.12	0.8 \pm 0.4	0.90 \pm 0.16	1.25 \pm 0.19	0.901 \pm 0.013	2.1 \pm 1.4
	0.05	2.704 \pm 0.020	0.227 \pm 0.004	$=$	0.65 \pm 0.08	0.89 \pm 0.04	0.9 \pm 0.3	1.1 \pm 0.5	1.21 \pm 0.22	1.29 \pm 0.22	1.8 \pm 0.8	
A 189	0.05	1.020 \pm 0.021	0.178 \pm 0.016	0.7 \pm 0.3	0.27 $^{+0.44}_{-0.21}$	0.42 \pm 0.23	1.4 \pm 0.7	0.7 \pm 0.4	0.08 \pm (< 0.62)	0.14 \pm 0.08	0.88 \pm 0.13	—
A 262	0.2	2.264 \pm 0.013	0.192 \pm 0.003	0.76 \pm 0.10	0.93 \pm 0.22	0.94 \pm 0.21	0.93 \pm 0.11	0.95 \pm 0.07	0.85 \pm 0.13	1.27 \pm 0.18	0.726 \pm 0.012	2.6 \pm 2.4
	0.05	1.957 \pm 0.015	0.188 \pm 0.004	$=$	0.59 \pm 0.08	0.95 \pm 0.15	1.01 \pm 0.09	0.87 \pm 0.16	1.2 \pm 0.8	1.08 \pm 0.22	0.9 \pm (< 2.8)	
A 496	0.2	3.754 \pm 0.012	0.273 \pm 0.003	1.03 \pm 0.12	1.16 \pm 0.20	0.86 \pm 0.20	0.90 \pm 0.13	0.96 \pm 0.05	0.90 \pm 0.10	1.0 \pm 0.4	0.729 \pm 0.006	1.3 \pm 0.3
	0.05	3.007 \pm 0.012	0.229 \pm 0.003	$=$	0.82 \pm 0.25	0.94 \pm 0.13	1.03 \pm 0.05	0.97 \pm 0.11	1.04 \pm 0.12	0.947 \pm 0.010	1.6 \pm 0.4	
A 1795	0.2	5.15 \pm 0.04	0.318 \pm 0.013	1.7 \pm 0.4	1.5 \pm 0.4	0.63 \pm 0.15	0.6 \pm 0.4	1.1 \pm 0.6	1.0 \pm 0.3	1.4 \pm 0.4	0.581 \pm 0.010	2.1 \pm 0.6
	0.05	4.18 \pm 0.04	0.298 \pm 0.013	$=$	0.65 \pm 0.18	0.8 \pm 0.5	0.99 \pm 0.17	1.4 \pm 0.4	0.7 \pm 0.5	0.683 \pm 0.018	3.5 \pm 1.1	
A 1991	0.2	2.28 \pm 0.03	0.202 \pm 0.007	0.9 \pm 0.3	0.5 \pm 0.3	0.66 \pm 0.15	0.85 \pm 0.07	1.18 \pm 1.3	1.2 \pm 0.3	1.6 \pm 0.4	0.80 \pm 0.03	4 \pm 3
	0.05	2.00 \pm 0.04	0.205 \pm 0.009	$=$	0.68 \pm 0.19	0.81 \pm 0.09	1.3 \pm 0.3	1.2 \pm 0.4	0.7 \pm 0.5	1.14 \pm 0.07	0.6 \pm (< 2.9)	
A 2029	0.2	7.48 \pm 0.04	0.301 \pm 0.006	1.70 \pm 0.25	0.17 \pm (< 0.59)	0.5 \pm 0.3	0.8 \pm 0.3	0.41 \pm 0.16	0.96 \pm 0.20	0.710 \pm 0.006	1.58 \pm 0.22	
	0.05	6.44 \pm 0.04	0.292 \pm 0.009	$=$	0.7 \pm 0.5	0.7 \pm 0.3	0.67 \pm 0.09	0.39 \pm 0.20	0.75 \pm 0.15	0.885 \pm 0.012	2.1 \pm 1.1	
A 2052	0.2	2.931 \pm 0.012	0.244 \pm 0.003	0.84 \pm 0.09	0.82 \pm 0.16	0.57 \pm 0.06	0.86 \pm 0.11	0.8 \pm 0.4	0.75 \pm 0.13	0.702 \pm 0.008	2.6 \pm 0.7	
	0.05	2.554 \pm 0.016	0.234 \pm 0.004	$=$	0.57 \pm 0.08	0.92 \pm 0.22	0.95 \pm 0.09	0.91 \pm 0.18	1.28 \pm 0.24	0.917 \pm 0.017	1.1 \pm 0.9	

Table 3.4: continued.

Source	Region	kT (r_{500}) (keV)	σ_T	O/Fe	Ne/Fe	Mg/Fe	Si/Fe	Ar/Fe	Ca/Fe	Fe	Ni/Fe
A2199	0.2	4.111 \pm 0.011	0.289 \pm 0.003	1.12 \pm 0.14	1.17 \pm 0.23	0.76 \pm 0.05	0.94 \pm 0.10	0.92 \pm 0.05	0.86 \pm 0.11	1.27 \pm 0.13	0.581 \pm 0.004
	0.05	3.643 \pm 0.010	0.272 \pm 0.003	=	=	0.52 \pm 0.21	0.99 \pm 0.14	1.03 \pm 0.06	1.02 \pm 0.14	1.41 \pm 0.17	0.774 \pm 0.005
A2597	0.2	3.421 \pm 0.016	0.258 \pm 0.006	1.30 \pm 0.20	1.3 \pm 0.3	0.54 \pm 0.11	0.7 \pm 0.4	1.06 \pm 0.13	1.0 \pm 0.8	1.1 \pm 0.3	0.493 \pm 0.008
	0.05	3.035 \pm 0.016	0.242 \pm 0.007	=	=	0.59 \pm 0.14	0.6 \pm 0.4	0.9 \pm 0.5	1.4 \pm 1.1	0.9 \pm 0.4	0.564 \pm 0.011
A2626	0.2	3.06 \pm 0.03	0.204 \pm 0.015	0.9 \pm 0.3	0.8 \pm 0.5	0.42 \pm 0.16	0.76 \pm 0.07	0.99 \pm 0.18	0.9 \pm 0.3	0.9 \pm 0.4	0.0687 \pm 0.019
	0.05	2.77 \pm 0.05	0.183 \pm 0.019	=	=	0.8 \pm 0.3	0.86 \pm 0.12	0.55 \pm 0.20	1.5 \pm 0.5	0.23 \pm (< 0.74)	0.90 \pm 0.04
A3112	0.2	4.502 \pm 0.019	0.289 \pm 0.005	0.84 \pm 0.11	0.42 \pm 0.20	0.5 \pm 0.3	0.64 \pm 0.14	0.85 \pm 0.07	0.71 \pm 0.13	1.35 \pm 0.16	0.814 \pm 0.006
	0.05	3.696 \pm 0.019	0.250 \pm 0.005	=	=	0.5 \pm 0.3	0.6 \pm 0.3	0.76 \pm 0.07	1.0 \pm 0.6	1.22 \pm 0.22	1.116 \pm 1.116
A3526	0.2	3.137 \pm 0.007	0.2745 \pm 0.0012	0.67 \pm 0.04	0.74 \pm 0.10	0.97 \pm 0.20	0.99 \pm 0.07	1.04 \pm 0.03	0.9 \pm 0.3	1.33 \pm 0.06	1.104 \pm 0.005
	0.05	2.554 \pm 0.006	0.2381 \pm 0.0010	=	=	0.540 \pm 0.020	0.99 \pm 0.08	1.12 \pm 0.08	1.08 \pm 0.04	1.36 \pm 0.06	1.675 \pm 0.06
A3581	0.05	1.637 \pm 0.008	0.132 \pm 0.003	0.77 \pm 0.08	0.85 \pm 0.20	0.75 \pm 0.18	0.86 \pm 0.19	0.86 \pm 0.08	1.19 \pm 0.08	0.7 \pm 0.5	1.37 \pm 0.19
	0.05	3.120 \pm 0.013	0.225 \pm 0.005	1.09 \pm 0.24	(< 0.6)	0.86 \pm 0.08	0.86 \pm 0.18	1.09 \pm 0.08	0.9 \pm 0.6	1.00 \pm 0.19	0.547 \pm 0.007
A4038	0.05	3.117 \pm 0.021	0.233 \pm 0.007	=	=	0.5 \pm (< 0.9)	0.88 \pm 0.05	0.98 \pm 0.11	1.1 \pm 0.3	1.3 \pm 0.3	0.673 \pm 0.013
	0.05	3.956 \pm 0.017	0.294 \pm 0.004	0.76 \pm 0.11	0.91 \pm 0.21	0.64 \pm 0.06	0.85 \pm 0.15	0.87 \pm 0.15	0.78 \pm 0.07	0.85 \pm 0.14	0.756 \pm 0.016
AS1101	0.2	3.275 \pm 0.018	0.271 \pm 0.004	=	=	0.67 \pm 0.09	0.92 \pm 0.21	0.97 \pm 0.09	0.76 \pm 0.19	0.98 \pm 0.22	1.069 \pm 0.019
	0.05	2.503 \pm 0.007	0.170 \pm 0.003	0.75 \pm 0.10	0.69 \pm 0.14	0.7 \pm 0.1	0.76 \pm 0.11	0.81 \pm 0.17	0.76 \pm 0.07	0.95 \pm 0.13	0.503 \pm 0.005
A4059	0.05	2.359 \pm 0.011	0.163 \pm 0.005	=	=	0.63 \pm 0.09	0.79 \pm 0.19	0.88 \pm 0.08	0.91 \pm 0.17	1.08 \pm 0.21	1.013 \pm 0.010
	0.05	3.753 \pm 0.010	0.240 \pm 0.004	1.20 \pm 0.18	0.4 \pm 0.15	0.82 \pm 0.15	0.91 \pm 0.09	0.96 \pm 0.04	0.9 \pm 0.3	1.32 \pm 0.09	1.069 \pm 0.004
EXO4022	0.2	2.904 \pm 0.020	0.182 \pm 0.011	1.1 \pm 0.18	1.1 \pm 0.3	0.9 \pm 0.21	0.64 \pm 0.12	1.14 \pm 0.05	1.09 \pm 0.10	1.3 \pm 0.07	1.171 \pm 0.111
	0.05	2.655 \pm 0.023	0.162 \pm 0.014	=	=	0.63 \pm 0.14	0.97 \pm 0.07	0.96 \pm 0.13	0.23 \pm 0.13	0.28 \pm 0.13	0.817 \pm 0.023
Formax	0.05	1.321 \pm 0.007	0.15 \pm 0.004	0.64 \pm 0.10	0.56 \pm 0.19	0.82 \pm 0.06	1.0 \pm 0.3	1.2 \pm 0.6	1.0 \pm 0.6	0.9 \pm 0.3	0.856 \pm 0.021

3.D Best-fit temperature and abundances

Table 3.4: continued.

Source	Region	kT (r_{500})	σ_T	O/Fe	Ne/Fe	Mg/Fe	Si/Fe	S/Fe	Ar/Fe	Ca/Fe	Fe	Ni/Fe
HCG62	0.05	0.958 \pm 0.007	0.128 \pm 0.004	0.77 \pm 0.11	1.14 \pm 0.23	0.79 \pm 0.09	1.0 \pm 0.3	1.3 \pm 0.6	1.4 \pm 0.4	0.8 (< 1.6)	0.70 \pm 0.04	—
Hydra A	0.2	3.450 \pm 0.010	0.269 \pm 0.003	1.3 \pm 0.3	0.53 \pm 0.26 —	0.42 \pm 0.09	0.72 \pm 0.24	0.9 \pm 0.4	0.75 \pm 0.18	1.00 \pm 0.22	0.488 \pm 0.005	2.1 \pm 0.5
M49	0.05	3.303 \pm 0.015	0.257 \pm 0.005	=	=	0.33 \pm 0.10	0.69 \pm 0.29	1.0 \pm 0.3	0.9 (< 1.6)	0.5 \pm 0.3 1.01 \pm	0.601 \pm 0.010	3.1 \pm 0.8
M60	0.05	1.148 \pm 0.004	0.269 \pm 0.003	0.64 \pm 0.10	0.78 \pm 0.20	0.83 \pm 0.23	1.04 \pm 0.13	1.18 \pm 0.09	1.0 \pm 0.3	1.0 \pm 0.3	0.928 \pm 0.022	—
M84	0.05	0.923 \pm 0.003	0.442 \pm 0.004	0.66 \pm 0.07	1.2 \pm 0.4 0.13	1.1 \pm 0.3 0.13	0.8 \pm 0.3	1.0 \pm 0.4	0.4 (< 1.5)	0.478 \pm 0.011	—	—
M86	0.05	0.967 \pm 0.006	0.120 \pm 0.004	0.24	0.22 \pm 0.18	2.7 \pm 2.0 0.18	1.4 \pm 0.6 0.18	2.6 \pm 2.2 0.96 \pm	1.3 (< 2.7)	0.0 \pm 1.0 \pm 0.3	0.37 \pm 0.03	—
M87	0.05	2.0517 \pm 0.0018	0.1572 \pm 0.0005	1.06 \pm 0.17	0.61 \pm 0.12	0.707 \pm 0.014	1.13 \pm 0.05	1.30 \pm 0.16	1.21 \pm 0.20	1.55 \pm 0.16	0.7546 \pm 0.0014	2.6 \pm 0.4
M89	0.05	0.646 \pm 0.018	0.10*	2.0 \pm 0.6	1.1 \pm 0.7	—	1.4 \pm 5.3 —	—	—	0.30 \pm	—	—
MKV3s	0.2	3.637 \pm 0.013	0.254 \pm 0.004	0.84 \pm 0.23	0.72 \pm 0.22	0.9 \pm 0.3	0.84 \pm 0.18	0.89 \pm 0.07	0.84 \pm 0.16	1.29 \pm 0.18	0.607 \pm 0.007	2.0 \pm 0.4
MKV4	0.2	1.909 \pm 0.011	0.121 \pm 0.004	0.66 \pm 0.12	0.87 \pm 0.26	0.77 \pm 0.07	0.81 \pm 0.14	0.97 \pm 0.14	0.75 \pm 0.14	1.01 \pm 0.19	0.863 \pm 0.013	0.9 \pm 0.5
NGC507	0.05	1.257 \pm 0.008	0.131 \pm 0.005	0.69 \pm 0.39 0.18	0.14 \pm 0.66 0.06	0.73 \pm 0.08	0.9 \pm 0.3	1.3 \pm 0.5	1.46 \pm 0.25	1.0 \pm 0.4	0.89 \pm 0.03	(< 3.0)
NGC1316	0.05	0.768 \pm 0.012	0.235 \pm 0.016	1.2 \pm 0.4	1.0 \pm 0.4	1.0 \pm 0.9	0.66 \pm 0.12	0.9 \pm 0.6	0.7 (< 2.3)	—	0.34 \pm	—
NGC1404	0.05	0.64 \pm 0.003	0.359 \pm (< 0.018)	0.89 \pm 0.11	0.60 \pm 0.22	—	0.8 \pm 0.4	—	—	0.0 \pm 0.17	0.03	—
NGC1550	0.05	1.328 \pm 0.004	0.088 \pm 0.003	0.088 \pm 0.11	0.23 \pm 0.04	0.68 \pm 0.04	0.95 \pm 0.19	1.09 \pm 0.13	1.1 \pm 0.6	1.17 \pm 0.20	0.607 \pm 0.010	—
NGC3411	0.05	0.933 \pm 0.006	0.32 \pm 0.021	0.95 \pm 0.04	0.9 \pm 0.3 0.25	1.3 \pm 0.5	1.0 \pm 0.3	1.13 \pm 0.23	0.8 \pm 0.6 —	0.0 \pm (< 1.7)	0.59 \pm 0.03	—
NGC4261	0.05	0.940 \pm 0.012	0.071 \pm 0.010	0.65 \pm 0.18	1.1 \pm 0.4 0.18	0.50 \pm 0.16	1.2 \pm 0.6 1.19 \pm	1.3 \pm 1.0 1.1 \pm 0.3	1.7 \pm 1.0 1.23 \pm	1.7 \pm 1.0 1.6 \pm 1.6 (< 4.1)	0.64 \pm 0.06	—
NGC4325	0.05	0.931 \pm 0.012	0.103 \pm 0.004	0.85 \pm 0.07	0.87 \pm 0.10	0.74 \pm 0.10	0.93 \pm 0.15	1.3 \pm 0.3 0.14	1.4 \pm 0.5 0.14	1.5 \pm 0.3 0.14	0.668 \pm 0.010	—
NGC4636	0.05	0.7498 \pm 0.0025	0.0811 \pm 0.0011	—	—	—	—	—	—	—	—	—
NGC5044	0.05	0.9741 \pm 0.0020	—	—	—	—	—	—	—	—	—	—

Table 3.4: continued.

Source	Region	kT (r_{500})	σ_T	O/Fe	Ne/Fe	Mg/Fe	Si/Fe	Ar/Fe	Ca/Fe	Fe	Ni/Fe
NGC5813	0.05	0.7275 ± 0.0016	0.092 ± 0.003	0.76 ± 0.07	0.42 ± 0.09	1.45 ± 0.09	1.1 ± 0.3	1.2 ± 0.5	1.0 ± 0.6	0.715 ± 0.020	—
NGC5846	0.05	0.7585 ± 0.0023	0.128 ± 0.004	0.99 ± 0.11	0.90 ± 0.15	0.89 ± 0.14	1.3 ± 0.3	1.22 ± 0.13	1.3 ± 0.4	0.659 ± 0.017	—
Pegasus	0.2	4.865 ± 0.004	0.3177 ± 0.0006	1.24 ± 0.18	1.05 ± 0.16	0.74 ± 0.09	0.83 ± 0.03	0.87 ± 0.09	0.9 ± 0.3	< 1.4) ± 0.97	1.8 ± 0.5
	0.05	3.905 ± 0.003	0.2752 ± 0.0007	=	=	0.45 ± 0.15	0.81 ± 0.04	0.90 ± 0.11	0.9 ± 0.3	1.04 ± 0.18	0.7543 ± 0.0015

L'Univers est ce qu'il est. Il n'a que faire de nos préjugés.

The Universe is what it is. It does not care about our preconceptions.

– Hubert Reeves, *Patience dans l'azur*

4

Origin of central abundances in the hot intra-cluster medium II. Chemical enrichment and supernova yield models

F. Mernier, J. de Plaa, C. Pinto, J. S. Kaastra, P. Kosec, Y.-Y. Zhang, J. Mao,
N. Werner, O. R. Pols, and J. Vink
(Astronomy & Astrophysics, Volume 595, id.A126, 19 pp.)

Abstract

The hot intra-cluster medium (ICM) is rich in metals, which are synthesised by supernovae (SNe) and accumulate over time into the deep gravitational potential well of clusters of galaxies. Since most of the elements visible in X-rays are formed by type Ia (SNIa) and / or core-collapse (SNcc) supernovae, measuring their abundances gives us direct information on the nucleosynthesis products of billions of SNe since the epoch of the star formation peak ($z \sim 2-3$). In this study, we compare the most accurate average X/Fe abundance ratios (compiled in a previous work from *XMM-Newton* EPIC and RGS observations of 44 galaxy clusters, groups, and ellipticals), representative of the chemical enrichment in the nearby ICM, to various SNIa and SNcc nucleosynthesis models found in the literature. The use of a SNcc model combined to any favoured standard SNIa model (deflagration or delayed-detonation) fails to reproduce our abundance pattern. In particular, the Ca/Fe and Ni/Fe ratios are significantly underestimated by the models. We show that the Ca/Fe ratio can be reproduced better, either by taking a SNIa delayed-detonation model that matches the observations of the Tycho supernova remnant, or by adding a contribution from the “Ca-rich gap transient” SNe, whose material should easily mix into the hot ICM. On the other hand, the Ni/Fe ratio can be reproduced better by assuming that both deflagration and delayed-detonation SNIa contribute in similar proportions to the ICM enrichment. In either case, the

fraction of SNIa over the total number of SNe (SNIa+SNcc) contributing to the ICM enrichment ranges within 29–45%. This fraction is found to be systematically higher than the corresponding SNIa/(SNIa+SNcc) fraction contributing to the enrichment of the proto-solar environment (15–25%). We also discuss and quantify two useful constraints on both SNIa (i.e. the initial metallicity on SNIa progenitors and the fraction of low-mass stars that result in SNIa) and SNcc (i.e. the effect of the IMF and the possible contribution of pair-instability SNe to the enrichment) that can be inferred from the ICM abundance ratios. Finally, we show that detonative sub-Chandrasekhar WD explosions (resulting, for example, from violent WD mergers) cannot be a dominant channel for SNIa progenitors in galaxy clusters.

4.1 Introduction

Since the emergence and progress of stellar nucleosynthesis models over the past century, it is now well known that all the heavy elements in the Universe (i.e. except H, He, and traces of Li and Be, which were produced shortly after the Big Bang) have been produced by stars and stellar remnants (Cameron 1957b; Burbidge et al. 1957). In particular, α - and Fe-peak elements ($8 \leq Z \leq 28$) are mostly synthesised by nuclear fusion reactions during stellar lifetimes and supernova (SN) explosions, and are then released into and beyond the interstellar medium (e.g. Arnett 1973; Tinsley 1980). On the one hand, oxygen (O), neon (Ne), magnesium (Mg), silicon (Si), and sulfur (S), are thought to be mostly produced by core-collapse supernovae (SNcc). On the other hand, Type Ia supernovae (SNIa) produce predominantly argon (Ar), calcium (Ca), chromium (Cr), manganese (Mn), iron (Fe), and nickel (Ni). Finally, when low-mass stars ($< 6 M_{\odot}$) leave the main sequence and enter into their asymptotic giant branch (AGB) phase, they are efficient in releasing lighter metals, such as carbon (C) or nitrogen (N), via powerful winds. Although this general picture of synthesis (and recycling) of metals through cosmic ages is now well established, many issues are still unsolved and still bring a great deal of uncertainty when identifying the specific origins of each element.

First, it is well known that SNcc result from the end-of-life explosion of massive stars (~ 10 – $140 M_{\odot}$). However, several parameters, such as the mass cut that separates the collapsing core from the supernova remnant (SNR) or the final kinetic energy of the explosion, are poorly constrained. Consequently, some differences in the predicted abundance pattern from proposed SNcc models proposed by different groups still remain (for a re-

view, see Nomoto et al. 2013). Moreover, the relative amount of unburned elements depends on the initial mass and metallicity of the progenitor star (e.g. Woosley & Weaver 1995). These two parameters are not always easy to constrain, especially when considering a whole population of (massive) stars, whereas the universality of the initial mass function (IMF) is still under debate (e.g. Treu et al. 2010; Dutton et al. 2012).

Second, despite their fundamental role both in the Galactic chemical evolution (e.g. Timmes et al. 1995; Kobayashi & Nomoto 2009) and as standard candles for cosmological distances (Riess et al. 1998; Schmidt et al. 1998), the nature of SNIa progenitors is still elusive (for reviews, see Howell 2011; Maoz & Mannucci 2012; Hillebrandt et al. 2013; Maoz et al. 2014). It seems likely that the explosion results from an accreting carbon-oxygen white dwarf (WD), which ignites shortly before reaching its Chandrasekhar mass. However, it is not clear whether the mass transfer is due to a normal stellar companion (single degenerate scenario; Whelan & Iben 1973) or a second white dwarf (double degenerate scenario; Webbink 1984; Iben & Tutukov 1984). Furthermore, the physics of the SNIa explosion itself is poorly constrained (for a review, see Hillebrandt & Niemeyer 2000). In most models, the explosion starts with a deflagration (i.e. the burning front propagates subsonically). The currently favoured explosion models suggest that when the burning front reaches a certain critical density, it propagates supersonically, and the deflagration becomes a detonation. These so-called delayed-detonation models (Khokhlov 1989), in particular their variant of deflagration-to-detonation transition (DDT), have been studied in detail (Khokhlov 1991; Niemeyer & Woosley 1997; Gamezo et al. 2005; Seitenzahl et al. 2013b, e.g.), but not yet fully understood. Moreover, some peculiar SNIa (e.g. the 2002cx supernovae, Kromer et al. 2013) seem to be better explained by invoking a pure deflagration explosion (Branch et al. 2004; Jha et al. 2006; Phillips et al. 2007). What is clear, however, is that the abundance pattern of the elements synthesised by SNIa is very sensitive to their explosion mechanism.

Many attempts to constrain all these SNcc and SNIa uncertainties have been made by studying the optical and X-ray spectra of SNRs and, particularly, their abundance pattern (e.g. Badenes et al. 2006; Yasumi et al. 2014). However, such an approach is difficult in practice, mostly because only a few Galactic SNRs are suitable for studying the composition of their ejecta, preventing any statistical study over large samples; the emitting plasma of the SNRs is far from being in ionisation equilibrium, making its spec-

troscopy complicated and not yet fully understood; and the ejected material from the SNR easily mixes with the surrounding ISM, making it a challenge to correctly estimate the metal abundances from the SN itself.

An interesting alternative approach to investigating nucleosynthesis products from supernovae (SNe) is to consider the chemical enrichment at the scale of galaxy clusters. In fact, the hot intra-cluster medium (ICM) pervading the volume of galaxy clusters and groups, and accounting for no less than $\sim 80\%$ of their total baryonic matter, is rich in α - and Fe peak elements (for reviews, see Werner et al. 2008; Böhringer & Werner 2010). These metals, which can be observed via their emission lines from X-ray spectroscopy, must have been synthesised by SNIa and SNcc inside the cluster galaxies, and have enriched the ICM, especially around $z \simeq 2-3$, during the major cosmic epoch of star formation (Hopkins & Beacom 2006; Madau & Dickinson 2014). Assuming that the large gravitational potential well of clusters/groups make them behave like a closed-box system, the metal abundances of the ICM are a remarkable signature of the yields of billions of SNIa and SNcc over time. Moreover, the ICM is well known to be in (or very close to) collisional ionisation equilibrium state, making its spectroscopy less complex than SN spectra and its abundances relatively easy to derive.

Several previous studies have already attempted to use abundance measurements in the ICM in order to constrain SNIa and SNcc yield models. For instance, de Plaa et al. (2007) compiled a sample of 22 cool-core clusters, and found that the standard SNIa models fail to reproduce the Ar/Ca and Ca/Fe abundance ratios. They also showed that the fraction of SNIa over the total number of SNe highly depends of the considered models. De Grandi & Molendi (2009) showed that Si/Fe abundance ratios are remarkably uniform over a sample of 26 cool-core clusters observed with *XMM-Newton*, arguing for a similar enrichment process within cluster cores. However, they concluded that systematic uncertainties between the SN models are too large to precisely estimate the relative contribution of SNIa and SNcc. Finally, many abundance studies have been performed on individual objects as well (e.g. Werner et al. 2006b; de Plaa et al. 2006; Sato et al. 2007a; Simionescu et al. 2009b, Chapter 2). From these studies, and considering the instrumental performance of current X-ray observatories, it appears that higher quality data (i.e. with longer exposure time), collected over larger samples, are needed to clarify the picture of the pre-

cise origin of metals in the ICM.

In this paper, we make use of ICM abundances measured in two previous works (Chapter 3; de Plaa et al. 2017) and compare them with predictions from theoretical SNIa and SNcc yield models. These measurements consist of the average X/Fe abundance ratios of ten elements (O/Fe, Ne/Fe, Mg/Fe, Si/Fe, S/Fe, Ar/Fe, Ca/Fe, Cr/Fe, Mn/Fe, and Ni/Fe) in the ICM of 44 cool-core clusters, groups, and ellipticals, using the *XMM-Newton* EPIC and RGS instruments. To our knowledge, this is the most complete and robust abundance pattern measured in the ICM available to date.

This paper is structured as follows. In Sect. 4.2 we present the sample and briefly recall the data reduction, as well as the spectral analysis used to derive the abundance ratios. We then discuss the comparison between various SNIa and SNcc models and our average ICM abundance pattern (Sect. 4.3) on the one hand, and the proto-solar abundances (Sect. 4.4) on the other hand. Section 4.5 summarises our discussion and addresses future prospects. Throughout this paper we assume cosmological parameters of $H_0 = 70 \text{ km s}^{-1} \text{ Mpc}^{-1}$, $\Omega_m = 0.3$, and $\Omega_\Lambda = 0.7$. The abundances presented in this paper are taken relative to the proto-solar values of Lodders et al. (2009). All the error bars are given at a 68% confidence level.

4.2 Observations and spectral analysis

We start by briefly summarising the main steps of the data reduction and the spectral analysis that were necessary to provide the average X/Fe abundance pattern (Fig. 4.1), representative of the ICM of cool-core objects. The detailed presentation, reduction, and spectral analysis of our observations can be found in Chapter 3 and in de Plaa et al. (2017).

Our sample consists of the CHEERS¹ catalogue (de Plaa et al. 2017), and is detailed in Table 3.1 (see also Pinto et al. 2015; de Plaa et al. 2017). It includes 44 nearby ($z < 0.1$) cool-core clusters, groups, and elliptical galaxies for which the O VIII 1s–2p line at 19 Å is detected by the RGS instrument with $>5\sigma$. Recent *XMM-Newton* observations (AO-12, PI: de Plaa) have been combined with archival data. We reduced the EPIC and RGS data using the *XMM-Newton* Science Analysis System (SAS) software v14.0.0. After having filtered them from solar-flare events, we obtain cleaned EPIC MOS 1, MOS 2, and pn data of ~ 4.5 , ~ 4.6 , and ~ 3.7 Ms, respectively.

¹CHEMical Enrichment Rgs Sample

4.3 Chemical enrichment in the ICM

The EPIC spectra were extracted within a circle of a radius of either $0.2r_{500}$ (for $kT_{\text{mean}} > 1.7 \text{ keV}$, i.e. the farther clusters) or $0.05R_{500}$ (for $kT_{\text{mean}} < 1.7 \text{ keV}$, i.e. the nearer groups/ellipticals). The RGS spectra were extracted with a cross-dispersion width of $0.8'$. We carefully checked that the difference in these EPIC and RGS extraction regions did not affect our final results (Chapter 3).

We used the SPEX fitting package (Kaastra et al. 1996) v2.05 to perform our spectral fits. The EPIC and RGS spectra were fitted with a `gdem` and a `2T` (i.e. `cie+cie`) thermal model, respectively. The EPIC (X-ray and particle) background components were carefully modelled following the method detailed in Chapter 2. The free parameters in our fits were the emission measure (or normalisation), the temperature parameters (kT_{mean} and σ_T for a `gdem` model; kT_{up} and kT_{low} for a `2T` model), and the abundances of O, Ne, Mg, Si, S, Ar, Ca, Fe, and Ni for EPIC, and O, Ne, Mg, and Fe for RGS. We were also able to constrain the EPIC sample-averaged abundances of Cr and Mn by converting the equivalent width of their line fluxes (at rest-frame energies of $\sim 5.7 \text{ keV}$ and $\sim 6.2 \text{ keV}$, respectively) as described in Chapter 2.

We finally computed a weighted average of all the considered X/Fe abundance ratios (taking O/Fe and Ne/Fe from RGS, and Mg/Fe, Si/Fe, S/Fe, Ar/Fe, Ca/Fe, Cr/Fe, Mn/Fe, and Ni/Fe from EPIC), carefully taking account of all the possible systematic uncertainties that could affect our measurements. This final abundance pattern, reasonably representative of the ICM enrichment in the cool cores of clusters, groups, and ellipticals, is shown in Fig. 4.1 (see also Fig. 3.7). The Cr/Fe, Mn/Fe, and Ni/Fe abundance ratios are found to differ significantly from the proto-solar values. The ICM average abundance pattern, as well as the proto-solar estimates² and their uncertainties (Lodders et al. 2009), can now be directly compared to various sets of SN yield models.

4.3 Chemical enrichment in the ICM

Since the metals present in the ICM are the product of billions of SNe that exploded mostly in the cluster galaxies, the average abundance ratios measured in the ICM bear witness to the contribution of both SNIa and SNcc

²The proto-solar abundances used in this paper (Lodders et al. 2009) are currently the most representative abundances of the solar system at its formation as they are based on meteoritic compositions.

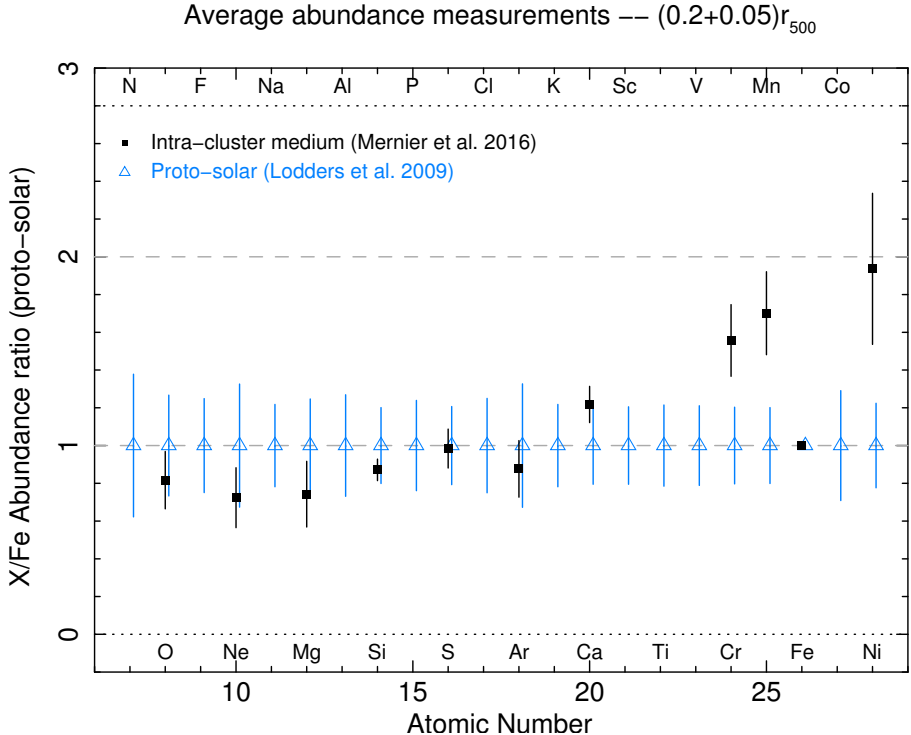


Figure 4.1: Average abundance ratios measured in the ICM (black filled squares, see Chapter 3) versus proto-solar abundances (blue empty triangles, adapted from Lodders et al. 2009) and their 1σ uncertainties.

to the chemical enrichment of galaxy clusters and groups. Following several past attempts (Werner et al. 2006b; de Plaa et al. 2006, 2007, Chapter 2), we fit a combination of SNIa and SNcc nucleosynthesis models to our ICM average abundance pattern. More quantitatively, the total number of atoms of the i -th element in the ICM can be expressed as a linear combination of the number of atoms expected from SNIa ($N_{i,\text{Ia}}$) and SNcc ($N_{i,\text{cc}}$) contributions (e.g. Werner et al. 2006b)

$$N_{i,\text{tot}} = a N_{i,\text{Ia}} + b N_{i,\text{cc}}, \quad (4.1)$$

where a and b are multiplicative factors corresponding respectively to the number of SNIa and SNcc that released their metal contents into the ICM. Since $N_{i,\text{Ia}}$ and $N_{i,\text{cc}}$ can be easily converted into abundances, we can fit this linear combination to our average abundance pattern (ten data points), and

infer the SNIa-to-SNe fraction

$$\frac{\text{SNIa}}{\text{SNIa} + \text{SNcc}}, \quad (4.2)$$

which represents the relative number of SNIa over the total number of SNe responsible for the enrichment. As noted by Matteucci & Chiappini (2005), the equations above assume an instantaneous recycling of the metals, and such a ratio should not be interpreted as the true relative number of SNIa over the entire lifetime of the clusters, but rather as the SNIa ratio necessary to enrich the ICM (de Plaa et al. 2007).

Throughout this paper, many SNIa and SNcc yield models are considered. They are all summarised in Table 4.5, and described further in the text when needed. In Fig. 4.2, we plot the X/Fe abundance pattern predicted from several individual SNIa (upper panel) and SNcc (lower panel) models. In particular, we emphasise the differences in the nucleosynthesis of SNIa deflagration and delayed-detonation explosions (upper panel), and the effects of the initial metallicity (Z_{init}) of massive stars on their predicted SNcc yields (lower panel). Specific comparisons are also discussed in this paper.

4.3.1 Abundance pattern of even-Z elements

In this section, we consider only the ratio of even-Z elements (i.e. O/Fe, Ne/Fe, Mg/Fe, Si/Fe, S/Fe, Ar/Fe, Ca/Fe, Cr/Fe, and Ni/Fe) as part of the ICM abundance pattern. In fact, the Mn/Fe ratio is particular, in the sense that it may depend on the metallicity of the SNIa progenitors, which has not been fully taken into account in most of the yield models so far. For this reason, Mn/Fe needs to be considered separately. In Sect. 4.3.2, we discuss this initial metallicity dependence extensively and we derive other useful information related to SNIa progenitors in general from the observed Mn/Fe ratio.

Classical SNIa and Nomoto SNcc yields

One set of SNIa models commonly referred to in the literature (hereafter the “Classical” models, Table 4.5) is from Iwamoto et al. (1999), who predicted nucleosynthesis products regarding different one-dimensional (1-D) explosion mechanisms. Two initial central densities (ρ_0 , given in units of 10^9 g/cm^3) are considered (C and W models, see Table 4.5). The W7 and

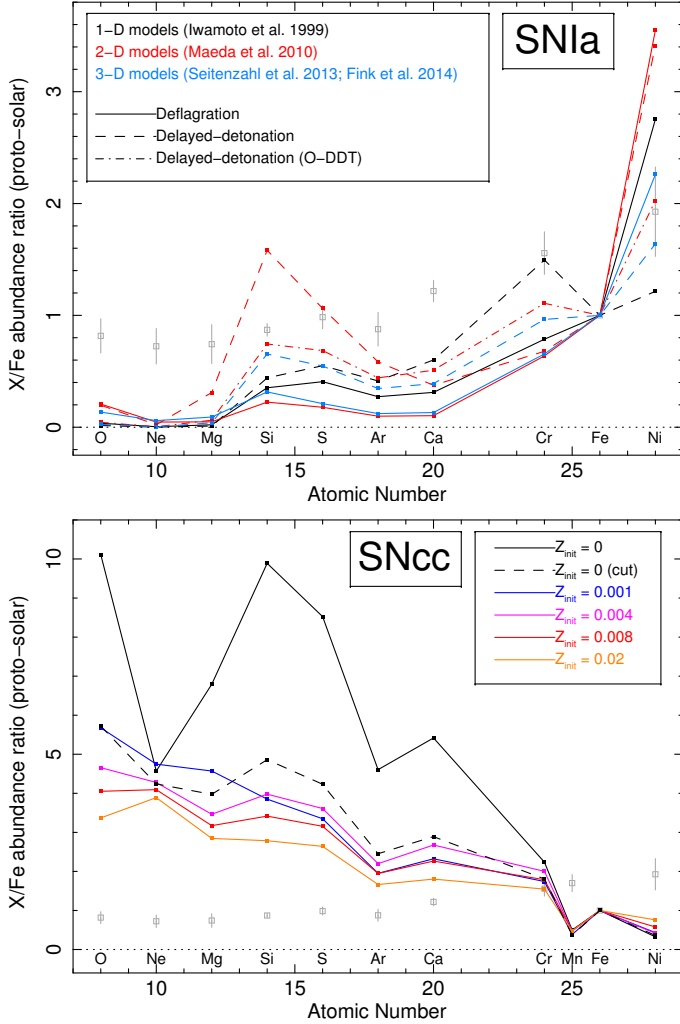


Figure 4.2: Predicted X/Fe abundances from various SNIa and SNcc yield models. For comparison, the ICM average abundance ratios (inferred from Chapter 3) are also plotted. *Top:* SNIa yield models: 1-D (W7 and WDD2 from Iwamoto et al. 1999), 2-D (C-DEF, C-DDT, and O-DDT from Maeda et al. 2010), and 3-D (N100def and N100 from Fink et al. (2014) and Seitenzahl et al. (2013b), respectively) models are indicated in black, red, and blue, respectively. A distinction is also made between the explosion models: deflagration (W7, C-DEF, and N100def; solid lines) and delayed-detonation (dashed lines for WDD2, C-DDT, and N100; dash-dotted lines for O-DDT). The Mn/Fe ratio is not shown here because it highly depends on the initial metallicity of SNIa progenitors (Sect. 4.3.2). *Bottom:* SNcc models, all taken from Nomoto et al. (2013), assuming a Salpeter IMF. Various initial metallicities (Z_{init}) for SNcc progenitors are compared. The dashed line corresponds to the $Z0_{\text{cut}}$ model (see text).

W70 models assume a pure deflagration during the SNIa event, while the WDD and CDD models assume a delayed-detonation, with three possible transition densities ($\rho_{T,7}$, given in units of 10^7 g/cm 3). The models currently favoured by the supernova community are the delayed-detonation models, and among these, WDD2 is usually preferred (Iwamoto et al. 1999).

A well-referenced set of SNcc models was given by Nomoto et al. (2006) and has been recently updated by Nomoto et al. (2013, hereafter the “Nomoto” models), who estimated nucleosynthesis products of a SNcc as a function of the mass and the initial metallicity ($Z_{\text{init}} = 0, 0.001, 0.004, 0.008$, or 0.02) of its progenitor. In order to estimate the total yield mass $M_{i,\text{SNcc}}$ of the i -th element coming from SNcc explosions, we integrate these models (following Tsujimoto et al. 1995) over a power-law IMF between 10 – $40 M_\odot$ (or 10 – $140 M_\odot$ when $Z_{\text{init}} = 0$; Nomoto et al. 2013), as

$$M_{i,\text{SNcc}} = \frac{\int_{10M_\odot}^{(1)40M_\odot} M_i(m) m^{-(1+x)} dm}{\int_{10M_\odot}^{(1)40M_\odot} m^{-(1+x)} dm}, \quad (4.3)$$

where $M_i(m)$ is the mass yield of the i -th element at a given mass m of the main sequence progenitor and x is the power index of the IMF. Here we assume that the fraction of metals resulting from the SNcc enrichment have been generated by a population of massive stars having a Salpeter IMF ($x = 1.35$; Salpeter 1955) and sharing a common Z_{init} . We note that in the case $Z_{\text{init}} = 0$, the stellar yields beyond $40 M_\odot$ are available for $100 M_\odot$ and $140 M_\odot$ only. Consequently, a precise integration over the IMF (Eq. 4.3) within the 40 – $140 M_\odot$ range is not trivial, and the IMF-weighted abundance ratios of the Z0 model might be somewhat altered by the choice of the mass binning. For this reason, in the following we also consider the Z0_cut model, similar to the Z0 model, but restricted to $\leq 40 M_\odot$ (Table 4.5 and Fig. 4.2 top; see also Nomoto et al. 2006).

Considering all the possible combinations of a Classical SNIa model plus a Nomoto SNcc model, our best fit (Fig. 4.3) is reached for a WDD2 model and a SNcc initial metallicity $Z_{\text{init}} = 0.008$. With a reduced χ^2 of ~ 2.8 , this fit is quite poor. In particular, the Ar/Fe, Ca/Fe, and Ni/Fe ratios are underestimated with $>1\sigma$, $>3\sigma$, and $>2\sigma$ respectively, while Si/Fe is overestimated with $>2\sigma$. In Table 4.1 (top panel) we indicate the five best fits (including this one) that we find with this Classical combination of models, as well as their respective estimated SN fractions. The errors on the SN fractions are typically about ± 5 – 6% . Although all these fits are poor, the delayed-detonation models are always favoured. The SNIa rates

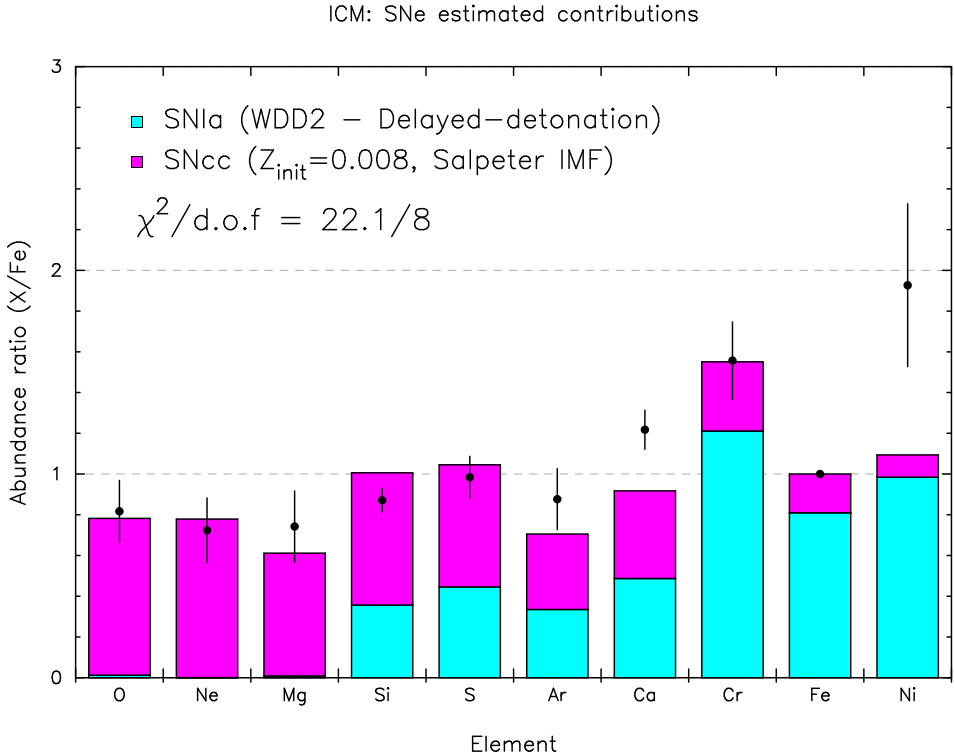


Figure 4.3: Average abundance ratios versus atomic numbers in the average ICM abundance pattern (Chapter 3). The histograms show the yields contribution of a best-fit combination of one Classical SNIIa model (WDD2) and one Nomoto SNcc ($Z_{\text{init}} = 0.008$, and Salpeter IMF) model.

are always comparable, ranging between $\sim 29\%$ and $\sim 35\%$. We note that the WDD2 model with $Z = 0.02$ used in de Plaa et al. (2007) has a reduced χ^2 of ~ 2.9 , and also shows clear discrepancies in Ca/Fe ($>3\sigma$), and Ni/Fe ($>2\sigma$). Clearly, these combinations fail to reproduce our measured ICM abundance pattern.

Ca/Fe ratio: A contribution from Ca-rich SNe?

In previous studies and in this work the Ca/Fe measured ratio in the ICM was found to be higher than expected. Using the same Classical models (together with the SNcc models of Nomoto et al. 2006), Werner et al. (2006b), de Plaa et al. (2006), de Plaa et al. (2007), and Chapter 2 reported a signifi-

cant underestimate of the Ca / Fe expected yields compared to the measurements. Also in stellar populations, chemical evolution models from Crosby et al. (2016) (who made use of the Classical SNIa yields predictions as well) failed to reproduce observations of Ca/Fe. Although residual systematic biases in the Ca abundance measurements cannot be excluded, this possibility is quite unlikely. Indeed, atomic databases have been considerably improved during the past decades, the continuum and line fluxes in this work have been fitted carefully, the EPIC MOS and pn instruments agree very well in their Ca / Fe measurements, and no line feature around ~ 4 keV has been reported so far in the EPIC effective areas or in the particle background (for more details, see Chapter 3).

As one possibility of solving this conundrum, de Plaa et al. (2007) made use of an alternative delayed-detonation SNIa model, which provides the best description of the spectra of the Tycho SNR (Badenes et al. 2006). More specifically, de Plaa et al. (2007) showed that the DDTc model of Bravo et al. (1996) better fits the measured Ar/Fe and Ca/Fe ratios. In this paper, we test three models (DDTa, DDTc, and DDTe; hereafter the “Bravo” models) introduced in Badenes et al. (2003) and Badenes et al. (2006) that are based on the calculations of Bravo et al. (1996) and that reasonably reproduce the spectral features of Tycho. The best fit using these models is shown in Fig. 4.4 (top left) and Table 4.1 (second panel).

Similarly to de Plaa et al. (2007), we obtain the best fit to our abundance pattern when using the DDTc model. The fits are significantly better than in the Classical models (for the best fit, $\chi^2/\text{d.o.f.} \simeq 1.3$), essentially because this alternative successfully reproduces the observed Si/Fe, Ar/Fe, and (above all) Ca/Fe ratios. However, the Ni/Fe ratio is still clearly underestimated ($>2\sigma$). The SNIa-to-SNe fraction ranges from $\sim 29\%$ to $\sim 35\%$, which is similar to what was found for the Nomoto+Classical case.

Another possibility has been recently proposed by Mulchaey et al. (2014), and suggests a significant additional contribution from Ca-rich gap transients to the ICM enrichment. Although spectroscopically defined as Type Ib/Ic, this recently discovered subclass of SNe (Filippenko et al. 2003; Perets et al. 2010, 2011) is thought to originate from a He-accreting WD (Waldman et al. 2011; Foley 2015) rather than a core-collapse object, and will be further considered as being part of the SNIa contribution. Their nebular spectrum is dominated by Ca, they show large photospheric velocities (Kasliwal et al. 2012), and they preferentially explode far from galaxies (Yuan et al. 2013), likely making their nucleosynthesis products easily mixed into the ICM

(see below). We explore this possibility by adding one "Ca-rich gap" yield model to the Classical SNIa and Nomoto SNcc models. We base this additional contribution on a set of yield models calculated by Waldman et al. (2011), who considered various masses of the CO core and the He upper layer of the accreting WD (as well as, for instance, a 2% mass fraction of N in the He layer, or a mixing of 30% between the CO core and the He layer). The decimal numbers in the model acronyms refer to the mass of each considered layer (in M_{\odot} ; see Waldman et al. 2011, and Table 4.5).

The best fit is obtained for a Z0.008+W70+CO.5HE.2N.02 combination, with a reduced χ^2 of ~ 0.7 . Compared to the Nomoto+Classical models, the fit is thus significantly improved and fully acceptable. The enriching fraction of SNIa over the total number of SNe is estimated to be $\sim 40\%$, thus similar to (although somewhat higher than) what was found in the previous cases.

However, based on this best fit, we estimate that the relative fraction of Ca-rich gap transients over the total number of SNIa contributing to the enrichment, SNIa(Ca)/SNIa, is $\sim 34\%$. This is much larger than recent estimates of the Ca-rich SNe rate over the total SNIa rate from the literature; i.e. $7 \pm 5\%$ (Perets et al. 2010), $< 20\%$ (Li et al. 2011), and $\sim 16\%$ (Mulchaey et al. 2014). Since Ca-rich gap transients occur preferably in the outskirts of galaxies (or even in the intra-cluster light) and have large photospheric velocities (see above), one interesting possibility is that they may be significantly more efficient in enriching the ICM than classical SNIa (whose metals may be more easily locked in the gravitational well of galaxy members). The fraction SNIa(Ca)/SNIa contributing to the enrichment might thus naturally be higher than the absolute Ca-rich/SNIa rate (for comparison with the solar neighbourhood enrichment, see also Sect. 4.4). On the other hand, the amount of produced Ca highly depends on the models. In particular, assuming 30% of mixing between the CO core and the He layer in the accreting WD produces significantly more Ca during the explosion (Waldman et al. 2011), and thus requires a smaller contribution from Ca-rich gap transients to the total enrichment. Considering this particular case (i.e. taking the CO.5HE.2C.3 model only; see Table 4.1, third panel), the best fit is achieved for the combination Z0.001+WDD2+CO.5HE.2C.3 (with a reduced χ^2 of ~ 1.1 , thus formally acceptable as well), which is plotted in Fig. 4.4 (top right). We then obtain SNIa(Ca)/SNIa $\simeq 9\%$, which is in agreement with the estimated rates from the literature. The enriching SNIa-to-SNe fraction is $\sim 35\text{--}40\%$. It is important to note, in this case, the

need for a SNIa delayed-detonation model (WDD2) instead of a deflagration model, in order to predict a consistent Cr/Fe ratio³. However, the use of a delayed-detonation model again underestimates the Ni/Fe ratio, as noted previously (Fig. 4.3 and 4.4 top left). This shows that the choice of a specific Ca-rich gap contribution has a significant impact on favouring one of the two possible SNIa explosion mechanisms. A further discussion of the Ni/Fe ratio and the choice of a SNIa explosion model can be found in Sect. 4.3.1.

At this stage, we must point out that the assumption of a significant fraction of the ICM enrichment coming from Ca-rich gap transient SNe is purely speculative. However, as demonstrated in this section, this may be a realistic possibility, as it successfully reproduces the high Ca/Fe abundance ratio measured in the ICM. Whereas in the rest of our analysis we choose to constrain the most realistic Ca-rich gap model regarding the current estimates of the Ca-rich/SNIa rate (i.e. allowing the CO.5HE.2C.3 model only), we must note that such rates are not well constrained yet by the observations. Alternatively, more precise measurements of the abundances in the ICM using the next generation of X-ray satellites could potentially help to constrain this rate as well (see also Sect. 4.5.1).

Ni/Fe ratio: Diversity in SNIa explosions?

During SNcc explosions most of the Ni remains locked in the collapsing core, while in SNIa explosions the Ni production depends on the electron capture efficiency in the core. In particular, delayed-detonation models (i.e. the models currently favoured by the supernova community) should produce limited amounts of Ni. Dupke & White (2000) used *ASCA* to measure a large Ni/Fe abundance ratio of ~ 4 in the central region of three clusters. They deduced that this ratio is more consistent with SNIa deflagration models and inconsistent with delayed-detonation models. Böhringer et al. (2005) measured the abundances of O, Si, and Fe in four clusters, and favour predictions from WDD models. Other papers based on the abundance ratios of more Si-group elements (de Plaa et al. 2007, Chapter 2) also show a better consistency with the delayed-detonation models. How-

³In addition to Ca, the CO.5HE.2N.02 model produces a significant fraction of Cr. The fits then favour SNIa deflagration models because in compensation they predict a limited Cr/Fe ratio and match the high observed Ni/Fe ratio. On the contrary, the CO.5HE.2C.3 model does not produce Cr, and the Cr/Fe ratio can only be successfully reproduced by using a delayed-detonation model for the SNIa contribution.

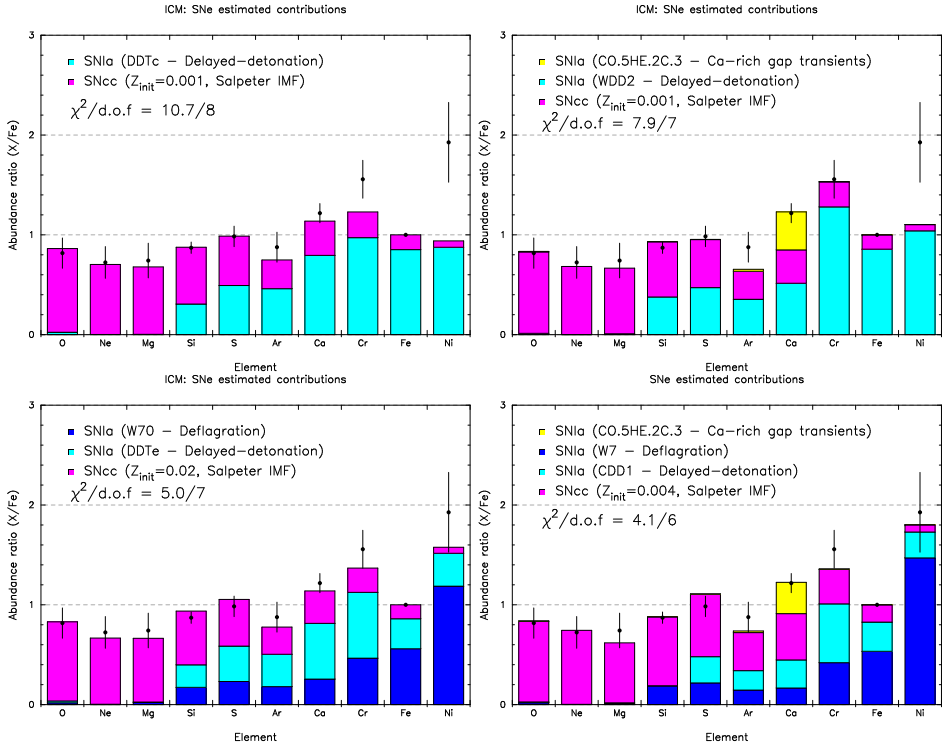


Figure 4.4: Same as Fig. 4.3, but fitting alternative sets of models. In every case, only one SNcc model (Nomoto) has been fitted ($Z_{\text{init}} = 0, 0.001, 0.004, 0.008$ or 0.02 ; Salpeter IMF). *Top left:* Delayed-detonation SNia model based on the observation of Tycho supernova remnant (Bravo, DDTc). *Top right:* Combination of a Classical delayed-detonation SNia model (WDD2) and a Ca-rich gap transients population model (CO.5HE.2C.3). *Bottom left:* Combination of a Classical deflagration SNia model (W70) and a delayed-detonation SNia model based on the observation of Tycho SN remnant (Bravo, DDTe). *Bottom right:* Combination of a Classical deflagration SNia model (W7), a Ca-rich gap transients population model (CO.5HE.2C.3), and a Classical delayed-detonation SNia model (CDD1).

4.3 Chemical enrichment in the ICM

Table 4.1: Results of various combinations of SN fits to the average ICM abundance pattern (Chapter 3). In each case, only one SNcc model has been fitted ($Z_{\text{init}} = 0, 0.001, 0.004, 0.008$, or 0.02 ; Salpeter IMF), and we only show the five best fits, sorted by increasing $\chi^2/\text{d.o.f.}$ (degrees of freedom). The choice of the CO.5HE.2C.3 model, indicated by a (*), has been fixed (see text).

SNcc		SNIa		$\frac{\text{SNIa}}{\text{SNIa+SNcc}}$	$\frac{\text{SNIa(Ca)}}{\text{SNIa}}$	$\frac{\text{SNIa(def)}}{\text{SNIa}}$	$\chi^2/\text{d.o.f.}$
Nomoto	Classical	—	—				
Z0.008	WDD2			0.31	—	—	22.1/8
Z0.02	WDD2			0.29	—	—	22.8/8
Z0.001	WDD2			0.35	—	—	22.8/8
Z0.008	CDD2			0.30	—	—	23.0/8
Z0.004	WDD2			0.29	—	—	23.0/8
Nomoto	Bravo	—	—				
Z0.001	DDTc			0.35	—	—	10.7/8
Z0.008	DDTc			0.32	—	—	11.3/8
Z0.02	DDTc			0.29	—	—	11.6/8
Z0.004	DDTc			0.33	—	—	12.4/8
Z0_cut	DDTc			0.32	—	—	16.5/8
Nomoto	Classical	Ca-rich gap	—				
Z0.001	WDD2	CO.5HE.2C.3(*)		0.38	0.09	—	7.9/7
Z0.02	WDD2	CO.5HE.2C.3(*)		0.33	0.10	—	8.1/7
Z0.02	CDD2	CO.5HE.2C.3(*)		0.31	0.11	—	8.3/7
Z0.001	CDD2	CO.5HE.2C.3(*)		0.37	0.11	—	8.4/7
Z0.008	WDD3	CO.5HE.2C.3(*)		0.31	0.12	—	9.5/7
Nomoto	Classical	Bravo	—				
Z0.001	W70	DDTe		0.40	—	0.58	5.0/7
Z0.02	W70	DDTe		0.35	—	0.58	6.6/7
Z0.001	W7	DDTe		0.42	—	0.50	6.8/7
Z0.001	WDD3	DDTe		0.38	—	—	7.5/7
Z0.02	W7	DDTe		0.36	—	0.51	8.1/7
Nomoto	Classical	Classical	Ca-rich gap				
Z0.004	W7	CDD1	CO.5HE.2C.3(*)	0.36	0.07	0.57	4.1/6
Z0.008	W7	CDD1	CO.5HE.2C.3(*)	0.35	0.08	0.56	4.1/6
Z0.004	W70	CDD1	CO.5HE.2C.3(*)	0.35	0.07	0.70	5.5/6
Z0.008	W70	CDD1	CO.5HE.2C.3(*)	0.34	0.08	0.68	5.6/6
Z0_cut	W7	CDD1	CO.5HE.2C.3(*)	0.35	0.07	0.54	5.9/6

ever, when measured, the Ni/Fe ratio is very often found to be super-solar (e.g. Tamura et al. 2009; De Grandi & Molendi 2009, Chapter 3). Comparing their Ni/Fe value of 1.5 ± 0.3 solar with the ones found by Dupke & White (2000), Finoguenov et al. (2002) suggested that both deflagration and delayed-detonation SNIa could participate in the enrichment of the ICM.

We explore this compromise by modelling one additional Classical contribution of SNIa to our two combinations already described in Sect. 4.3.1. Again, we choose to use the CO.5HE.2C.3 model as the most reasonable possibility for the Ca-rich gap contribution (Sect. 4.3.1). The five best fits of the Nomoto+Classical+Bravo and Nomoto+Classical+Classical+Ca-rich gap models are presented in Table 4.1 (last two panels). The best fits of these two cases are shown in Fig. 4.4 (bottom left and bottom right, respectively). These two combinations of models are now fully consistent ($\lesssim 1\sigma$) with all our average abundance ratios. With a reduced χ^2 of ~ 0.7 in both cases, the fits are better than all our previous attempts discussed above. From Table 4.1 (last two panels), it also appears that at least four out of the five best fits of these combinations include a contribution of one deflagration and one delayed-detonation model. The relative number of deflagration SNIa over the total number of SNIa contributing to the enrichment, SNIa(def)/SNIa, is typically in the range of 50–70%. It is, however, very difficult to discriminate between the best fits of each case. Similarly, we cannot clearly favour either of the two cases above since their respective best fits reproduce the average abundance pattern equally well within the uncertainties (Fig. 4.4 lower panels). However, no matter which case we select, again the SNIa-to-SNe fraction (34–42%) is comparable with the estimates in the cases discussed earlier.

Such a possibility for a SNIa bimodality in the enrichment processes of the ICM is interesting. In many respects, the bimodal nature of SNIa has already been clearly established. For instance, it seems that $\sim 50\%$ of SNIa explode promptly ($\sim 10^8$ years after the starburst), while the other half explode much later, following an exponential decrease with a time scale of ~ 3 Gy (Mannucci et al. 2006). Furthermore, while a population of luminous SNIa with a slow magnitude decline is mostly found in late-type galaxies, another population of subluminous SNIa has a steeper decline, and seems to explode preferentially in old elliptical galaxies (Hamuy et al. 2000). It is likely that the bright, slowly declining SNIa correspond to the “prompt” population, while the subluminous and fast declining SNIa correspond to the “delayed” population. Similarly, while the supernova community is

still debating the nature of the SNIa progenitors (see also Sect. 4.3.2), recent results suggest that both the single-degenerate and the double-degenerate scenarios might co-exist in nature (e.g. Li et al. 2001; Scalzo et al. 2014; Cao et al. 2015; Olling et al. 2015) (see however Branch 2001). Considering all these indications of diversity in SNIa, a bimodal population of deflagration and delayed-detonation SNIa responsible for the enrichment of the ICM remains possible. Moreover, it should be noted that such a diversity in the explosion mechanisms of SNIa has already been proposed, from results of an optical study (Hatano et al. 2000). This might bring one more piece to the complex puzzle of SNIa and their progenitors.

Some alternative scenarios to explain the high Ni/Fe ratio can be also considered. There is compelling evidence that some SNIa produce large fractions of Ni (e.g. Yamaguchi et al. 2015). On the other hand, some SNcc may overproduce Ni as well, sometimes at a super-solar level (Jerkstrand et al. 2015), and it is possible that the current yield models actually underestimate the Ni production within SNcc. Finally, the Ni/Fe ratio from SNIa contribution may be sensitive to the initial metallicity of the SNIa progenitors (see further discussion in Sect. 4.3.2).

Despite these intriguing possibilities, it is important to note that measuring the Ni abundance is a challenge using the current X-ray capabilities. In the abundance pattern derived in Chapter 3 and used for this work, substantial systematic uncertainties have been taken into account to overcome the large disagreement between MOS and pn. Moreover, the hard band (7–9 keV) in which the main Ni-K lines reside is often significantly contaminated by the instrumental background. Despite the very careful background modelling performed in Chapter 3, we cannot fully exclude that the background still affects our Ni/Fe measurements in both MOS and pn detectors (see also discussion in Chapter 3). Finally, the SN models themselves have uncertainties in their yield predictions (e.g. related to the electron capture rates adopted in SNIa models, see Appendix 4.A), and prevent us from firmly favouring one specific combination of models (De Grandi & Molendi 2009). A better future constraint on the Ni/Fe ratio, coupled to updated SNIa and SNcc yield models, will help us to favour one particular SNIa explosion model, and perhaps to confirm (or rule out) the co-existence of two explosion mechanisms (Sect. 4.5.1).

Two- and three-dimensional SNIa yield models

Whereas all the nucleosynthesis yields considered so far are based on calculations assuming a 1-D (i.e. spherically symmetric) explosion, several authors have recently published various sets of SNIa yields, assuming two-dimensional (2-D) or even three-dimensional (3-D) explosions. In this section, we compare these updated yields with our observations in order to determine whether predictions from multi-dimensional SNIa calculations better reproduce our ICM abundance pattern.

We take the 2-D models (deflagration and delayed-detonation) from Maeda et al. (2010), as well as the 3-D delayed-detonation and the 3-D deflagration models from Seitenzahl et al. (2013b) and Fink et al. (2014), respectively. These models (hereafter "2D" and "3D") are mentioned in Table 4.5 (see also Fig. 4.2 top). In addition to the symmetrical (deflagration and delayed-detonation) cases, the 2D models also propose an asymmetrical delayed-detonation explosion (O-DDT), where the ignition is slightly offset from the WD centre. In the 3D models, various numbers of ignition spots (usually close to the WD centre) are successively considered, sometimes with changing values for ρ_9 . In order to check whether such multi-dimensional models better agree with our ICM abundance pattern, we re-fit our results, this time replacing the Classical (1-D) models successively by the 2D and the 3D models. The full results are shown in Tables 4.2 and 4.3 (for the 2D and 3D cases, respectively). We note that the available Bravo and Ca-rich gap models have only been calculated for one dimension so far, so we could not apply any 2-D or 3-D extensions to those.

From Table 4.2, it clearly appears that the use of the 2D models does not improve our fit. In fact, while the (C- and O-) DDT models largely overestimate ($>4\sigma$) the Si/Fe ratio, the C-DEF model overestimates ($>2\sigma$) the Ni/Fe ratio (see also Fig. 4.2 top). Moreover, unlike in Sect. 4.3.1, using two 2D SNIa models does not improve the quality of the fit. The best fit, obtained for the combination Z0.02+O-DDT+CO.5HE.2C.3 ($\chi^2/\text{d.o.f.} \simeq 4.3$) is shown in Fig. 4.5 (left panel).

The 3D models (Table 4.3) look somewhat more encouraging. Although the combination Nomoto+3D clearly does not reproduce the ICM abundance pattern (see Sect. 4.3.1), the addition of a Ca-rich gap contribution significantly improves the quality of the fit. In particular, this confirms the Ca/Fe problem discussed earlier, and strengthens the need for an additional contribution, for instance, from Ca-rich gap transients. The favoured SNIa model (N100H) assumes a delayed-detonation explosion, where the

4.3 Chemical enrichment in the ICM

Table 4.2: Same as Table 4.1, but considering 2-D SNIa models instead of the 1-D Classical SNIa models.

SNcc		SNIa		$\frac{\text{SNIa}}{\text{SNIa} + \text{SNcc}}$	$\frac{\text{SNIa(Ca)}}{\text{SNIa}}$	$\frac{\text{SNIa(def)}}{\text{SNIa}}$	$\chi^2/\text{d.o.f.}$
Nomoto	2D	—	—				
Z0.02	O-DDT			0.35	—	—	56.0/8
Z0.001	O-DDT			0.41	—	—	60.0/8
Z0.008	O-DDT			0.37	—	—	63.1/8
Z0.004	O-DDT			0.39	—	—	69.0/8
Z0.008	C-DEF			0.36	—	—	79.9/8
Nomoto	2D	Ca-rich gap		—			
Z0.02	O-DDT	CO.5HE.2C.3(*)		0.39	0.10	—	30.2/7
Z0.001	O-DDT	CO.5HE.2C.3(*)		0.45	0.09	—	32.7/7
Z0.02	C-DEF	CO.5HE.2C.3(*)		0.38	0.09	—	36.8/7
Z0.008	O-DDT	CO.5HE.2C.3(*)		0.41	0.09	—	39.5/7
Z0.008	C-DEF	CO.5HE.2C.3(*)		0.40	0.08	—	40.1/7
Nomoto	2D	2D	Ca-rich gap				
Z0.02	C-DEF	O-DDT	CO.5HE.2C.3(*)	0.39	0.10	0.13	26.3/6
Z0.001	C-DEF	O-DDT	CO.5HE.2C.3(*)	0.45	0.09	0.07	30.3/6
Z0.008	C-DEF	O-DDT	CO.5HE.2C.3(*)	0.41	0.09	0.16	33.9/6
Z0.004	C-DEF	O-DDT	CO.5HE.2C.3(*)	0.43	0.08	0.18	39.9/6
Z0.02	C-DEF	C-DDT	CO.5HE.2C.3(*)	0.40	0.09	0.79	41.9/6

Table 4.3: Same as Table 4.1, but considering 3-D SNIa models instead of the 1-D Classical SNIa models.

SNcc		SNIa		$\frac{\text{SNIa}}{\text{SNIa} + \text{SNcc}}$	$\frac{\text{SNIa(Ca)}}{\text{SNIa}}$	$\frac{\text{SNIa(def)}}{\text{SNIa}}$	$\chi^2/\text{d.o.f.}$
Nomoto	3D	—	—				
Z0.008	N100H			0.26	—	—	47.2/8
Z0.004	N100H			0.28	—	—	47.3/8
Z0.02	N100H			0.25	—	—	49.8/8
Z0.001	N100H			0.30	—	—	55.1/8
Z0.02	N150			0.31	—	—	55.6/8
Nomoto	3D	Ca-rich gap		—			
Z0.02	N100H	CO.5HE.2C.3(*)		0.31	0.17	—	11.8/7
Z0.008	N100Hdef	CO.5HE.2C.3(*)		0.44	0.11	—	12.0/7
Z0.02	N100Hdef	CO.5HE.2C.3(*)		0.43	0.12	—	12.8/7
Z0.004	N100Hdef	CO.5HE.2C.3(*)		0.45	0.10	—	12.9/7
Z0.008	N100H	CO.5HE.2C.3(*)		0.32	0.15	—	13.1/7
Nomoto	3D	3D	Ca-rich gap				
Z0.008	N100Hdef	N100H	CO.5HE.2C.3(*)	0.42	0.11	0.77	11.2/6
Z0.02	N100Hdef	N150	CO.5HE.2C.3(*)	0.41	0.12	0.69	11.3/6
Z0.02	N100Hdef	N100L	CO.5HE.2C.3(*)	0.43	0.11	0.76	11.4/6
Z0.02	N100Hdef	N100	CO.5HE.2C.3(*)	0.41	0.12	0.75	11.6/6
Z0.02	N100Hdef	N100H	CO.5HE.2C.3(*)	0.40	0.12	0.76	11.7/6

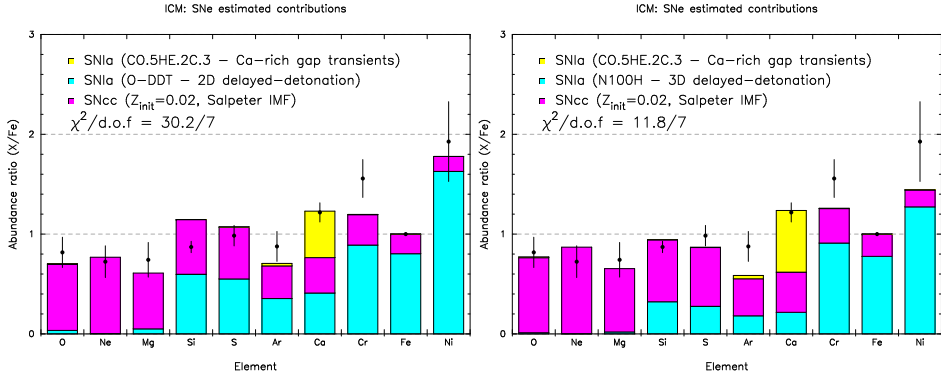


Figure 4.5: Left: Same as Fig. 4.4 (top right), but considering a 2-D SNIa model instead of a Classical SNIa model. Right: Same as Fig. 4.4 (top right), but considering a 3-D SNIa model instead of a Classical SNIa model.

core density of the pre-exploding WD is quite high (5.5×10^9 g/cm³). We also note that considering two channels of SNIa explosion (as in Sect. 4.3.1) does not improve the quality of the fit (Table 4.3). In fact, the estimated contribution from delayed-detonation SNIa is clearly marginal (typically $\sim 10\%$ of the total SNIa contribution). The best fit, obtained for the combination Z0.02+N100H+CO.5HE.2C.3 (with a reduced χ^2 of ~ 1.7) is shown in Fig. 4.5 (right panel).

Moreover, although the 3D models agree better with our ICM abundance pattern than the 2D models, we stress that the Classical and / or Bravo (i.e. 1-D) models still significantly provide the best match to our observations (Table 4.1). This is partly because the multi-dimensional delayed-detonation SNIa models predict a higher Si/Fe ratio than in the 1-D case, making a full compensation by the SNcc yields difficult, since the predicted O/Fe and Si/Fe ratios from SNcc must be rather similar (Fig. 4.2 top). Moreover, the 2-D and 3-D deflagration SNIa models predict systematically lower S/Si and Ar/Si ratios (Fig. 4.2 top), which cannot reproduce our measurements even when accounting for the SNcc contribution.

4.3.2 Mn/Fe ratio

In Chapter 3, we were able to detect Mn in the ICM with $>7\sigma$ (MOS and pn combined), and to constrain an average Mn/Fe abundance under reasonable uncertainties ($\sim 13\%$). To our knowledge, this is the first time that the

abundance of an odd-Z element has been measured in the ICM. It is commonly known that the bulk of Mn comes from SNIa explosions as SNcc are very inefficient in producing Mn (Fig. 4.2 bottom). In this section, we discuss two interesting consequences that the observed ICM Mn/Fe ratio (again, witnessing the explosion of billions of SNIa) can have on the SNIa progenitors.

Metallicity of the SNIa progenitors

Seitenzahl et al. (2013b) calculated the yields from their N100 (3-D delayed-detonation) model, assuming four different initial metallicities ($0.01Z_{\odot}$, $0.1Z_{\odot}$, $0.5Z_{\odot}$, and $1Z_{\odot}$) of SNIa progenitors, $Z_{\text{init}}(\text{SNIa})$. Interestingly, the result (Fig. 4.6) shows a slight, but clear dependence of the Mn/Fe abundance ratio with $Z_{\text{init}}(\text{SNIa})$ (see also Seitenzahl et al. 2015). Since the bulk of the Mn observed in the ICM is produced by SNIa, we can use our observed Mn/Fe abundance ratio to derive constraints on the average metallicity of the progenitors of SNIa responsible for the enrichment. Following the 1-D yield models best reproducing our abundance pattern, we estimate that respectively $\sim 95\%$ and $\sim 82\%$ of the Mn and Fe are produced by SNIa. Taking these factors into account, the average Mn/Fe abundance ratio in the ICM coming from SNIa is 1.97 ± 0.25 . Again assuming the N100 model for the SNIa contribution, the interpolation of the yields from Seitenzahl et al. (2013b) involves a lower limit of $Z_{\text{init}}(\text{SNIa}) \gtrsim Z_{\odot}$ (Fig. 4.7).

The lack of yield models with $Z > 1Z_{\odot}$ combined with the uncertainties in our Mn/Fe ICM measurement prevents us from inferring further constraints such as an upper limit to $Z_{\text{init}}(\text{SNIa})$. We also recall that our inferred lower limit depends on the assumed limited Mn production by SNcc. If, for some reason, the Mn production is revised upwards in upcoming SNcc yield models, it would have a strong impact on the inferred limits of the initial metallicities of SNIa progenitors. Moreover, a more complete understanding of the precise relation between $Z_{\text{init}}(\text{SNIa})$ and the Mn yields could only be achieved by comparing this $Z_{\text{init}}(\text{SNIa})$ dependence in various SNIa yield models. Except N100, no other available deflagration/delayed-detonation model has been calculated for several successive values of $Z_{\text{init}}(\text{SNIa})$. For this reason, we prefer to treat Mn as a peculiar element, and therefore, Mn/Fe was not included in the previous fits (Sect. 4.3.1).

Finally, it is worth noting (see Fig. 4.6) that the Ni/Fe ratio from SNIa contributions may also vary with $Z_{\text{init}}(\text{SNIa})$ (at least for metallicities be-

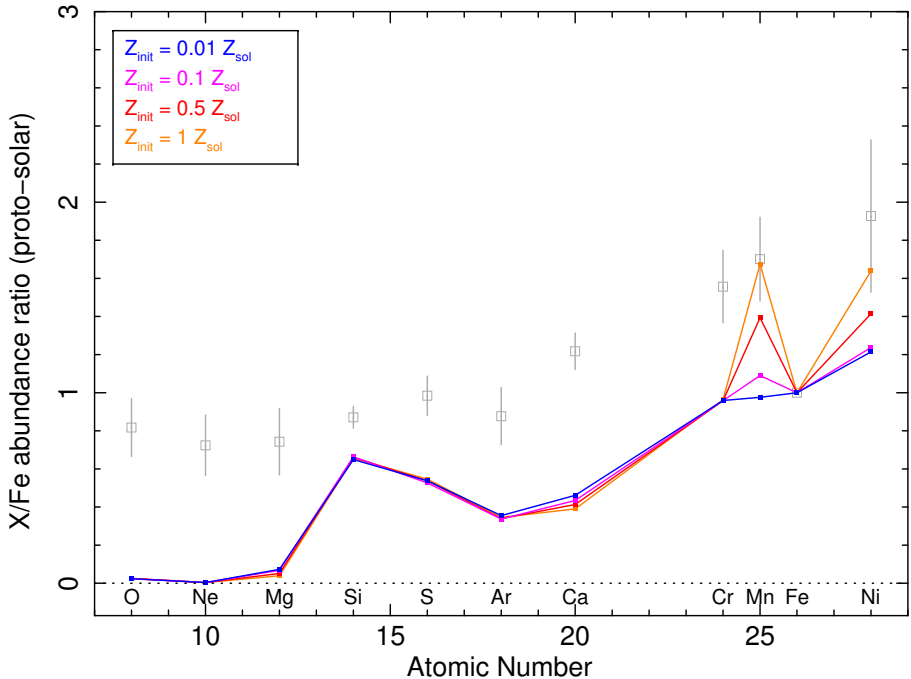


Figure 4.6: Predicted effects of the initial metallicity of the SNIa progenitor on the X/Fe abundance ratios. The comparison is made using the N100_Z0.01, N100_Z0.1, N100_Z0.5, and N100 3-D delayed-detonation models from Seitenzahl et al. (2013b). For comparison, the ICM average abundance ratios (inferred from Chapter 3) are also plotted.

yond $\sim 0.5 Z_{\odot}$). If such a trend is demonstrated in other delayed-detonation models (e.g. 1-D), a high initial metallicity for SNIa progenitors could be an interesting alternative to the need of an additional deflagration channel, as it might reconcile the high Ni/Fe ratio with the rest of the ICM abundance pattern (Sect. 4.3.1). However, a clear relation between Ni/Fe and Z_{init} has not yet been established, and the large uncertainties in our measured Ni/Fe ratio do not allow us to explore this possibility further.

Clues on the nature of SNIa progenitors

In principle, the formation channel of the binary system leading to the SNIa explosion (i.e. single-degenerate versus double-degenerate scenario) affects the explosion itself. In the single-degenerate scenario, the explosion occurs during the accretion process from the stellar companion as the to-

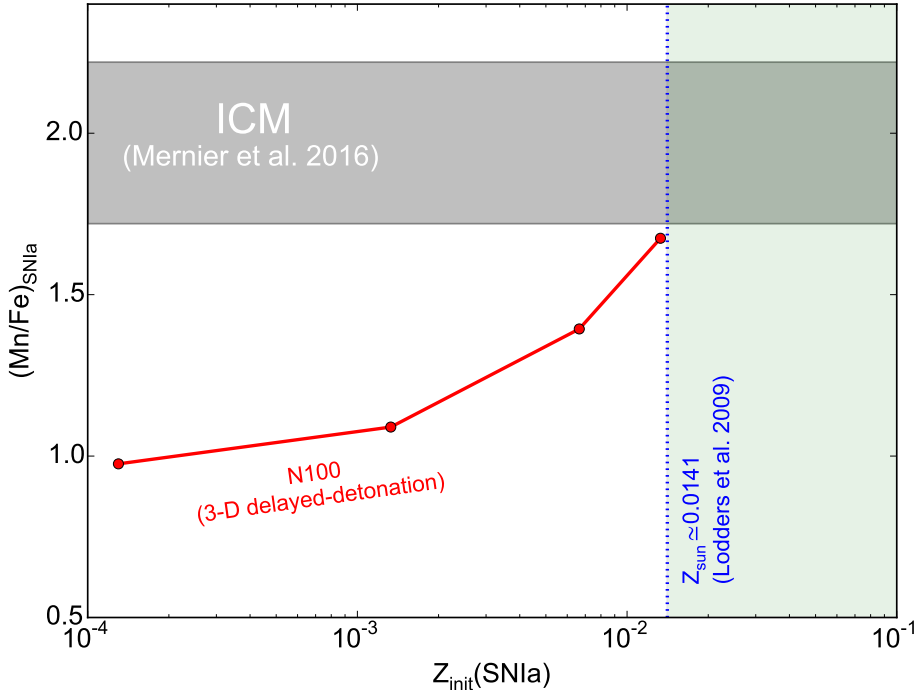


Figure 4.7: Mn/Fe yields expected from SNIa as a function of the initial metallicity of SNIa progenitors. The red solid line interpolates the estimated Mn/Fe ratio for four SNIa initial metallicities by Seitenzahl et al. (2013b), and is compared to the Mn/Fe measurement (expected from SNIa contributions) in the ICM (Chapter 3 and this work) is shown in grey. The dotted blue line shows the solar metallicity (Lodders et al. 2009).

tal mass of the WD approaches the Chandrasekhar mass limit (near- M_{Ch}) and leads to the deflagration and/or delayed-detonation explosion mechanisms discussed earlier. In the double-degenerate scenario, when assuming a violent merger of the two WDs (without accretion disc), the explosion is thought to occur well below the Chandrasekhar mass limit (sub- M_{Ch}) of either WD, and should lead to a pure detonation explosion. Another possibility is that the less massive WD gets disrupted and forms a thick disc that the more massive WD gradually accretes. If the WD rotates rapidly, C may be ignited in its core and lead to a SNIa with a deflagration or a delayed-detonation explosion (e.g. Piersanti et al. 2003).

Recently, Seitenzahl et al. (2015) suggested that the Mn K α line emissivity inferred from the X-ray spectra of SNIa could bring a tight constraint

on the scenarios mentioned above as the near- M_{Ch} models produce significantly more ^{55}Fe (later decaying into stable ^{55}Mn) than the sub- M_{Ch} models. On the other hand, Seitenzahl et al. (2013a) showed that sub- M_{Ch} explosion models from Pakmor et al. (2012, ; violent WD merger with respective masses of $1.1 M_{\odot}$ and $0.9 M_{\odot}$) and Ruiter et al. (2013, ; violent WD merger with masses of $0.6 M_{\odot}$ each) systematically predict sub-solar Mn/Fe abundance ratios, and can hardly explain the proto-solar value of Mn. Although Mn yields from SNIa may be metallicity-dependent (Sect. 4.3.2), Seitenzahl et al. (2015) noted that even the highest- Z_{init} (i.e. $1 Z_{\odot}$) sub- M_{Ch} model produces two times less Mn than the lowest- Z_{init} (i.e. $0.01 Z_{\odot}$) near- M_{Ch} model.

Again assuming that $\sim 95\%$ of the Mn/Fe ratio measured in the ICM originates from SNIa explosions, our super-proto-solar ICM Mn/Fe ratio constrains this result even more, and suggests that the WD violent merger scenario should be excluded as a dominant SNIa progenitor channel (at least assuming that such a merger produces a pure detonation).

To confirm this claim in a larger context, we re-fit our ICM abundance pattern, this time by including the publicly available yields from the WD violent merger model of Pakmor et al. (2010). This sub- M_{Ch} yield is only available for the violent merger of two WDs with equal masses ($M_{\text{WD}1} = M_{\text{WD}2} = 0.9 M_{\odot}$; see also Table 4.5). We consider two specific cases:

1. All SNIa (excluding Ca-rich gap transients) originate from violent WD mergers (both of equal mass $M_{\text{WD}1} = M_{\text{WD}2} = 0.9 M_{\odot}$), and they occur as sub- M_{Ch} explosions (i.e. the Nomoto+sub- M_{Ch} +Ca-rich gap combination);
2. One part of the SNIa originate from violent WD mergers, the other part originate from another channel, occurring as near- M_{Ch} explosions, either deflagration or delayed-detonation (i.e. the Nomoto+sub- M_{Ch} +3D+Ca-rich gap combination).

In the first case, the fit fails to find any positive contribution for the sub- M_{Ch} model. In the second case, the contribution of the sub- M_{Ch} SNIa to the enrichment is limited to $\sim 1.3\%$ of the total number of SNIa, with similar best fits to those we reported in Sect. 4.3.1 (Nomoto+Classical+Ca-rich combination). This occurs because the Si/Fe ratio predicted by the 0.9_0.9 model is dramatically higher (~ 8) than the observed ratio in the ICM. Again, this favours near- M_{Ch} explosions, and discards the violent

WD mergers scenario (leading to sub- M_{Ch} explosions) as a significant contributor to SNIa nucleosynthesis, at least for the two specific combinations of initial masses discussed above ($1.1 M_{\odot} + 0.9 M_{\odot}$ and $0.9 M_{\odot} + 0.9 M_{\odot}$). We must note, however, that this result does not necessarily discard all the subchannels of the double-degenerate scenario. For instance, as mentioned above, a disruption of the least massive WD, followed by the creation of a thick torus that could feed the most massive WD, may lead to a near- M_{Ch} explosion, and to similar yields as used in the Classical, 2D and 3D models. Moreover, we recall that our discussion is entirely based on the current yield predictions. Any substantial change in upcoming yield models of sub- M_{Ch} explosions (for instance in the initial masses that are assumed) may potentially challenge our interpretation.

4.3.3 Fraction of low-mass stars that become SNIa

Since SNcc explosions are the result of the end-of-life of massive stars ($\geq 10 M_{\odot}$), the bulk of SNcc events occur very rapidly ($\lesssim 40$ Myr) after its associated episode of star formation. On the contrary, SNIa events require a considerable time delay (up to several Gyr), from their zero age low-mass star progenitors to the end of the binary evolution of the corresponding WD(s). In our Galaxy, multiple episodes of star formation continuously generate low-mass stars, and make it difficult to directly compare the number of SNIa events and the corresponding number of low-mass stars that have generated them.

In galaxy clusters, however, the situation is different. In fact, since the bulk of the star formation occurred at the epoch of cluster formation ($z \simeq 2-3$), and has now dramatically quenched, clusters are an interesting laboratory which allow us to relate the estimated number of low-mass stars to the number of SNIa, and thus estimate the SNIa efficiency, η_{Ia} (i.e. the fraction of low-mass stars that eventually result in SNIa). Following the approach of de Plaa et al. (2007), in this section we attempt to estimate η_{Ia} from the ICM abundance measurements and their best-fit SN yield models.

Quantitatively, assuming a power-law IMF, we can write (de Plaa et al. 2007)

$$\frac{\text{SNIa}}{\text{SNIa+SNcc}} = \frac{\eta_{\text{Ia}} \int_{M_{\text{low}}}^{M_{\text{cc}}} m^{-(1+x)} dm}{\eta_{\text{Ia}} \int_{M_{\text{low}}}^{M_{\text{cc}}} m^{-(1+x)} dm + \int_{M_{\text{cc}}}^{M_{\text{up}}} m^{-(1+x)} dm}, \quad (4.4)$$

where M_{low} and M_{cc} are respectively the lower and upper mass limit of

stars that eventually result in SNIa, and M_{up} is the upper mass limit of massive stars contributing to the ICM enrichment. Low-mass stars are thus comprised between $M_{\text{low}} < M < M_{\text{cc}}$ (i.e. η_{Ia} is estimated for the stars within this range), and massive stars (all producing SNcc) are comprised between $M_{\text{cc}} < M < M_{\text{up}}$.

Based on all our previous fits that are of acceptable quality (i.e. $\chi^2/\text{d.o.f} \lesssim 2$ in Tables 4.1, 4.2, and 4.3), the SNIa-to-SNe fraction responsible for the enrichment varies within $\sim 29\text{--}45\%$. The typical M_{low} values found in the literature vary between $M_{\text{low}} = 0.9 M_{\odot}$ (the minimum mass allowed for a star to end its life within the Hubble time) and $M_{\text{low}} = 1.5 M_{\odot}$ (to allow the accreting WD to reach a value close to its Chandrasekhar limit within a binary system, e.g. Matteucci & Recchi 2001; de Plaa et al. 2007). We also assume that the bulk of high-mass stars responsible for the enrichment (i.e. via SNcc explosions) has a non-zero initial metallicity, and therefore we limit M_{up} to $50 M_{\odot}$. Finally, we allow M_{cc} to vary between $\sim 8 M_{\odot}$ (e.g. Smartt 2009) and $\sim 10 M_{\odot}$ (e.g. Nomoto et al. 2013). We also assume a Salpeter IMF. From Eq. (4.4), and exploring the different limits reported above, we obtain $\eta_{\text{Ia},0.9} \simeq 1.5\text{--}4\%$ and $\eta_{\text{Ia},1.5} \simeq 3\text{--}9\%$ as the fraction of low-mass stars, respectively with $M \geq 0.9 M_{\odot}$ and $M \geq 1.5 M_{\odot}$, that eventually become SNIa. These two estimates are in agreement with previous typical values of 3–10% reported in the literature (e.g. Yoshii et al. 1996; Matteucci & Recchi 2001; Maoz & Mannucci 2012; Loewenstein 2013). Similarly, Maoz (2008) compiled various observational estimates of η_{Ia} from the literature, this time adopting $M_{\text{low}} = 3 M_{\odot}$, i.e. the most appropriate value for the double-degenerate scenario. In particular, he shows that under this condition the estimate ($\eta_{\text{Ia}} \simeq 14\text{--}40\%$) of de Plaa et al. (2007) brings larger upper limits than the other estimates, always below $\sim 20\%$ (e.g. Lin et al. 2003; Dahlen et al. 2004; Mannucci et al. 2005; Sullivan et al. 2006). In that context, we reconsider our estimate of η_{Ia} , this time by assuming $M_{\text{low}} = 3 M_{\odot}$. We find $\eta_{\text{Ia},3} \simeq 9\text{--}27\%$, hence lowering the maximum estimate of the fraction of low-mass stars that become SNIa.

We recall, however, that we use the instantaneous recycling approximation for such an estimate, and the SN fractions introduced in this work should be interpreted as the fraction of SNIa and SNcc contributing to the ICM enrichment. In particular, a higher SNcc lock-up efficiency (i.e. the efficiency for SNcc products to be recycled back into stars instead of enriching the ICM; Loewenstein 2013) would make the true SNIa-to-SNe fraction (i.e. accounting for the total number of SNIa and SNcc) somewhat lower

than our current estimate and, consequently, would lower η_{Ia} as well. Nevertheless, this consideration requires detailed calculations of stellar and galactic evolutionary models, which is beyond the scope of the present paper.

4.3.4 Clues on the metal budget conundrum in clusters

Previous studies clearly report that, in the ICM of massive ($\gtrsim 10^{14}\text{--}10^{15} M_\odot$) galaxy clusters, the measured Fe content is far above expectations if we assume the currently favoured SN efficiencies, star formation, IMF, and Fe production rate by SNIa and SNcc (e.g. Renzini et al. 1993; Loewenstein 2006, 2013; Renzini & Andreon 2014; Yates et al. 2017). This conundrum on the metal budget in galaxy clusters has not yet been solved. In this section, we explore two possibilities that have been proposed in the literature, and that directly depend on the ICM abundance pattern we report in this work.

Effect of the IMF on core-collapse yields

One of the possible solutions to this conundrum would be a completely different IMF in galaxy clusters from that measured in the field. In particular, if low-metallicity environments favour formation of higher mass stars, invoking a top-heavy (i.e. flat, $x = -1$) IMF could potentially boost the Fe production by SNcc and reconcile the Fe stellar production and the Fe mass in the ICM on clusters scales (e.g. Nagashima et al. 2005).

We explore this possibility by fitting the same combinations of SN models discussed above to our measured ICM abundance pattern, this time integrating the SNcc yields over a top-heavy IMF. As can be seen in Fig. 4.8, the slope of the IMF has an effect on the relative abundance of all the α -elements, in particular on the Ne/Mg ratio. Assuming a top-heavy IMF, the Nomoto+Classical case gives slightly more acceptable results, improving the best-fit reduced χ^2 from ~ 2.8 (Z0.008+WDD2, Salpeter IMF) to ~ 2.6 (Z0.008+WDD2, top-heavy IMF). In all other cases, however, these best fits are either comparable to or less acceptable than when assuming a Salpeter IMF. In other words, despite our effort in constraining the X/Fe abundance uncertainties, the large error bars of O/Fe, Ne/Fe, and Mg/Fe prevents us from deriving any firm conclusion on the IMF in galaxy clusters/groups.

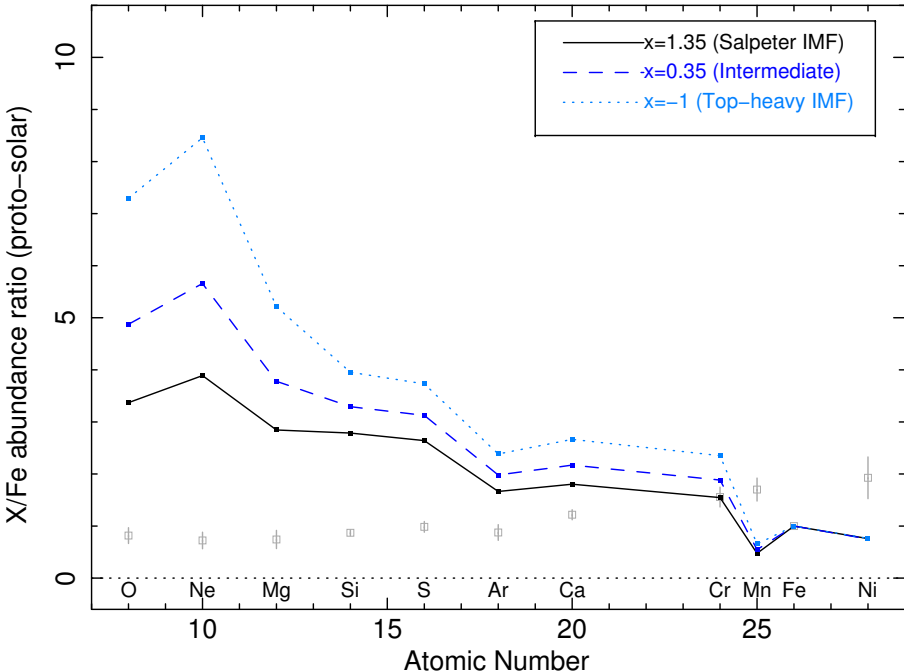


Figure 4.8: Predicted X/Fe abundances from the Z0.02 SNcc yield model (Nomoto), computed for three different IMFs (Salpeter IMF, intermediate case, and top-heavy IMF). For comparison, the ICM average abundance ratios (inferred from Chapter 3) are also plotted.

Contribution from pair-instability supernovae?

As an alternative to a different IMF in cluster galaxies, Morsony et al. (2014) suggest that the large Fe content found in the ICM may be explained by accounting for the contribution of pair-instability supernovae (PISNe) to the overall enrichment. In fact, by convention, the IMF is often restricted to an upper limit of $\sim 40 M_{\odot}$ or $\sim 140 M_{\odot}$ (depending on the assumed Z_{init} for SNcc), whereas PISNe (typically estimated to occur between 140 – $300 M_{\odot}$) are thought to produce much larger amounts of metals than SNcc or SNIa. To explore this possibility, we redo the same abundance fits as described above, this time by incorporating nucleosynthetic yields of PISNe, and by extending the upper mass limit of the Salpeter IMF to the largest mass for which PISNe can produce and eject metals. We assume that only stars with $Z_{\text{init}} = 0$ can give rise to PISNe (Nomoto et al. 2013). Two distinct models (see Table 4.5 and Fig. 4.9) are considered here.

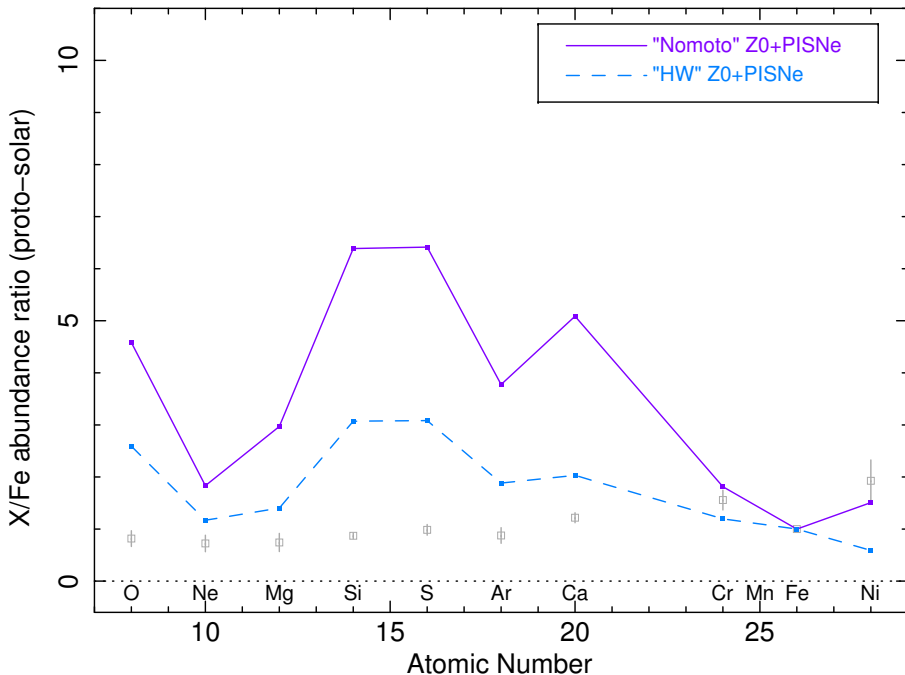


Figure 4.9: Predicted X/Fe abundances from two $Z_{\text{init}}=0$ SNcc models with an additional yields contribution from PISNe (Nomoto and HW Z0+PISN models, see also Table 4.5). For comparison, the ICM average abundance ratios (inferred from Chapter 3) are also plotted.

1. The Nomoto Z0+PISNe model: the Z0 model presented earlier (up to $140 M_{\odot}$) from Nomoto et al. (2013), combined with the PISNe model ($140\text{--}300 M_{\odot}$) from Umeda & Nomoto (2002).
2. The "HW" Z0+PISNe model: the $Z_{\text{init}}=0$ model for SNcc (up to $100 M_{\odot}$, where we assume equal contributions from models with SNcc energies of $0.3, 0.6, 0.9, 1.2, 1.5, 2.4$, and 3.0×10^{51} erg) from Heger & Woosley (2010), combined with the PISNe model ($140\text{--}260 M_{\odot}$) from Heger & Woosley (2002). This model has also been considered in order to remain consistent with the analysis of Morsony et al. (2014).

When using these extended models instead of the regular SNcc models used so far, we find that the fits are always significantly poorer than previously reported. In particular, the O/Ne and O/Mg ratios, as well as the Si/Fe ratios (and sometimes S/Fe), are dramatically overestimated by the models. This strongly suggests that a contribution from PISNe to the

enrichment is unlikely (or insufficient) to explain the large amount of metals found in the ICM. Nevertheless, as mentioned earlier, such a claim is dependent on the model yields proposed so far.

4.4 Enrichment in the solar neighbourhood

In addition to the ICM average abundance pattern presented in Chapter 3 and this work, the X/Fe abundance ratios from our solar system (Fig. 4.1) offers an interesting additional dataset to test predictions from SN yield models. In particular, it is reasonable to assume that the SNIa explosion channel(s) enriching galaxy clusters and the solar neighbourhood must be the same, presumably with a different relative fraction of SNIa and SNcc having contributed to the enrichment. This potentially brings an additional constraint on the specific SNIa explosion models to favour. However, the SNcc progenitors that enriched the Milky Way and the ICM did not necessarily have the same average initial metallicity. Consequently, the various sets of SN yield models presented in this paper should be fitted separately to the ICM abundance pattern (Sect. 4.3) on the one hand, and to the proto-solar values (this section) on the other hand.

In the following we always assume a Salpeter IMF. Similarly to Sect. 4.3.1, we ignore the proto-solar Mn/Fe ratio because of its possible dependence on the metallicity of SNIa progenitors, which itself depends on the considered SNIa model (Sect. 4.3.2). We also note that a significant part of the nitrogen, fluorine, and sodium yields is thought to be produced by AGB stars, which we do not consider in this work. Therefore, in the following we also ignore the proto-solar N/Fe, F/Fe, and Na/Fe ratios.

We start by considering sets of one SNcc and one SNIa model, namely the Nomoto+Classical, Nomoto+Bravo, Nomoto+2D, and Nomoto+3D combinations. The five best fits of each combination are listed in Table 4.4. With a reduced χ^2 of ~ 3.8 , the best fit is obtained for a combination Z0.02+WDD2, and is shown in Fig. 4.10. Clearly, these sets of models do not reproduce well the proto-solar abundance pattern. The main reason is that the ratios of Cl/Fe, K/Fe, Sc/Fe, Ti/Fe, V/Fe, and Co/Fe are systematically underestimated (with $>2\sigma$, $>3\sigma$, $>3\sigma$, $>1\sigma$, $>2\sigma$, and $>1\sigma$, respectively) by all the models. In some cases, the Cr/Fe ratio is somewhat overestimated. Such discrepancies have already been reported in the literature by using Galactic evolution models (e.g. Kobayashi et al. 2006; Romano et al. 2010; Kobayashi et al. 2011; Nomoto et al. 2013). Although the problem has not yet been

4.4 Enrichment in the solar neighbourhood

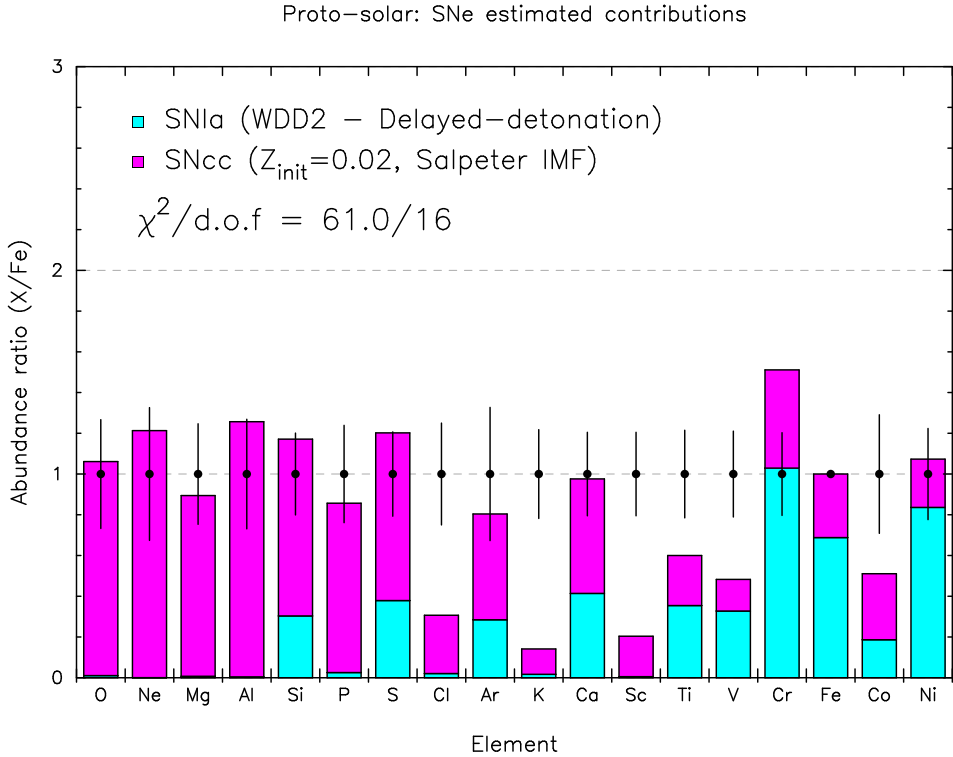


Figure 4.10: Abundance ratios versus atomic numbers in the proto-solar abundance pattern (Lodders et al. 2009). The histograms show the yields contribution of a best-fit combination of one Classical SNIA model (WDD2) and one Nomoto SNCC ($Z_{\text{init}} = 0.02$, and Salpeter IMF) model.

discussed in detail, it is possible that the ν -process significantly increases the production of these elements in SNCC (Kobayashi et al. 2011; Nomoto et al. 2013). Except for these specific cases, the ratios of the other elements (mostly even-Z) are correctly reproduced. For comparison, if we include only the X/Fe ratios of the even-Z elements that could be measured in the ICM, we find that the best fit is obtained for a Z0.02+WDD3 combination, with a reduced χ^2 of ~ 0.6 , and a SN fraction of $\sim 20\%$. Based on Table 4.4, some additional remarks are worth mentioning.

First, all the best fits are reached for a SNCC initial metallicity $Z_{\text{init}} = 0.02$. In fact, the Z0.02 model is clearly favoured by the O/Fe, Ne/Fe, Mg/Fe, and Al/Fe abundance ratios, whose elements are almost entirely produced by SNCC. Of course, an enrichment of the solar system with SNCC

Table 4.4: Results of various SN fits to the proto-solar abundance ratios adapted from Lodders et al. (2009). Only one SNIa and one SNcc model have been fitted, and for each case we only show the five best fits (sorted by increasing $\chi^2/\text{d.o.f.}$).

SNcc	SNIa	$\frac{\text{SNIa}}{\text{SNIa+SNcc}}$	$\chi^2/\text{d.o.f.}$
Nomoto	Classical		
Z0.02	WDD2	0.20	61.0/16
Z0.02	CDD2	0.19	61.8/16
Z0.02	WDD3	0.18	62.7/16
Z0.02	W70	0.19	72.3/16
Z0.008	WDD3	0.18	75.6/16
Nomoto	Bravo		
Z0.02	DDTc	0.20	64.5/16
Z0.02	DDTa	0.15	66.2/16
Z0.008	DDTa	0.15	77.6/16
Z0.008	DDTc	0.21	80.0/16
Z0.004	DDTa	0.16	94.2/16
Nomoto	2D		
Z0.02	O-DDT	0.24	67.8/16
Z0.008	O-DDT	0.25	81.4/16
Z0.004	O-DDT	0.27	97.1/16
Z0.001	O-DDT	0.30	99.5/16
Z0_cut	O-DDT	0.28	111.5/16
Nomoto	3D		
Z0.02	N100H	0.18	62.0/16
Z0.02	N40	0.20	63.9/16
Z0.02	N100	0.21	64.1/16
Z0.02	N20	0.17	64.4/16
Z0.02	N150	0.22	64.6/16

already having solar initial metallicities is not possible. On the other hand, $Z_{\text{init}} = 0.008$ may be on the low side for the average contributing SNcc, and no model assuming intermediate values of Z_{init} is available so far. Therefore, Z0.02 is the most suitable model, but this statement must be carefully interpreted. Because of the poor quality of the fits, it is more difficult to favour one specific SNIa model. However, it appears that the delayed-detonation models are systematically preferred to the deflagration models. The preference of the WDD2, DDTc, O-DDT, and N100H models, respectively in the Classical, Bravo, 2D, and 3D categories, is also consistent with the best fits of the ICM abundance pattern (Tables 4.1, 4.2, and 4.3).

Second, the proto-solar abundance pattern does not need an additional contribution from Ca-rich gap transients as the Ca/Fe ratio is already successfully reproduced. Such a result may not be surprising if, as already discussed in Sect. 4.3.1, Ca-rich gap SNe explode preferably in the galaxy outskirts, hence easily enriching the ICM, while their contribution in enriching the solar neighbourhood should be quite limited.

Similarly, an additional SNIa component (to account for the possible diversity of SNIa explosions, Sect. 4.3.1) does not improve the quality of the fits. Quantitatively, when fitting an additional SNIa model to the proto-solar abundance pattern, the contribution of delayed-detonation SNIa to the local enrichment is systematically $\gtrsim 10$ times more important than any additional contribution of deflagration SNIa.

Finally, the estimated enriching SNIa-to-SNe fraction is systematically lower for the enrichment of the solar neighbourhood ($\sim 15\text{--}30\%$) than for the ICM enrichment. Here again, this is not surprising. If the bulk of local SNIa progenitors result from a recent star formation, most of them had not yet exploded at the epoch of the formation of the Sun, and could not have contributed to the enrichment of the solar neighbourhood (on the contrary of SNcc progenitors, which explode shortly after their formation). On the other hand, in galaxy clusters, almost all potential SNIa have exploded (except perhaps those with extremely long delay times) giving rise to a substantial fraction of SNIa yields. We cannot exclude, however, that other effects (e.g. different lock-up efficiencies) may also play a role to explain the difference between local and cluster SNIa-to-SNe fractions.

We must emphasise that our approach in comparing the SN yield models to the proto-solar abundance ratios is purely empirical as we are just interested in a direct comparison between local and ICM enrichments. Ideally, a full Galactic enrichment study would require a complete evolution-

ary model (taking account of star formation, infall, outflows, Galactic age, binary populations, etc.) to be compared to the abundances in stars in the solar neighbourhood (e.g. Kobayashi et al. 2006; Kobayashi & Nomoto 2009; Romano et al. 2010; Kobayashi et al. 2011). However, such a detailed study is beyond the scope of this present work.

4.5 Summary and conclusions

In this paper, we have made use of the most precise and complete average X/Fe abundance ratios measured in the ICM so far (derived in Chapter 3), in order to constrain properties of SNIa, SNcc, and their relative contribution to the enrichment at the scale of galaxy clusters. Our main results can be summarised as follows.

- Whereas a simple combination of one Classical SNIa and one Nomoto SNcc model is sufficient to explain most of the X/Fe abundance ratios in the solar neighbourhood, this is clearly not the case in the ICM. In particular, this set of models cannot explain the high Ca/Fe and Ni/Fe ratios found in the ICM. In other words, the ICM seems to be particularly Ca- and Ni-rich.
- The Ca/Fe ratio can be successfully reproduced if we assume a significant contribution to the enrichment from Ca-rich gap transients, a recently discovered class of SNe which explode as WDs and are surprisingly rich in Ca. Based on the available models, a significant mixing ($\sim 30\%$ in mass) between the C-O core and the He layer of the pre-exploding WD is necessary to reconcile the enriching fraction of Ca-rich gap transients to the rates inferred from optical observations (less than $\sim 10\%$ of the total number of SNIa events). However, a higher Ca-rich SNe contribution to the enrichment (this time assuming no mixing of the WD material) cannot be excluded as these objects preferentially explode far away from the galactic centres, and their yields could thus be easily mixed into the ICM, as compared to the Galaxy or solar neighbourhood. This could also explain why no significant Ca-rich SNe contribution is necessary in the enrichment of the solar neighbourhood.

Alternatively to this scenario, the Ca/Fe predicted ratio can be reconciled with our measurement by using a SNIa delayed-detonation

model based on the Tycho supernova remnant (Badenes et al. 2006). Unfortunately, the uncertainties in our measurements do not allow us to favour one of these two scenarios.

- The best way to successfully reproduce the Ni/Fe ratio in the ICM (simultaneously with the other X/Fe ratios) is to invoke a diversity in SNIa explosions, with $\sim 50\text{--}77\%$ of deflagration SNIa, and the remaining fraction of delayed-detonation SNIa. On the other hand, the proto-solar abundance pattern does not require such a diversity in SNIa, and clearly favours the delayed-detonation explosion as the dominant channel ($\gtrsim 90\%$ of SNIa).
- The Mn/Fe ratio — measured in the ICM for the first time — can in principle bring useful constraints on the initial metallicity of SNIa progenitors. Assuming a limited ($\sim 5\%$) Mn production from SNcc, we find that $Z_{\text{init}}(\text{SNIa}) \gtrsim 1Z_{\odot}$. This result is, of course, very dependent on the assumed yields, and more SNIa models (with varying values of $Z_{\text{init}}(\text{SNIa})$) are clearly needed to extend the discussion further. The initial metallicity of SNIa progenitors also affects the Ni production, and could be considered as a possible alternative to the co-existence of both delayed-detonation and deflagration SNIa explosions.

In addition to this consideration, the high Mn/Fe ratio suggests a negligible contribution from a hypothetical sub- M_{Ch} SNIa channel (associated with a detonative explosion). Considering the models available so far, this could imply that the majority of SNIa contributing to the ICM (and Galactic) enrichment were not produced by violent WD mergers.

- Interestingly, the recent 2-D (Maeda et al. 2010) and 3-D (Seitenzahl et al. 2013b; Fink et al. 2014) SNIa models are less efficient in reproducing the ICM (and proto-solar) abundance pattern than the basic 1-D (Iwamoto et al. 1999; Badenes et al. 2006) SNIa models. In particular, the multi-dimensional models tend to overproduce Si, whereas the Si/Fe ratio in the ICM is very well constrained by our observations.
- Based on all the models that reasonably reproduce our ICM abundance pattern, we estimate that $\sim 29\text{--}45\%$ of the SNe contributing to the enrichment are SNIa, the remaining part coming from SNcc.

This fraction is systematically higher than in the solar neighbourhood ($\sim 15\text{--}25\%$), and could be explained by the rapid quenching of star formation in galaxy clusters shortly after their assembling. Such a SNIa fraction in the ICM also implies, under rough assumptions, that the fraction of low-mass stars that become SNIa ranges between 1.5% and 27% (depending on the assumed lower mass limit), in agreement with most of the observations.

- The uncertainties in the ICM abundance ratios prevent us from putting tight constraints on the IMF, the initial parameters of the deflagration/delayed-detonation WD explosion leading to SNIa, or the initial metallicity of SNcc progenitors. For the latter, however, our measurements can reasonably exclude a SNcc enrichment with a zero initial metallicity, meaning that the SNcc progenitors that enriched the ICM must have been previously pre-enriched. Similarly, a significant enrichment of the ICM by PISNe (in addition to SNcc) can reasonably be excluded.

4.5.1 Future directions

As we have seen throughout this paper, the determination of several SNIa and SNcc properties (as well as their relative contribution to the ICM enrichment) can, in principle, be constrained from the ICM (and proto-solar) abundance pattern. Although we showed that some combinations of models and hypotheses can be ruled out with a high degree of certainty, it is still impossible to clearly favour one specific combination of SN models. For instance, as we have shown in Sect. 4.3.1, if one wants to confirm (or rule out) the bimodality in SNIa explosions that enrich the ICM, a very precise determination of the Ni/Fe ratio is essential, but currently not possible. Similarly, although the amount of metals released by SNcc is in principle sensitive to the shape of the IMF, we cannot clearly favour one specific IMF with our current results and the available models (Sect. 4.3.4). Finally, despite our detailed discussion on the possible contribution of Ca-rich gap transients to the enrichment, the high Ca/Fe ratio measured in the ICM remains an open issue. In order to better constrain the stellar origins of the ICM enrichment, further improvements on many aspects are clearly needed.

First, both SNIa and SNcc yield models still suffer from uncertainties (e.g. see discussion in Appendix 4.A). Major improvements of these mod-

els (in particular, better agreements in the yields of physically comparable models) are thus crucial for the purpose of this study. Second, an ongoing effort should be made to reduce the systematic uncertainties in the solar and meteoritic abundances, as, together with ICM abundances, they may provide further constraints to SNIa and SNcc yield models. Third, future direct studies of SNe will be complementary to this work. In particular, improvements in estimating the relative fraction of SNIa, and particularly of Ca-rich gap transients, exploding in the Galaxy and in galaxy clusters could bring additional valuable constraints on the SN models to favour. Conversely, the estimates from our study may be useful to complement future direct observations of SNe.

Finally, the uncertainties in the ICM abundances must be reduced as well. For instance, the discrepancies between atomic data have been greatly reduced over the past decades, but the atomic codes should be continuously updated (see also Chapter 5). Similarly, calibration issues in the current X-ray instruments have been improved, but still largely contribute to the current uncertainties (e.g. Schellenberger et al. 2015, Chapter 2; Chapter 3). In Chapter 3 we showed that adding more cluster data would not reduce the current uncertainties in the ICM abundance pattern. Therefore, next-generation X-ray missions (in particular using micro-calorimeter arrays, which should significantly improve the spectral resolution currently achieved with CCDs) are crucial to provide a better general understanding of the ICM enrichment and the origin of metals in the Universe.

Acknowledgements

We thank the anonymous referee for useful comments which helped to improve the paper. This work is partly based on the *XMM-Newton* AO-12 proposal “*The XMM-Newton view of chemical enrichment in bright galaxy clusters and groups*” (PI: de Plaa), and is a part of the CHEERS (CHEmical Evolution Rgs cluster Sample) collaboration. The authors thank its members, as well as Liyi Gu and Craig Sarazin for helpful discussions. P.K. thanks Steve Allen and Ondrej Urban for support and hospitality at Stanford University. Y.Y.Z. acknowledges support from the German BMWI through the Verbundforschung under grant 50 OR 1506. This work is based on observations obtained with *XMM-Newton*, an ESA science mission with instruments and contributions directly funded by ESA member states and the USA (NASA). The SRON Netherlands Institute for Space Research is sup-

ported financially by NWO, the Netherlands Organisation for Scientific Research.

4.A The effect of electron capture rates on the SNIa nucleosynthesis yields

Because the electron gas in the core of WDs is highly degenerate, the electron capture process can play an important role during the SNIa explosion, and has a significant impact on the nucleosynthesis of intermediate-mass and Fe-group elements. The Classical SNIa yield models referred to in this paper are taken from Iwamoto et al. (1999), who used the electron capture rates of Fuller et al. (1982). These rates were tabulated for light (i.e. *sd*-shell) nuclei only. Later on, Brachwitz et al. (2000) showed that updated calculations of heavier (*pf*-shell) nuclei (e.g. Langanke & Martínez-Pinedo 1998; Langanke & Martínez-Pinedo 2001) lead to a significant reduction in the electron capture rates compared to the previous estimates. In principle, these lowered rates affect the overall nucleosynthesis predicted by the SNIa models.

In Fig. 4.11, we compare the X/Fe ratios predicted by the Classical W7 model, using first the older and then the more recent electron capture rates. These two W7 models are directly adopted from Iwamoto et al. (1999) and Maeda et al. (2010), respectively. The largest difference in the X/Fe ratios from the more recent calculations is found for Cr/Fe, with a decrease of 39% compared to the older electron capture rates. The other abundance ratios, however, show less pronounced differences (~20% at most).

Except W7, no other Classical (or Bravo) model incorporating these updated electron capture rates is explicitly available in the literature. Although we do not expect this issue to alter the conclusions of this paper, this illustrates well that SN yield models may suffer from uncertainties, and that care must be taken when interpreting the ability of the models to strictly reproduce the measured abundance ratios in the ICM.

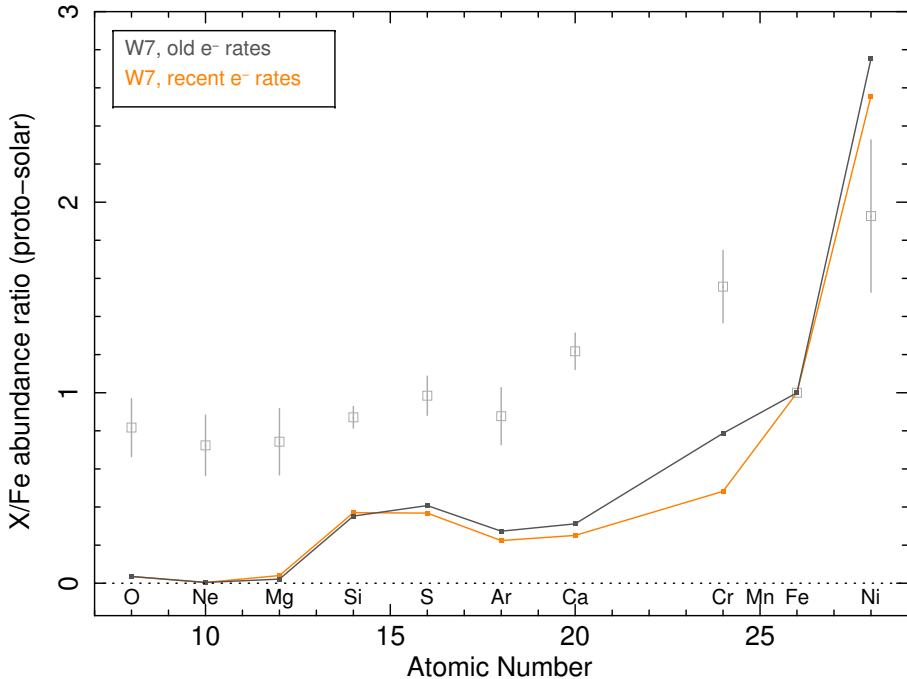


Figure 4.11: Predicted X/Fe abundances from the Classical W7 model (SNIa), adopted from Iwamoto et al. (1999, brown) and Maeda et al. (2010, orange). The two models assume different electron capture rates, leading to different X/Fe ratios, both for intermediate-mass and Fe-group elements (see text). For comparison, the ICM average abundance ratios (inferred from Chapter 3) are also plotted.

4.B List of SN yield models used in this work

Table 4.5: SNIa and SNcc yield models, taken from literature and used in this work. The inner core densities ρ_9 are given in units of 10^9 g/cm^3 . The transitional deflagration-to-detonation densities $\rho_{T,7}$ are given in units of 10^7 g/cm^3 . The masses of the CO core and of the He layer (respectively M_{CO} and M_{He} , "Ca-rich gap" models), and the mass of each of the two merging WD (M_{WD} , "DD channel" model) are given in units of M_{\odot} .

Category	Name	Ref.	Remarks
SNIa			
Classical	W7	1	Deflagration, $\rho_9 = 2.12$
Classical	W70	1	Deflagration, $\rho_9 = 2.12$, zero initial metallicity
Classical	WDD1	1	Delayed-detonation, $\rho_9 = 2.12$, $\rho_{T,7} = 1.7$
Classical	WDD2	1	Delayed-detonation, $\rho_9 = 2.12$, $\rho_{T,7} = 2.2$
Classical	WDD3	1	Delayed-detonation, $\rho_9 = 2.12$, $\rho_{T,7} = 3.0$

4.B List of SN yield models used in this work

Table 4.5: Continued.

Category	Name	Ref.	Remarks
Classical	CDD1	1	Delayed-detonation, $\rho_9 = 1.37$, $\rho_{T,7} = 1.7$
Classical	CDD2	1	Delayed-detonation, $\rho_9 = 1.37$, $\rho_{T,7} = 2.2$
Bravo	DDTa	2,3	Delayed-detonation, fits the Tycho SNR, $\rho_{T,7} = 3.9$
Bravo	DDTc	2,3	Delayed-detonation, fits the Tycho SNR, $\rho_{T,7} = 2.2$
Bravo	DDTe	2,3	Delayed-detonation, fits the Tycho SNR, $\rho_{T,7} = 1.3$
Ca-rich gap	CO.45HE.2	4	Ca-rich SNe, $M_{\text{CO}} = 0.45$, $M_{\text{He}} = 0.2$
Ca-rich gap	CO.5HE.2	4	Ca-rich SNe, $M_{\text{CO}} = 0.5$, $M_{\text{He}} = 0.2$
Ca-rich gap	CO.5HE.15	4	Ca-rich SNe, $M_{\text{CO}} = 0.5$, $M_{\text{He}} = 0.15$
Ca-rich gap	CO.5HE.2N.02	4	Ca-rich SNe, $M_{\text{CO}} = 0.5$, $M_{\text{He}} = 0.2$, 2% N in He layer
Ca-rich gap	CO.5HE.2C.03	4	Ca-rich SNe, $M_{\text{CO}} = 0.5$, $M_{\text{He}} = 0.2$, 30% mixing core-He layer
Ca-rich gap	CO.5HE.3	4	Ca-rich SNe, $M_{\text{CO}} = 0.5$, $M_{\text{He}} = 0.3$
Ca-rich gap	CO.55HE.2	4	Ca-rich SNe, $M_{\text{CO}} = 0.55$, $M_{\text{He}} = 0.2$
Ca-rich gap	CO.6HE.2	4	Ca-rich SNe, $M_{\text{CO}} = 0.6$, $M_{\text{He}} = 0.2$
2D	C-DEF	5	2D deflagration, $\rho_9 = 2.9$
2D	C-DDT	5	2D delayed-detonation, $\rho_9 = 2.9$, $\rho_{T,7} = 1.0$
2D	O-DDT	5	2D delayed-detonation, $\rho_9 = 2.9$, $\rho_{T,7} = 1.0$, off-centre ignition
3D	N1def	6	3D deflagration, $\rho_9 = 2.9$, 1 ignition spot
3D	N3def	6	3D deflagration, $\rho_9 = 2.9$, 3 ignition spots
3D	N5def	6	3D deflagration, $\rho_9 = 2.9$, 5 ignition spots
3D	N10def	6	3D deflagration, $\rho_9 = 2.9$, 10 ignition spots
3D	N20def	6	3D deflagration, $\rho_9 = 2.9$, 20 ignition spots
3D	N40def	6	3D deflagration, $\rho_9 = 2.9$, 40 ignition spots
3D	N100Ldef	6	3D deflagration, $\rho_9 = 1.0$, 100 ignition spots
3D	N100def	6	3D deflagration, $\rho_9 = 2.9$, 100 ignition spots
3D	N100Hdef	6	3D deflagration, $\rho_9 = 5.5$, 100 ignition spots
3D	N150def	6	3D deflagration, $\rho_9 = 2.9$, 150 ignition spots
3D	N200def	6	3D deflagration, $\rho_9 = 2.9$, 200 ignition spots
3D	N300Cdef	6	3D deflagration, $\rho_9 = 2.9$, 300 centred ignition spots
3D	N1600def	6	3D deflagration, $\rho_9 = 2.9$, 1600 ignition spots
3D	N1600Cdef	6	3D deflagration, $\rho_9 = 2.9$, 1600 centred ignition spots
3D	N1	7	3D delayed-detonation, $\rho_9 = 2.9$, 1 ignition spot
3D	N3	7	3D delayed-detonation, $\rho_9 = 2.9$, 3 ignition spots
3D	N5	7	3D delayed-detonation, $\rho_9 = 2.9$, 5 ignition spots
3D	N10	7	3D delayed-detonation, $\rho_9 = 2.9$, 10 ignition spots
3D	N20	7	3D delayed-detonation, $\rho_9 = 2.9$, 20 ignition spots
3D	N40	7	3D delayed-detonation, $\rho_9 = 2.9$, 40 ignition spots
3D	N100L	7	3D delayed-detonation, $\rho_9 = 1.0$, 100 ignition spots
3D	N100	7	3D delayed-detonation, $\rho_9 = 2.9$, 100 ignition spots
3D	N100H	7	3D delayed-detonation, $\rho_9 = 5.5$, 100 ignition spots
3D	N150	7	3D delayed-detonation, $\rho_9 = 2.9$, 150 ignition spots
3D	N200	7	3D delayed-detonation, $\rho_9 = 2.9$, 200 ignition spots
3D	N300C	7	3D delayed-detonation, $\rho_9 = 2.9$, 300 centred ignition spots
3D	N1600	7	3D delayed-detonation, $\rho_9 = 2.9$, 1600 ignition spots
3D	N1600C	7	3D delayed-detonation, $\rho_9 = 2.9$, 1600 centred ignition spots
Sub- M_{Ch}	0.9_0.9	8	WD-WD violent merger, $M_{\text{WD}} \simeq 0.9$, $\rho_9 = 1.4 \times 10^{-2}$ SNcc
Nomoto	Z0	9,10,11	$Z_{\text{init}} = 0$

Table 4.5: Continued.

Category	Name	Ref.	Remarks
Nomoto	Z0_cut	9,10,11	$Z_{\text{init}} = 0$, restricted to $\leq 40 M_{\odot}$
Nomoto	Z0.001	9,10,11	$Z_{\text{init}} = 0.001$
Nomoto	Z0.004	9,10,11	$Z_{\text{init}} = 0.004$
Nomoto	Z0.008	11	$Z_{\text{init}} = 0.008$
Nomoto	Z0.02	9,10,11	$Z_{\text{init}} = 0.02$
Nomoto	Z0+PISNe	9,10,11,12	$Z_{\text{init}} = 0$, incl. contribution from PISNe (up to $300 M_{\odot}$)
HW	Z0+PISNe	13,14	$Z_{\text{init}} = 0$, incl. contribution from PISNe (up to $260 M_{\odot}$)

(1) Iwamoto et al. (1999); (2) Badenes et al. (2003); (3) Badenes et al. (2006); (4) Waldman et al. (2011); (5) Maeda et al. (2010); (6) Fink et al. (2014); (7) Seitenzahl et al. (2013b); (8) Pakmor et al. (2010); (9) Nomoto et al. (2006); (10) Kobayashi et al. (2006); (11) Nomoto et al. (2013); (12) Umeda & Nomoto (2002); (13) Heger & Woosley (2002); (14) Heger & Woosley (2010).

Don't fear mistakes. There are none.

– Miles Davis

5

Origin of central abundances in the hot intra-cluster medium

III. The impact of spectral model improve- ments on the abundance ratios

F. Mernier, J. de Plaa, J. S. Kaastra, A. J. J. Raassen, L. Gu, J. Mao, and
I. Urdampilleta

(submitted to Astronomy & Astrophysics)

Abstract

The hot intra-cluster medium (ICM) permeating galaxy clusters and groups is rich in metals, which were synthesised by billions of supernovae and have accumulated in cluster gravitational wells for several Gyrs. Since Type Ia (SNIa) and core-collapse supernovae (SNcc) produce different elements in quantities that depend on their explosions and/or progenitors, measuring accurately the abundances in the ICM can help to bring further constraints on the SNIa and SNcc models to favour. In a series of previous papers (Chapters 3 and 4), we compiled *XMM-Newton* observations of 44 cool-core clusters, groups, and massive ellipticals (the CHEERS catalogue) in order to establish an average abundance pattern representative of the nearby ICM, and to compare it to SNIa and SNcc yield models taken from the literature. In this paper, we revisit our previous abundance measurements by using an updated version of the spectral code and atomic database (SPEXACT) to fit the *XMM-Newton* EPIC spectra. We find that the Fe abundance in the less massive groups ($kT < 1.7$ keV) has been systematically underestimated in our previous results, up to a factor of 2 for the coolest systems. Because small model-to-data discrepancies in the unresolved Fe-L complex may lead to a large Fe bias, and because even the up-to-date spectral models do not well reproduce the shape of this complex below $kT \simeq 1$ keV, we conclude that the Fe content of these cool systems is still very uncertain. Moreover, the updated average Ni/Fe

ratio is found to be $\sim 28\%$ lower than our previous estimate. This implies that the ICM abundance pattern can be reasonably reproduced when assuming delayed-detonation as the sole explosion mechanism in SNIa.

5.1 Introduction

Because galaxy clusters host the largest gravitational potential wells known in our Universe, they act as “closed-box” systems and retain all the baryons they have accreted during their formation. This is particularly interesting, because the hot gas — or intra-cluster medium (ICM) — permeating galaxy clusters is rich in heavy elements, which are thought to have been produced by stars and supernovae mostly during the peak of cosmic star formation (Madau & Dickinson 2014). After a significant fraction of these metals escape from their stellar and galactic hosts, they easily mix with the ICM, and become observable through X-ray observatories via the emission lines of their highly ionised ions (for recent reviews, see Werner et al. 2008; de Plaa 2013; de Plaa & Mernier 2017). Consequently, metals in the ICM are a valuable imprint of the integral yields of billions of supernovae having exploded within galaxy clusters over cosmic time.

Different supernova (SN) types produce elements in different amounts. Core-collapse supernovae (SNcc) are thought to produce large quantities of oxygen (O), neon (Ne), and magnesium (Mg), and negligible amounts of chromium (Cr), manganese (Mn), iron (Fe), and nickel (Ni). On the contrary, Type Ia supernovae (SNIa) are thought to produce Cr, Mn, Fe, and Ni in large amounts, but almost no O, Ne, nor Mg. Intermediate elements, like silicon (Si), sulfur (S), argon (Ar), and calcium (Ca) are thought to be produced by both types of supernovae in comparable quantities. On the other hand, the exact yields produced by SNIa and SNcc depend on several factors. First, the relative yields produced by SNIa are sensitive to the propagation of the burning flame triggering the explosion (e.g. Iwamoto et al. 1999). Deflagration models predict that the flame propagates sub-sonically, which produces larger amounts of Ni and moderate amounts of intermediate elements. Delayed-detonation models, on the contrary, predict that the flame becomes super-sonic below a specific density, which produces less Ni and more intermediate elements. Second, the relative yields produced by a population of SNcc depend on the initial mass function (IMF) and the average initial metallicity of their stellar progenitors (e.g. Nomoto et al. 2013).

Because the ICM is in collisional ionisation equilibrium (CIE) and optical depth effects are negligible, abundances of O, Ne, Mg, Si, S, Ar, Ca, Fe, and Ni (and, to some extent, Cr and Mn) can be robustly constrained in the ICM. Therefore, the abundances of various elements X (or their ratio relative to Fe, X/Fe) can be directly compared to predictions of SNIa and SNcc yield models, in order to bring further constraints on SNIa explosions, stellar populations, and the relative fraction of SNIa and SNcc to enrich galaxy clusters. Several studies were devoted to this aspect over the last decades (e.g. Mushotzky et al. 1996; Finoguenov et al. 2002; de Plaa et al. 2007; Sato et al. 2007a).

Recently, we compiled deep *XMM-Newton* EPIC and RGS observations of 44 nearby cool-core ellipticals, galaxy groups, and clusters (the CHEERS¹ catalogue, see Sect. 5.2.1) in order to measure accurately the X/Fe abundance ratios of the 10 elements mentioned above, and to derive a complete abundance pattern, representative of the nearby ICM as a whole (Chapter 3). We then compared this abundance pattern with commonly used and / or recent SNIa and SNcc yield models, in order to provide reliable constraints on SNIa/SNcc explosions and / or progenitors (Chapter 4). Among the results presented in Chapter 4, we could note that, interestingly, a diversity in SNIa explosions (with both deflagration and delayed-detonation models) was required to reproduce successfully all the average estimated X/Fe ratios.

Of course, for such a study, it is crucial to fully understand (and, possibly, reduce) the systematic uncertainties affecting the measurements of the X/Fe abundance ratios in the ICM. In Chapter 3, we showed that these uncertainties were actually largely dominating over the statistical uncertainties. While many sources of systematic uncertainties were taken into account in that study (including local continuum biases in the instrumental response, EPIC cross-calibration uncertainties, intrinsic scatter, assumed thermal structure of the ICM, differences in the studied spatial regions, as well as a careful modelling of the background), our results relied on the up-to-date version (2.06) of the plasma models from the SPEX fitting package (Kaastra et al. 1996) at that time. Recently, however, a major update of SPEX has been performed (see Sect. 5.2.2 for more details). Since, by essence, the estimated abundances of a CIE plasma depend on the input atomic calculations in the spectral model that is used, studying the effects of these improvements on our previous measurements is essential for set-

¹CHEMical Enrichment Rgs Sample

ting correct constraints on supernova yield models.

In this work, we explore the effects of such spectral model improvements on our previously measured average abundance pattern in the cool-core ICM, in particular with *XMM-Newton* EPIC (Chapter 3). As a second step, we discuss the implications of these effects on our previous interpretation of the ICM enrichment by SNIa and SNcc (Chapter 4). This paper is organised as follows. Section 5.2 is devoted to the reanalysis of the data presented in Chapter 3. Our updated results are presented in Sect. 5.3, and their implications regarding to previous studies are discussed in Sect. 5.4. We sum up our findings in Sect. 5.5. Throughout this paper, we assume $H_0 = 70 \text{ km s}^{-1} \text{ Mpc}^{-1}$, $\Omega_m = 0.3$, and $\Omega_\Lambda = 0.7$. Unless otherwise stated, the error bars are given within a 68% confidence interval. All the abundances mentioned in this work are given with respect to their proto-solar values derived from Lodders et al. (2009).

5.2 The sample and the reanalysis of our data

5.2.1 The sample

The sample, the data reduction, and the spectral analysis and strategies are all described in detail in Chapter 3. Like our present work, that previous study focused on the *XMM-Newton* observations of 44 nearby cool-core clusters, groups, and ellipticals, all being part of the CHEERS sample (see also Pinto et al. 2015; de Plaa et al. 2017). In addition to their limited redshift ($z < 0.2$), the main criterion of the sample is that the oxygen abundance (mainly traced by its O VIII emission line) measured by the RGS instrument must be detected with $>5\sigma$ of significance. In this way, we ensure selecting clusters with prominent metal lines in their cores. This allows a robust determination of most of the metal abundances also with the EPIC instruments.

Starting from the same filtered data and spectra as in Chapter 3, we adopt the same definitions and we split our sample into two subsamples.

1. The hot "clusters" (23 objects), which exhibit a central mean temperature of $kT > 1.7 \text{ keV}$. They can be investigated within $0.2r_{500}$ (and sometimes beyond).
2. The cool "groups" (21 objects, also including ellipticals), which exhibit a central mean temperature of $kT < 1.7 \text{ keV}$. By selection, their

$0.2r_{500}$ limit often falls outside the EPIC field of view, but they can be investigated within $0.05r_{500}$.

The elliptical galaxy M 87 is an exception. As the brightest central galaxy of a large cluster (Virgo), its mean temperature is about ~ 2 keV, but the galaxy is too nearby to allow the ICM for being investigated within $0.2r_{500}$. Following Chapter 3, we choose to consider it as part of the group subsample.

In order to maximise our statistics, and unless mentioned otherwise, in the rest of the paper we focus on the $(0.2+0.05)r_{500}$ sample, i.e. where the abundances in our clusters and our groups are investigated within $0.2r_{500}$ and $0.05r_{500}$, respectively. A complete discussion of the effects of adopting different extraction radii on our abundance measurements can be found in Chapter 3.

5.2.2 From SPEXACT v2 to SPEXACT v3

Since 1996, the original `mekal` code, used to model thermal plasmas (Mewe 1972; Mewe et al. 1985, 1986), has been developed independently within the SPEX spectral fitting package (Kaastra et al. 1996) and gradually improved. Up to the version 2.06, the code made use of an atomic database and a collection of routines that are all referred to SPEXACT² v2. Since 2016, however, a major update has been performed on both the atomic database and the corresponding routines, leading to SPEXACT v3. For example, the atomic database contains now hundreds of thousands of energy transitions (from hydrogen to zinc) whose updated collisional excitation and deexcitation rates, radiative transition probabilities and auto-ionisation and dielectronic recombination rates have been obtained from the literature or consistently calculated using the FAC³ code (Gu 2008). All these transitions, much more numerous than in SPEXACT v2, cover now atomic levels with principle quantum number up to 20 for H-like, and up to 16 for He-like ions. On the other hand, significant improved calculations of the radiative recombination (Badnell 2006; Mao & Kaastra 2016) and collisional ionisation coefficients (Urdampilleta et al. 2017) have been achieved. The updated version of the fitting package, namely SPEX v3, allows to use either SPEXACT v2 or SPEXACT v3, depending on the user's requirements.

After the release of SPEXACT v3, we noted in Chapter 6 (see also de Plaa et al. 2017) that the choice of the SPEXACT version could lead to sig-

²SPEX Atomic Code and Tables; see also the SPEX manual.

³<https://www-amdis.iaea.org/FAC>

nificant changes in the abundances measured with RGS and EPIC, respectively. Since all the spectral analysis in Chapter 3 has been done using SPEXACT v2, in this paper we aim to quantify the changes on the average ICM abundance ratios when using SPEXACT v3. A straight forward way to do so would be to re-process entirely the spectral analysis for all our observations before re-stacking the results in a similar way as in Chapter 3. However, the very large number of new lines in the updated atomic database considerably expands the computing time required for each single fit, making this approach technically unrealistic. Instead, we choose a similar alternative already presented in de Plaa et al. (2017) and Chapter 6.

In Chapter 3, the abundances of O, Ne, Cr, and Mn were either measured with SPEXACT v3 or already corrected to their SPEXACT v3 estimates. Therefore, there is no need to include them in our simulations. To estimate the impact of spectral model improvements on the Mg, Si, S, Ar, Ca, Fe, and Ni abundances, we first use SPEXACT v3 to simulate 24 spectra of an absorbed multi-temperature CIE plasma, namely `gdem`, which mimics a plasma with a Gaussian temperature distribution⁴. Each spectrum is simulated at a fixed mean temperature (kT_{mean}) between 0.6 and 6 keV (i.e. the typical range of temperatures that are measured in the core of our systems), assuming the recent ionisation balance of Urdampilleta et al. (2017), and each model is convolved with the EPIC MOS and pn instrumental responses. The abundances of all the elements are fixed to the proto-solar unity. The redshift (z), hydrogen column density (N_{H}), the emission measure ($Y = \int n_e n_{\text{H}} dV$) and the width of the Gaussian temperature distribution (σ_T) are set to 0.039 (corresponding to a distance of ~ 172 Mpc), $1.14 \times 10^{25} \text{ m}^{-2}$, $7.17 \times 10^{72} \text{ m}^{-3}$, and 0.18, respectively. These parameters are adapted from the best-fit results of EXO 0422, a typical cluster of intermediate redshift, temperature, and abundances (see Chapter 3). To minimise the statistical biases, all the spectra are simulated for a 100 ks exposure (which is comparable to the typical net exposure of each object). Furthermore, we keep the Poisson noise to zero to obtain the exact mean number of counts that is expected in each bin (see de Plaa et al. 2017). This approach is clearly faster than the Monte Carlo method since we do not need to simulate a large number of spectra with Poisson noise.

As a second step, we fit all these spectra, this time using SPEXACT v2, leaving free the emission measure, the mean temperature, and the aforementioned abundances that we could reasonably measure with EPIC. These

⁴For more details, see Chapter 3 and the SPEX manual.

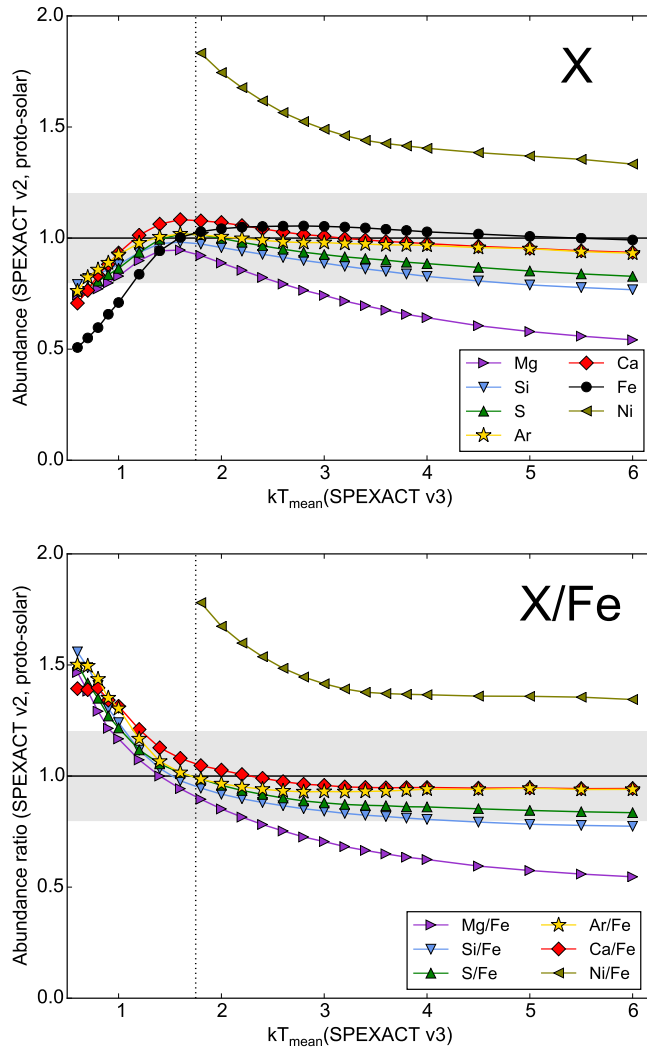


Figure 5.1: Top: Abundance results from (gdem) local fits with SPEXACT v2 to simulated SPEXACT v3 spectra for a range of temperatures (see also Fig. 6.9). The measured abundances are shown and compared to their input value of 1 proto-solar. The grey shaded area shows the $\pm 20\%$ level of uncertainty. The vertical dotted line indicates our (arbitrary) separation between clusters and groups. Bottom: Same figure, this time for the X/Fe abundance ratios.

fits are done assuming the ionisation balance of Bryans et al. (2009), as assumed in Chapter 3. To be consistent with our previous analysis (Chapter 3), after having fixed the temperature parameter, the abundance parameters are re-estimated through a local fit (i.e. within a band encompassing their corresponding K-shell lines).

The result of this exercise, illustrating the differences between the two latest SPEXACT versions in measuring the absolute abundances (X), is shown in the upper panel of Fig. 5.1 (see also Fig. 6.9). The lower panel provides the same quantities, this time reported relative to the Fe abundance (X/Fe).

Finally, based on these simulated estimates, we correct the estimated absolute/relative abundances of each observed spectrum by applying a corresponding SPEXACT v2–v3 correction factor. These factors obviously depend on the measured mean temperature, and are simply taken as the inverse of the values reported in Fig. 5.1. The individual corrections applied here are further commented in the next sections.

5.3 Results

Before applying the correction method described in Sect. 5.2.2 to our previous data (Chapter 3), we discuss the ratios in Fig. 5.1. In the upper panel, Fe appears to be well recovered in the cluster regime ($kT_{\text{mean}} > 1.7 \text{ keV}$), in which the Fe abundance is essentially measured via its K-shell complex ($\sim 6.4 \text{ keV}$). However, for cooler systems ($kT_{\text{mean}} < 1.7 \text{ keV}$), in which the Fe L-shell lines become clearly dominant, the Fe abundance is systematically underestimated by SPEXACT v2, up to a factor of 2 for the coolest plasmas ($kT_{\text{mean}} \simeq 0.6 \text{ keV}$). This underestimate has an effect on the X/Fe ratios, which are measured $\sim 50\%$ higher using SPEXACT v2 than using SPEXACT v3 (Fig. 5.1 bottom). Besides Fe, two other elements (and their corresponding X/Fe ratios) deserve some attention, in particular at cluster temperatures. When measured with SPEXACT v2, the Ni abundance is clearly overestimated, from $\sim 30\%$ in the hottest plasmas to $\sim 80\%$ when approaching the group regime (where the Ni K-shell lines become difficult to detect with the current instruments). On the other hand, the Mg abundance can be biased low to $\sim 50\%$.

5.3.1 The Fe bias in cool plasmas

The dramatic underestimate of the Fe abundance by SPEXACT v2 with respect to SPEXACT v3 in cool groups/ellipticals appears quite surprising at first glance. Since it has a considerable impact on the measured X/Fe abundance ratios for cool ($kT_{\text{mean}} \lesssim 1 \text{ keV}$) plasmas (Fig. 5.1 bottom), it is essential to understand the precise reasons for such a bias.

To investigate the behaviour of the Fe abundance estimate in the cool ICM, we use SPEXACT v3 to simulate the EPIC MOS 1, MOS 2, and pn spectra of a $kT = 0.7 \text{ keV}$ plasma, taken as single-temperature (i.e. $\sigma_T = 0$) for convenience. We verify that the impact of σ_T is negligible for the rest of the analysis. For an easy comparison, we set the input Y and Fe parameters to $1 \times 10^{72} \text{ m}^{-3}$ and the proto-solar unity, respectively. The z and n_{H} parameters are left unchanged compared to our previous simulations (based on the best-fit values of EXO 0422), and the Poisson noise is also set to zero (Sect. 5.2.2). We fit these spectra simultaneously with a SPEXACT v2 model, leaving free the Y , kT , and the abundance parameters.

After a visual inspection of the best-fit model (Fig. 5.2), it appears that most of the residuals lie in the Fe-L complex, in particular within $\sim 1.1\text{--}1.3 \text{ keV}$ (rest frame), where they reach up to $\sim 20\%$. With the release of SPEXACT v3, many new lines of Fe XVII, Fe XVIII, and Fe XIX significantly emitting in this energy band have been added to the CIE models, resulting in an excess that SPEXACT v2 models fail to reproduce. The fit compensates these residuals by raising the emission measure of the continuum while lowering the Fe abundance parameter in order to minimise the C-stat value over the whole spectrum. This effect is also illustrated in Fig. 5.2. To demonstrate (and further quantify) this effect, we report in Table 5.1 ("Sv2, gl" method) the best-fit values of Y , kT , and Fe when fitting a SPEXACT v2 model to our simulated spectrum after (i) keeping all these parameters free (i.e. same as above); (ii) fixing Y to its simulated value ($1 \times 10^{72} \text{ m}^{-3}$); (iii) fixing kT to its simulated value (0.7 keV); and (iv) fixing the Fe abundance to its simulated value (proto-solar unity). The small value of C-stat/d.o.f. is due to the fact that we did not add Poisson noise to our simulated spectra. Clearly, both the emission measure and the temperature conspire to bias the true abundance value. Although the temperature remains always close to its simulated input value (overestimated by 6% at most), its effect on the best-fit models may be important (see Table 5.1 when we fix kT to its simulated value).

As a second test, and in order to confirm that our Fe bias is predomi-

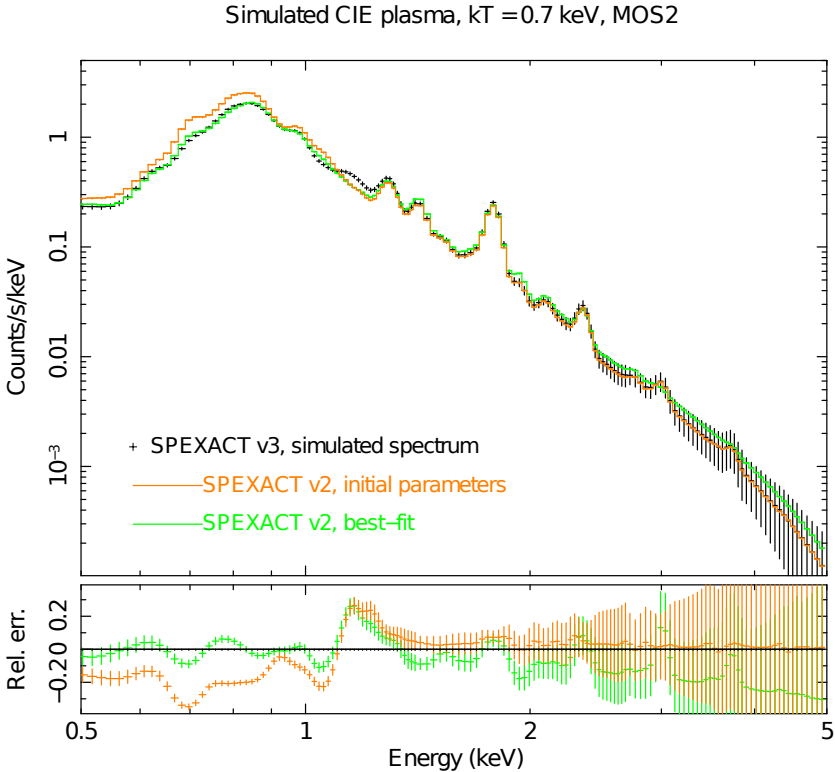


Figure 5.2: EPIC MOS 2 simulated spectrum of a $kT = 0.7$ keV CIE plasma, using SPEXACT v3 (see also Table 5.1, first row). For comparison, we show the same model calculated using SPEXACT v2 (orange). When thawing the Y , kT , and abundance parameters, the best-fit SPEXACT v2 model (green, see also Table 5.1, second row) tries to compensate for the residuals in the Fe-L complex.

nantly caused by the residuals in the $\sim 1.1\text{--}1.3$ keV energy band, we re-do a complete set of fittings of SPEXACT v3 simulated spectra with SPEXACT v2 models at various plasma temperatures (as described in Sect. 5.2.2), this time by ignoring that specific energy band (i.e. where the residuals are the largest). While we still find a reasonable agreement for $kT_{\text{mean}} \gtrsim 1$ keV plasmas, the Fe bias in cool plasmas is now reduced by a factor ~ 2.5 , with an Fe abundance underestimate of $\sim 20\%$ (or less) with respect to the SPEXACT v3 initial value. This is also illustrated in Table 5.1, where we report the Y , kT , and Fe abundance best-fit parameters of our simulated $kT = 0.7$ keV single-temperature spectra as described above after

Table 5.1: Effects of EPIC spectral fits using different atomic codes (and fixing specific parameters) on a SPEXACT v3 simulated single-temperature plasma of $kT = 0.7$ keV (with no Poisson noise). Parameter values marked by an asterisk (*) are fixed in the fits. The "Sv2" and "Sv3" abbreviations stand for SPEXACT v2 and SPEXACT v3, respectively. The "sim", "gl" and, "exc" abbreviations indicate whether the spectra are the simulation input, fitted globally, or fitted excluding the $\sim 1.1\text{--}1.3$ keV band, respectively.

Method	Y ($\times 10^{72}$ m $^{-3}$)	kT (keV)	Fe	C-stat/d.o.f.
Sv3, sim	1.0*	0.70*	1.0*	—
Sv2, gl	1.24 ± 0.03	0.7502 ± 0.0021	0.637 ± 0.023	1337/710
Sv2, gl	1.0*	0.7564 ± 0.0019	0.816 ± 0.005	1383/711
Sv2, gl	1.73 ± 0.04	0.70*	0.390 ± 0.009	1764/711
Sv2, gl	0.841 ± 0.005	0.7619 ± 0.0018	1.0*	1473/711
Sv2, exc	0.83 ± 0.04	0.7403 ± 0.0023	0.95 ± 0.06	438/677
Sv2, exc	1.0*	0.7372 ± 0.0021	0.775 ± 0.005	459/678
Sv2, exc	1.13 ± 0.04	0.70*	0.63 ± 0.03	745/678
Sv2, exc	0.796 ± 0.005	0.7413 ± 0.0021	1.0*	439/678

ignoring the $\sim 1.1\text{--}1.3$ keV energy band ("Sv2, exc" method). Finally, using SPEXACT v2 only, we verify that we obtain a similar trend in the EPIC spectra of the 6 coolest objects of our sample (namely NGC 1404, M 89, NGC 5813, NGC 4636, NGC 5846, and NGC 1316; all showing $kT_{\text{mean}} < 0.8$ keV). When we ignore the $\sim 1.1\text{--}1.3$ keV energy band in the fits, the measured Fe abundance of these objects is on average $\sim 84\%$ higher than their full-band estimates reported in Chapter 3. This is consistent with our estimates based on simulated spectra (see above). We conclude that, although its major part originates from the $\sim 1.1\text{--}1.3$ keV energy band where most residuals are found, the Fe bias in cool plasmas is a result of an incorrect fitting of the whole Fe-L complex, even where residuals are on the order of a few per cent.

One important question is whether SPEXACT v3 is able to reproduce correctly the spectra of real cool systems. As mentioned in Sect. 5.2.2, the very expensive computing time required by SPEXACT v3 for fitting EPIC spectra unfortunately prevents us from updating directly our previous results (Chapter 3). Nevertheless, here we choose to focus on one system, NGC 5846, as a typical cool galaxy group with excellent statistics and central temperatures of about 0.75 keV. Using successively SPEXACT v2 and SPEXACT v3, we fit simultaneously the MOS 1, MOS 2 and pn spectra of

the two pointings of NGC 5846 with a `gdem` model. The observed MOS 2 spectrum of the first pointing is plotted together with its best-fit models in Fig. 5.3. When using SPEXACT v3 instead of SPEXACT v2, the best-fit Fe abundance increases from 0.659 ± 0.017 (see also table C.1. in Chapter 3) to 1.07 ± 0.04 with reduced C-stat values of 2.64 and 2.36, respectively. Again, this supports our above results based on simulated spectra. However, while we note a substantial improvement in the best-fit at ~ 1.1 – 1.2 keV (due to the incorporation of many more Fe XVII, Fe XVIII lines), we note that even the SPEXACT v3 model generates significant residuals (within $\sim \pm 20\%$), especially at ~ 0.65 keV (i.e. in the vicinity the O Ly α line) and within ~ 1.2 – 1.3 keV. We verify that the `apec` model v3.0.7 (available in the XSPEC package) also fails to reproduce these features.

At first glance, these residuals may originate from various sources of incorrect modelling. For instance, they can be due to a more complex thermal structure of the gas, an additional and unaccounted AGN and/or non-thermal emission, turbulence in the gas, an incorrect hydrogen column density absorption, or issues in the calibration of instruments. We successively check these hypotheses, and find that none of them is likely to explain such residuals. In particular, we find no significant change when we:

- assume a different temperature emission model (e.g. single-temperature, two-temperatures, or a `wdem`⁵ model),
- add an additional absorbed power law,
- assume a large turbulence parameter in the plasma model,
- free the hydrogen column density parameter.

Finally, we also find similar residuals in other very cool (< 1 keV) objects, namely NGC 4636, NGC 5813, and possibly M 60, NGC 1404, and NGC 5044 in both MOS and pn detectors. Such features have also been reported in previous studies, either in cool groups (Grange et al. 2011) or even in stellar coronae (Brickhouse et al. 2000), and seem to be typical of < 1 keV plasmas. For these reasons, we can also reasonably discard the possibility of calibration issues to explain the discrepancies. The only explanation we are left with is that current spectral models still do not reproduce well the spectral features of the Fe-L complex (and its surrounding energy bands) in cool plasmas. Because, as shown above, tiny differences in modelling the Fe-L

⁵See the SPEX manual for more details.

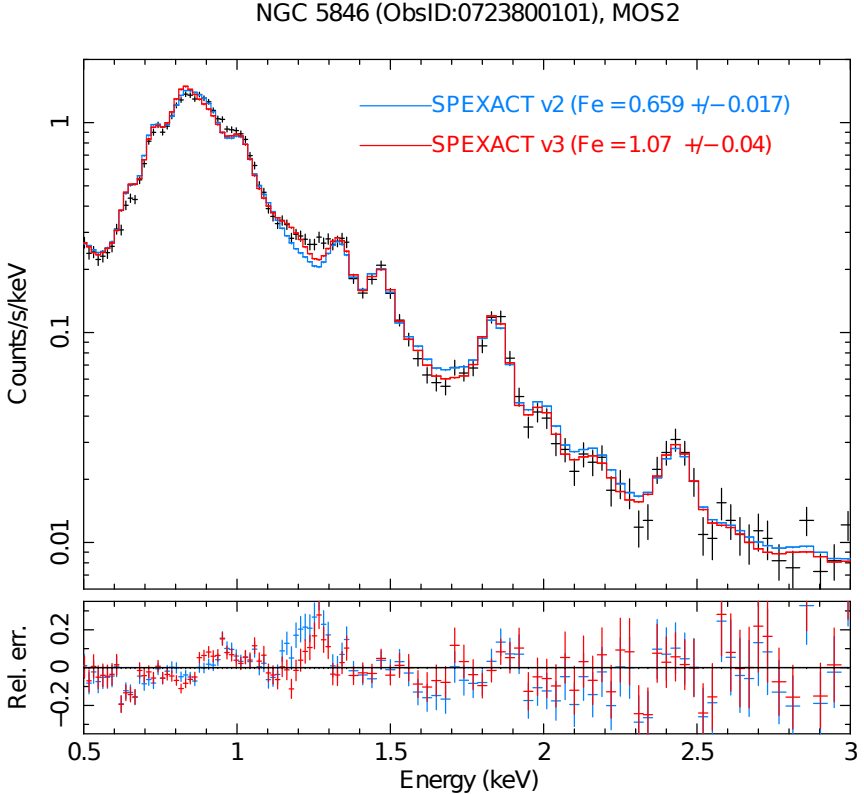


Figure 5.3: EPIC MOS 2 spectrum of NGC 5846 (ObsID:0723800101). The data are fitted with a `gdem` model, using successively the SPEXACT v2 and the SPEXACT v3 tables and routines.

complex may lead to large discrepancies in the measured Fe abundance measurements (up to a factor of 2), we conclude that the Fe abundance in NGC 5846 and other cool systems cannot be further constrained, at least within a factor of 2 of uncertainty.

To sum up, we have demonstrated that very small changes in the (unresolved) shape of the Fe-L complex may lead to dramatic biases of the Fe abundance in cool ($kT \lesssim 1$ keV) plasmas. Since the CIE models calculated by `apc`, SPEXACT v2 and SPEXACT v3 fail to reproduce thoroughly the Fe-L complex in EPIC spectra, we conclude regrettably that the Fe abundance measured with CCD instruments in cool groups and/or ellipticals is highly uncertain. For this reason, in the following we choose to exclude

all the objects of the CHEERS sample exhibiting lower central temperatures than 1 keV (14 objects), leaving us with 30 hotter objects ($1 \text{ keV} \leq kT_{\text{mean}} \leq 7 \text{ keV}$) for which the measured abundances are much better constrained.

Finally, it should be noted that this Fe bias reported in cool plasmas may have a considerable impact on the interpretation of the ICM temperature-metallicity relation discussed in several previous studies. We tackle this aspect in Sect. 5.4.1.

5.3.2 The Ni bias

Another striking feature from Fig. 5.1 is the overestimate of the Ni abundance by SPEXACT v2 compared to SPEXACT v3. Since the Ni abundance is estimated from the Ni-K complex ($\sim 7.8 \text{ keV}$) only, it is instructive to compare the old and new spectral models in this energy window. Such a comparison is shown for a moderately hot ($kT = 3 \text{ keV}$) plasma in Fig. 5.4. In both models, all the abundances are set to the proto-solar unity. Within this energy band ($\sim 7.5\text{--}8 \text{ keV}$), only Fe and Ni ions produce emission lines. We separate the transitions of these two elements in the upper and lower panels, respectively.

Although the emissivities of many Ni lines have been notably revised with the latest update of SPEXACT, we note that the overall equivalent width of all the Ni-K lines remain comparable between SPEXACT v2 and SPEXACT v3 (Fig. 5.4 bottom). On the contrary, while the older version includes only one Fe transition in the Ni-K complex (Fe XXV at $\sim 7.88 \text{ keV}$), SPEXACT v3 shows that many more Fe lines (mostly from Fe XXIII, Fe XXIV, and Fe XXV) contaminate this energy band (Fig. 5.4 top). Assuming that SPEXACT v3 reproduces realistically all the transitions that contribute to the Ni-K bump observed with EPIC, the high Ni/Fe abundance ratio measured in Chapter 3 can be naturally explained. Indeed, in order to compensate for the total equivalent width of the unaccounted Fe lines in the Ni-K complex, the SPEXACT v2 models incorrectly raises the Ni parameter until it fully fits the Ni-K bump.

Of course, as already detailed in Chapter 3, other biases may affect the Ni abundance estimate. In particular, the large discrepancy between MOS and pn measurements suggests that the Ni/Fe ratio is very sensitive to the instrumental background. In fact, we note the presence of an instrumental line at the location of the Ni-K complex, which may explain the inconsistent values between MOS and pn. Nevertheless, the large error bars adopted in Chapter 3 and in this work (Sect. 5.3.3) cover such discrepancies and make

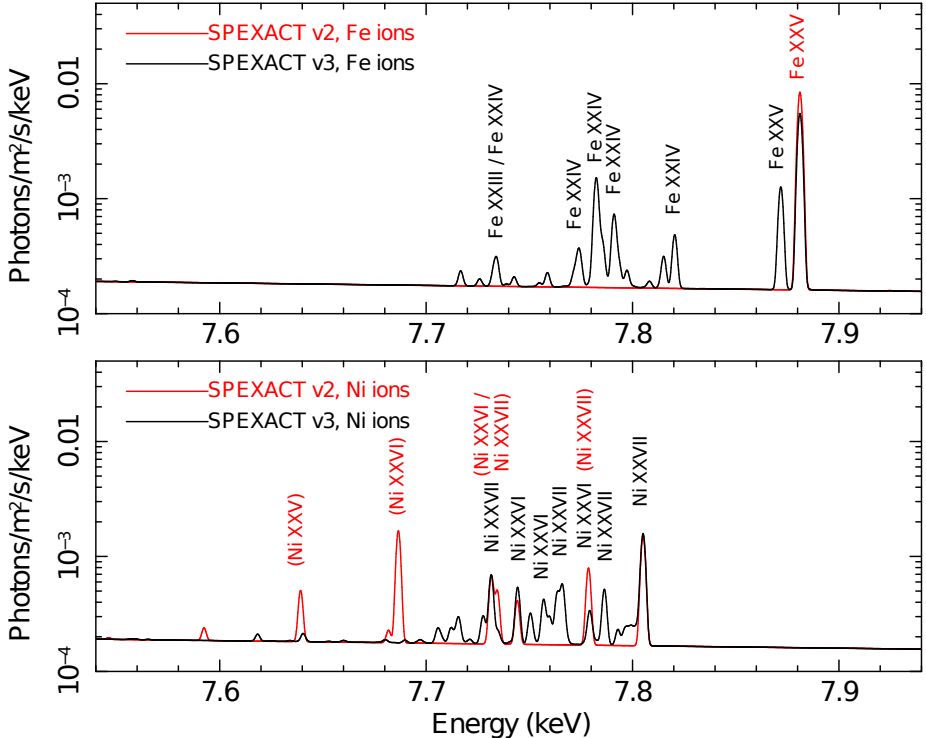


Figure 5.4: Comparison between SPEXACT v2 and SPEXACT v3 models for a $kT = 3$ keV plasma, zoomed on the Ni-K complex (~ 7.5 – 8 keV). The transitions of the Fe and Ni ions are shown separately in the upper and lower panels, respectively. The transitions of other elements do not occur in this band.

our final estimates conservative.

5.3.3 Updated average abundance ratios

We now apply the SPEXACT v2–v3 correction factors (Sect. 5.2.2) on each individual observation, before averaging the results. This is done following the same procedure as described in Chapter 3. As explained in Sect. 5.3.1, we exclude the 14 coolest systems from the rest of the analysis.

Similarly to our previous results, we do not see any correlation between the updated individual X/Fe ratios and the central temperatures of the systems. Instead, and keeping in mind they may be affected by an intrinsic scatter, the X/Fe distributions remain fairly uniform within the considered

temperature range (\sim 1–7 keV). This agrees with our previous conclusions that the relative SNIa to SNcc enrichment do not (or very poorly) depend on the temperature (and, by extension, the mass) of the systems, and that the enrichment mechanisms at play in ellipticals, galaxy groups and clusters must be quite similar (Chapter 3, see also De Grandi & Molendi 2009). This also means that our attempt to average the X/Fe abundance ratios in the ICM is fully relevant.

The updated average X/Fe abundance ratios and their respective statistical (σ_{stat}) and systematic uncertainties are listed in Table 5.2. This table can thus be directly compared with Table 3.2 of Chapter 3, to which we refer the reader for an extensive description of the estimated systematic uncertainties — σ_{int} (the intrinsic scatter), σ_{region} (the uncertainty related to the different size of the extraction regions), and $\sigma_{\text{cross-cal}}$ (the uncertainty in the cross-calibration of the different instruments). All the uncertainties are added in quadrature to obtain σ_{tot} , our total estimated uncertainties. Evidently, improvements in the spectral models have no impact on the discrepancies in the measurements made by the different instruments. Therefore, the Ar/Fe and Ni/Fe abundance ratios still suffer from consequent additional cross-calibration uncertainties, which we take into account in our final estimates.

The updated average ICM abundance pattern is also shown in Fig. 5.5, together with the comparison of our previous estimates from Chapter 3 (i.e. the full sample, fitted with SPEXACT v2). It clearly appears that, for most ratios, the changes are quite small. In particular, although the Mg bias appears to be quite important in Fig. 5.1, we note that Mg is more accurately determined in cooler gas. Therefore, and because the individual Mg/Fe ratios are affected by a non-negligible scatter, the updated average Mg/Fe ratio remains fully consistent with its old estimate. Some attention, however, should be devoted to Si/Fe and S/Fe, as these ratios are slightly revised upwards (of \sim 21% and \sim 12%, respectively). Contrary to Mg, the Si and S abundances are easier to constrain in hot plasmas, and their average respective X/Fe ratios are thus weighted toward hot systems, where the SPEX v2–v3 corrections are the most important. Another noticeable change is seen on the Ni/Fe ratio, for which our new value is \sim 28% lower than the old one. Although the (large) total uncertainties of our two Ni/Fe measurements are formally consistent with each other, we will see in Sect. 5.4 that such a change has a substantial impact in the selection of specific SNIa yield models to explain the ICM enrichment.

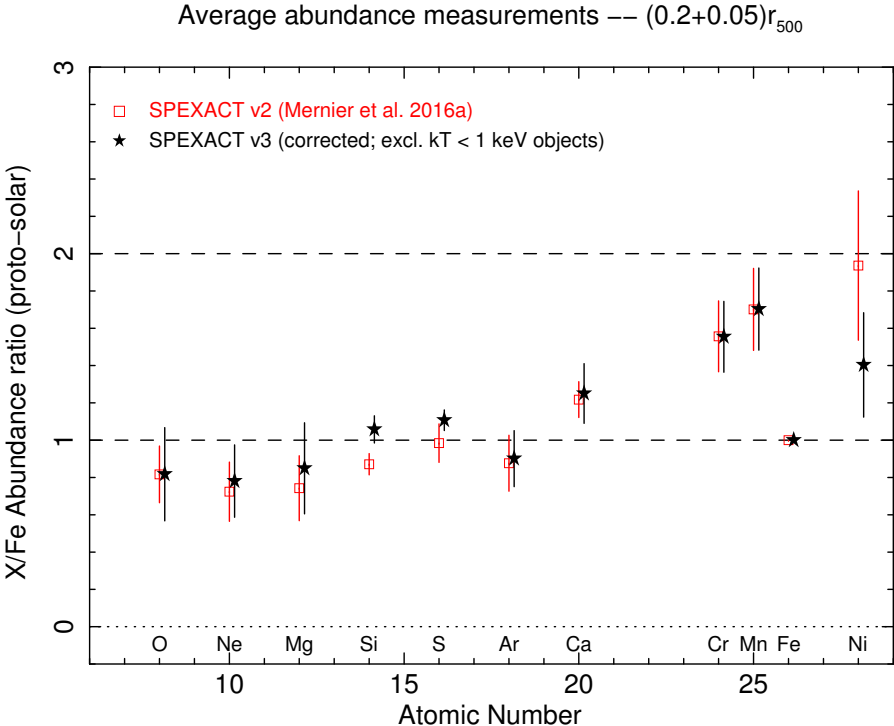


Figure 5.5: Average abundance ratios in our $(0.05+0.2)r_{500}$ sample, and their total statistical and systematic uncertainties (σ_{tot}). The red empty squares show our previous estimates (using SPEXACT v2; see Chapter 3), while the black filled stars show our updated measurements, after we apply the SPEXACT v2–v3 correction factors and exclude the 14 coolest systems (see text).

5.4 Discussion

5.4.1 Implications for the iron content in groups and clusters

As we have shown that the Fe abundance may be severely biased for low temperature objects, we may need to revise the relation between the Fe content versus the temperature (or, indirectly, the mass) of the systems. Several previous studies noted that groups appear significantly less Fe-enriched than clusters (e.g. Rasmussen & Ponman 2009; Sun 2012). This picture has also been supported by our previous results (see Fig. 3.1) and by Yates et al. (2017), who compiled many temperature and metallicity measurements from the literature within consistent radii. From a theoretical perspective,

Table 5.2: Average abundance ratios re-estimated from the $(0.05 + 0.2)r_{500}$ sample (using the SPEXACT v2–v3 correction factors and excluding the $kT < 1$ keV objects), as well as their statistical, systematic, and total uncertainties. An absence of value (–) means that no further uncertainty was required.

Element	Mean value	σ_{stat}	σ_{int}	σ_{region}	$\sigma_{\text{cross-cal}}$	σ_{tot}
O/Fe	0.818	0.021	0.200 ± 0.049	–	–	0.250
Ne/Fe	0.78	0.04	(< 0.19)	–	–	0.194
Mg/Fe	0.849	0.013	0.206 ± 0.038	–	–	0.244
Si/Fe	1.058	0.019	(< 0.051)	0.049	–	0.073
S/Fe	1.107	0.016	(< 0.053)	–	–	0.055
Ar/Fe	0.90	0.03	(< 0.04)	0.09	0.11	0.15
Ca/Fe	1.25	0.03	0.11 ± 0.5	–	–	0.16
Cr/Fe	1.56	0.19	–	–	–	0.19
Mn/Fe	1.70	0.22	–	–	–	0.22
Ni/Fe	1.40	0.08	–	–	0.27	0.28

however, this trend is not trivial to explain. For example, when comparing the observational trend with a semi-analytic model, Yates et al. (2017) did not succeed to reproduce such an increase of metallicity with temperature in groups and ellipticals. Instead, the metal content in low-mass systems is systematically overestimated by their model (however, see Liang et al. 2016).

In this context, and from the results presented in this work (Sect. 5.3.1), two main outcomes should be emphasised: (i) for $1 \text{ keV} \lesssim kT_{\text{mean}} \lesssim 1.7 \text{ keV}$ plasmas, updated SPEXACT calculations significantly revise up the Fe abundance (based on the dominant Fe-L complex); and (ii) for very cool groups and ellipticals ($\lesssim 1 \text{ keV}$), even the most updated atomic codes cannot well reproduce the shape of the Fe-L complex, resulting in too much uncertainty on their Fe content.

The first outcome is interesting, as it suggests that spectral code uncertainties may explain the apparent deficit of metals measured in less massive systems. To better quantify this scenario, we apply the SPEXACT v2–v3 corrections on the Fe abundance of all the 30 selected ($kT_{\text{mean}} > 1 \text{ keV}$) objects of our sample, and we compare their distribution for clusters ($> 1.7 \text{ keV}$) and groups ($< 1.7 \text{ keV}$) separately (Fig. 5.6). While a similar compari-

son from Chapter 3 (Fig. 3.3) argued in favour of a deficit of metals in the cooler groups, our present results suggest that cluster and group cores may be equally enriched.

This updated trend appears to better match (at least qualitatively) the model predictions of Yates et al. (2017). If further confirmed, this result is potentially important, as it suggests that significant metal removal in group cores (by either stellar or AGN feedback), as usually invoked so far (e.g. Rasmussen & Ponman 2009), may not be necessary. Unfortunately, the situation is still unclear and prevents us to draw any firm conclusion, mainly for three reasons:

1. In the updated comparison between cluster and group metallicities presented here, only 7 groups are comprised within $1 \text{ keV} < kT_{\text{mean}} < 1.7 \text{ keV}$, preventing us from establishing a robust study over a reasonable number of nearby groups;
2. As shown in Sect. 5.3.1, the Fe abundance of the systems with $kT_{\text{mean}} < 1 \text{ keV}$ cannot be robustly constrained even with current spectral models;
3. The measurements on group metallicities made in previous studies are from various versions of SPEX and/or apec models, and can thus hardly be compiled and compared in a consistent way.

In conclusion, although we propose the intriguing possibility that the lack of metals observed in less massive systems might be entirely due to a bias in the spectral models, we stress that this astrophysical question is not yet solved. Synergy between further observations of galaxy groups (for which the Fe abundance is measured consistently) and improvements in CIE plasma models and atomic codes will help to clarify the picture of the metal content in clusters and groups.

In addition to the Fe bias discussed in this work, we also note from Table 5.1 that fitting the spectra of cool systems with outdated plasma codes may also bias high the emission measure and the temperature by $\sim 24\%$ and $\sim 7\%$, respectively. In turn, these biases may have consequences on the estimates of further interesting quantities. For instance, based on our test described in Sect. 5.3.1, we estimated that the ICM pressure, usually defined as $P = n_e kT$ can be biased high by $\sim 19\%$ in the case of a $\sim 0.7 \text{ keV}$ plasma. Unlike the pressure, the ICM entropy, usually defined as $K = kT/n_e^{2/3}$, remains very close to its true value, with a underestimate of less than $\sim 1\%$.

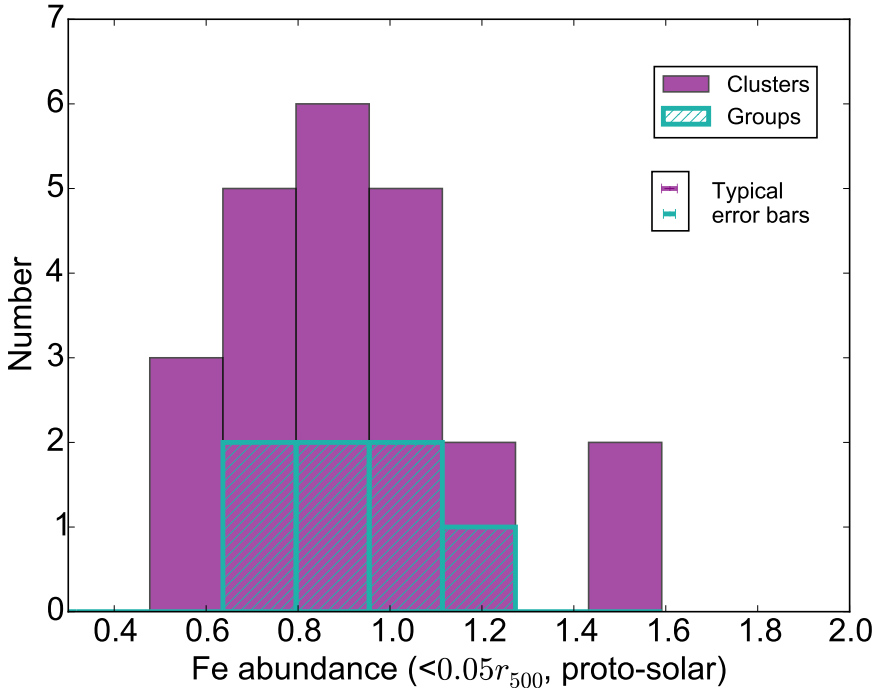


Figure 5.6: Histograms showing the Fe abundance distribution in groups and clusters. The typical error bars on the Fe abundances in each subsample are also indicated.

5.4.2 Implications for supernovae yield models

In Sect. 5.3.3, we have presented the average ICM abundance ratios as estimated when updating the spectral models to the new SPEXACT (v3). We have emphasised a couple of interesting changes and effects from the previous measurements using SPEXACT v2 (Chapter 3). In this section, we interpret the updated ICM abundance pattern in terms of ICM enrichment by SNIa and SNcc, and explore the consequences of our new measurements in favouring specific SN models.

The full method used for testing and interpreting SNIa and SNcc models is extensively described in Chapter 4, to which we refer the reader for more details. In summary, we use the least squares method to fit our ICM abundance pattern with the combination of one SNIa and one SNcc yield model. Among the SN yield models we employ (the full list and their corresponding acronyms are listed in Table 4.5, we can distinguish:

1. The SNcc models of Nomoto et al. (2013, "Nomoto"), that we average over a Salpeter IMF (Salpeter 1955) between 10–40 M_{\odot} . Each model assumes a different initial metallicity Z_{init} (0, 0.001, 0.004, 0.008, or 0.02).
2. The SNIa models of Iwamoto et al. (1999, one dimensional deflagration and delayed-detonation, "Classical"), Bravo et al. (1996, one dimensional delayed-detonation, "Bravo"), Maeda et al. (2010, two dimensional deflagration and delayed-detonation, "2D"), Seitzenzahl et al. (2013b, three dimensional delayed-detonation, "3D"), and Fink et al. (2014, three dimensional deflagration, "3D").

Table 5.3 reports the combinations of the one-dimensional models providing the best fits to our updated abundance pattern. In each case, only the five best combinations are listed. Our method also allows to estimate the enriching fraction of SNIa over the total number of SNe, namely $\frac{\text{SNIa}}{\text{SNIa} + \text{SNcc}}$ (see Chapter 4 for more details). Table 5.3 can be directly compared to Table 4.1 of Chapter 4, where the old (SPEXACT v2) abundance ratios were taken as a reference. Back to that study, we encountered problems in recovering the Ca/Fe ratio, as the latter was systematically underestimated in the case of any "Nomoto+Classical" combination. We also showed that the Ca/Fe ratio can be better recovered if we use a Bravo instead of a Classical model as the SNIa enriching contribution (see also de Plaa et al. 2007). As Badenes et al. (2006) demonstrated that the Bravo DDTa, DDTc, and DDTe models successfully reproduce most of the spectral features of the Tycho SN remnant, these models are believed to be as realistic as the Classical ones. Alternatively, the excess of Ca might come from the Ca-rich gap transients. These recently discovered SNIa usually explode far away from their galaxy host and are particularly efficient in releasing Ca via their ejecta (see also Mulchaey et al. 2014). The latter possibility has been tested in Chapter 4 by adopting the Ca-rich gap transient nucleosynthesis models of Waldman et al. (2011) as an additional component to the previous SNIa+SNcc combinations. Among these, we systematically adopted the CO.5HE.2C.3 model, because it successfully reproduced our measured Ca/Fe ratio while keeping the enriching fraction of Ca-rich SNe over the total number of SNIa consistent with current observations (<20%; Perets et al. 2010; Li et al. 2011; Mulchaey et al. 2014). Since our updated Ca/Fe ratio is measured very close to the old one (albeit with a slightly larger total uncertainty), the whole picture described in Chapter 4 is very similar to

Table 5.3: Results of various combinations of (one-dimensional) SN fits to the average ICM abundance pattern (see Chapter 4 for details). In each case, only one SNcc model has been fitted ($Z_{\text{init}} = 0, 0.001, 0.004, 0.008, \text{ or } 0.02$; Salpeter IMF), and we only show the five best fits, sorted by increasing $\chi^2/\text{d.o.f.}$ (degrees of freedom). The choice of the CO.5HE.2C.3 model, indicated by a (*), has been fixed (see text).

SNcc	SNIa	$\frac{\text{SNIa}}{\text{SNIa+SNcc}}$	$\frac{\text{SNIa(Ca)}}{\text{SNIa}}$	$\chi^2/\text{d.o.f.}$
Nomoto	Classical	—		
Z0.008	WDD2	0.27	—	6.7/8
Z0.004	WDD2	0.29	—	6.9/8
Z0.004	CDD2	0.27	—	7.0/8
Z0.008	CDD2	0.26	—	7.7/8
Z0.02	WDD2	0.25	—	8.9/8
Nomoto	Bravo	—		
Z0.004	DDTc	0.30	—	6.4/8
Z0.008	DDTc	0.28	—	6.5/8
Z0_cut	DDTc	0.28	—	8.4/8
Z0.02	DDTc	0.26	—	9.0/8
Z0.001	DDTc	0.32	—	10.4/8
Nomoto	Classical	Ca-rich gap		
Z0.008	WDD2	CO.5HE.2C.3(*)	0.08	3.1/7
Z0.004	WDD2	CO.5HE.2C.3(*)	0.07	3.5/7
Z0.004	CDD2	CO.5HE.2C.3(*)	0.08	3.6/7
Z0.008	CDD2	CO.5HE.2C.3(*)	0.09	4.0/7
Z0.02	WDD2	CO.5HE.2C.3(*)	0.10	4.6/7

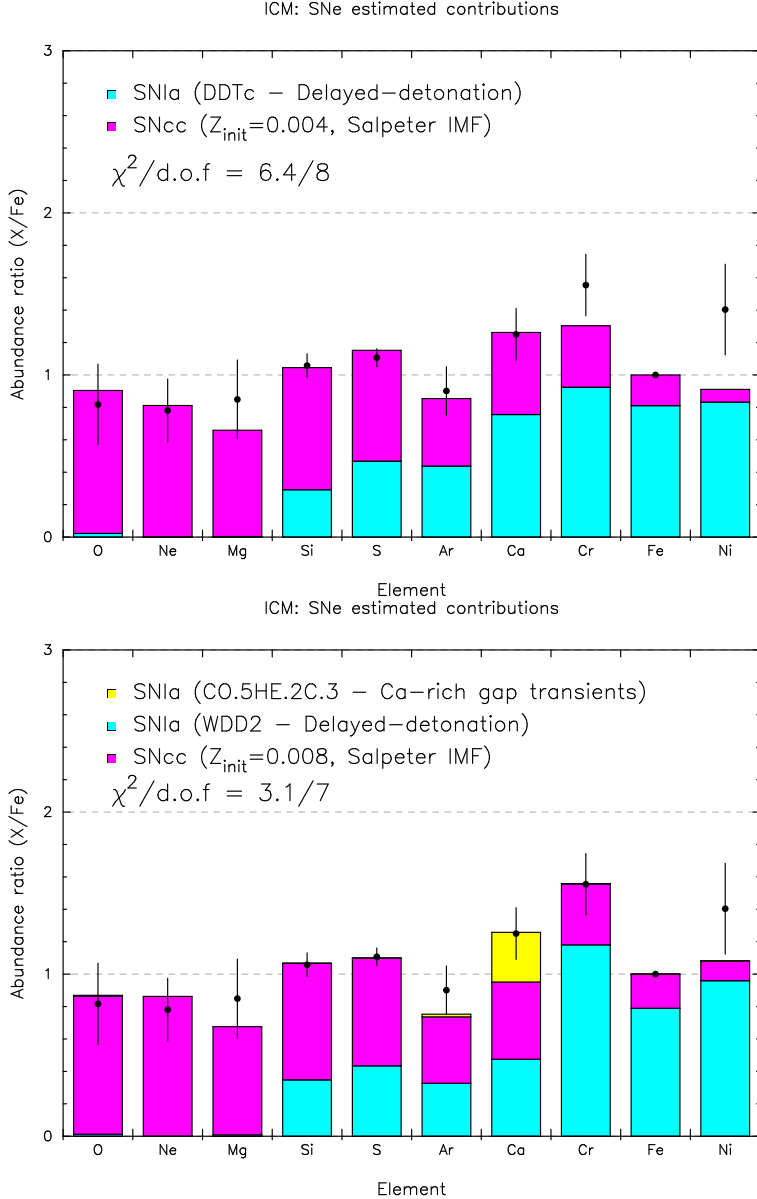


Figure 5.7: Average abundance ratios versus atomic numbers in the average ICM abundance pattern (Chapter 4). The histograms show the yields contribution of a best-fit combination SNIA and SNcc models. *Top:* The SNIA model is a Bravo model (see text and Chapter 4). *Bottom:* The SNIA model is a Classical model. To reproduce successfully the Ca/Fe ratio, we add a Ca-rich gap model (see text and Chapter 4).

Table 5.4: Same as Table 5.3, but considering 2-D SNIa models instead of the 1-D Classical SNIa models.

SNcc	SNIa		$\frac{\text{SNIa}}{\text{SNIa} + \text{SNcc}}$	$\frac{\text{SNIa(Ca)}}{\text{SNIa}}$	$\chi^2/\text{d.o.f.}$
Nomoto	2D	—			
Z0.02	O-DDT		0.30	—	22.3/8
Z0.001	O-DDT		0.36	—	23.5/8
Z0.008	O-DDT		0.32	—	27.8/8
Z0.004	O-DDT		0.33	—	33.0/8
Z0_cut	O-DDT		0.32	—	43.1/8
Nomoto	2D	Ca-rich gap			
Z0.02	O-DDT	CO.5HE.2C.3(*)	0.33	0.10	12.5/7
Z0.001	O-DDT	CO.5HE.2C.3(*)	0.40	0.09	13.6/7
Z0.008	O-DDT	CO.5HE.2C.3(*)	0.35	0.08	18.1/7
Z0.004	O-DDT	CO.5HE.2C.3(*)	0.37	0.08	23.2/7
Z0_cut	O-DDT	CO.5HE.2C.3(*)	0.36	0.08	31.1/7

our present results. The best one-dimensional fits incorporating a solution to the Ca/Fe (i.e. the Nomoto+Bravo and Nomoto+Classical+Ca-rich gap combinations) are shown in Fig. 5.7.

What has substantially changed, however, is the Ni/Fe ratio and its consequent interpretation. In Chapter 4, we showed that the high measured value of Ni/Fe (1.93 ± 0.40) could not be conciliated with any of the model combinations, unless we assumed that both deflagration and delayed-detonation SNIa coexist and enrich the ICM in similar proportions. From Fig. 5.7, it clearly appears that the lower Ni/Fe ratio is now much closer to the simple model predictions. Table 5.7 shows that, unlike our previous results (see Table 4.1), the fits are now formally acceptable, and no additional SNIa contribution is necessary. In particular, it is worth noting that the fits systematically favour the delayed-detonation explosions.

Table 5.4 and the upper panel of Fig. 5.8 report similar results, this time when adopting 2D models for the SNIa yields. Finally, Table 5.5 and the lower panel of Fig. 5.8 show the best-fit combinations when adopting 3D models for the SNIa yields. Here again, except the fact that Ni/Fe is now well consistent with the model predictions, we do not observe notable

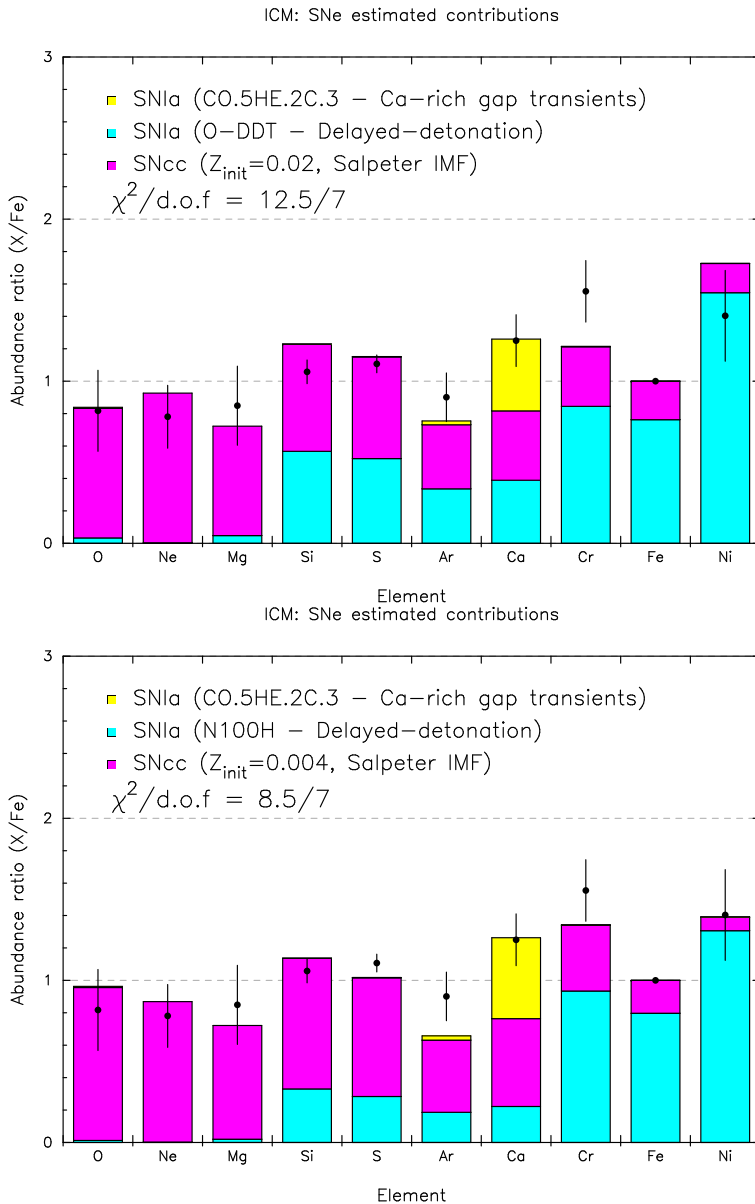


Figure 5.8: Top: Same as Fig. 5.7 (top right), but considering a 2-D SNIa model instead of a Classical SNIa model. Bottom: Same as Fig. 5.7 (top right), but considering a 3-D SNIa model instead of a Classical SNIa model.

Table 5.5: Same as Table 5.3, but considering 3-D SNIa models instead of the 1-D Classical SNIa models.

SNcc	SNIa		$\frac{\text{SNIa}}{\text{SNIa} + \text{SNcc}}$	$\frac{\text{SNIa(Ca)}}{\text{SNIa}}$	$\chi^2/\text{d.o.f.}$
Nomoto	3D	—			
Z0.004	N100H		0.25	—	16.9/8
Z0.008	N100H		0.23	—	18.5/8
Z0.02	N150		0.27	—	20.6/8
Z0.008	N150		0.29	—	21.8/8
Z0_cut	N100H		0.23	—	22.0/8
Nomoto	3D	Ca-rich gap			
Z0.004	N100H	CO.5HE.2C.3(*)	0.29	0.14	8.5/7
Z0.008	N100H	CO.5HE.2C.3(*)	0.28	0.15	10.0/7
Z0.02	N150	CO.5HE.2C.3(*)	0.32	0.12	10.1/7
Z0_cut	N100H	CO.5HE.2C.3(*)	0.28	0.14	10.9/7
Z0.008	N150	CO.5HE.2C.3(*)	0.33	0.11	11.6/7

changes from the corresponding results in Chapter 4 (Tables 4.2 and 4.3). In this case as well, the delayed-detonation scenario is the explosion channel that is favoured by our results. Interestingly, these fits are slightly worse than when adopting one-dimensional (Classical or Bravo) SNIa models. As discussed in Chapter 4, this is mainly due to the significant overestimate of Si predicted by these multi-dimensional models. This larger tension between our data and the most recent and complete SN yield models clearly emphasises the efforts that have to be pursued in modelling SN yields — together with cluster data and SN observations — in order to provide further constraints on the physics of SNe, as well as their relative role in enriching the ICM.

5.5 Conclusions

In this work, we have investigated how the updated version of the CIE models in SPEX affects the abundances that are measured using *XMM-Newton* EPIC spectra. Based on mock EPIC spectra simulated assuming a SPEXACT v3 CIE plasma model and fitted with its SPEXACT v2 equivalent version on a grid of various temperatures, we have estimated the correc-

tion factors that should be applied to the EPIC abundances initially measured using the old SPEX versions. After having corrected accordingly the abundance estimates from Chapter 3, we have obtained updated estimates of the average X/Fe ratios in the ICM, which we have compared to nucleosynthesis models following Chapter 4. Our results can be summarised as follows.

- For hot (>1.7 keV) plasmas, the Fe abundance measured with SPEXACT v3 is in excellent agreement with the previous estimates obtained using SPEXACT v2. For cool plasmas, in which the Fe abundance is mostly determined by fitting the Fe-L complex (unresolved with CCD-like instruments), we observe a substantial discrepancy between the old (SPEXACT v2) and the new (SPEXACT v3) measurements. This bias can reach up to a factor of 2 for $kT \simeq 0.6$ keV. After a careful investigation on real EPIC spectra from the coolest objects of the CHEERS sample, we confirm that the combined effect of the emission measure and the Fe abundance parameters used to fit the Fe-L complex leads to a large Fe bias, even though SPEXACT v2 and SPEXACT v3 eventually provide similar best-fit qualities. Since even the up-to-date plasma codes do not well reproduce the shape of the Fe-L complex in the coolest ($\lesssim 1$ keV) systems, we conclude that their Fe abundances are still highly uncertain. Besides, we propose that this newly discovered Fe bias might explain the lower gas-phase metallicity previously observed in groups and ellipticals, and which has been difficult to conciliate with predictions so far (e.g. Rasmussen & Ponman 2009; Yates et al. 2017). Similarly, spectral model improvements may also slightly affect the gas density, temperature, and pressure measurements of low-mass systems. The impact on the entropy measurement, however, is more limited.
- If we restrict our results to ≥ 1 keV systems (see above), we find that the spectral model uncertainties on the Si, S, Ar, and Ca abundances are always less than $\sim 20\%$. Consequently, their respective X/Fe ratios averaged over the 30 hottest objects sample are very close to the previous estimates from Chapter 3, with a $>1\sigma$ discrepancy observed only in Si/Fe (because of the very limited total uncertainties affecting this ratio). While there is a large difference in the Mg abundance estimate between SPEXACT v2 and SPEXACT v3 for high temperature plasmas, the Mg/Fe ratio is better constrained in cooler objects.

This, together with the large intrinsic scatter affecting the individual Mg/Fe measurements, explains why the Mg/Fe ratio averaged over the sample does not change significantly.

- Unlike the other elements, spectral model improvements have a considerable impact on the individual and average Ni/Fe ratios, as well as on its interpretation in terms of ICM enrichment by SNIa. Because the Ni-K complex at ~ 7.8 keV contains several Fe XXIII, Fe XXIV, and Fe XXV transitions that were not included in SPEXACT v2, previous fits of cluster spectra overestimated the Ni/Fe ratio by $\sim 40\%$ on average. Whereas the previous average Ni/Fe estimate could only be reproduced by SN yield models when invoking a diversity in the explosion channels of SNIa (Chapter 4), such an assumption is not necessary anymore. The whole ICM abundance pattern now highly favours delayed-detonation as the dominant (and perhaps exclusive) explosion channel of SNIa.
- Except SNIa explosion model(s), we do not observe other noticeable changes from the conclusions made in Chapter 4. Our results still suggest that the enriching ratio of SNIa over the total number of SNe ranges within ~ 0.23 – 0.40 , and that the SNcc having enriched the ICM had been previously enriched by a former generation of massive stars. Finally, we highlight the fact that compared to outdated one-dimensional calculations (Iwamoto et al. 1999), updated two- and three-dimensional SNIa yield models (Seitenzahl et al. 2013b; Fink et al. 2014; Maeda et al. 2010) are less successful in reproducing our average ICM abundance pattern. This should be a source of motivation to keep improving both spectral plasma models and predictions for SNIa and SNcc yields in the upcoming years.

Acknowledgements

This work is partly based on the XMM-Newton AO-12 proposal “*The XMM-Newton view of chemical enrichment in bright galaxy clusters and groups*” (PI: de Plaa), and is a part of the CHEERS (CHEmical Evolution Rgs cluster Sample) collaboration. This work is based on observations obtained with XMM-Newton, an ESA science mission with instruments and contributions directly funded by ESA member states and the USA (NASA). The SRON

Netherlands Institute for Space Research is supported financially by NWO,
the Netherlands Organisation for Scientific Research.

You don't have to see the whole staircase, just take the first step.

– Martin Luther King Jr.

6

Radial metal abundance profiles in the intra-cluster medium of cool-core galaxy clusters, groups, and ellipticals

F. Mernier, J. de Plaa, J. S. Kaastra, Y.-Y. Zhang¹, H. Akamatsu, L. Gu, P. Kosec, J. Mao, C. Pinto, T. H. Reiprich, J. S. Sanders, A. Simionescu, and N. Werner

(Astronomy & Astrophysics, in press, arXiv:1703.01183)

Abstract

The hot intra-cluster medium (ICM) permeating galaxy clusters and groups is not pristine, as it has been continuously enriched by metals synthesised in Type Ia (SNIa) and core-collapse (SNcc) supernovae since the major epoch of star formation ($z \simeq 2\text{--}3$). The cluster/group enrichment history and mechanisms responsible for releasing and mixing the metals can be probed via the radial distribution of SNIa and SNcc products within the ICM. In this paper, we use deep XMM-Newton/EPIC observations from a sample of 44 nearby cool-core galaxy clusters, groups, and ellipticals (CHEERS) to constrain the average radial O, Mg, Si, S, Ar, Ca, Fe, and Ni abundance profiles. The radial distributions of all these elements, averaged over a large sample for the first time, represent the best constrained profiles available currently. Specific attention is devoted to a proper modelling of the EPIC spectral components, and to other systematic uncertainties that may affect our results. We find an overall decrease of the Fe abundance with radius out to $\sim 0.9r_{500}$ and $\sim 0.6r_{500}$ for clusters and groups, respectively, in good agreement with predictions from the most recent hydrodynamical simulations. The average

¹This paper is dedicated to the memory of our wonderful colleague Yu-Ying Zhang, who passed away on December 11, 2016.

radial profiles of all the other elements (X) are also centrally peaked and, when rescaled to their average central X/Fe ratios, follow well the Fe profile out to at least $\sim 0.5r_{500}$. As predicted by recent simulations, we find that the relative contribution of SNIa (SNcc) to the total ICM enrichment is consistent with being uniform at all radii, both for clusters and groups using two sets of SNIa and SNcc yield models that reproduce the X/Fe abundance pattern in the core well. In addition to implying that the central metal peak is balanced between SNIa and SNcc, our results suggest that the enriching SNIa and SNcc products must share the same origin and that the delay between the bulk of the SNIa and SNcc explosions must be shorter than the timescale necessary to diffuse out the metals. Finally, we report an apparent abundance drop in the very core of 14 systems ($\sim 32\%$ of the sample). Possible origins of these drops are discussed.

6.1 Introduction

Galaxy clusters and groups are more than a simple collection of galaxies (and dark matter haloes), as they are permeated by large amounts of very hot gas. This intra-cluster medium (ICM) was heated up to 10^7 – 10^8 K during the gravitational assembly of these systems, and is glowing in the X-ray band, mainly via bremsstrahlung emission, radiative recombination, and line radiation (for a review, see Böhringer & Werner 2010). Since the first detection of a Fe-K emission feature at ~ 7 keV in its X-ray spectra (Mitchell et al. 1976; Serlemitsos et al. 1977), it is well established that the ICM does not have a primordial origin, but has been enriched with heavy elements, or metals, up to typical values of ~ 0.5 – 1 times solar (for reviews, see Werner et al. 2008; de Plaa 2013). Since the ICM represents about $\sim 80\%$ of the total baryonic matter in clusters, this means that there is more mass in metals in the ICM than locked in all the cluster galaxies (e.g. Renzini & Andreon 2014).

Despite the first detection of several K-shell metal lines with the *Einstein* observatory in the early 1980s (e.g. Canizares et al. 1979; Mushotzky et al. 1981), before 1993 only the iron (Fe) abundance could be accurately measured in the ICM. After the launch of *ASCA*, abundance studies in clusters could extend (although with a limited accuracy) to oxygen (O), neon (Ne), magnesium (Mg), silicon (Si), sulfur (S), argon (Ar), calcium (Ca), and nickel (Ni), thus opening a new window on the ICM enrichment (e.g. Mushotzky et al. 1996; Baumgartner et al. 2005). However, the most spectacular step forward in the field has been achieved by the latest generation of X-ray observatories, i.e. *Chandra*, *XMM-Newton*, and *Suzaku*, which al-

lowed much more accurate abundance measurements of these elements thanks to the significantly improved effective area and spectral resolution of their instruments (e.g. Tamura et al. 2001; de Plaa et al. 2006; Werner et al. 2006a). With excellent *Suzaku* and *XMM-Newton* exposures, the abundance of other elements, such as carbon, nitrogen (e.g. Werner et al. 2006a; Sanders & Fabian 2011, Mao et al. 2017, to be submitted), or even chromium and manganese (Tamura et al. 2009, see also Chapter 3), could be reasonably constrained as well.

Metals present in the ICM must have been synthesised by stars and supernovae (SNe) explosions, mainly within cluster galaxies. While O, Ne, and Mg are produced almost entirely by core-collapse supernovae (SNcc), the Fe-peak elements mostly originate from Type Ia supernovae (SNIa). Intermediate elements (e.g. Si, S, and Ar) are synthesised by both SNIa and SNcc (for a review, see Nomoto et al. 2013). Since the current X-ray missions allow the measurement of the abundance of all these elements with a good level of accuracy in the core of the ICM (i.e. where the overall flux and the metal line emissivities are the highest), several attempts have been made to use these abundances to provide constraints on SNIa and SNcc yield models in individual objects (e.g. Werner et al. 2006b; de Plaa et al. 2006; Bulbul et al. 2012a) or in samples (e.g. de Plaa et al. 2007; Sato et al. 2007a, and Chapter 4). From these studies, it appears that the typical fraction of SNIa (SNcc) contributing to the enrichment lies within $\sim 20\text{--}45\%$ (55–80%), depending (mainly) on the selected yield models.

Beyond the overall elemental abundances, witnessing the time-integrated enrichment history in galaxy clusters and groups since the major epoch of star formation ($z \simeq 2\text{--}3$; for a review, see Madau & Dickinson 2014) determining the distribution of metals within the ICM is also of crucial importance. Indeed, this metal distribution constitutes a direct signature of, first, the locations and epoch(s) of the enrichment and, second, the dominant mechanisms transporting the metals into and across the ICM. In turn, these transport mechanisms must also play a fundamental role in governing the thermodynamics of the hot gas. Since the *ASCA* discovery of a strong metallicity gradient in Centaurus (Allen & Fabian 1994; Fukazawa et al. 1994), a systematically peaked Fe distribution in cool-core clusters and groups (i.e. showing a strong ICM temperature decrease towards the centre) has been confirmed by many studies (e.g. Matsushita et al. 1997; De Grandi & Molendi 2001; Gastaldello & Molendi 2002; Thölken et al. 2016). On the contrary, non-cool-core clusters and groups (i.e. with no central

ICM temperature gradient) do not exhibit any clear Fe abundance gradient in their cores (De Grandi & Molendi 2001). It is likely that the Fe central excess in cool-core clusters has been produced predominantly by the stellar population of the brightest cluster galaxy (BCG) residing in the centre of the gravitational potential well of the cluster during or after the cluster assembly (Böhringer et al. 2004a; De Grandi et al. 2004). However, this excess is often significantly broader than the light profile of the BCG, suggesting that one or several mechanisms, such as turbulent diffusion (Rebusco et al. 2005, 2006) or active galactic nucleus (AGN) outbursts (e.g. Guo & Mathews 2010), may efficiently diffuse metals out of the cluster core. Alternatively, the higher concentration of Fe in the core of the ICM may be caused by the release of metals from infalling galaxies via ram-pressure stripping (Domainko et al. 2006) together with galactic winds (Kapferer et al. 2007, 2009). Other processes, such as galaxy-galaxy interactions, AGN outflows, or an efficient enrichment by intra-cluster stars, may also play a role (for a review, see Schindler & Diaferio 2008). In addition to this central excess, there is increasing evidence of a uniform Fe enrichment floor extending out to r_{200} ² and probably beyond (Fujita et al. 2008; Werner et al. 2013; Thölken et al. 2016). This suggests an additional early enrichment by promptly exploding SNIa, i.e. having occurred and efficiently diffused before the cluster formation. However, a precise quantification of this uniform level is difficult, since clusters outskirts are very dim and yet poorly understood (Molendi et al. 2016).

Whereas the ICM radial distribution of the Fe abundance (rather well constrained thanks to its Fe-K and Fe-L emission complexes, accessible to current X-ray telescopes) has been extensively studied in recent decades, the situation is much less clear for the other elements. Several studies report a rather flat O (and/or Mg) profile, or similarly, an increasing O/Fe (and/or Mg/Fe) ratio towards the outer regions of the cool-core ICM (e.g. Tamura et al. 2001; Matsushita et al. 2003; Tamura et al. 2004; Werner et al. 2006a). As for Fe, there are also indications of a positive and uniform Mg (and other SNcc products) enrichment out to r_{200} (Simionescu et al. 2015; Ezer et al. 2017). This apparent flat distribution of SNcc products, contrasting with the enhanced central enrichment from SNIa products, has led to the picture of an early ICM enrichment by SNcc (and prompt SNIa, see above), when galaxies underwent important episodes of star forma-

² r_Δ is defined as the radius within which the gas density corresponds to Δ times the critical density of the Universe.

tion. These metals would have mixed efficiently before the cluster assembled, contrary to delayed SNIa enrichment originating from the red and dead BCG. This picture, however, has been questioned by recent observations, suggesting centrally peaked O (and / or Mg) profiles instead (e.g. Matsushita et al. 2007; Sato et al. 2009; Simionescu et al. 2009b; Lovisari et al. 2011, and Chapter 2). The radial distribution of Si, produced by both SNIa and SNcc, is also unclear, as the Si/Fe profile has been reported to be sometimes flat, sometimes increasing with radius (e.g. Rasmussen & Ponman 2007; Lovisari et al. 2011; Million et al. 2011; Sasaki et al. 2014).

In all the studies referred to above, the O, Mg, Si, S, Ar, Ca, and Ni radial abundance profiles have been measured either for individual (mostly cool-core) objects or for very restricted samples (≤ 15 objects). Consequently, in most cases, these profiles suffer from large statistical uncertainties. In parallel, little attention has been drawn to systematic effects that could potentially bias some results. Building average abundance profiles (not only for Fe, but for all the other possible elements mentioned above) over a large sample of cool-core (and, if possible, non-cool-core) systems is clearly needed to clarify the picture of the SNIa and SNcc enrichment history in galaxy clusters and groups.

In this paper, we use deep *XMM-Newton*/EPIC observations from a sample of 44 nearby cool-core galaxy clusters, groups, and ellipticals to derive the average O, Mg, Si, S, Ar, Ca, Fe, and Ni abundance profiles in the ICM. In order to make our results as robust as possible, specific attention is devoted to understanding all the possible systematic biases and reducing them when possible. This paper is structured as follows. We describe the observations and our data reduction in Sect. 6.2, the adopted spectral modelling in Sect. 6.3, and the averaging of the individual profiles over the sample in Sect. 6.4. Our results, and an extensive discussion on the remaining systematic uncertainties, are presented in Sect. 6.5 and Sect. 6.6, respectively. We discuss the possible implications of our findings in Sect. 6.7 and conclude in Sect. 6.8. Throughout this paper, we adopt the cosmological parameters $H_0 = 70 \text{ km s}^{-1} \text{ Mpc}^{-1}$, $\Omega_m = 0.3$, and $\Omega_\Lambda = 0.7$. Unless otherwise stated, the error bars are given at 68% confidence level, and the abundances are given with respect to the proto-solar abundances of Lodders et al. (2009).

6.2 Observations and data preparation

All the observations considered here are taken from the CHEERS³ catalogue (de Plaa et al. 2017, Chapter 3). This sample, optimised to study chemical enrichment in the ICM, consists of 44 nearby cool-core galaxy clusters, groups, and ellipticals for which the O VIII 1s–2p line at ~ 19 is detected with $>5\sigma$ in their *XMM-Newton*/RGS spectra. This includes archival *XMM-Newton* data and several recent deep observations that were performed to complete the sample in a consistent way (de Plaa et al. 2017).

We reduce the EPIC MOS 1, MOS 2, and pn data using the XMM Science Analysis System (SAS) v14.0 and the calibration files dated by March 2015. The standard pipeline commands `emproc` and `epproc` are used to extract the event files from the EPIC MOS and pn data, respectively. We filter each observation from soft-flare events by applying the appropriate good time interval (GTI) files following the 2σ -clipping criterion (Chapter 2). After filtering, the MOS 1, MOS 2, and pn exposure times of the full sample are ~ 4.5 Ms, ~ 4.6 Ms, and ~ 3.7 Ms, respectively (see Table 3.1). Following the usual recommendations, we keep the single-, double- and quadruple-pixel events ($\text{pattern} \leq 12$) in MOS, and we only keep the single-pixel events in pn ($\text{pattern}=0$), since the pn double events may suffer from charge transfer inefficiency⁴. In both MOS and pn, only the highest quality events are selected (`flag=0`). The point sources are detected in four distinct energy bands (0.3–2 keV, 2–4.5 keV, 4.5–7.5 keV, and 7.5–12 keV) using the task `edetect_chain` and further rechecked by eye. We discard these point sources from the rest of the analysis, by excising a circular region of $10''$ of radius around their surface brightness peak. This radius is found to be the best compromise between minimising the fraction of contaminating photons from point sources and maximising the fraction of the ICM photons considered in our spectra (Chapter 2). In some specific cases, however, photons from very bright point sources may leak beyond $10''$, and consequently we adopt a larger excision radius.

In each dataset, we extract the MOS 1, MOS 2, and pn spectra of eight concentric annuli of fixed angular size ($0' - 0.5'$, $0.5' - 1'$, $1' - 2'$, $2' - 3'$, $3' - 4'$, $4' - 6'$, $6' - 9'$, and $9' - 12'$), all centred on the X-ray peak emission seen on the EPIC surface brightness images. The redistribution matrix file (RMF) and

³CHEMical Enrichment Rgs Sample

⁴See the *XMM-Newton* Current Calibration File Release Notes, XMM-CCF-REL-309 (Smith, Guainazzi & Saxton 2014).

the ancillary response file (ARF) of each spectrum are produced via the `rmfgen` and `arfgen` SAS tasks, respectively.

6.3 Spectral modelling

The spectral analysis is performed using the SPEX⁵ package (Kaastra et al. 1996), version 2.05. Following the method described in Chapter 3, we start by simultaneously fitting the MOS 1, MOS 2, and pn spectra of each pointing. When a target includes two separate observations, we fit their spectra simultaneously. Since the large number of fitting parameters does not allow us to fit more than two observations simultaneously, we form pairs of simultaneous fits when an object contains three (or more) observations. We then combine the results of the fitted pairs using a factor of $1/\sigma_i^2$, where σ_i is the error on the considered parameter i . We also note that the second EPIC observation of M 87 (ObsID:0200920101) is strongly affected by pile-up in its core, owing to a sudden activity of the central AGN (Werner et al. 2006a). Therefore, the radial profiles within 3' are only estimated with the first observation (ObsID:0114120101).

Because of calibration issues in the soft X-ray band of the CCDs ($\lesssim 0.5$ keV) and beyond ~ 10 keV, we limit our MOS and pn spectral fittings to the 0.5–10 keV and 0.6–10 keV energy bands, respectively. We rearrange the data bins in each spectrum via the optimal binning method of Kaastra & Bleeker (2016) to maximise the amount of information provided by the spectra while keeping reasonable constraints on the model parameters.

6.3.1 Thermal emission modelling

In principle, we can model the ICM emission in SPEX with the (redshifted and absorbed) `cie` thermal model. This single-temperature model assumes that the plasma is in (or close to) collisional ionisation equilibrium (CIE), which is a reasonable assumption (e.g. Sarazin 1986).

Although the `cie` model may be a good approximation of the emitting ICM in some specific cases (i.e. when the gas is nearly isothermal), the temperature structure within the core of clusters and groups is often complicated and a multi-temperature model is clearly required. In particular, fitting the spectra of a multi-phase plasma with a single-temperature model can dramatically affect the measured Fe abundance, leading to the

⁵<https://www.sron.nl/astrophysics-spex>

"Fe-bias" (Buote & Canizares 1994; Buote & Fabian 1998; Buote 2000) or to the "inverse Fe-bias" (Rasia et al. 2008; Simionescu et al. 2009b; Gastaldello et al. 2010). Taking this caveat into account, we model the ICM emission with a `gdem` model (e.g. de Plaa et al. 2006), which is also available in SPEX. This multi-temperature component models a CIE plasma following a Gaussian-shaped temperature distribution,

$$Y(x) = \frac{Y_0}{\sigma_T \sqrt{2\pi}} \exp\left(\frac{(x - x_{\text{mean}})^2}{2\sigma_T^2}\right), \quad (6.1)$$

where $x = \log(kT)$, $x_{\text{mean}} = \log(kT_{\text{mean}})$, kT_{mean} is the mean temperature of the distribution, σ_T is the width of the distribution, and Y_0 is the total integrated emission measure. The other parameters are similar as in the `cie` model. By definition, a `gdem` model with $\sigma_T = 0$ reproduces a `cie` (i.e. single-temperature) model. The free parameters of the `gdem` model are the normalisation (or emission measure) $Y_0 = \int n_e n_H dV$, the temperature parameters kT_{mean} and σ_T , and the abundances of O, Ne, Mg, Si, S, Ar, Ca, Fe, and Ni (given with respect to the proto-solar table of Lodders et al. 2009, see Sect. 6.1). Because these analyses are out of the scope of this paper, we devote the radial analyses of the temperatures, emission measures, and subsequent densities and entropies for a future work. The abundances of the $Z \leq 7$ elements are fixed to the proto-solar unity, while the remaining abundances are fixed to the Fe value. As mentioned by Leccardi & Molendi (2008), constraining the free abundance parameters to positive values only (for obvious physical reasons) may result in a statistical bias when averaging out the profiles. Therefore, we allow all the best-fit abundances to take positive and negative values. Following Chapter 3, the measured O abundances have been corrected from updated parametrisation of the radiative recombination rates (see also de Plaa et al. 2017). Since Ne abundances measured with EPIC are highly unreliable (because the main Ne emission feature is entirely blended with the Fe-L complex at EPIC spectral resolution), we do not consider them in the rest of the paper.

The absorption of the ICM photons by neutral interstellar matter is reproduced by a `hot` model, where the temperature parameter is fixed to 0.5 eV (see the SPEX manual). Because adopting the column densities of Willingale et al. (2013) — taking both atomic and molecular hydrogen into account — sometimes leads to poor spectral fits, we perform a grid search of the best-fit N_{H} parameter within the limits

$$N_{\text{HI}} - 5 \times 10^{19} \text{ cm}^{-2} \leq N_{\text{H}} \leq N_{\text{H,tot}} + 1 \times 10^{20} \text{ cm}^{-2}, \quad (6.2)$$

where N_{HI} and $N_{\text{H,tot}}$ are the atomic and total (atomic and molecular) hydrogen column densities, respectively (for further details, see Chapter 3).

6.3.2 Background modelling

Whereas in the core of bright clusters the ICM emission is largely dominant, in cluster outskirts the background plays an important role and sometimes may even dominate. For extended objects, a background subtraction applied to the raw spectra is clearly not advised because a slightly incorrect scaling may lead to dramatic changes in the derived temperatures (de Plaa et al. 2006). In turn, since the metal line emissivities depend on the assumed plasma temperature, this approach may lead to erroneous abundance measurements outside the cluster cores. Moreover, the observed background data (usually obtained from blank-field observations) may significantly vary with time and position on the sky.

Instead, we choose to model the background directly in the spectral fits by adopting the method extensively described in Chapter 2. The total background emission is decomposed into five components as follows:

1. The Galactic thermal emission (GTE) is modelled by an absorbed `c ie` component with proto-solar abundances.
2. The local hot bubble (LHB) is modelled by a (unabsorbed) `c ie` component with proto-solar abundances.
3. The unresolved point sources (UPS), whose accumulated flux can account for a significant fraction of the background emission, are modelled by a power law of index $\Gamma_{\text{UPS}} = 1.41$ (De Luca & Molendi 2004).
4. The hard particle background (HP, or instrumental background) consists of a continuum and fluorescence lines. The continuum is modelled by a (broken) power law, whose parameters can be constrained using filter wheel closed observations, and the lines are modelled by Gaussian functions. Because this is a particle background, we leave this modelled component unfolded by the effective area of the CCDs.
5. The quiescent soft-protons (SP) may contribute to the total emission, even after filtering of the flaring events. This component is modelled by a power law with an index varying typically within $0.7 \lesssim \Gamma_{\text{SP}} \lesssim 1.4$. Similarly to the HP background, this component is not folded by the effective area.

The background components have been first derived from spectra covering the total EPIC field of view to obtain good constraints on their parameters. In particular, this approach allows us to determine both the mean temperature of the ICM (which is the dominant emission below ~ 2 keV) and the slope of the SP component (better visible beyond ~ 2 keV), while these two parameters are usually degenerate when only analysing one outer annulus. In addition to the g_{dem} component, the free parameters of the background components in the fitted annuli are the normalisations of the HP continuum, HP Gaussian lines (because their emissivities vary with time and across the detector), and quiescent SP (beyond $6'$ only).

6.3.3 Local fits

As discussed extensively in Chapters 2 and 3, the abundances measured from a fit covering the full EPIC energy band may be significantly biased, especially for deep exposure datasets. In fact, a slightly incorrect calibration in the effective area may result in an incorrect prediction of the local continuum close to an emission line. Since the abundance of an ion is directly related to the measured equivalent width of its corresponding emission lines, a correct estimate of the local continuum level is crucial to derive accurate abundances.

Therefore, in the rest of the analysis, we measure the O, Mg, Si, S, Ca, Ar, and Ni abundances by fitting the EPIC spectra within several narrow energy ranges centred around their K-shell emission lines (hereafter the "local" fits; Chapter 3). The temperature parameters (kT_{mean} and σ_T) are fixed to their values derived from initial fits performed within the broad energy band (hereafter the "global" fits). In order to assess the systematic uncertainties related to remaining cross-calibration issues between the different EPIC detectors (Sect. 6.4.3), we perform our local fits in MOS (i.e. the combined MOS 1+MOS 2) and pn spectra independently. Finally, the Fe abundance can be measured in EPIC using both the K-shell lines (~ 6.4 keV) and the L-shell line complex (~ 0.9 – 1.2 keV, although not resolved with CCD instruments). For this reason, in the rest of the paper we use the global fits to derive the Fe abundances.

6.4 Building average radial profiles

Following the approach of Chapter 3, in addition to the full sample we consider further in this paper, we also split the sample into two subsamples, namely the "clusters" (23 objects) and the "groups" (21 objects), for which the mean temperature within $0.05r_{500}$ is greater or lower than 1.7 keV, respectively (see also Table 6.4). One exception is M 87, an elliptical galaxy with $kT_{\text{mean}}(0.05r_{500}) = (2.052 \pm 0.002)$ keV, which we treat in the following as part of the "groups" subsample.

6.4.1 Exclusion of fitting artefacts

Since little ICM emission is expected at large radii, one may reasonably expect large statistical uncertainties on our derived fitting parameters in the outermost annuli of every observation. In a few specific cases, however, suspiciously small error bars are reported at large radii, often together with unphysical best-fit values. These peculiar measurements are often due to issues in the fitting process, consequently to bad spectral quality together with a number of fitted parameters that is too large. Since these artefact measurements may significantly pollute our average profiles, we prefer to discard them from the analysis and select outer measurements with reasonably large error bars on their parameters only. To be conservative, we choose to exclude systematically the Fe abundance measurements showing error bars smaller than 0.01, 0.02, and 0.03 in their 4'-6', 6'-9', and 9'-12' annuli, respectively. A similar filtering is applied to the other abundances, this time when their measurements show error bars smaller than 0.01, 0.02, 0.05, and 0.07 in their 3'-4', 4'-6', 6'-9', and 9'-12' annuli, respectively. These discarded artefacts represent a marginal fraction ($\sim 4\%$) of all our data. We list the maximum radial extend for each cluster and all the elements considered ($r_{\text{out},X}$) in Table 6.4. Finally, we exclude further specific measurements either because their spectral quality could simply not provide reliable estimates or because of possible contamination by the AGN emission. These unaccounted annuli are specified in Table 6.1.

6.4.2 Stacking method

Since spectral analysis was performed within annuli of fixed angular sizes regardless of the distances or the cosmological redshifts of the sources, care must be taken to build average radial profiles within consistent spa-

6.4 Building average radial profiles

Table 6.1: List of the specific measurements that were discarded from our analysis.

Name	Discarded radii	Element(s)	Comments
2A 0335	$\geq 6'$	all	Bad quality
A 4038	$\geq 9'$	all	Bad quality
A 3526	$\geq 9'$	Mg	HP contamination
Hydra A	$\geq 6'$	all	Bad quality
M 84	$\leq 0.5'$	all	AGN contamination
M 86	$\geq 6'$	all	Bad quality
M 87	$\leq 0.5'$	all	AGN contamination
M 89	all	Mg, S, Ar, Ca, Ni	Bad quality
	$\leq 0.5'$	Fe, Si	AGN contamination
NGC 4261	$\leq 0.5'$	all	AGN contamination
NGC 5044	$\geq 9'$	all	Bad quality
NGC 5813	$\leq 0.5'$	all	AGN contamination
	$\leq 6'$	Mg	Poor fit in the 1–2 keV band
NGC 5846	$\leq 6'$	Mg	Poor fit in the 1–2 keV band

tial scales. As commonly used in the literature, we rescale all the annuli in every object in fractions of r_{500} . We adopted the values of r_{500} , given for each cluster in Table 6.4, from Pinto et al. (2015) and references therein. Another unit widely used in the literature is r_{180} , as it is often considered (close to) the virial radius of relaxed clusters. Nevertheless, the conversion $r_{500} \simeq 0.6r_{180}$ is quite straightforward (e.g. Reiprich et al. 2013).

The number and extent of the reference radial bins of the average profiles are selected such that each bin contains approximately 15–25 individual measurements. The maximum extent of our reference profiles corresponds to the maximum extent reached by the most distant observation: i.e. $1.22r_{500}$ (based on A 2597) and $0.97r_{500}$ (based on A 189) for clusters and groups, respectively (see Table 6.4). After this selection, the average profiles for the full sample and the cluster and group subsamples contain 16, 9, and 8 reference radial bins, respectively. The outermost radial bin of the full sample and the cluster and group subsamples contain 17, 16, and 11 individual measurements, which are located within 0.55 – $1.22 r_{500}$, 0.5 – $1.22 r_{500}$, and 0.26 – $0.97 r_{500}$, respectively. Stacking our individual profiles over the reference bins defined above is not trivial, since some measurements may share their radial extent with two adjacent reference bins. To over-

come this issue, we employ the method proposed by Leccardi & Molendi (2008). The average abundance profile $X_{\text{ref}}(k)$, as a function of the k -th reference radial bin (defined above), is obtained as

$$X_{\text{ref}}(k) = \left(\sum_{j=1}^N \sum_{i=1}^8 w_{i,j,k} \frac{X(i)_j}{\sigma_{X(i)_j}^2} \right) \Big/ \left(\sum_{j=1}^N \sum_{i=1}^8 w_{i,j,k} \frac{1}{\sigma_{X(i)_j}^2} \right), \quad (6.3)$$

where $X(i)_j$ is the individual abundance measurement of the j -th observation at its i -th annulus (as defined in Sect. 6.2), $\sigma_{X(i)_j}$ is its statistical error (and thus $1/\sigma_{X(i)_j}^2$ weights each annulus with respect to its emission measure), N is the number of observations, depending of the (sub)sample considered, and $w_{i,j,k}$ a weighting factor. This factor, taking values between 0 and 1, represents the linear overlapping geometric area fraction of the k -th reference radial bin on the i -th annulus (belonging to the j -th observation).

6.4.3 MOS-pn uncertainties

After stacking the measurements as described above, for each element we are left with $X_{\text{ref, MOS}}(k)$ and $X_{\text{ref, pn}}(k)$; i.e. an average MOS and pn abundance profile, respectively, except O, which could only be measured with the MOS instruments, and Fe, which we measured in simultaneous EPIC global fits (see Sect. 6.3.3). The average EPIC (i.e. combined MOS+pn) profiles are then computed as follows:

$$X_{\text{ref, EPIC}}(k) = \left(\frac{X_{\text{ref, MOS}}(k)}{\sigma_{\text{ref, MOS}}^2(k)} + \frac{X_{\text{ref, pn}}(k)}{\sigma_{\text{ref, pn}}^2(k)} \right) \Big/ \left(\frac{1}{\sigma_{\text{ref, MOS}}^2(k)} + \frac{1}{\sigma_{\text{ref, pn}}^2(k)} \right), \quad (6.4)$$

where $\sigma_{\text{ref, MOS}}(k)$ and $\sigma_{\text{ref, pn}}(k)$ are the statistical errors of $X_{\text{ref, MOS}}(k)$ and $X_{\text{ref, pn}}(k)$, respectively. As shown in Chapter 3, abundance estimates using MOS and pn may sometimes be significantly discrepant. Unsurprisingly, we also find MOS-pn discrepancies in some radial bins of our average abundance profiles. We take this systematic effect into account when combining the MOS and pn profiles by increasing the error bars of the EPIC combined measurements until they cover both their MOS and pn counterparts.

6.5 Results

6.5.1 Fe abundance profile

The average Fe abundance radial profile, measured for the full sample, is shown in Fig. 6.1, and the numerical values are detailed in Table 6.2. The profile shows a clear decreasing trend with radius with a maximum at $0.014\text{--}0.02r_{500}$, and a slight drop below $\sim 0.01r_{500}$. Such a drop is also observed in the Fe profile of several individual objects (Figs. 6.18 and 6.19) and is discussed in Sect. 6.7.2. The very large total exposure time of the sample (~ 4.5 Ms) makes the combined statistical uncertainties $\sigma_{\text{stat}}(k)$ very small — less than 1% in the core, up to $\sim 7\%$ in the outermost radial bin. The scatter of the measurements (grey shaded area in Fig. 6.1), expressed as

$$\sigma_{\text{scatter}}(k) = \sqrt{\sum_{j=1}^N \sum_{i=1}^8 w_{i,j,k} \left(\frac{X(i)_j - X_{\text{ref}}(k)}{\sigma_{X(i)_j}} \right)^2} / \sqrt{\sum_{j=1}^N \sum_{i=1}^8 w_{i,j,k} \frac{1}{\sigma_{X(i)_j}^2}} \quad (6.5)$$

for each k -th reference bin, is much larger (up to $\sim 36\%$ in the innermost bin).

We parametrise this profile by fitting the empirical function

$$\text{Fe}(r) = A(r - B)^C - D \exp \left(-\frac{(r - E)^2}{F} \right), \quad (6.6)$$

where r is given in units of r_{500} , and A , B , C , D , E , and F are constants to determine. The first term on the right hand side of Eq. (6.6) is a power law that is used to model the decrease beyond $\gtrsim 0.02r_{500}$. To model the inner metal drop, we subtract a Gaussian (second term) from the power law. The best fit of our empirical distribution is shown in Fig. 6.1 (red dashed curve) and can be expressed as

$$\text{Fe}(r) = 0.21(r + 0.021)^{-0.48} - 6.54 \exp \left(-\frac{(r + 0.0816)^2}{0.0027} \right), \quad (6.7)$$

which provides a reasonable fit to the data ($\chi^2/\text{d.o.f.} = 10.3/9$). We also look for possible hints towards a flattening at the outskirts. When assuming

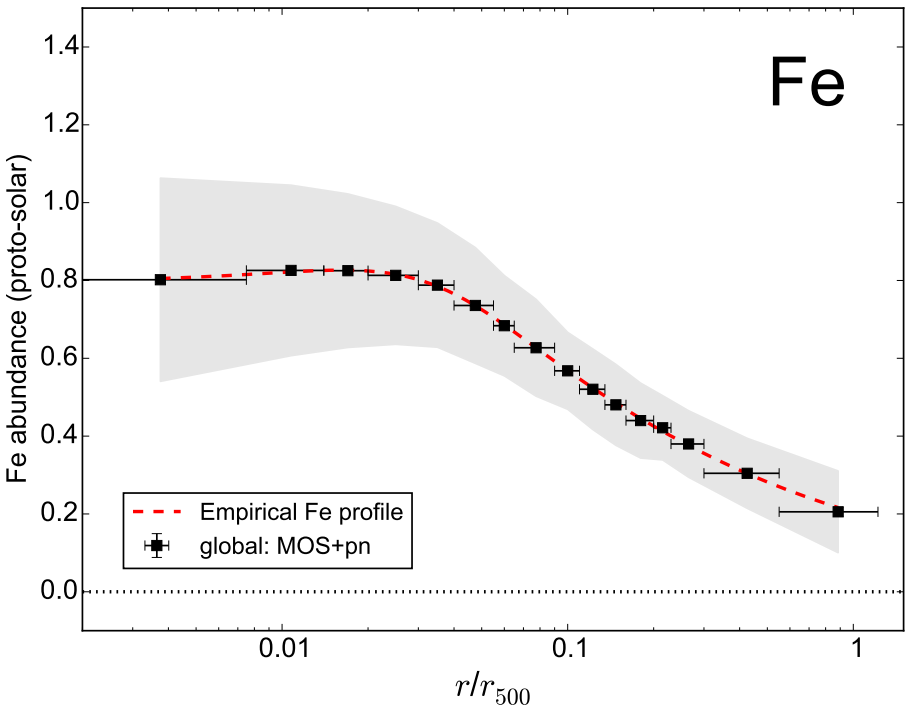


Figure 6.1: Average radial Fe abundance profile for the full sample. Data points show the average values and their statistical uncertainties (σ_{stat} , barely visible on the plot). The shaded area shows the scatter of the measurements (σ_{scatter} , see text).

a positive Fe floor in the outskirts (by injecting an additive constant G into Eq. (6.7)), the fit does not improve ($\chi^2/\text{d.o.f.} = 10.3/10$, with $G = 0.009$) and remains comparable to the former case. Therefore, our data do not allow us to formally confirm the presence of a uniform Fe distribution in the outskirts. The empirical Fe abundance profile of Eq. (6.7) is compared to the radial profiles of other elements further in our analysis (Sect. 6.5.2).

We now compute the average radial Fe abundance profiles separately for the clusters ($>1.7 \text{ keV}$) and groups ($<1.7 \text{ keV}$) of our sample. The result is shown in Fig. 6.2 (where the dashed lines indicate the average profile over the full sample) and Table 6.3. The Fe abundance in clusters and groups can be robustly constrained out to $\sim 0.9r_{500}$ and $\sim 0.6r_{500}$, respectively, and also show a clear decrease with radius. Although both profiles show a similar

Table 6.2: Average radial Fe abundance profile for the full sample, as shown in Fig. 6.1.

Radius ($/r_{500}$)	Fe	σ_{stat}	σ_{scatter}
0 – 0.0075	0.802	0.005	0.261
0.0075 – 0.014	0.826	0.004	0.219
0.014 – 0.02	0.825	0.004	0.197
0.02 – 0.03	0.813	0.003	0.177
0.03 – 0.04	0.788	0.003	0.160
0.04 – 0.055	0.736	0.003	0.149
0.055 – 0.065	0.684	0.004	0.129
0.065 – 0.09	0.627	0.003	0.124
0.09 – 0.11	0.568	0.004	0.099
0.11 – 0.135	0.520	0.004	0.104
0.135 – 0.16	0.480	0.005	0.104
0.16 – 0.2	0.440	0.005	0.096
0.2 – 0.23	0.421	0.006	0.082
0.23 – 0.3	0.380	0.006	0.086
0.3 – 0.55	0.304	0.006	0.090
0.55 – 1.22	0.205	0.011	0.105

slope, we note that at each radius, the average Fe abundance for groups is systematically lower than for clusters. The two exceptions are the innermost radial bin (where the cluster and group Fe abundances show consistent values) and the outermost radial bin of these two profiles (where the group Fe abundances appear somewhat higher than in clusters). We discuss this further in Sect. 6.7.1.

6.5.2 Abundance profiles of other elements

While the Fe-L and Fe-K complexes, which are both accessible in the X-ray band, make the Fe abundance rather easy to estimate with a good degree of accuracy, the other elements considered in this paper (O, Mg, Si, S, Ar, Ca, and Ni) can be measured by CCD instruments only via their K-shell main emission lines. Consequently, their radial abundance profiles are in general difficult to constrain in the ICM of individual objects. The deep total exposure of our sample allows us to derive the average radial abundance profiles of elements other than Fe, which we present in this section.

Table 6.3: Average radial Fe abundance profile for clusters (>1.7 keV) and groups (<1.7 keV), as shown in Fig. 6.2.

Radius ($/r_{500}$)	Fe	σ_{stat}	σ_{scatter}
Clusters			
0 – 0.018	0.822	0.003	0.241
0.018 – 0.04	0.8167	0.0020	0.1725
0.04 – 0.068	0.7190	0.0022	0.1369
0.068 – 0.1	0.626	0.003	0.106
0.1 – 0.18	0.511	0.003	0.089
0.18 – 0.24	0.432	0.005	0.075
0.24 – 0.34	0.357	0.006	0.081
0.34 – 0.5	0.309	0.008	0.079
0.5 – 1.22	0.211	0.011	0.102
Groups			
0 – 0.009	0.812	0.009	0.199
0.009 – 0.024	0.779	0.005	0.130
0.024 – 0.042	0.685	0.007	0.189
0.042 – 0.064	0.640	0.009	0.175
0.064 – 0.1	0.524	0.007	0.175
0.1 – 0.15	0.430	0.007	0.129
0.15 – 0.26	0.330	0.010	0.133
0.26 – 0.97	0.268	0.016	0.139

First, and similarly to Fig. 6.1, we compute and compare the radial profiles of O, Mg, Si, S, Ar, and Ca, averaged over the full sample. The Ni profile could only be estimated for clusters because the lower temperature of groups and ellipticals prevents a clear detection of the Ni K-shell emission lines. These profiles are shown in Fig. 6.3 and their numerical values can be found in Table 6.5. A question of interest is whether these derived profiles follow the shape of the average Fe profile. This can be checked by comparing these radial profiles to the empirical $\text{Fe}(r)$ profile proposed in Eq. (6.7) and Fig. 6.1, shown by the red dashed lines in Fig. 6.3. Obviously, the average profile of an element X is not expected to strictly follow the average Fe profile, as the X/Fe ratios may be larger or smaller than unity. A more consistent comparison would be thus to define the empirical $X(r)$

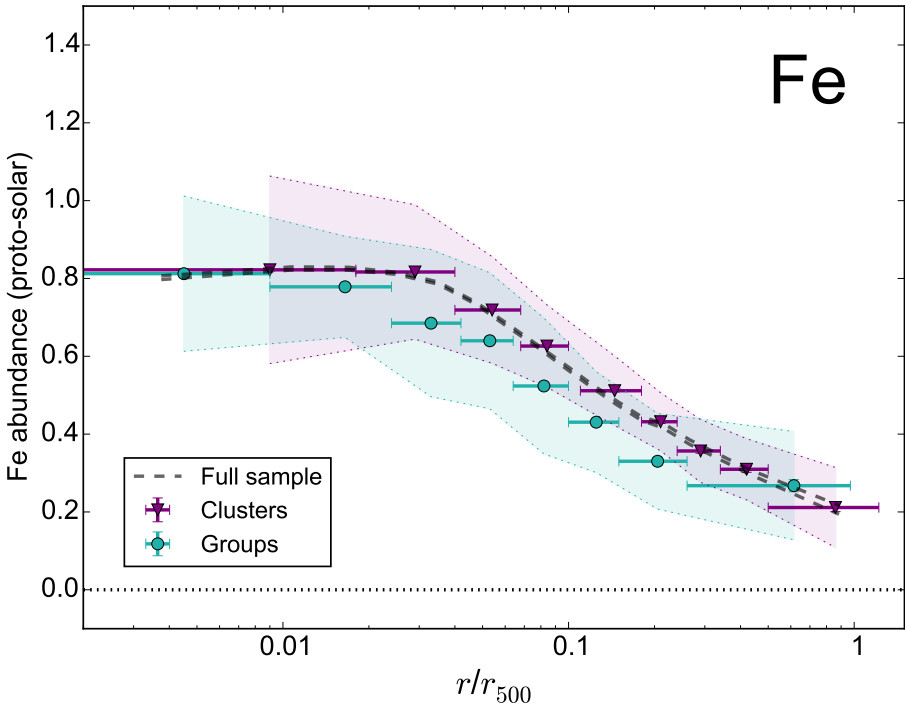


Figure 6.2: Average Fe profile for clusters (>1.7 keV, purple) and groups (<1.7 keV, green) within our sample. The corresponding shaded areas show the scatter of the measurements. The two dashed lines indicate the upper and lower statistical error bars of the Fe profile over the full sample (Fig. 6.1) without scatter for clarity.

profiles as

$$X(r) = \eta \text{Fe}(r), \quad (6.8)$$

where η is the average X/Fe ratio estimated using our sample, within $0.2r_{500}$ when possible or $0.05r_{500}$ otherwise, and tabulated in Table 3.2. These normalised empirical profiles are shown by the blue dashed lines in Fig. 6.3 and can be directly compared with our observational data.

The case of Si is particularly striking, as we find a remarkable agreement ($<1\sigma$) between our measurements and the empirical $\text{Si}(r)$ profile in all the radial bins, except the outermost one ($<2\sigma$). Within $\sim 0.5r_{500}$, the Ca and Ni profiles follow their empirical counterparts very well ($<2\sigma$).

The O, Mg, and S profiles are somewhat less consistent with their re-

spective $X(r)$ profiles. The O central drop is significantly more pronounced than the Fe drop, while the Mg profile does not show any clear central drop and appears significantly shallower than expected (blue dashed line). Finally, the S measured profile falls somewhat below the empirical prediction within $0.04\text{--}0.1r_{500}$. However, such discrepancies are almost entirely introduced by a few specific observations. As we show further in Sect. 6.6.4, when ignoring (temporarily) these single observations from our sample, a very good agreement is obtained between the data and empirical profiles, both for O, Mg, and S. Moreover, the large plotted error bars at outer radii in the Mg profile are almost entirely due to the MOS-pn discrepancies; while the MOS measurements (located at the lower side of the error bars) follow very well the empirical profile, the pn measurements (located at the upper side of the error bars) increase with radius; this is probably because of contamination of the Mg line with the instrumental Al-K α line (see Sect. 6.6.6 for an extended discussion). Finally, as we show further in this section, the average O/Fe, Mg/Fe, and S/Fe profiles (compiled from O/Fe and Mg/Fe measurements of individual observations) show a good agreement with being radially flat.

The case of Ar is the most interesting one. Despite the large error bars (only covering the MOS-pn discrepancies), the average radial slope of this element appears systematically steeper than its empirical profile. A similar behaviour is found in the average Ar/Fe profile (see further). Unlike the O, Mg, and S profiles, we cannot suppress this overall trend by discarding a few specific objects from the sample (Sect. 6.6.4). Although we discuss one possible reason for these differences in Sect. 6.7.2, we note that they cannot be confirmed when the scatters are taken into account.

We also note that in many cases, the average measured abundances in the outermost radial bin are systematically biased low with respect to the empirical prediction. As we show below, this feature is also reported in most of the X/Fe profiles. While at these large distances the scatter is very large and still consistent with the empirical expectations, these values that are systematically lower than expected may emphasise the radial limits beyond which the background uncertainties prevent any robust measurement (see Sect. 6.6.3).

Second, and similarly to Fig. 6.2, we compute the average O, Mg, Si, S, Ar, and Ca abundance profiles (and their respective scatters) for clusters, on the one hand, and for groups, on the other hand. These profiles are shown in Fig. 6.4 and Table 6.6. For comparison, the average profiles us-

6.5 Results

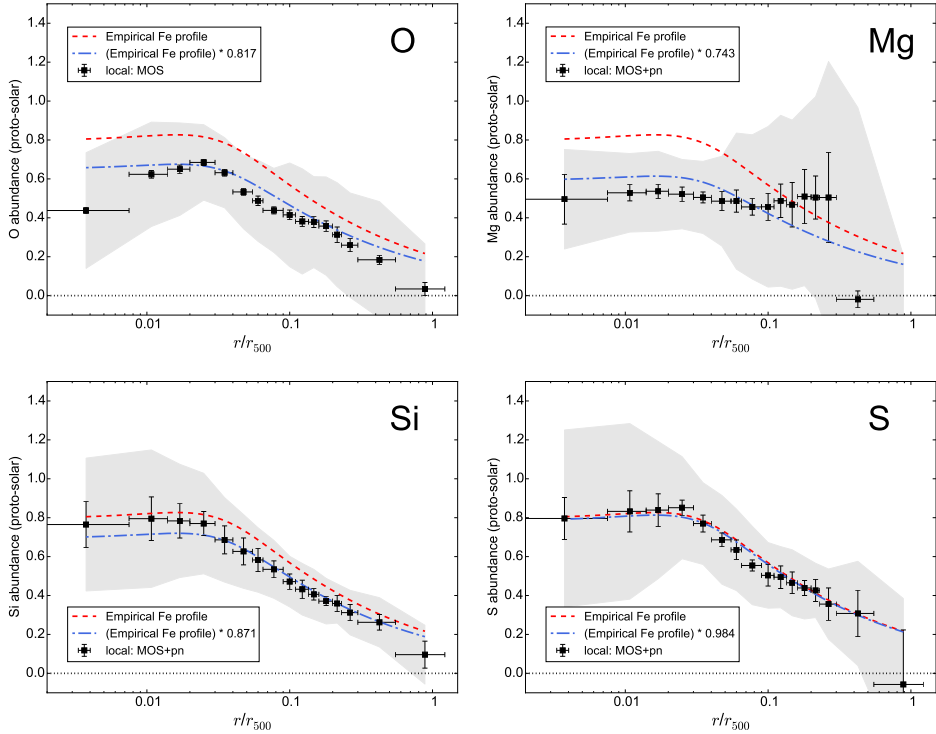


Figure 6.3: Average radial abundance profiles of all the objects in our sample. The error bars contain the statistical uncertainties and MOS-pn uncertainties (Sect. 6.4.3) except for the O abundance profiles, which are only measured with MOS. The corresponding shaded areas show the scatter of the measurements. The Ni profile has only been averaged for clusters (> 1.7 keV).

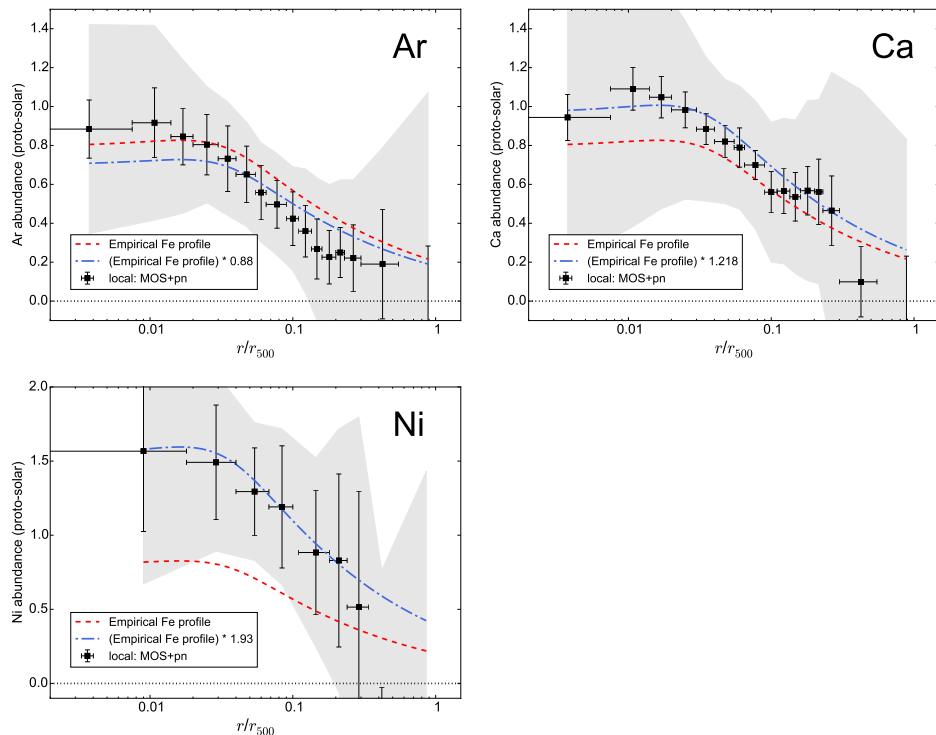


Figure 6.3 (Continued)

ing the full sample (Fig. 6.3, without scatter) are also shown (dashed grey lines). All the profiles (groups and clusters) show an abundance decrease towards the outskirts. Globally, the clusters and groups abundance profiles are very similar for a given element. We note, however, the exception of the O profiles, for which the groups show on average a lower level of enrichment (similar to the case of Fe). A drop in the innermost bin for groups is also clearly visible for O (however, see Sect. 6.6.4). Moreover, the Ca profile for groups also suggests a drop in the innermost bin, followed by a more rapidly declining profile towards the outskirts. While these global trends are discussed further in Sect. 6.7.1, we must recall that the large scatter of our measurements (shaded areas) prevents us from deriving any firm conclusion regarding possible differences in the cluster versus group profiles presented here.

Another method for comparing the Fe abundance profile with the abundance profiles of other elements is to compute the X/Fe abundance ratios in each annulus of each individual observation. We stack all these measurements over the full sample as described in Sect. 6.4 to build average X/Fe profiles. These Fe-normalised profiles are shown in Fig. 6.5. In each panel, we also indicate $(X/\text{Fe})_{\text{core}}$, the average X/Fe ratio measured within the ICM core (i.e. $\leq 0.05r_{500}$ when possible, $\leq 0.2r_{500}$ otherwise) adopted from Chapter 3, and their total uncertainties (dotted horizontal lines; including the statistical errors, intrinsic scatter, and MOS-pn uncertainties). As mentioned earlier, the Ni/Fe profile could only be reasonably derived for clusters. Despite a usually large scatter (in particular in the outskirts), the X/Fe profiles are all in agreement with being flat, hence following the Fe average profile, and are globally consistent with their respective average $(X/\text{Fe})_{\text{core}}$ values. Despite this global agreement, we note the clear drop of Ar/Fe beyond $\sim 0.064r_{500}$. This outer drop corresponds to the steeper Ar profile seen in Fig. 6.3 and reported above. Finally, and similarly to Fig. 6.3, most of the outermost average X/Fe values are biased low with respect to their $(X/\text{Fe})_{\text{core}}$ counterparts (often coupled with very large scatters), perhaps indicating the observational limits of measuring these ratios.

6.6 Systematic uncertainties

In the previous section, we presented the average abundance profiles measured for our full sample (CHEERS) and for the clusters and groups subsamples. Before discussing their implications on the ICM enrichment, we

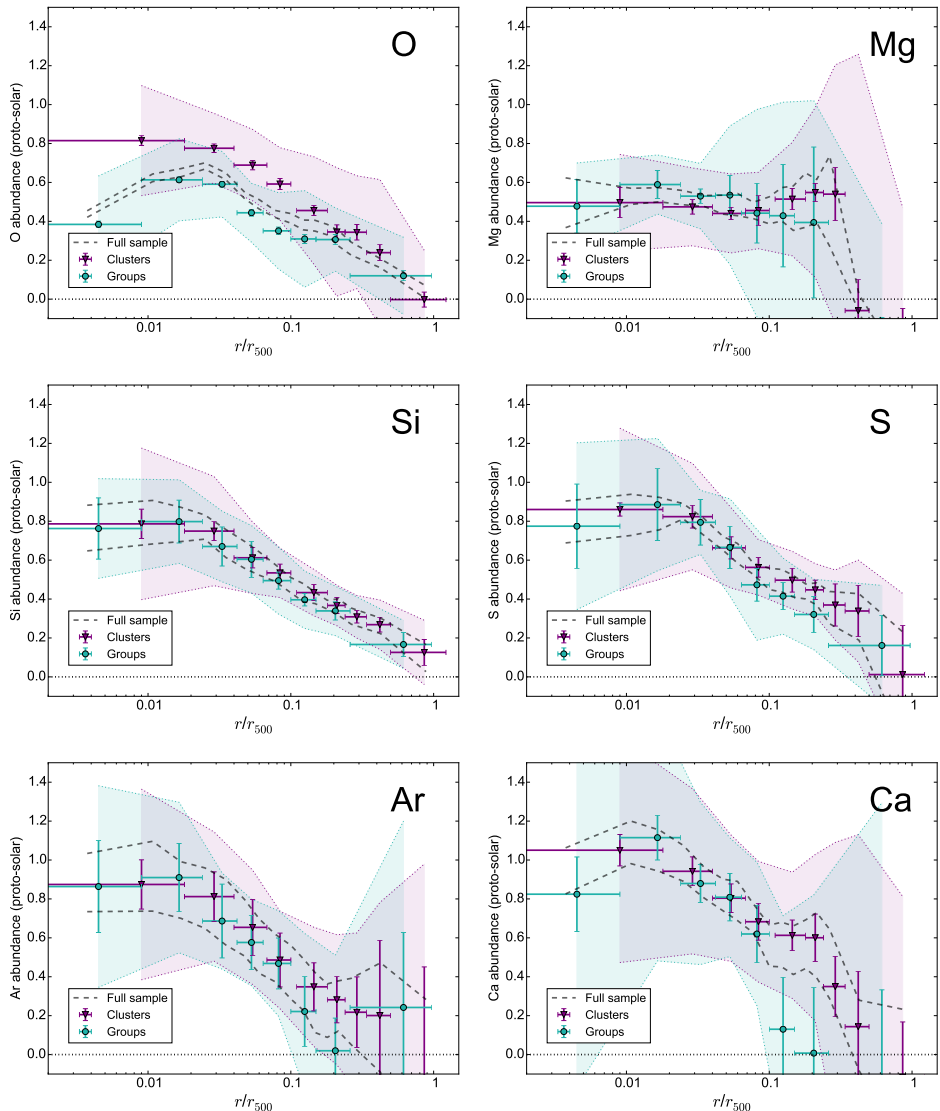


Figure 6.4: Comparison of the average abundance radial profiles between clusters (>1.7 keV) and groups/ellipticals (<1.7 keV). The error bars contain the statistical uncertainties and MOS-pn uncertainties (Sect. 6.4.3) except for the O abundance profiles, which are only measured with MOS. The corresponding shaded areas show the scatter of the measurements. The two dashed lines indicate the upper and lower error bars of the corresponding profiles over the full sample (Fig. 6.3), without scatter for clarity.

6.6 Systematic uncertainties

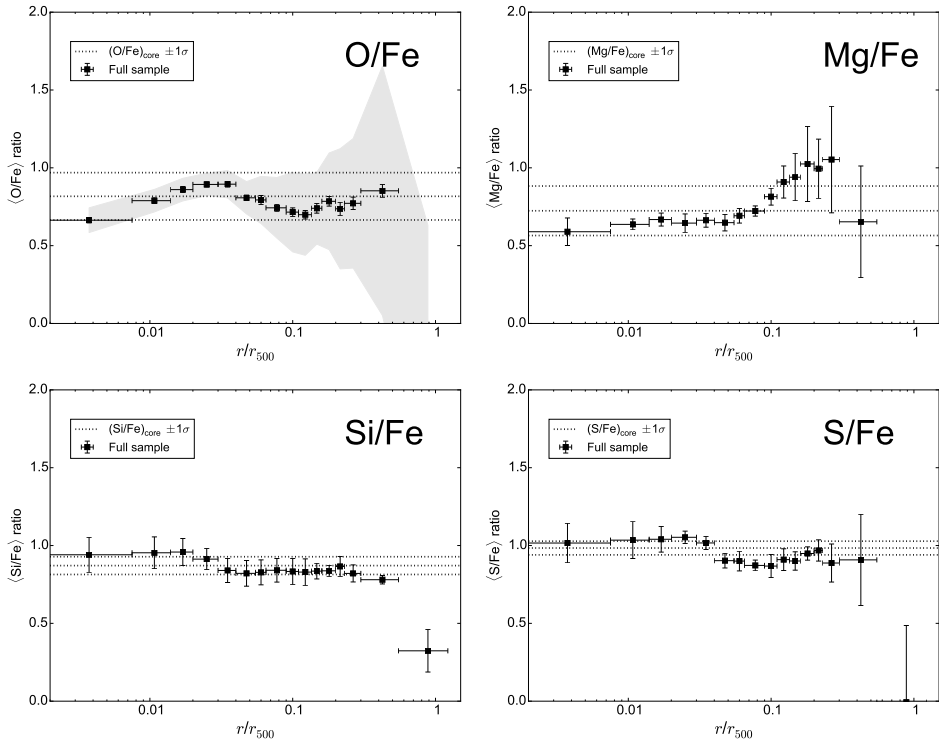


Figure 6.5: Individual radial X/Fe ratio measurements averaged over the full sample. The error bars contain the statistical uncertainties and MOS-pn uncertainties (Sect. 6.4.3) except for the O/Fe abundance profiles, which are only measured with MOS. The corresponding shaded areas show the scatter of the measurements. The average X/Fe abundance ratios (and their uncertainties) measured in the ICM core in Chapter 3, namely $(X/\text{Fe})_{\text{core}}$, are also plotted.

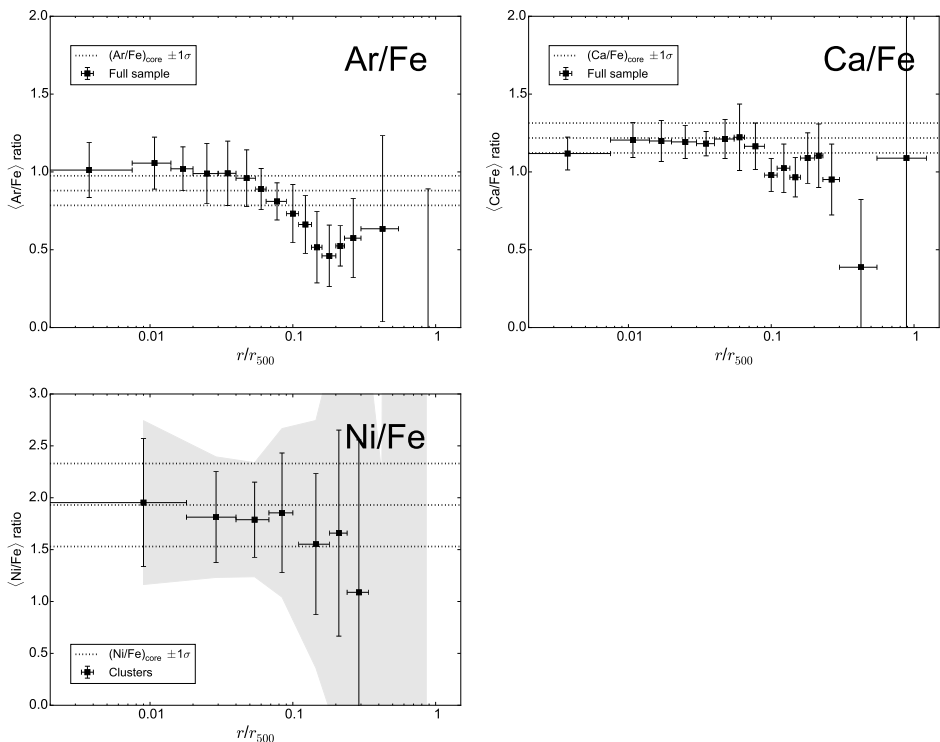


Figure 6.5 (Continued)

must ensure that our results are robust and do not (strongly) depend on the assumptions we invoke throughout this paper. In this section, we explore the systematic uncertainties that could potentially affect our results. They can arise from: (i) the intrinsic scatter in the radial profiles of the different objects of our sample; (ii) MOS-pn discrepancies in the abundance measurements due to residual EPIC cross-calibration issues; (iii) projection effects on the plane of the sky; (iv) uncertainties in the thermal structure of the ICM; (v) uncertainties in the background modelling; and (vi) the weight of a few individual highest quality observations, which might dominate the average measurements.

We already took items (i) and (ii) into account in our analysis (Sect. 6.5.1 and 6.4.3, respectively), and here we focus on items (iii), (iv), (v), and (vi).

6.6.1 Projection effects

Throughout this paper, we report the average abundance profiles of the ICM as observed by *XMM-Newton*/EPIC, i.e. projected on the plane of the sky. Several models are currently available to deproject cluster data and estimate the radial metal distribution contained in concentric spherical shells (e.g. Churazov et al. 2003; Kaastra et al. 2004; Johnstone et al. 2005; Russell et al. 2008). However, all of them assume a spherical symmetry in the ICM distribution, which may not always be true. Moreover, some methods are known for introducing artefacts in the deprojected measurements (for a comparison, see Russell et al. 2008), as deprojection methods assume a dependency between all the fitted annuli. We thus prefer to work with projected results to keep a statistical independence in the radial bins.

Several past works investigated the effects of deprojection on the abundance estimates at different radii. The general outcome is that these effects have a very limited impact on the abundance measurements (e.g. Rasmussen & Ponman 2007; Russell et al. 2008). Therefore, we do not expect them to be a source of significant systematic uncertainty for the purpose of this work.

6.6.2 Thermal modelling

As explained in Sect. 6.3.1, the abundance determination is very sensitive to the assumed thermal structure of the cluster/group. Therefore, it is crucial to fit our spectra with a thermal model that reproduces the projected temperature structure as realistically as possible. In particular, a `cje` (single-

temperature) model is clearly not optimal for our analysis. The thermal model used in this work (`gdem`) has been used in many previous studies and is thought to be rather successful at reproducing the true temperature structure of some clusters (e.g. Simionescu et al. 2009b; Frank et al. 2013), as it represents one of the simplest way of accounting for a continuous mixing of temperatures in the ICM (coming from either projection effects or a locally intrinsic multi-phase plasma). The precise temperature distribution is however difficult to determine with the current spectrometers and may somewhat differ from the `gdem` assumption. Alternatively, some previous works suggest that the temperature distribution in cool-core clusters may be reasonably approximated by a truncated power law (typically between $0.2 \text{ keV} \lesssim kT \lesssim 3 \text{ keV}$, with more emission towards higher temperatures; see e.g. Kaastra et al. 2004; Sanders et al. 2008). Such a distribution can be modelled in SPEX via the `wdem` model (for more details, see e.g. Kaastra et al. 2004).

Using a `wdem` model instead of a `gdem` model can potentially lead to differences in the measured abundances, hence contributing to add further systematic uncertainties to the derived profiles (for a RGS comparison, see de Plaa et al. 2017). Unfortunately, the large computing time required by the `wdem` model in the fits does not allow us to perform a full comparison between the two models over the whole sample. We thus select one cluster, MKW 3s, and we explore how the use of a `wdem` model affects its Fe profile. MKW 3s has the advantage of emitting a moderate ICM temperature ($\sim 3.4 \text{ keV}$) inside $0.05r_{500}$, which is very close to the mean temperature of the clusters in the sample ($\sim 3.2 \text{ keV}$) within this radius. Moreover, the Fe radial profile of MKW 3s (Fig. 6.18) is rather similar to the average Fe profile presented in Fig. 6.1. The `gdem-wdem` comparison on the Fe radial profile of MKW 3s is presented in Fig. 6.6. The use of a `wdem` model in MKW 3s systematically predicts higher Fe abundances than using a `gdem` model, where the increase may vary from +6% (core) up to +20% (outskirts). Since there is a difference of temperature between the core ($kT_{\text{mean}} \simeq 3.5 \text{ keV}$) and the outskirts ($kT_{\text{mean}} \simeq 1 \text{ keV}$), this may suggest a temperature dependence (see also de Plaa et al. 2017). However, there is no substantial change in the slope of the overall profile. The same trend is also found for the abundance profiles of the other elements. For comparison, we also check that we obtain similar results for NGC 507, i.e. a cooler group. In conclusion, we do not expect any variation in the shape of the average abundance profiles owing to the use of another temperature distribution in our modelling. The

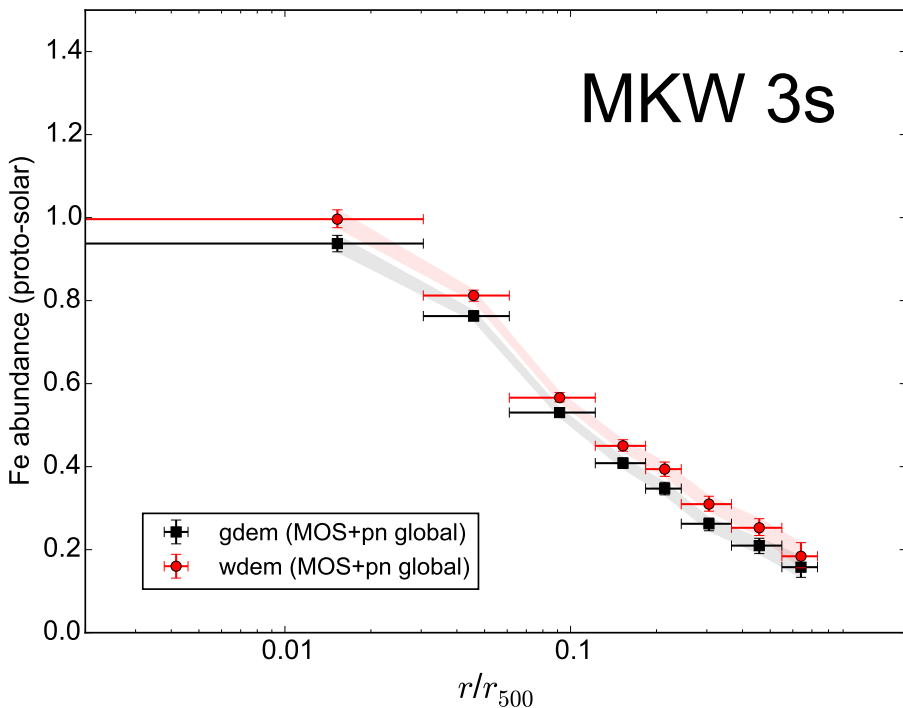


Figure 6.6: Comparison of the radial Fe profiles derived in MKW 3s by assuming successively a Gaussian (`gdem`, black) and a power law (`wdem`, red) temperature distribution (see text for more details).

normalisation of these profiles, which might slightly be revised upwards in the case of a `wdem` model, still lies within the scatter of our measurements and does not affect our results.

Nevertheless, as said above, it is worth keeping in mind that the current spectral resolution offered by CCDs does not allow us to resolve the precise temperature structure in the ICM. Further improvements on the thermal assumptions invoked here are expected with X-ray micro-calorimeter spectrometers on board future missions.

6.6.3 Background uncertainties

As mentioned in Sect. 6.3.2, a proper modelling of the background is crucial for a correct determination of the abundances in the ICM. This is especially

true in the outskirts, where the background contribution is significant and may easily introduce systematic biases when deriving spectral properties. Presumably, the Si, S, Ar, Ca, Fe, and Ni abundances are more sensitive to the modelling of the non-X-ray background, as the HP and SP components dominate beyond ~ 2 keV. On the other hand, the O abundance is more sensitive to the X-ray background, in particular the GTE and LHB components, which may have their greatest influence below ~ 1 keV. We investigate the effects of background-related uncertainties on the abundance profiles using two different approaches.

First, similar to Sect. 6.6.2, we take MKW 3s as an object representative of the whole sample. In each annulus and for all the EPIC instruments, we successively fix the normalisations of the HP and SP background components to $\pm 10\%$ of their best-fit values. We then refit the spectra and measure the changes in the best-fit Si and Fe profiles. We do the same for the O profile, this time by fixing the normalisations of the GTE and LHB components together to $\pm 10\%$ of their best-fit values. The results are shown in the upper panel of Fig. 6.7, where the Si and Fe profiles were shifted up for clarity. In all cases, the changes in the best-fit abundances are smaller than (or similar to) the statistical uncertainties from our initial fits. This clearly illustrates that a slightly ($\lesssim 10\%$) incorrect scaling of the modelled background has a limited impact on our results, even at large radii. Moreover, we may reasonably expect that the possible deviations from the true normalisation of the background components average out when stacking all the objects.

Second, and despite the encouraging previous indication that the background-related systematic uncertainties are under control, we still consider the possibility that the outer regions of every observation would be too contaminated and should be discarded from the analysis. In this respect, in the lower panel of Fig. 6.7 we rebuild the average Fe profile by successively ignoring the $\geq 9'$, $\geq 6'$, and $\geq 4'$ regions (corresponding to keeping only the first seven, six, and five annuli, respectively) from each observation. Restricting our analysis to $< 6'$ still allows us to derive a mean Fe abundance in the outermost average radial bin ($0.55\text{--}1.22r_{500}$). However, most of the area from the only two measurements that partly fall into this bin (A 2597 and A 1991) overlap the inner reference bin ($0.3\text{--}0.55r_{500}$). This spatial resolution issue may thus explain the slight ($\sim 30\%$, albeit non-significant) increase of the average Fe value observed in outermost bin when truncating the $\geq 6'$ regions. A similar explanation can be invoked for the $< 4'$ case, in the second outermost bin ($0.3\text{--}0.55r_{500}$), where an average increase of $\sim 12\%$ is

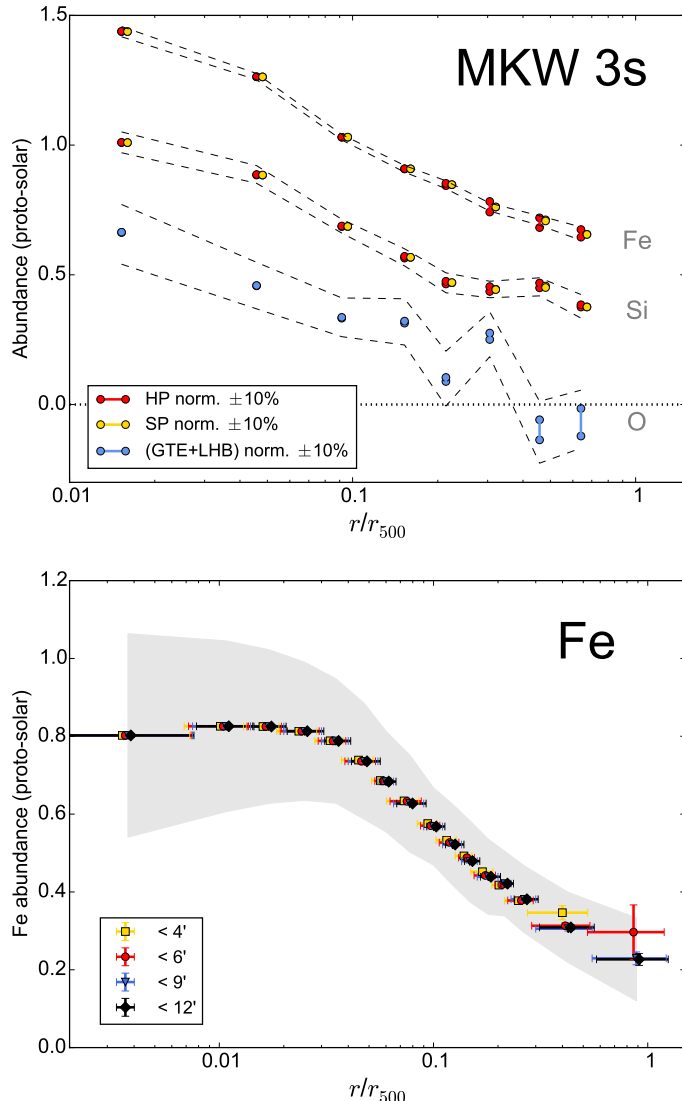


Figure 6.7: *Top:* Effects of the background model uncertainties on the Fe, Si, and O radial profiles of MKW 3s. The normalisation of the HP, SP, and GTE+LHB were successively fixed to $\pm 10\%$ of their best-fit values (see text). The dashed lines show the range constrained by the statistical uncertainties for each profile. For clarity, the Si and Fe profiles are shifted up by 0.25 and 0.5, respectively. *Bottom:* Comparison of the average Fe profile for different truncated radii adopted in each observation. Data points with different colours are slightly shifted for clarity.

observed (though less than 2σ significant). In any case, the changes related to the truncation of the profiles at different radii are always smaller than the scatter (grey area) even in the outskirts. Therefore, this scatter can reasonably be seen as a conservative limit encompassing all the background uncertainties mentioned here.

In summary, our results clearly suggest that our careful modelling of the background allows us to keep all its related systematic uncertainties on the abundances under control, even at larger radii. However, it is not impossible that the background dominates in the outermost radial bin ($\geq 0.55r_{500}$) too much, thereby biasing low the average abundances of some elements (Sect. 6.5.2).

6.6.4 Weight of individual observations

Among the 44 objects of our sample, the three brightest objects (A 3526 a.k.a. Centaurus, M 87, and Perseus) benefit from excellent data quality, leading to very small statistical uncertainties ($\sigma_{X(i),j}^2$) of their measured abundances. Consequently, these observations may have an important contribution in shaping the average abundance profiles (as $1/\sigma_{X(i),j}^2 \gg 1$). The consequences of this weighting selection effect is explored in this section.

In Fig. 6.8 (top left panel), we show how the average Fe profile changes when we exclude A 3526, M 87, and Perseus from the sample. Compared to the initial Fe profile (blue empty boxes; see also Fig. 6.1), the largest effect is an increase of $\sim 8\%$ in the innermost average radial bin ($\leq 7.5 \times 10^{-3}r_{500}$), while the rest of the radial profile varies a few per cent at most.

Similarly, this weighting effect may affect the other abundance profiles. In Fig. 6.3, we showed that the average Si, Ca, and Ni radial profiles follow very well the fitted average Fe radial profile normalised by the average X/Fe ratio found in the core. However, the innermost region ($\leq 0.01r_{500}$) shows an O drop about $\sim 20\%$ lower than predicted by our empirical profile, while the Mg profile looks significantly flatter than expected. Similarly, some deviations from the expected S profile are also observed within $0.04\text{--}0.1r_{500}$. In this section, we show that these profiles are more affected by the weight of a few individual observations, and that the empirical O/Mg/S profiles can be very well reproduced when temporarily ignoring these peculiar measurements.

When we exclude M 49, M 60, and NGC 4636 from the analysis, we find a much better agreement between the O abundance and its correspond-

6.6 Systematic uncertainties

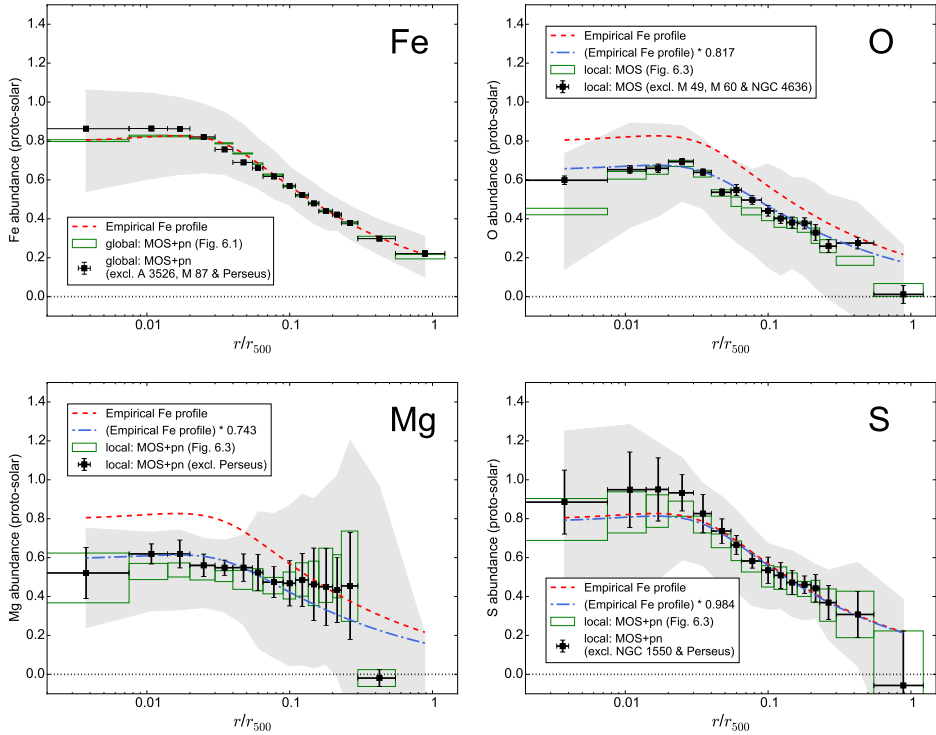


Figure 6.8: Same as Figs. 6.1 and 6.3 (Fe, O, Mg, and S, blue empty boxes), where we discard A 3526, M 87, and Perseus from the Fe average profile (*top left*), M 49, M 60, and NGC 4636 from the O average profile (*top right*), Perseus from the Mg average profile (*bottom left*), and NGC 1550 and Perseus from the S average profile (*bottom right*). These modified profiles are shown by the black squares.

ing empirical prediction in the innermost bin (Fig. 6.8 top right). Indeed, these three ellipticals/groups are characterised by a suspiciously low O abundance within their respective $<0.5'$ annuli (inconsistent with the values found within $0.8'$ with RGS by de Plaa et al. 2017), which, together with very small errors bars, contribute to substantially lower the average O abundance in the $\leqslant 7.5 \times 10^{-3} r_{500}$ region.

When we exclude Perseus from the analysis, the average Mg measurements agree much better with the expected empirical profile, especially within $\sim 0.01\text{--}0.05 r_{500}$ (Fig. 6.8 bottom left panel). The significant MOS-pn discrepancies measured in the Perseus spectra make the Mg abundance somewhat uncertain over the region considered above. However, and coincidentally, combining these (discrepant) MOS/pn measurements from Perseus with those from the rest of the sample brings the average MOS and pn estimates of Mg at very similar levels, thereby dramatically reducing the total MOS-pn uncertainties that we consider in Sect. 6.4.3. This case is thus a good illustration that care must be taken when combining individual systematic uncertainties over a large data sample. Finally, the exclusion of NGC 1550 and Perseus from the sample contributes to a better agreement of the measured S profile with its empirical expectation (Fig. 6.8 bottom right).

To sum up, in addition to showing that the average measured radial abundance profiles for all elements can reproduce very well their empirical counterparts, this section illustrates that care must be taken when strictly interpreting the error bars shown in the figures of this paper, as only one or two individual observations may slightly (usually, within a few per cent) but significantly raise or lower our measurements. That said, in the rest of the paper we consider our full sample, including the peculiar measurements discussed here.

6.6.5 Atomic code uncertainties

The CIE model employed to fit our EPIC spectra is based on the `mekal` model (Mewe et al. 1985, 1986, also present in XSPEC), with important updates up to now. The atomic database and routines on which this model relies is called SPEXACT⁶. Whereas the initial version of SPEXACT can be simply attributed to the original `mekal` model, the version used in this work (corresponding to the atomic code that was regularly updated between

⁶SPEX Atomic Code and Tables

1996 and 2016) is referred to SPEXACT v2. In recent months, substantial efforts have been devoted towards a major update of the code (SPEXACT v3), followed by a newly released version of SPEX (de Plaa et al. 2017). For example, this new version includes a more precise parametrisation of the radiative recombination rates (Mao & Kaastra 2016), updated collisional ionisation coefficients (Urdampilleta et al. 2017), and the calculation of many more transitions. Following Chapter 3, we included the correction of this latest update on our O abundance measurements (Sect. 6.3.1). However the abundances of the other elements may also be affected by such improved calculations.

Unfortunately, fitting all our EPIC spectra using SPEXACT v3 would require unrealistic amounts of computing time and resources. Therefore, we evaluate the impact of these atomic code differences on the EPIC abundances by following a similar approach as carried out by de Plaa et al. (2017) for RGS (see also Chapter 5). Here, we simulate EPIC spectra assuming a `gdem` distribution calculated from SPEXACT v3, for a range of mean temperatures from 0.6 keV to 6.0 keV and by setting all the abundances to 1. We then fit these mock spectra locally with a `gdem` model calculated from SPEXACT v2 (i.e. the version used in this work), and we measure the changes in the best-fit abundances. The result is shown in Fig. 6.9.

For temperatures hotter than \sim 1.5 keV, most of the abundances do not change by more than \sim 20%. The two exceptions are Mg and Ni, which can change by almost a factor of 2 at high and low temperatures, respectively. For temperatures cooler than \sim 1.5 keV, we see a dramatic decrease (by more than a factor of 2) of the measured Fe abundance. The main difference between the spectral models generated by SPEXACT v2 and SPEXACT v3 resides in the Fe-L complex, which is foremost used by the fits to determine the Fe abundance in cool ($kT \lesssim 2$ keV) plasmas.

Since most of the computed abundances remain fairly constant within the typical temperature range (\sim 1–5 keV) of all the spectra of our sample, such atomic code uncertainties are not expected to affect our results. Nevertheless, we note that these changes between SPEXACT v2 and SPEXACT v3 may have a non-negligible impact on the integrated abundances (and X/Fe abundance ratios) reported in previous works. For instance, if updated atomic calculations indeed revise the average Ni/Fe abundance downwards (so far measured to be surprisingly high; e.g. Chapters 3 and 4), a more simple agreement than previously assumed between the ICM abundance pattern and SN yield models may be expected. This issue (and

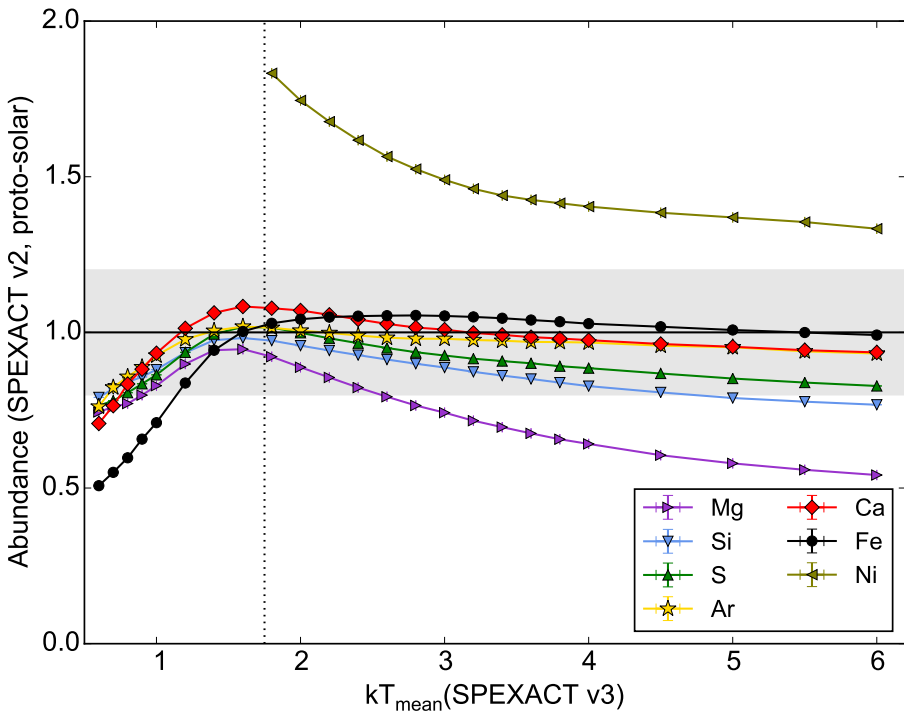


Figure 6.9: Abundance results from (gdem) local fits with SPEXACT v2 to simulated SPEXACT v3 spectra for a range of temperatures (see also Fig. 5.1). The measured abundances are shown and compared to their input value of 1 proto-solar. The grey shaded area shows the $\pm 20\%$ level of uncertainty. The vertical dotted line indicates our (arbitrary) separation between clusters and groups.

further use of SPEXACT v3 on real cluster data) is discussed extensively in Chapter 5.

6.6.6 Instrumental limitations for O and Mg abundances

Finally, we must warn that the EPIC instruments have limitations in deriving accurate O and Mg abundances.

The main K-shell transitions of O (~ 0.6 keV rest-frame) are situated close to the oxygen absorption edge, and the interstellar absorption may affect the O abundance determination, as the EPIC spectral resolution cannot resolve the emission and absorption features within this band (see e.g.

de Plaa et al. 2004). Moreover, and despite our considerations from Sect. 6.6.3, the Galactic foreground may play a more important role than expected, which can potentially bias the O abundance, especially when the background dominates. Although affecting on average 3–4% of the XMM-Newton observations, solar wind charge exchange might also be a source of (limited) bias for the O abundance, as it may affect the O VII and O VIII lines in the contaminated spectra (e.g. Snowden et al. 2004; Carter et al. 2011).

On the other hand, the main K-shell emission line of Mg (\sim 1.5 keV rest-frame) falls partly into the Fe-L complex, which is unresolved by the EPIC instruments. Moreover, measuring the Mg abundance in clusters outskirts is challenging because the EPIC hard particle background is contaminated by the Al $K\alpha$ fluorescence line, which is also situated at \sim 1.5 keV both in MOS and pn instruments (Chapter 2), and thus impossible to disentangle from the Mg K-shell ICM emission lines using the EPIC spectrometers.

Despite all these limitations, the good agreement of our average O and Mg profiles with their respective empirical predictions (at least out to \sim 0.3 r_{500} , and after discarding specific observations from the sample, see Sect. 6.6.4) is very encouraging, and makes us confident about the results presented in this work.

6.7 Discussion

We derived the average radial abundance profiles of 44 galaxy clusters, groups, and elliptical galaxies. In Sect. 6.5, we were able to provide constraints on the radial ICM distributions of Fe, but also O, Mg, Si, S, Ar, Ca, and Ni, comparing them within clusters ($>$ 1.7 keV) and groups ($<$ 1.7 keV). In the previous section, we also showed that the major systematic uncertainties are kept under control. We now discuss our results and we compare them with measurements and predictions from previous studies.

6.7.1 Enrichment in clusters and groups

In Fig. 6.2, we compared the radial Fe abundance profile averaged over clusters, on the one hand, and groups, on the other hand. Although the scatter in each profile is large, the average enrichment level in clusters is slightly higher than in groups. This result is not surprising, as an increase of the ICM metallicity with the cluster/group temperature (at least up to

$kT \simeq 3$ keV) has been commonly observed in previous studies (e.g. Rasmussen & Ponman 2009; Yates et al. 2017). This trend is also consistent with the results of Chapter 3, where we analysed the same sample with the same data and same definition for clusters versus groups/ellipticals. They found that, within $0.05r_{500}$, the Fe abundance in clusters is on average $\sim 22\%$ higher than in groups. We find a similar Fe enhancement (on average $\sim 21\%$) in our profiles for clusters and groups at all radii, except in their respective innermost and outermost radial bins (see also Sect. 6.5.1). The absence of difference of Fe abundance in the innermost bin of clusters and groups can be explained by the important weight of a few individual clusters, as already discussed in Sect. 6.6.4. In particular, the cores of Perseus and A 3526 show deep and significant Fe drops (see also Sect. 6.7.2), which tend to lower the innermost average Fe abundance for clusters. Removing these two objects from the sample increases this innermost Fe abundance (Fig. 6.8 top left), and, therefore, should contribute towards keeping a similar enhancement between clusters and groups within $\sim 0.01r_{500}$. On the other hand, among the 11 measurements in the outermost radial bin of the groups profile, only 2 ($\sim 18\%$) are located beyond $0.5r_{500}$, i.e. covering the outermost bin of the clusters profile. The Fe abundance averaged over this outermost bin of the groups profile is thus weighted towards the measurements at smaller radii, roughly at the location of the third ($<0.34r_{500}$) and second ($0.34\text{--}0.5r_{500}$) outermost bins of the clusters profile. This explains the illusion of a Fe enhancement in the outskirts of groups with respect to those of clusters.

In summary, the average Fe profile of clusters is consistent with being more enhanced in a similar way not only in the core, but also at all radial distances at least out to $0.5r_{500}$. The origin of such a difference of ICM enrichment between cooler and hotter objects is still unclear, and has been already debated in the literature (e.g. Rasmussen & Ponman 2009; Liang et al. 2016; Yates et al. 2017). For example, in contrast to clusters, galaxy groups may not be closed boxes (e.g. McCarthy et al. 2011) and AGN feedback may contribute to remove enriched material out of the groups. It may even be possible that part of this apparent difference of enrichment could be due to underestimated Fe abundances in low temperature plasmas, as mentioned in Sect. 6.6.5. A thorough discussion of these aspects is somewhat beyond the scope of this paper. However, our radial profiles may provide useful constraints on the dominant mechanisms that are responsible for such a difference.

Interestingly, the same trend between clusters and groups is not clearly observed in the average profiles of other elements. Instead, these abundance profiles are consistent within clusters and groups (Fig. 6.4). In fact, we report a slight (but not significant) enhancement in the X/Fe ratio profiles of groups compared to those of clusters, up to $0.03r_{500}$, whose effect is visible in the Si/Fe and S/Fe profiles of the full sample (Fig. 6.5). However, the large error bars (including systematic uncertainties from the MOS-pn cross-calibration) prevent us from firmly confirming this trend. We also note the exception of the O profiles, which clearly show an enhancement in the case of clusters with respect to that of groups. However, we must recall that O measurements using EPIC may be still uncertain (Sect. 6.6.6). Moreover, the measured O abundance in hotter systems may be biased high compared to its true value, essentially owing to issues in determining the correct continuum coupled to the weak emissivity of the O VIII line at these temperatures (Rasia et al. 2008).

6.7.2 The central metallicity drop

As seen in Figs. 6.18 and 6.19, some clusters and groups clearly exhibit a central drop in their Fe abundances. The presence of drops in these systems also appear in Fig. 6.1, where a slight central decrease is observed in the average Fe abundance profile. Figures 6.3 and 6.5 suggest that these drops are not exclusive to Fe, as the other metals seem to be concerned. In this section, we attempt to quantify these abundance drops (focussing mainly on Fe) and then discuss their possible origins.

One way of quantifying the Fe drops is to measure their "depths". We choose arbitrarily the quantity $\text{Fe}(r_{\max})/\text{Fe}_{\text{drop}}$: we divide the Fe abundance at its off-centre peak (or the Fe abundance at its second innermost bin, if the profile is monotonically decreasing) by the Fe abundance at the first innermost bin. With this definition, all the objects with $\text{Fe}(r_{\max})/\text{Fe}_{\text{drop}}$ significantly greater than 1 are considered to host a significant drop. We find that 14 objects ($\sim 32\%$) of our sample show a decrease of Fe abundance in their very core. Three of these objects (2A 0335+096, A 3526, and Perseus) are classified as clusters (i.e. $\sim 13\%$ of the subsample), while the remaining 11 (A 189, A 3581, Fornax, HCG 62, M 49, M 86, NGC 4325, NGC 4636, NGC 5044, NGC 5813, and NGC 5846) are classified as groups (i.e. $\sim 52\%$ of the subsample). This apparent larger proportion of groups hosting a central metallicity drop should be treated with caution because the larger distance of many clusters does not allow us to investigate their very core with the

same spatial resolution as for nearer groups and ellipticals. Similarly, the drop seen in the average Fe profile (Fig. 6.1) is smoothed by the lower spatial resolution of more distant systems, and thus appears less pronounced than in individual nearby objects.

In most cases, the Fe drop is only seen in the innermost bin. However, some objects (e.g. Perseus, Fornax, M 49, and NGC 5044) clearly exhibit a drop extending within several radial bins. Therefore, for each object we also evaluate r_{\max}/r_{500} , i.e. the location of the (off-centre) Fe peak, in units of r_{500} . For objects not showing any apparent drop, we adopt the extent of the innermost bin, which only provides an upper limit. Figure 6.10 shows a diagram of $\text{Fe}(r_{\max})/\text{Fe}_{\text{drop}}$ versus r_{\max}/r_{500} (i.e. the depth of the drops versus the location of the Fe off-centre peaks). The grey shaded area corresponds to the objects with no apparent drop ($\text{Fe}(r_{\max})/\text{Fe}_{\text{drop}} \leq 1$), where only an upper limit of r_{\max}/r_{500} could be constrained. When restricting ourselves to the objects exhibiting a drop (white area), we do not find evidence for a clear correlation ($\rho \simeq 0.19$) between the depth and radial extent of the drops. In fact, the error bars and scatter of the measurements are quite large and prevent us from deriving any firm conclusion on this assessment. The ACIS instrument on board *Chandra* could help to reduce the error bars and to confirm (or rule out) this correlation. Such a detailed study, however, is beyond the scope of this present paper, and we leave it for future work.

This is not the first time that central metallicity drops have been found in the core of the ICM (e.g. Sanders & Fabian 2002; Johnstone et al. 2002; Sanders & Fabian 2007; Rafferty et al. 2013). However, their interpretation is not yet established. Below we discuss several possibilities that could explain the metallicity drops found in this work.

First, these apparent drops in metallicity could be the result of an artefact when fitting the spectra of the central regions. For example, an inappropriate modelling of the X-ray emission of the central AGN (or cumulated X-ray binaries in the BCG) could potentially introduce an incorrect estimate of the continuum of the ICM emission and underestimate the abundances in the very core. However, the abundance decrease extends sometimes outside the innermost region (Fig. 6.19, see e.g. Fornax, M 49, and NGC 5044), where no contamination from AGN emission is expected. Similarly (and perhaps more interestingly), the presence of non-thermal electrons in X-ray cavities could produce an additional power law component, which would underestimate the abundances if not properly

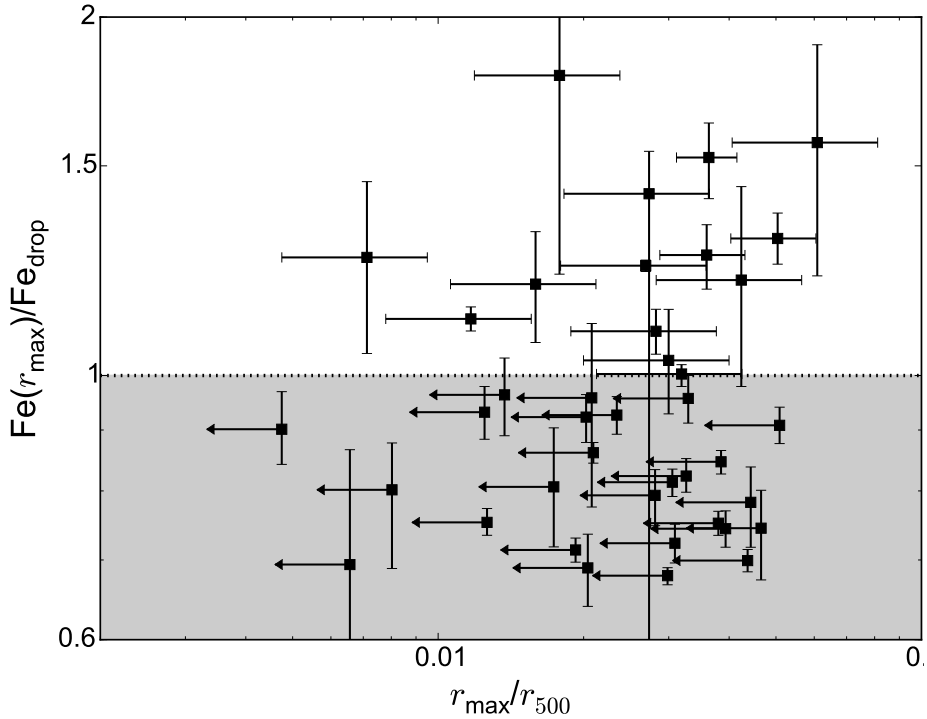


Figure 6.10: Depth of the central Fe drop ($\text{Fe}(r_{\max})/\text{Fe}_{\text{drop}}$) vs. location of the Fe off-centre maximum (r_{\max}/r_{500}) for all the objects of our sample. A value $\text{Fe}(r_{\max})/\text{Fe}_{\text{drop}} \lesssim 1$ (grey area below the dotted horizontal line) means that no Fe drop could be significantly detected and only upper limits of r_{\max}/r_{500} could be estimated.

modelled. However, we would then expect a good match between cavities extents (and morphologies) and abundance drops, which is not actually observed (Panagoulia et al. 2015; Sanders et al. 2016). Another possibility would be that the abundances measured in the very core suffer from the Fe/Si/S-bias (e.g. Buote 2000) owing to too simple assumptions concerning the thermal modelling. While accounting for a multi-temperature structure may sometimes help to remove the abundance drop (e.g. in 2A 0335+096; Werner et al. 2006b), this is not necessarily true for all the sources (e.g. Sanders et al. 2004; Panagoulia et al. 2013). Moreover, we must recall that all our spectra are fitted with a `gdem` model, which already assumes a multi-phase plasma. As a test, we also checked that the use of a `wdem` model does not remove the central drop in A 3526. We admit, however, that a better

knowledge of the true temperature distribution in cooling cores would be required to investigate in detail its impact on the very central abundance measurements. We can also discard other artificial effects such as projection on the plane of the sky (Sanders & Fabian 2007) or resonant scattering (Sanders & Fabian 2006b), since they are not efficient enough to fully remove the drops. Finally, the underestimate of the Fe abundance at CCD resolution for low temperatures (Sect. 6.6.5) could be an alternative fitting bias to explain the abundance drops. Although this could explain some abundance drops found in very cool group cores (e.g. NGC 5813), this bias can hardly be invoked in the case of core temperatures above ~ 1 keV still exhibiting a drop (e.g. A 3526).

Second, assuming that the drops are real, it may be reasonable to speculate that a fraction of the central metal mass has been redistributed from the core, by either AGN feedback, or sloshing motions. Whereas it is now well established that AGN feedback may play a key role in transporting the metals outside of the very core via jets and / or buoyant bubbles, as already observed in M 87 (Simionescu et al. 2008) and in Hydra A (Simionescu et al. 2009b), simulations do not favour any clear formation of inner drops (e.g. Guo & Mathews 2010). Furthermore, we do not find any correlation between AGN radio luminosities ($L_{1.4\text{ GHz}}$) reported in the literature (e.g. Bîrzan et al. 2012) and the depths ($\text{Fe}(r_{\max})/\text{Fe}_{\text{drop}}$) or the radial extent (r_{\max}/r_{500}) of the drops in our sample. Similarly, while the extended drop seen in NGC 5044 might be partly explained by its peculiar metal distribution in the sloshed gas (O’Sullivan et al. 2014), sloshing process can probably not explain the (narrower) drops seen in other objects (Roediger et al. 2011, 2012).

Third, and alternatively, the drops could be the result of the depletion of a part of the ICM-phase metals into dust grains. In the scenario proposed by Panagoulia et al. (2013, 2015), a significant part of the metals released by SNe within the BCG remain in the form of cold dust grains (Voit & Donahue 2011) and become incorporated into the central dusty filaments. These dust grains are then dragged out by buoyant bubbles caused by the AGN activity and are released back in the hot ICM phase out of the very core, thereby forming the off-centre Fe peak. This idea is supported by the presence of dust in most of the objects studied by Panagoulia et al. (2015) and showing a metallicity drop. The authors emphasise that such a scenario can be tested by the behaviour of the Ne and Ar radial profile in the very core of clusters and groups. Indeed, while elements like Fe, Si, and S are

known to be easily embedded in dust grains, Ne and Ar are noble gases and are not expected to be incorporated into dust⁷. Consequently, their radial abundance profiles should not show any sign of drop or flattening in the innermost regions. As mentioned in Sect. 6.3.1, the EPIC spectral resolution does not allow us to investigate the Ne radial distribution. Interestingly, the radial Ar distribution does not follow well the (rescaled) Fe distribution as it shows a sharper gradient than expected by the empirical Fe profile (Figs. 6.3 and 6.5). This sharper gradient is consistent with the different average Ar/Fe ratios measured in Chapter 4 in the $\leq 0.05r_{500}$ and the $\leq 0.2r_{500}$ regions. Similarly, the central ($\lesssim 0.02r_{500}$) measured Ar abundances lie somewhat higher than expected. As an (speculative) explanation for this particular feature seen only in the Ar profile, dust depletion in the cool-core ICM (presumably affecting all the considered elements, except Ar) might play a substantial role in shaping the abundance profiles of depleted elements, in particular within $\sim 0.1r_{500}$. However, our average Ar profile points towards the presence of a flattening (if not a drop) in the innermost bin (Fig. 6.3), suggesting that dust depletion only may not be sufficient to explain the innermost metal drops. That said, the very large scatter of the Ar abundance prevents us from claiming any firm evidence for/against this scenario. When investigating the individual abundance profiles of Perseus and A 3526 (i.e. the two objects hosting an abundance drop and providing the best statistics), as shown in Fig. 6.11, we find that the MOS measurements in A 3526 suggest a monotonic increase of Ar towards the centre. The other measurements (pn in A 3526, and MOS and pn in Perseus) instead suggest that Ar follows the Fe drop. To summarise, although we are not able to firmly favour or rule out this dust depletion scenario, our results might suggest a non-negligible effect of dust depletion of gas-phase metals in clusters, but do not confirm that metals that are embedded in dust in the very core of clusters/groups would be the unique origin of the abundance drops.

Fourth, the apparent drops may be the result of an underestimate of the helium content in the very core of such objects. Because He transitions do not occur at X-ray energies, it is impossible to provide any direct constraint on the He abundance in the ICM. In all our fits (as in the majority of the similar studies found in the literature), we assume that He follows the primordial abundance ($\sim 25\%$ of mass fraction; e.g. Peimbert et al.

⁷Dusty Ar might appear in the form of cold molecular gas $^{36}\text{ArH}^+$ (Barlow et al. 2013), but the presence of such a gas in cluster cores still remains highly uncertain.

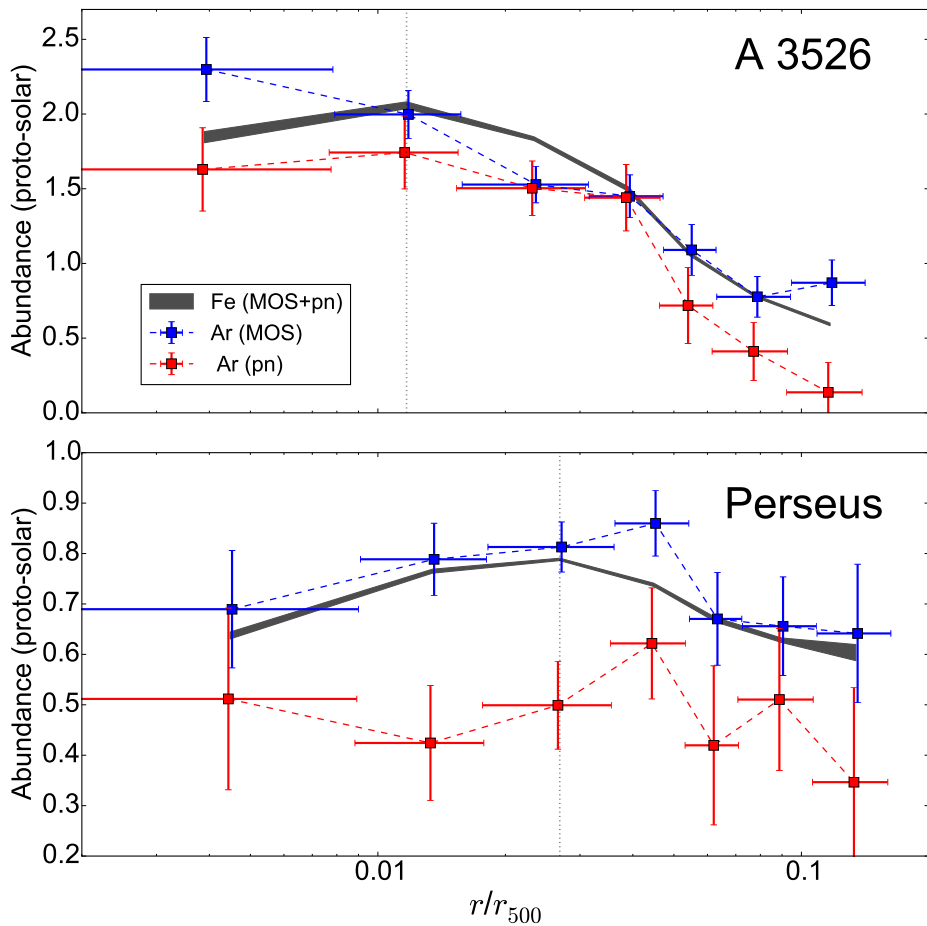


Figure 6.11: Ar radial profiles in A 3526 (upper panel) and Perseus (lower panel) for independent MOS and pn measurements. The shaded areas show the (combined MOS+pn) Fe radial profiles. The grey vertical dotted lines indicate the Fe peaks.

2016). However, the large gravitational potential in the core of clusters and groups may be efficient in retaining He, which could be more centrally peaked than H (Fabian & Pringle 1977; Abramopoulos et al. 1981). If we effectively underestimate the He abundance in our fits of the core region, the net continuum would be overestimated, resulting in a bias of all our metal abundances towards lower values (e.g. Ettori & Fabian 2006). We illustrate this effect in Fig. 6.12, where we assume the He abundance in our fits of the innermost bin of A 3526 to be successively 1.25, 1.5, 1.75, 2, 2.25, and 2.50 times the primordial value. As can be seen, a He abundance that is 1.5 higher than previously assumed in the ICM core is sufficient to remove the inner Fe drop significantly. However, recent models point towards a less important He sedimentation in the very centre of cool-core clusters than in their surroundings ($\sim 0.4\text{--}0.8r_{500}$; Peng & Nagai 2009). Moreover, as already noted by Panagoulia et al. (2015), thermal diffusion may also play an important role in counteracting He sedimentation and in removing He and other metals (including Fe) out of the very core of clusters (Medvedev et al. 2014). Nevertheless, the relative importance of thermal diffusion is also expected to be significantly weaker than the importance of AGN feedbacks, especially in galaxy groups, where most of the Fe drops are found.

Finally, and interestingly, some hydrodynamical simulations (Schindler et al. 2005; Kapferer et al. 2009) predict a drop of central abundances when assuming galactic winds as the dominant mechanism transporting the metals from galaxies to the ICM. However, the typical extent of such a drop is ~ 400 kpc, which is always much larger than the typical extents derived from our observations (a few tens of kpc at most). Moreover, this suppression of metal enrichment by galactic winds should preferentially happen in hot and massive clusters, where the ICM pressure is high enough. Instead, we find metal drops for a large portion of less massive objects.

6.7.3 The overall Fe profile

Comparison with previous measurements

The average Fe radial profile of our full sample (Fig. 6.1) can be compared to other average profiles reported in the literature. Leccardi & Molendi (2008) measured radial metallicity profiles for a sample of 48 hot ($\gtrsim 3.3$ keV) intermediate redshift ($0.1 \lesssim z \lesssim 0.3$) clusters using *XMM-Newton*. Similar studies for nearby cool-core clusters have been carried out by Sander-son et al. (2009, *Chandra*, $z < 0.1$) and Matsushita (2011, *XMM-Newton*,

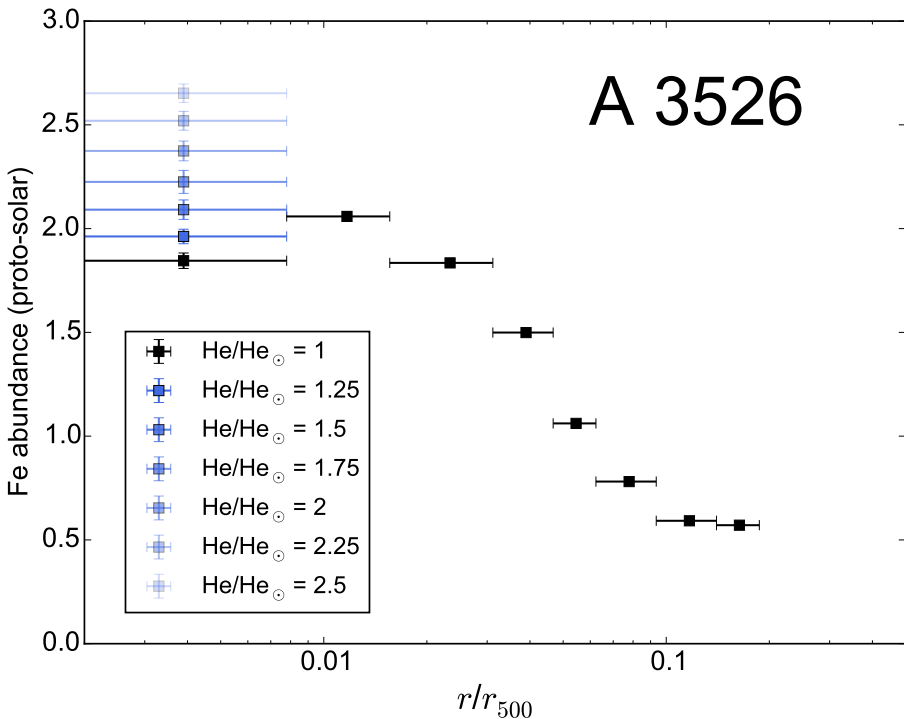


Figure 6.12: Effects of a hypothetical underestimate of the He fraction on the measured Fe abundance in the innermost bin of A 3526.

$z < 0.08$). Finally, Rasmussen & Ponman (2007) measured radial metallicity profiles for a sample of 15 nearby galaxy groups using *Chandra*. Figure 6.13 illustrates the comparison between our measurements and the three sample-based studies mentioned above. The choice of the reference (solar or proto-solar) abundance tables often varies in the literature; the most commonly used is Anders & Grevesse (1989). Before comparing the profiles, all the abundances were rescaled to the proto-solar values of Lodders et al. (2009) used in this work.

As seen in the upper panel of Fig. 6.13 (clusters), our Fe abundance profile is in excellent agreement with the measured profiles of Sanderson et al. (2009) and Matsushita (2011). Only the second outermost bin of the profile of Matsushita (2011) deviates from our values by $<2\sigma$, while all the other radial bins of these two profiles are 1σ consistent with our measure-

6.7 Discussion

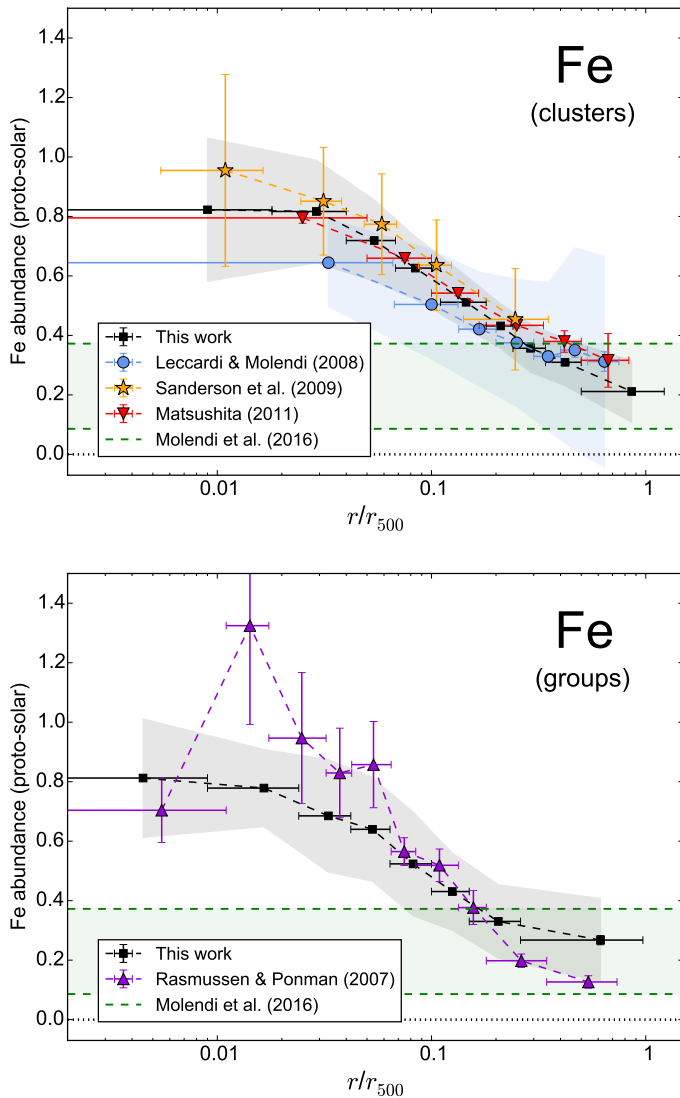


Figure 6.13: Comparison of our average radial Fe profiles (Fig. 6.2) with estimations from previous works for clusters (*top*) and groups (*bottom*). Green dashed lines (and the corresponding shaded area) show the best constrained limits of the Fe abundance at r_{180} ($\approx 1.7r_{500}$) derived by Molendi et al. (2016).

ments. The two innermost bins of the average profile of Leccardi & Molendi (2008), however, have significantly lower Fe abundances than this study. This can be easily explained, as the sample of Leccardi & Molendi (2008) contains both cool-core and non-cool-core clusters. Because of their substantially less steep abundance decrease (Sect. 6.1), including non-cool-core clusters in a sample naturally flattens its average metallicity profile. Interestingly (and encouragingly), the four compared profiles agree very well beyond $\sim 0.15r_{500}$ up to their respective outermost bins. This, together with the limited Fe scatter in the outermost radial bins of this work, may suggest a universal metallicity distribution outside cluster cores. We note that, however, from the 17 cool-core objects of the sample of Matsushita (2011), 13 are present in our sample as well (including M 87). Very similar abundance profiles were thus expected, even at the cluster outskirts. Nevertheless, none of the clusters from the sample of Leccardi & Molendi (2008) are also present in our sample, and the very similar average abundance (~ 0.2 – 0.3) found beyond $\sim 0.5r_{500}$ for both nearby and intermediate redshift clusters is clearly an interesting result. Finally, the average Fe abundance measured in this work is fully consistent with the (large but conservative) limits at r_{180} ($\simeq 1.7r_{500}$) established by Molendi et al. (2016).

The lower panel of Fig. 6.13 (groups) shows a comparison between our average Fe abundance profile for groups and the average profile derived by Rasmussen & Ponman (2007). There is an overlap of six groups between the two samples. While the results agree below $0.01r_{500}$ and within 0.07 – $0.2r_{500}$, disagreements can be seen elsewhere. Within 0.01 – $0.07r_{500}$, the Rasmussen & Ponman (2007) abundances are $<2\sigma$ consistent with our average groups profile. However, the authors detect a deep average central abundance drop, which does not appear in our stacked profile. This difference may be explained by the large variety of metallicity profiles within the very core of groups, as seen in Fig. 6.19 and in Rasmussen & Ponman (2007, see their fig. 3), and by the different groups selected in each respective sample. In particular, Rasmussen & Ponman (2007) consider MKW 4 part of their group sample, and using the ACIS instrument, they detect an off-centre Fe peak reaching ~ 5 – 10 times the proto-solar value, which is more than two times the Fe abundance in its centre. This extreme measured metallicity should partly explain the high value of their second innermost average bin (Fig. 6.13 bottom). On the other hand, mismatch is also found beyond $\sim 0.2r_{500}$, where the average metallicity of Rasmussen & Ponman (2007) in the outskirts is measured ~ 2 times lower than in this work (al-

though still within our inferred scatter). This issue is important to point out since Rasmussen & Ponman (2007) interpret the lower enrichment in the group outskirts as a different groups enrichment history compared to more massive clusters. While uncertainties in the respective background treatments of the studies might explain the disagreement with our results, we must point out that an updated *Chandra* calibration may revise upwards the Fe abundance in the outermost bins (e.g. $\sim +25\%$ for NGC4325 Rasmussen & Ponman 2009). Moreover (and perhaps more importantly), Rasmussen & Ponman (2007) measured the Fe abundances via only the Fe-L complex, and they assumed a single-temperature model in the spectra of each of their outermost bins. This may significantly underestimate the Fe abundance in case of a multi-phase plasma in the group outskirts.

Comparison with simulations

The average Fe radial profile derived in this work (Fig. 6.1) can also be compared with the average Fe profile predicted by hydrodynamical simulations. Two of the most recent simulation sets of the ICM including metal enrichment were performed by Planelles et al. (2014) and Rasia et al. (2015). Both sets use the smooth particle hydrodynamics code GADGET-3, assume a Chabrier initial mass function (IMF; Chabrier 2003), and incorporate the chemical evolution model (including metal production by SNIa, SNcc, and AGB stars) of Tornatore et al. (2007), taking SN-powered galactic winds and AGN feedback into account. The comparison of our average Fe profile with these two simulation sets is shown in Fig. 6.14.

The mean emission-weighted Fe profile from the "AGN set" of Planelles et al. (2014, derived from a sample of 36 hot nearby systems within 29 simulated regions), shown in solid red lines (with its scatter in the shaded red area) in Fig. 6.14, does not agree with our observations. In fact, a similar result was already discussed by the authors when comparing their predictions with the observations of Leccardi & Molendi (2008). However, as explained by Planelles et al. (2014), this significantly higher normalisation can be easily explained by outdated assumptions on the SN yields, the assumed IMF, the fraction of binary systems (eventually resulting in SNIa), and/or the SN efficiency to release metals into the ICM. The overall shape of the AGN set profile, however, is more crucial to confront with observational data, since AGN feedbacks presumably have a strong influence on (i) displacing metals from star-forming regions, (ii) suppressing star formation, and (iii) preventing cooling of the hot gas to temperatures emitting

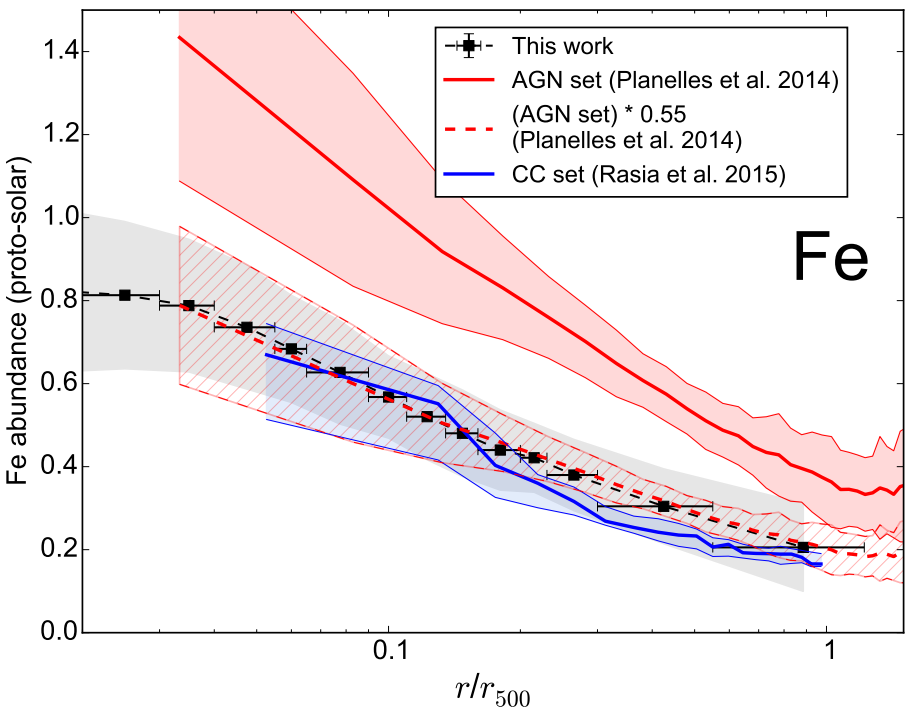


Figure 6.14: Comparison between our average Fe measured radial profile (Fig. 6.1) and predictions from hydrodynamical simulations from Planelles et al. (2014, solid red lines) and Rasia et al. (2015, solid blue lines), both modelling AGN feedback effects on the chemical enrichment. The red dashed lines show the same simulation set from Planelles et al. (2014) with a normalisation rescaled by a factor of 0.55.

outside of the X-ray energy band. Interestingly, when applying a factor of ~ 0.55 to the normalisation of this predicted Fe profile (dashed red lines in Fig. 6.14), we find an excellent agreement with our measurements. In other words, the simulations of Planelles et al. (2014) are remarkably successful at reproducing the measured chemical properties of the ICM, as long as the overall metal content produced and released in the gas phase is ~ 1.8 times lower than originally assumed. This is not impossible, as both SN yields and SNIa rates are still uncertain within a factor of ~ 2 (Wiersma et al. 2009). However, a direct comparison between our results and the simulations of Planelles et al. (2014) should be treated with caution. In fact, the simulation sets of Planelles et al. (2014) contain both relaxed and non-relaxed sys-

tems (and fail to recover the cool-core versus non-cool-core dichotomy), while our observation are only based on cool-core clusters. Moreover, the simulated profiles are extracted from three-dimensional spherical shells, whereas our results are projected on the plane of the sky. This latter difference, however, is not expected to strongly affect the present comparison (Sect. 6.6.1).

A significant improvement of the simulation sets of Planelles et al. (2014) has been achieved by Rasia et al. (2015), shown by the solid blue lines (with its scatter in the shaded blue area) in Fig. 6.14. This more recent set of simulations, also including AGN feedback effects, constitutes the first success of disentangling cool-core (shown in Fig. 6.14) and non-cool-core clusters. We find a reasonable agreement between the simulated profile of Rasia et al. (2015) and our observed profile within $\sim 0.05\text{--}0.2r_{500}$. Beyond $\sim 0.2r_{500}$, the simulated profile slightly underestimates our observations ($\sim 20\text{--}25\%$), but still lies within the scatter, which also includes possible systematic uncertainties (see Sect. 6.6). Here as well, care must be taken when directly comparing observations and simulations. Similar to Planelles et al. (2014), the simulated profile of Rasia et al. (2015) is also unprojected. Moreover, this profile is also mass weighted, while our measurements are directly derived from spectroscopy and are thus emission weighted. The conversion of mass weighted to emission weighted Fe profiles may result in a $\sim 30\%$ increase of the normalisation within r_{500} (Planelles et al. 2014). Such a change in the profile normalisation would lead to an excellent agreement with our results outside $\sim 0.2r_{500}$, but to predictions that are slightly too high below this radius.

Furthermore, from a numerical point of view, simulations of the chemodynamical state of the very core ($\lesssim 0.05r_{500}$) of the ICM are extremely challenging. Nevertheless, the good overall agreement between theoretical models and observations presented in this paper must emphasise the remarkable progress achieved by simulation groups in recent years. Future and more complete simulations will surely help to further improve the current picture of metal distributions in the ICM (e.g. Biffi et al. 2017).

6.7.4 Radial contribution of SNIa and SNcc products

From Figs. 6.3 and 6.5 and the discussion above (e.g. Sect. 6.6.4), it clearly appears that the radial abundance profiles of O, Mg, Si, S, Ar, Ca, and Ni decrease with radius. Except Ar (see Sect. 6.7.2), all these profiles also scale quite remarkably with the Fe radial distribution, keeping a constant X/Fe

ratio out to (and sometimes even beyond) $0.5r_{500}$. In particular, the uniform radial O/Fe ratio is an important result. It is in contradiction with the flat O profiles found in, for example A 496 (Tamura et al. 2001), M 87 (Böhringer et al. 2001; Matsushita et al. 2003; Werner et al. 2006a), NGC 5044 (Buote et al. 2003), AWM 7 (Sato et al. 2008), and a sample of 19 clusters (Tamura et al. 2004). On the contrary, this trend is consistent with the peaked O profiles found in, for example A S1101 (de Plaa et al. 2006), A 3526 (Sanders & Fabian 2006a), Hydra A (Simionescu et al. 2009b), A 3112 (Bulbul et al. 2012b), A 4059 (Chapter 2), and 5 cool-core clusters Lovisari et al. (2011).

In Fig. 6.15, we show a comparison of our measured Si/Fe profile (from Fig. 6.5) with two equivalent profiles reported from the literature. In their sample of 15 nearby galaxy groups, Rasmussen & Ponman (2007, purple triangles) measured a flat Si/Fe profile up to $0.2r_{500}$, followed by a dramatic increase in the outskirts (although observed with rather large error bars in two radial bins only). In a companion paper (Rasmussen & Ponman 2009), the same authors interpret this increase as a dominant enriching fraction of SNcc products in group outskirts, in agreement with the increasing O/Fe and / or Mg/Fe profiles observed in other studies (see above). Taking advantage of the low instrumental background of *Suzaku XIS*, Simionescu et al. (2015, four outermost green circles) reported a flat Si/Fe radial distribution in the outskirts of the Virgo cluster, in agreement with the Si/Fe ratios measured at smaller radii (Simionescu et al. 2010, two innermost green circles). Our flat Si/Fe profile is in agreement with the results of Simionescu et al. (2010, 2015) and contradicts the results of Rasmussen & Ponman (2007). Furthermore, our results are consistent with the Si/Fe predictions from the simulation sets of Planelles et al. (2014, solid red line), but we do not observe the slight predicted increase of Si relative to Fe towards the core below $0.1r_{500}$, expected from the suppression of cooling (predominantly processed by SNcc products) due to the AGN feedback (see also Fabjan et al. 2010). This issue was already discussed by Planelles et al. (2014), and could be due to efficient diffusion or transport mechanisms that were not yet implemented in the simulations.

In order to better quantify the radial contribution of SNIa and SNcc products, we fit the X/Fe abundance ratios in each radial bin with a combination of SNIa and SNcc yield models as described in Chapter 4. Based on their results, and because the large uncertainties of the measured abundances in individual bins do not allow us to favour any yield model in particular, we select the following two combinations of one SNIa and one

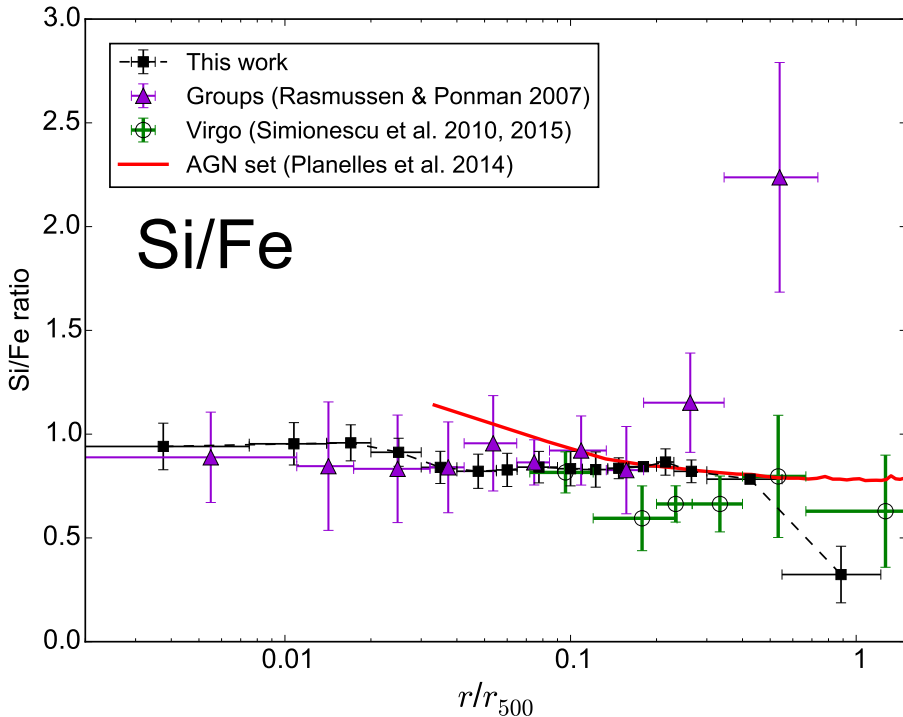


Figure 6.15: Comparison of the measured average radial Si/Fe profile (Fig. 6.5) with previous observations for galaxy groups (Rasmussen & Ponman 2007) and Virgo (Simionescu et al. 2010, 2015), and with the AGN simulation set of Planelles et al. (2014).

SNcc model that reproduce equally well the average abundance pattern within the ICM core ($0.2r_{500}$ or $0.05r_{500}$; Chapter 4):

1. The one-dimensional delayed-detonation SNIa yield model ("DDTc") introduced in Badenes et al. (2005) that reproduces the spectral features of the Tycho supernova remnant (Badenes et al. 2006), combined with the SNcc yield model from Nomoto et al. (2013) assuming an initial metallicity of stellar progenitors of $Z_{\text{init}} = 0.001$, and averaged over a Salpeter IMF (Salpeter 1955) between 10 and $40 M_{\odot}$ ("Z0.001");
2. The three-dimensional delayed-detonation SNIa yield model ("N100H") from Seitenzahl et al. (2013b), combined with the SNcc yield model from Nomoto et al. (2013), assuming an initial metallicity of stellar

progenitors of $Z_{\text{init}} = 0.008$ and IMF-averaged similarly as for the Z0.001 model ("Z0.008").

We fit the X/Fe abundance pattern measured in each radial bin (Fig. 6.5) successively with these two combinations of models. This allows us to estimate f_{SNIa} , the fraction of SNIa over the total number of SNe (i.e. SNIa+SNcc) contributing to the enrichment, as a function of the radial distance. This is shown in Fig. 6.16 (full sample) and Fig. 6.17 (clusters, upper panel; groups, lower panel). In all the (sub)samples, f_{SNIa} is fully consistent with being uniform up to $\sim 0.5r_{500}$, and agrees very well with the average values found in the ICM core (Chapter 4; dotted horizontal lines in the figures). In some radial bins, we observe slight but significant ($>1\sigma$) deviations from these core-averaged values. For example, we cannot exclude a slight increase of f_{SNIa} in groups, at least from $\sim 0.01r_{500}$ to $\sim 0.1r_{500}$. However, these deviations completely vanish when we account for the scatters of Fig. 6.5 in the estimation of f_{SNIa} (shaded areas). Such a radially uniform fraction has also been recently measured in A 3112 (Ezer et al. 2017).

As discussed in Sect. 6.6, the average values may be affected by systematic uncertainties and accounting for the scatters is conservative enough to keep all the systematic effects under control. Consequently, and although the flat radial behaviour of f_{SNIa} based on the average X/Fe ratios is quite remarkable (at least in clusters), we cannot fully exclude a changing SNIa-over-SNcc contribution to the enrichment beyond $\sim 0.2r_{500}$ in clusters and groups. Finally, and unsurprisingly, we find that a different choice of SN yield models only affects the absolute average f_{SNIa} value and not its relative radial distribution.

Implications for the enrichment history of the ICM

As discussed throughout this paper, our results are fully consistent with a uniform contribution of SNIa (SNcc) products in the ICM from its very centre up to (at least) $\sim 0.5r_{500}$. Although, accounting for various systematic uncertainties (including the population scatter, which dominates over the other uncertainties even at large radius), we cannot fully exclude an increase/decrease in the SNIa contribution to the enrichment outside $\sim 0.2r_{500}$, we do not observe a clear trend supporting that scenario. If true, the uniform radial contribution of SNIa products in the ICM has interesting consequences, as it provides valuable constraints on the enrichment history of galaxy clusters/groups.

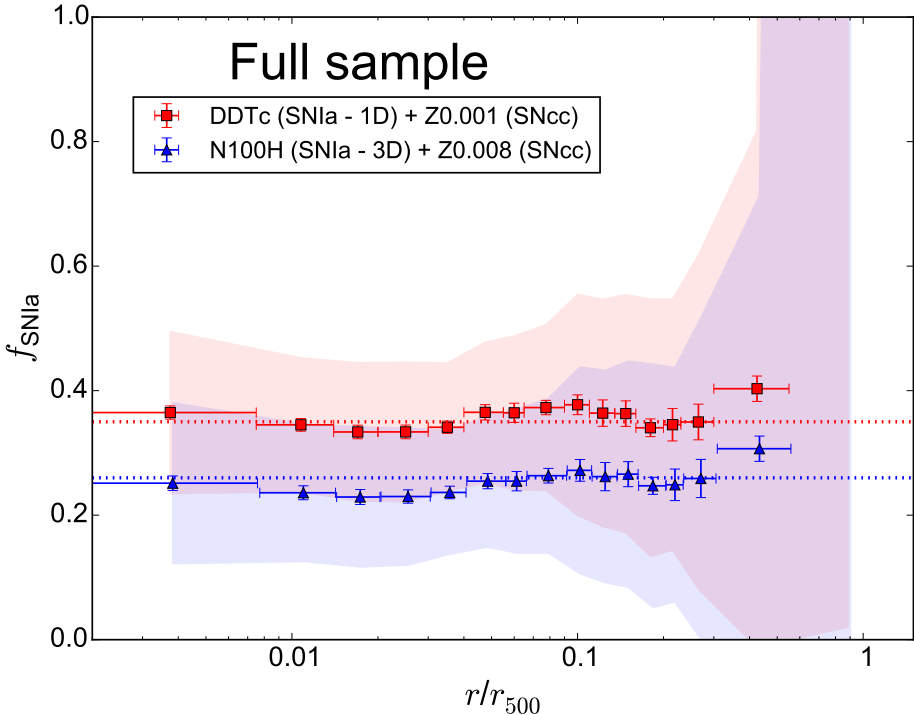


Figure 6.16: Radial dependency of the SNIa fraction contributing to the ICM enrichment (f_{SNIa}). Two combinations of SN yield models were adopted successively (see text). The corresponding shaded areas show the uncertainties when accounting for the scatter of the measurements. For each combination, the dotted line corresponds to f_{SNIa} estimated within the core ($0.2r_{500}$ or $0.05r_{500}$), averaged over the full sample (see Chapter 4).

One of the main pictures (Sect. 6.1) that had been proposed to explain the results showing a flat O profile in the previous literature, is that the bulk of SNcc events would have exploded early on, during or shortly before the formation of clusters / groups (~ 10 Gyr ago), and their products would have efficiently diffused within the entire cluster. The Fe central excess, tracing the SNIa products, would then mostly originate from the BCG at later cosmic time, hence supporting the idea that SNIa explode significantly later than the time required for more massive stars to release (mostly via SNcc explosions) and diffuse their metals into the ICM. One issue with this scenario was that, whereas one should expect a shallower Si profile than the Fe profile (since Si is synthesised by both SNIa and SNcc), many

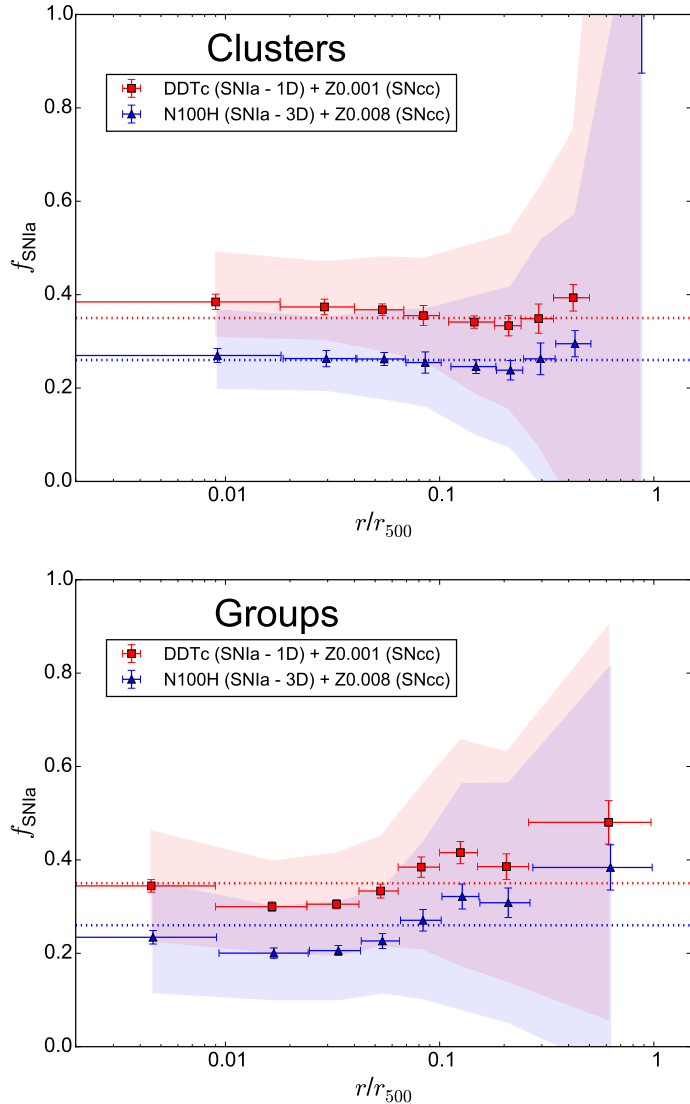


Figure 6.17: Same as Fig. 6.16, with a differentiation for clusters (>1.7 keV, top) and groups (<1.7 keV, bottom).

previous studies reported a constant (e.g. Sanders & Fabian 2006a; Sato et al. 2008) or sometimes even decreasing (Million et al. 2011) Si/Fe ratio across radius. To solve this paradox, Finoguenov et al. (2002) propose a diversity of SNIa to contribute to the ICM enrichment: promptly exploding SNIa (whose products are supposed to be efficiently mixed over the whole cluster) produce less Si than SNIa with longer delay times (mostly enriching the cluster core). Since our results suggest a uniform contribution of SNIa (SNcc) products in the core and in the outskirts, invoking a diversity in SNIa (as well as in their delay times) is not required anymore, and alternative scenarii should be considered.

In their study of the chemical enrichment in Hydra A, Simionescu et al. (2009b) found that the central O excess can be explained either if stellar winds are 3 to 8 times more efficient in releasing metals than previously predicted, or if $3\text{--}8 \times 10^8$ SNcc had exploded in the cluster core over the last ~ 10 Gyr. Alternatively, ram-pressure stripping may help to build a central peak of SNcc (and SNIa) products from infalling cluster galaxy members (Domainko et al. 2006); however such a process should also occur at rather large distances (~ 1 Mpc), while the O excess is only observed in Hydra A within ~ 120 kpc. Similarly, Million et al. (2011) found centrally peaked profiles for eight elements in the core of M87. In addition to the peaked Mg profile, they measured a steeper gradient for Si and S than for Fe, and interpret their findings as the result of efficient enriching winds from a central pre-enriched stellar population and/or intermittent formation of massive stars in the BCG.

If the central O (and / or Mg) excess is indeed due to a significant amount of concentrated SNcc explosions in the cluster core, one relevant question is whether this SNcc peak was produced prior to the formation of the BCG, or by the BCG itself at a later stage of the cluster assembly. Recent simulations (Tornatore et al. 2007; Fabjan et al. 2010) suggest that the enrichment time of both O and Fe in the inner $\sim 0.4r_{500}$ is significantly shorter than outside this radius, which may imply that the BCG is indeed responsible for the central excess in the ICM observed for both SNIa and SNcc products. Moreover, the recent analysis of WARPJ1415.1+3612 ($z \simeq 1$) by De Grandi et al. (2014) shows that the bulk of the central Fe excess was already present ~ 8 Gyr ago and that its slope is steeper than at present times. This suggests in turn that the BCG is the dominant source responsible for the enrichment in the ICM core, and that the metals released by the BCG spread out of the core with time via diffusive / mixing processes.

If the Fe peak indeed comes from the BCG (as the Fe mass in the ICM could suggest; Böhringer et al. 2004a; De Grandi et al. 2004) and has a similar (scaled) radial distribution as SNcc products, as our results suggest, this central SNcc enrichment may also originate from the BCG. Although most BCGs appear red and dead at present times (with typical star formation rates of a few M_{\odot}/yr at most; e.g. McDonald et al. 2011), their star formation was dramatically higher over the last ~ 9 Gyr (McDonald et al. 2016), and in some cases, can still reach a few tens to hundreds M_{\odot}/yr at $z \simeq 0$ (O'Dea et al. 2008). This past (and, sometimes, present) high star formation in BCGs could thus be responsible for the central excess of SNcc products seen in the ICM. In this case, and assuming that some mechanisms diffuse out the metals from the cluster core (see above), the consistency between the slopes of the radial SNIa and SNcc distributions suggests that the bulk of SNIa exploded quite shortly after the period of star formation in the BCG. More precisely, the typical delay time of SNIa should not be larger than the timescale of metal mixing/diffusing processes in the ICM.

More generally, and regardless of whether the central excess of SNcc products reported in this study originates from the BCG or not, the (lack of) radial dependence translates into a time dependence of the chemical enrichment patterns that we can infer. Specifically, the consistent radial profiles for all the measured abundances may suggest that the SNIa and SNcc components of the enrichment originate from the same astrophysical source(s) and have been occurring at similar epochs. Such a reasoning can be applied to the case of the intra-cluster stellar population. Both observations (e.g. Krick et al. 2006; Krick & Bernstein 2007) and simulations (Willman et al. 2004) provide increasing evidence for a significant fraction (10–50%) of stars that are unbound to any cluster galaxy and could potentially contribute to the ICM enrichment (Domainko et al. 2004). As it takes a substantial time for these stars to be ejected and travel away from their galaxy hosts, the intra-cluster population should essentially contain low-mass stars, and thus enrich the ICM predominantly with SNIa, likely providing a different radial distribution of SNIa products than that of SNcc products (coming from other sources). This picture disagrees with our present results. Therefore, under these assumptions, intra-cluster stars may not be the dominant source of the ICM enrichment. A similar conclusion is reached by Kapferer et al. (2010) on the basis of hydrodynamical simulations and SNIa expected rates.

In summary, while it was commonly thought from previous studies

that the bulk of the SNcc (SNIa) enrichment would contribute only at early (late) times, recent works — including our present study — have provided increasing evidence that the SNIa versus SNcc dichotomy is not pronounced since the chemical composition does not evolve dramatically with radius.

The astrophysical implications discussed here hold only if further and definitive confirmation of the uniform distribution of f_{SNIa} is achieved with more accurate instruments on board future missions. In particular, the high spectral resolution and effective area of *Athena* will be required to investigate the distribution of key elements, like O or Mg, with unprecedented accuracy from the core to the outskirts. Moreover, a complete discussion would be required to fully quantify the speculative arguments used here, and therefore, to pursue the extensive use of realistic hydrodynamical simulations, preferably including all the potential sources of (SNIa and SNcc) enrichment and all the mixing and diffusion mechanisms known so far.

6.8 Conclusions

In this work, we used deep *XMM-Newton*/EPIC observations of 44 nearby cool-core galaxy clusters, groups, and ellipticals (all taken from the CHEERS catalogue, i.e. ~ 4.5 Ms of total net exposure) to derive the average projected radial abundance profiles of eight elements in the ICM. Whereas average Fe and Si abundance profiles had been previously reported in the literature (though over limited samples only), the O, Mg, S, Ar, Ca, and Ni profiles are measured and averaged over a large sample for the first time. This allows an unprecedented estimation of the average radial contribution of SNIa and SNcc products in the ICM. Our results can be summarised as follows.

- The Fe abundance can be robustly constrained out to $\sim 0.9r_{500}$ and $\sim 0.6r_{500}$ in clusters and groups, respectively, while most of the other abundances are uncertain beyond $\sim 0.5r_{500}$. Owing to a robust and conservative modelling of the EPIC background, the systematic background uncertainties are limited typically to a few per cent, which are usually smaller than (or comparable to) the statistical uncertainties for each object. The other systematic uncertainties (related to MOS-pn discrepancies, projection effects, an uncertain temperature distribution, or selection effects) are always smaller than the population scatter derived in each average profile. Therefore, the latter can be considered as a conservative limit for our measurements.

- The average radial profiles of all the considered elements exhibit a centrally peaked distribution, and seem to converge at large radii consistently towards the limits (0.09–0.37 times proto-solar) assessed at r_{180} by Molendi et al. (2016). When rescaled by the X/Fe ratios measured previously in the ICM core (Chapter 3), the average profiles of all the elements (except perhaps Ar) follow the average Fe profile very well out to at least $\sim 0.5r_{500}$. Similarly, the average radial X/Fe profiles (again, with the possible exception of Ar) are remarkably uniform out to this radius.
- Subdividing our sample into clusters (>1.7 keV) and groups (<1.7 keV) subsamples, we find that groups are on average $\sim 21\%$ less enriched in Fe than clusters. From $0.01r_{500}$ to $0.5r_{500}$, this fraction is rather constant and no significant change is observed in the slopes of the two subsamples. Below and beyond this radial range, the similar enrichment level found in clusters and groups can be explained by selection and binning effects. Interestingly, no sign of metal enhancement towards more massive objects could be significantly detected in the other profiles (with the possible exception of the O profile).
- The average Fe profile for clusters reported here agrees remarkably well with previous observations (Leccardi & Molendi 2008; Sanderson et al. 2009; Matsushita 2011). The agreement of our average Fe profile for groups with the previous observations of Rasmussen & Ponman (2007) is less good, but still comparable within uncertainties. Although it should be treated with caution, the comparison of our measured Fe profile with predictions from recent hydrodynamical simulations, taking AGN feedback and galactic winds effects into account (Planelles et al. 2014; Rasia et al. 2015), is also very encouraging. Future cluster simulations will be interesting to compare with our measurements.
- In 14 systems ($\sim 32\%$ of our sample), we detect a significant central drop of the Fe abundance. This can also be observed in the average abundance profiles (both for Fe and the other elements) by an apparent flattening below $\sim 0.01r_{500}$. We do not see a clear correlation between the depth of such metal drops and their radial extent. These drops are probably real and could be related to dust depletion of metals in the very core of the ICM, before they are dragged out by AGN feedback and released back in the hot gas phase. The slightly steeper

profile of Ar (expected not to be incorporated in dust grains), compared to that of Fe, could (at least partly) witness dust depletion of the other elements within $\sim 0.1 r_{500}$. However, the (statistical and systematic) uncertainties prevent us from firmly confirming or ruling out the presence of a central Ar drop.

- Using the approach described in Chapter 4, we estimate the radial contribution of SNIa products to the ICM enrichment (f_{SNIa}). Although the scatter (and, by extension, the other systematic uncertainties) prevents us from excluding sudden changes in the outskirts, our observations suggest, on average, a remarkably uniform f_{SNIa} distribution out to, at least, $0.5r_{500}$. This result contrasts with the dramatic increase of SNcc contribution in the outskirts inferred by Rasmussen & Ponman (2009), but is consistent with more recent measurements (Simionescu et al. 2015; Ezer et al. 2017) and simulations (Fabjan et al. 2010; Planelles et al. 2014; Biffi et al. 2017). This suggests that the major fraction of the SNIa and SNcc enriching the ICM may share the same origins and may have both exploded before mixing and diffusion processes played a significant role in spreading out the metals. In particular, since there is increasing evidence that the central Fe excess originates from the BCG, it is likely that a past intense period of star formation in the BCG had released SNcc products in the ICM core in a similar way.
- Finally, we emphasise that, although the systematic uncertainties considered here are under control, the Ni abundance may be systematically overestimated when using SPEXACT v2. Whereas it should not have a significant impact on the shape of the Ni profile presented here, such a bias might affect the average Ni/Fe ratio (see also Chapter 3) and the subsequent constraints inferred on the SNIa yield models (see also Chapter 4). We devote Chapter 5 to that specific issue.

While the abundance profiles of some elements (such as Fe or Si) could be remarkably constrained thanks to the large statistics of our sample, this paper clearly shows that, apart from the apparent scatter of the measurements, the most important limitations encountered so far are the systematic uncertainties, in particular related to MOS-pn cross-calibration imperfections (see also Schellenberger et al. 2015, and Chapter 3). Using the current X-ray facilities, a significant improvement of the accuracy of our results

may only be achieved by improving the EPIC cross-calibration and better understanding all the systematic biases that could affect the EPIC instruments. Nevertheless, further improvement in interpreting these results could also come from studying a more representative sample, for example including non-cool-core systems as well.

Despite our current efforts and achievements, we must stress the considerable breakthrough that the next X-ray missions (e.g. *Athena*; Barret et al. 2013) will be able to achieve. On the one hand, the very large effective area of future instruments will allow us to probe a detailed view of the chemical state of cluster outskirts, which is still challenging for *XMM-Newton*, as demonstrated in this paper. On the other hand, the remarkable spectral resolution of micro-calorimeters on board these future missions will considerably reduce the uncertainties on both the thermal structure and the distribution of various metals within and outside cluster cores. Therefore, there is no doubt that the next generation of X-ray observatories will bring further light on this study and provide a valuable understanding of the full history of the ICM enrichment.

Acknowledgements

The authors are very thankful to the referee for valuable comments that helped to improve the paper. The authors would also like to thank Jesper Rasmussen and Alastair Sanderson for kindly providing their observational data, as well as Susana Planelles and Elena Rasia for kindly providing their simulation outputs and for useful discussions. This work is partly based on the *XMM-Newton* AO-12 proposal "*The XMM-Newton view of chemical enrichment in bright galaxy clusters and groups*" (PI: de Plaa), and is a part of the CHEERS (CHEMical Evolution Rgs cluster Sample) collaboration. H.A. acknowledges the support of NWO via a Veni grant. P.K. acknowledges financial support from STFC. C.P. acknowledges support from ERC Advanced Grant Feedback 340442. T.H.R. acknowledges support from the DFG through grant RE 1462/6 and through the Transregional Collaborative Research Centre TRR33 The Dark Universe, project B18. This project has been supported by the Lendület LP2016-11 grant awarded by the Hungarian Academy of Sciences. This work is based on observations obtained with *XMM-Newton*, an ESA science mission with instruments and contributions directly funded by ESA member states and the USA (NASA). The SRON Netherlands Institute for Space Research is supported finan-

| 6.8 *Conclusions*

cially by NWO, the Netherlands Organisation for Scientific Research.

6.A Cluster properties and individual Fe profiles

This section enumerates the objects of our sample (CHEERS) and provides supplementary information on their individual Fe profiles and radial extents. Table 6.4 lists all the sources considered in this paper and their r_{500} values (adapted from Pinto et al. 2015, and references therein). For each element X , we also provide $r_{\text{out},X}$, the maximum radius at which we evaluate the corresponding abundance (see Sect. 6.4.1 for further details). The Fe radial profiles of each source of our sample are shown in Figs. 6.18 (clusters) and 6.19 (groups).

6.B Average abundance profiles of O, Mg, Si, S, Ar, Ca, and Ni

In Sect. 6.5.1 we provided numerical values of the radial Fe profile in the full sample (Table 6.2) and after subdividing it into clusters and groups (Table 6.3). In this Appendix we extend these numbers to the average O, Mg, Si, Ar, Ca, and Ni profiles that are shown in Figs. 6.3 and 6.4 (see Sect. 6.5.2 for further details). These values are listed in Table 6.5 (full sample) and Table 6.6 (comparison between clusters and groups).

6.B Average abundance profiles of O, Mg, Si, S, Ar, Ca, and Ni

Table 6.4: Properties of the observations used in this paper (see Chapter 3 for further details).

Source	$z^{(a)}$	$r_{500}^{(b)}$	$r_{\text{out,O}}^{(c)}$	$r_{\text{out,Mg}}^{(c)}$	$r_{\text{out,Si}}^{(c)}$	$r_{\text{out,S}}^{(c)}$	$r_{\text{out,Ar}}^{(c)}$	$r_{\text{out,Ca}}^{(c)}$	$r_{\text{out,Fe}}^{(c)}$	$r_{\text{out,Ni}}^{(c)}$	Cluster	Group
	(Mpc)	(r_{500})	(r_{500})	(r_{500})	(r_{500})	(r_{500})	(r_{500})	(r_{500})	(r_{500})	(r_{500})		
2A 0335+096	0.0349	1.05	0.26	0.26	0.26	0.26	0.26	0.26	0.26	0.26	✓	—
A 85	0.0556	1.21	0.72	0.72	0.72	0.72	0.72	0.72	0.72	0.72	✓	—
A 133	0.0569	0.94	0.94	0.94	0.94	0.94	0.94	0.94	0.94	0.94	✓	—
A 189	0.0318	0.50	0.97	0.97	0.97	0.97	0.97	0.97	0.97	—	—	✓
A 262	0.0161	0.74	0.33	0.33	0.33	0.33	0.33	0.33	0.25	0.33	✓	—
A 496	0.0328	1.00	0.50	0.50	0.50	0.50	0.50	0.50	0.50	0.50	✓	—
A 1795	0.0616	1.22	0.79	0.79	0.79	0.79	0.79	0.79	0.79	0.79	✓	—
A 1991	0.0587	0.82	0.84	1.12	1.12	1.12	1.12	1.12	0.56	1.12	✓	—
A 2029	0.0767	1.33	0.91	0.91	0.91	0.91	0.91	0.91	0.91	0.91	✓	—
A 2052	0.0348	0.95	0.42	0.56	0.56	0.56	0.56	0.56	0.42	0.56	✓	—
A 2199	0.0302	1.00	0.46	0.46	0.46	0.46	0.46	0.46	0.46	0.46	✓	—
A 2597	0.0852	1.11	1.22	1.22	1.22	1.22	1.22	1.22	1.22	1.22	✓	—
A 2626	0.0573	0.84	1.06	1.06	1.06	1.06	1.06	1.06	1.06	1.06	✓	—
A 3112	0.0750	1.13	1.05	1.05	1.05	1.05	1.05	1.05	1.05	1.05	✓	—
A 3526 / Centaurus	0.0103	0.83	0.19	0.14	0.09	0.19	0.19	0.19	0.06	0.19	✓	—
A 3581	0.0214	0.72	0.45	0.45	0.45	0.45	0.45	0.45	—	—	✓	—
A 4038 / Klemola 44	0.0283	0.89	0.36	0.36	0.36	0.36	0.36	0.36	0.36	0.36	✓	—
A 4059	0.0460	0.96	0.74	0.74	0.74	0.74	0.74	0.74	0.74	0.74	✓	—
AS 1101 / Sérsic 159-03	0.0580	0.98	0.69	0.69	0.92	0.92	0.92	0.92	0.69	0.92	✓	—
AWM 7	0.0172	0.86	0.30	0.30	0.15	0.30	0.30	0.30	0.10	0.30	✓	—
EXO 0422	0.0390	0.89	0.67	0.67	0.67	0.67	0.67	0.67	0.67	0.67	✓	—
Fornax / NGC 1399	0.0046	0.40	0.17	0.17	0.17	0.17	0.17	0.17	—	—	✓	—
HCG 62	0.0146	0.46	0.36	0.48	0.48	0.48	0.48	0.48	0.24	—	—	✓
Hydra A	0.0538	1.07	0.39	0.39	0.39	0.39	0.39	0.39	0.39	0.39	✓	—
M 49 / NGC 4472	0.0044	0.53	0.12	0.12	0.12	0.12	0.12	0.12	0.12	—	—	✓
M 60 / NGC 4649	0.0037	0.53	0.11	0.11	0.11	0.11	0.11	0.11	0.06	—	—	✓
M 84 / NGC 4374	0.0034	0.46	0.14	0.14	0.14	0.14	0.14	0.14	—	—	✓	—
M 86 / NGC 4406	-0.0009	0.49	0.06	0.06	0.06	0.06	0.06	0.06	0.06	—	—	✓
M 87 / NGC 4486	0.0044	0.75	0.06	0.08	0.03	0.08	0.10	0.10	0.03	—	—	✓
M 89 / NGC 4552	0.0010	0.44	—	—	0.12	—	—	0.09	—	—	✓	—
MKW 3s	0.0450	0.95	0.73	0.73	0.73	0.73	0.73	0.73	0.37	0.73	✓	—
MKW 4	0.0200	0.62	0.49	0.49	0.49	0.49	0.49	0.49	0.49	0.49	✓	—
NGC 507	0.0165	0.60	0.42	0.42	0.42	0.42	0.42	0.42	0.42	—	—	✓
NGC 1316 / Fornax A	0.0059	0.46	0.19	0.19	0.19	0.19	0.19	0.19	0.19	—	—	✓
NGC 1404	0.0064	0.61	0.16	0.16	0.16	0.16	0.16	0.16	0.16	—	—	✓
NGC 1550	0.0123	0.62	0.30	0.30	0.22	0.30	0.30	0.30	0.30	—	—	✓
NGC 3411	0.0155	0.47	0.37	0.50	0.50	0.50	0.50	0.50	0.37	—	—	✓
NGC 4261	0.0074	0.45	0.25	0.25	0.25	0.25	0.25	0.25	0.19	—	—	✓
NGC 4325	0.0258	0.58	0.51	0.68	0.68	0.68	0.68	0.68	0.51	—	—	✓
NGC 4636	0.0037	0.35	0.14	0.14	0.14	0.14	0.14	0.14	0.14	—	—	✓
NGC 5044	0.0090	0.56	0.18	0.18	0.12	0.18	0.18	0.18	0.12	—	—	✓
NGC 5813	0.0064	0.44	0.16	0.22	0.22	0.22	0.22	0.22	0.16	—	—	✓
NGC 5846	0.0061	0.36	0.19	0.25	0.25	0.25	0.25	0.25	0.19	—	—	✓
Perseus	0.0183	1.29	0.26	0.26	0.11	0.26	0.26	0.26	0.07	0.26	✓	—

^(a) Redshifts were taken from Pinto et al. (2015, and references therein). ^(b) Values of r_{500} (in Mpc) were taken from Pinto et al. (2015, and references therein). ^(c) $r_{\text{out},X}$ (in units of r_{500}) corresponds to the maximum radial extent of the abundance measurements of element X (see text).

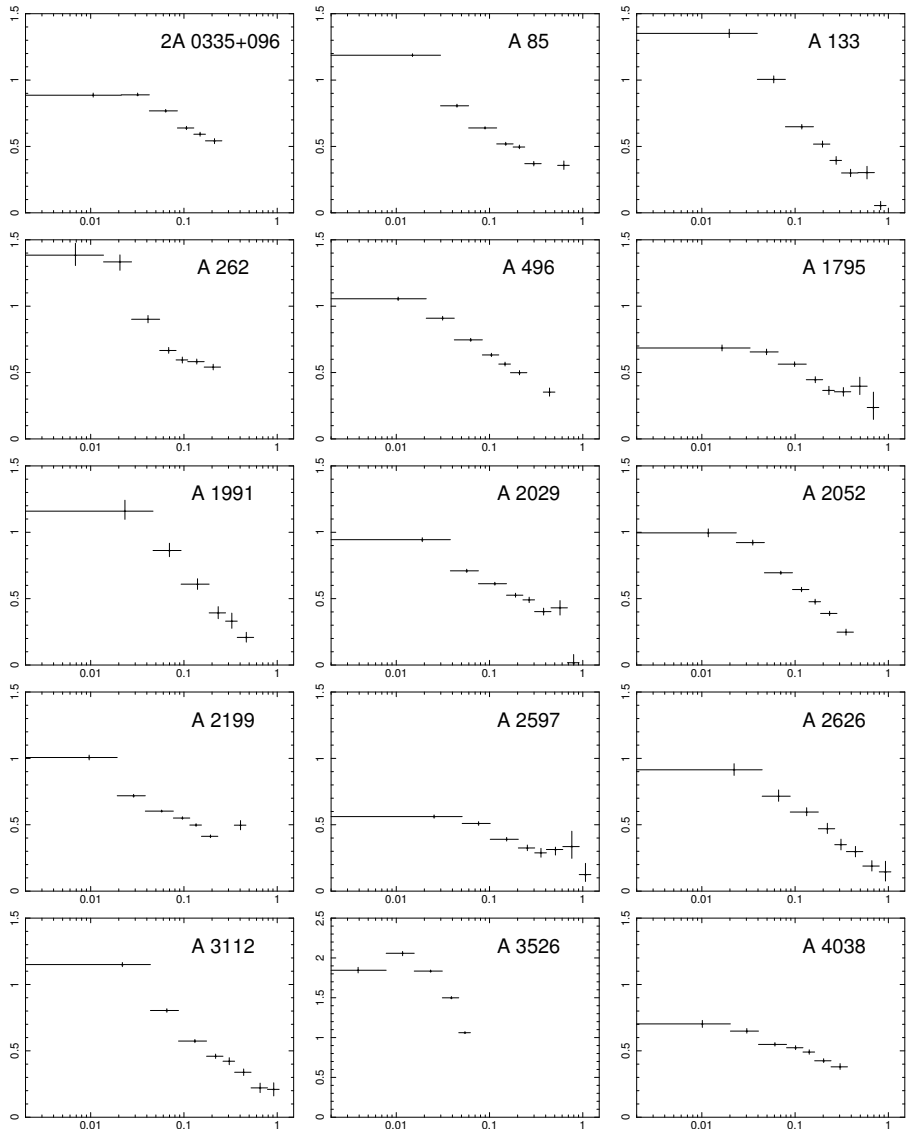


Figure 6.18: Radial Fe abundance profiles for all the clusters ($kT_{\text{mean}} > 1.7 \text{ keV}$) in our sample. The radial distances (x-axis) are expressed in fractions of r_{500} while the Fe abundances (y-axis) are given with respect to their proto-solar values (Lodders et al. 2009). Data points that were not included when computing the average profile have been removed (Sect. 6.4.1).

6.B Average abundance profiles of O , Mg , Si , S , Ar , Ca , and Ni

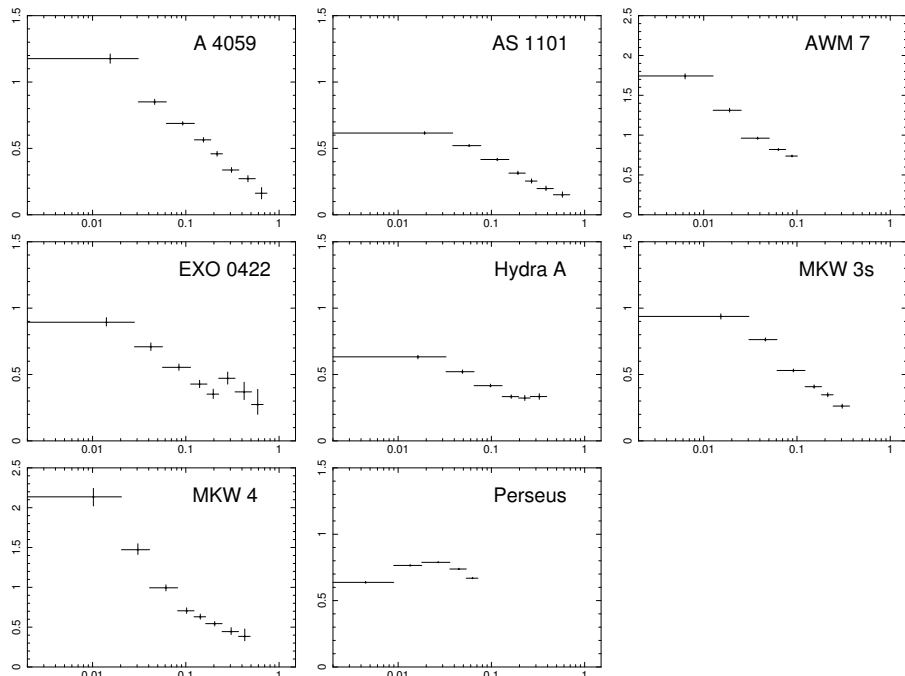


Figure 6.18 (Continued)

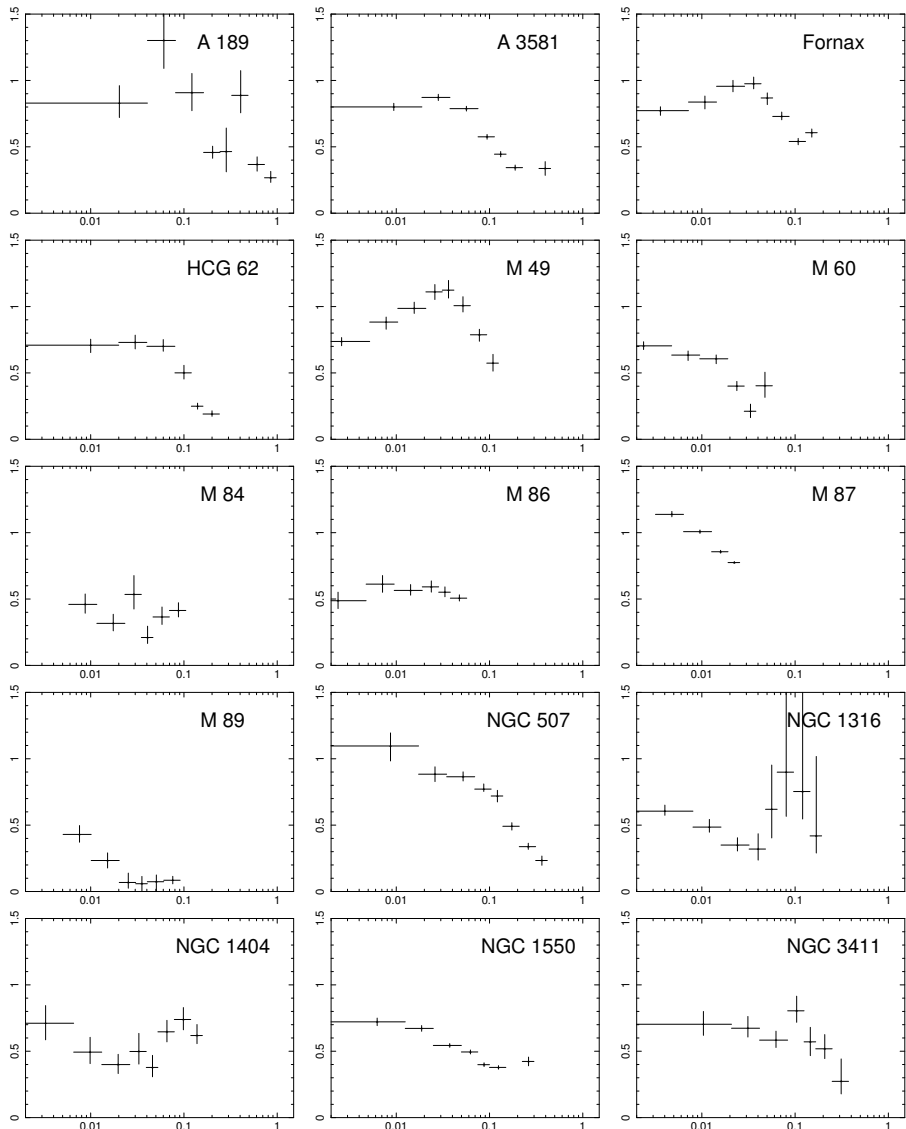


Figure 6.19: Radial Fe abundance profiles for all the groups/ellipticals ($kT_{\text{mean}} < 1.7 \text{ keV}$) in our sample. The radial distances (x-axis) are expressed in fractions of r_{500} while the Fe abundances (y-axis) are given with respect to their proto-solar values (Lodders et al. 2009). Data points that were not included when computing the average profile have been removed (Sect. 6.4.1).

6.B Average abundance profiles of O , Mg , Si , S , Ar , Ca , and Ni

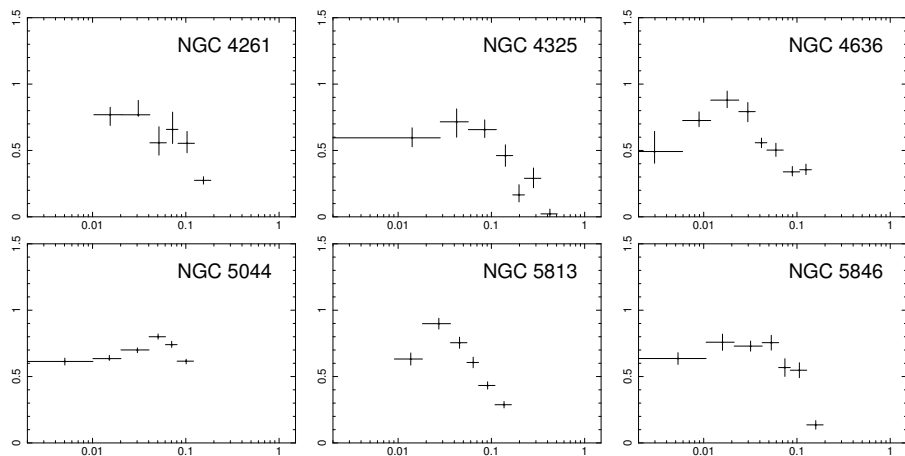


Figure 6.19 (Continued)

Table 6.5: Average radial abundance profiles for the full sample, as shown in Fig. 6.3. The error bars contain the statistical uncertainties and the MOS-pn uncertainties (Sect. 6.4.3), except for the O abundance profile, which is measured with MOS only.

Radius (r_{500})	O	Mg	Si	S	Ar	Ca
0 – 0.0075	0.437±0.017	0.50±0.13	0.76±0.12	0.80±0.11	0.88±0.15	0.95±0.12
0.0075 – 0.014	0.624±0.020	0.53±0.04	0.79±0.11	0.83±0.11	0.92±0.18	1.09±0.11
0.014 – 0.02	0.650±0.021	0.54±0.04	0.78±0.09	0.84±0.08	0.85±0.15	1.05±0.11
0.02 – 0.03	0.685±0.016	0.52±0.04	0.77±0.06	0.85±0.04	0.80±0.16	0.98±0.09
0.03 – 0.04	0.632±0.017	0.51±0.03	0.69±0.07	0.77±0.04	0.73±0.17	0.88±0.08
0.04 – 0.055	0.533±0.017	0.49±0.05	0.63±0.07	0.69±0.04	0.65±0.15	0.82±0.08
0.055 – 0.065	0.54±0.03	0.49±0.06	0.58±0.06	0.63±0.05	0.56±0.14	0.79±0.10
0.065 – 0.09	0.480±0.021	0.46±0.04	0.53±0.04	0.55±0.03	0.50±0.12	0.70±0.07
0.09 – 0.11	0.42±0.03	0.46±0.07	0.47±0.04	0.50±0.05	0.42±0.14	0.56±0.11
0.11 – 0.135	0.38±0.03	0.49±0.09	0.43±0.05	0.49±0.06	0.36±0.13	0.57±0.11
0.135 – 0.16	0.38±0.03	0.47±0.11	0.41±0.03	0.47±0.06	0.27±0.15	0.54±0.12
0.16 – 0.2	0.38±0.03	0.51±0.14	0.371±0.023	0.44±0.04	0.23±0.14	0.57±0.12
0.2 – 0.23	0.33±0.04	0.50±0.11	0.36±0.04	0.43±0.06	0.25±0.13	0.56±0.17
0.23 – 0.3	0.26±0.03	0.50±0.23	0.31±0.04	0.36±0.08	0.22±0.17	0.47±0.18
0.3 – 0.55	0.27±0.03	-0.02±0.04	0.26±0.04	0.31±0.12	0.2±0.3	0.10±0.18
0.55 – 1.22	0.01±0.05	-0.49±0.14	0.10±0.07	-0.1±0.3	-0.4±0.7	-0.1±0.4

6.B Average abundance profiles of O , Mg , Si , S , Ar , Ca , and Ni

Table 6.6: Average radial abundance profiles for clusters (>1.7 keV) and groups (<1.7 keV), as shown in Fig. 6.4. The error bars contain the statistical uncertainties and the MOS-pn uncertainties (Sect. 6.4.3), except for the O abundance profiles, which are measured with MOS only.

Radius ($/r_{500}$)	O	Mg	Si	S	Ar	Ca	Ni
Clusters							
0 – 0.018	0.815±0.025	0.50±0.08	0.79±0.08	0.86±0.03	0.87±0.13	1.05±0.08	1.6±0.5
0.018 – 0.04	0.776±0.021	0.47±0.04	0.75±0.05	0.82±0.06	0.81±0.13	0.94±0.07	1.5±0.4
0.04 – 0.068	0.689±0.024	0.44±0.03	0.61±0.05	0.66±0.06	0.65±0.14	0.80±0.07	1.3±0.3
0.068 – 0.1	0.59±0.03	0.46±0.08	0.53±0.04	0.56±0.05	0.49±0.14	0.68±0.09	1.2±0.4
0.1 – 0.18	0.46±0.025	0.51±0.05	0.43±0.04	0.50±0.06	0.35±0.12	0.61±0.08	0.9±0.4
0.18 – 0.24	0.35±0.04	0.55±0.03	0.37±0.04	0.45±0.05	0.28±0.12	0.60±0.12	0.8±0.6
0.24 – 0.34	0.34±0.04	0.54±0.14	0.31±0.03	0.37±0.11	0.22±0.18	0.35±0.15	0.5±0.8
0.34 – 0.5	0.37±0.05	–0.06±0.16	0.27±0.04	0.34±0.13	0.20±0.39	0.1±0.3	-0.9±0.4
0.5 – 1.22	-0.02±0.05	-0.27±0.22	0.13±0.07	0.01±0.25	-0.24±0.69	-0.1±0.3	-3.4±2.1
Groups							
0 – 0.009	0.384±0.017	0.48±0.14	0.76±0.16	0.77±0.22	0.86±0.24	0.82±0.19	–
0.009 – 0.024	0.613±0.015	0.59±0.07	0.80±0.11	0.89±0.18	0.91±0.18	1.11±0.11	–
0.024 – 0.042	0.591±0.015	0.53±0.04	0.67±0.10	0.79±0.12	0.69±0.19	0.88±0.10	–
0.042 – 0.064	0.460±0.018	0.53±0.10	0.60±0.09	0.67±0.11	0.58±0.14	0.81±0.12	–
0.064 – 0.1	0.366±0.024	0.44±0.15	0.49±0.04	0.47±0.08	0.47±0.13	0.62±0.15	–
0.1 – 0.15	0.309±0.023	0.4±0.3	0.40±0.03	0.41±0.07	0.22±0.18	0.13±0.27	–
0.15 – 0.26	0.327±0.03	0.4±0.4	0.34±0.05	0.32±0.09	0.01±0.17	0.01±0.34	–
0.26 – 0.97	0.19±0.04	-0.23±0.14	0.17±0.06	0.16±0.15	0.24±0.38	-0.3±0.7	–

The consequences of every act are included in the act itself.

– George Orwell, 1984

7

Future prospects for intra-cluster medium enrichment studies

7.1 Current limitations of abundance measurements

Throughout this thesis, we have seen repeatedly that systematic uncertainties dominate over statistical uncertainties for large samples of deep cluster observations. It would be difficult (if not impossible) to make an exhaustive list of all the limitations that could potentially affect the average X/Fe abundance ratios measured in the ICM by the *XMM-Newton* instruments. In this thesis (and based on additional work on RGS measurements of the O/Fe ratio by de Plaa et al. 2017) we have discussed and quantified:

- the intrinsic scatter of the measurements¹ (up to $\sim 25\%$);
- uncertainties in the spectral models and plasma codes (mostly below $\sim 20\%$, up to $\sim 40\text{--}50\%$ for Mg/Fe and Ni/Fe at a few specific plasma temperatures);
- uncertainties in the thermal structure of the ICM (up to $\sim 20\%$);
- uncertainties in the Galactic absorption, potentially affecting the O and N abundance measurements, when available (up to $\sim 40\%$ in a few specific cases);
- the difference in the extracted regions between different instruments, e.g. RGS vs. EPIC, or within the same instrument, e.g. EPIC $0.05r_{500}$

¹ Although the intrinsic scatter is partly natural and should not be considered as a systematic uncertainty, it clearly affects the total dispersion of our measurements and deserves to be well understood.

vs. EPIC $0.2r_{500}$ (up to $\sim 10\%$);

- uncertainties related to the cross-calibration between the instruments (up to $\sim 20\%$, depending on the energy band considered);
- uncertainties in the background and foreground modelling (difficult to quantify, as it depends on the data quality, the plasma temperature, the studied region, and the method used to deal with the background).

Apart from these limitations on the abundance ratios, we can also list additional systematic uncertainties (usually difficult to quantify) that may affect the abundance measurements in general:

- projection effects ;
- possible unaccounted radiative effects (charge exchange, resonant scattering, etc.);
- uncertainties related to possible spatially unresolved substructures with possibly different enrichment levels.

Some items can be identified as systematic effects from spectral fitting (e.g. atomic uncertainties, uncertainties in the Galactic absorption), while some others are clearly due to the limitations of the current instrumentation (e.g. cross-calibration uncertainties, non-X-ray background). In some cases, however, the distinction is less easy to do. For instance, the uncertainties in the ICM thermal structure are related to both the choice of the thermal model in the fits (single-temperature, g_{dem} , etc.) and to the limited spectral resolution of the instruments, which prevents to favour any particular thermal model.

One more complication is that some uncertainties might depend on others. For instance, if the studied region of the ICM contains unresolved substructures (for example small clumps of cold, enriched gas), this will have a simultaneous impact on (i) the derived average abundances directly and (ii) the derived average temperature and / or the assumptions made on the temperature structure. In turn, this incorrectly modelled temperature structure may play a role in bringing further uncertainties on the (already biased) average abundances.

What needs to be done to further improve our measurements? The answer to this question is not trivial, as it depends on which uncertainties one

wants to reduce. While deeper individual exposures with current missions may help to better understand some limitations (Sect. 7.2), it is clear that substantial efforts should be pursued on other aspects. In particular, the two most crucial improvements that are needed are

1. improvements on the spectral codes and atomic calculations (Sect. 7.3);
2. more advanced X-ray instruments, including better spectral resolution, spatial resolution, and effective area (Sect. 7.4 and 7.5).

Finally, further comprehensive studies on Galactic absorption effects, on the X-ray background and foreground, and on how to interpret the projected spectra (e.g. using mock datasets from 3-D chemodynamical simulations) would also help to better understand and correct some of the systematic biases mentioned above.

7.2 The future of *XMM-Newton* in intra-cluster enrichment studies

7.2.1 Nearby clusters and supernova models

Since, for large nearby samples like the CHEERS sample, systematic uncertainties of the abundance measurements dominate over the statistical ones, collecting more photons will not help to improve significantly the results that were obtained in this analysis. Therefore, one of the most important take-home messages of this thesis is that we have probably reached the limits of what can be possibly achieved with *XMM-Newton*.

This conclusion, however, should be somewhat nuanced. First, as discussed by de Plaa et al. (2017), the high quality of the data may be used to reveal unexpected systematic biases. In turn, this may lead to a better understanding of some systematic uncertainties, and contribute to substantially improve the global accuracy of the results. Second, deep observations of each object of the sample are very useful to constrain and eventually better understand the intrinsic scatter. Outliers can be then isolated and studied in more detail. Finally, increasing the exposure of each source of the CHEERS sample would allow to build detailed 2-D metal maps and study the possible azimuthal asymmetries in a more comprehensive way.

In addition to the systematic uncertainties discussed above, the interpretation of our measured abundances is limited by the accuracy of the

current SN models. Indeed, when one wants to constrain SN models from the ICM abundance ratios, additional uncertainties affecting the yield predictions should be also considered. They may be due to the input physics, the initial conditions and assumptions, or the computational methods that were used. For example, similar SNcc yield models proposed in the literature by different groups do not perfectly agree (see e.g. De Grandi & Molendi 2009; Nomoto et al. 2013). Such discrepancies are also found in SNIa yield models, for example when comparing one- and multi-dimensional approaches, or when using updated electron capture rates (Maeda et al. 2010, see also Chapter 4). In that respect, it will be crucial to improve the convergence between the SN yield predictions obtained by the different groups over the next few years.

Regardless of the future convergence between the nucleosynthesis yield models for SNIa explosions, another possible improvement that may be achieved by the SNIa theoretical community is on the yields predicted by the different SNIa progenitor channels. As explained in Chapter 1, the main unsolved question regarding SNIa is whether they occur in a single-degenerate (SD) or double-degenerate (DD) system. Since we have shown that ICM observations can easily favour and/or rule out some explosion mechanisms, a clear differentiation of the yields predicted by SD and DD scenarios would also allow us to bring substantial clues on the dominant SNIa progenitor channel. If the white dwarf (WD) density is high, electron captures are quite efficient and produce large amounts of neutronised species, such as ^{58}Ni and ^{55}Co , further decaying into ^{55}Mn . If we assume the SD channel to result from a slow accretion by the WD (thus approaching the Chandrasekhar mass, M_{Ch}) and the DD channel to result from the direct merger between two WDs (whose masses remain well below M_{Ch}), the SD scenario should produce significantly more Mn and Ni than the DD scenario (e.g. Seitenzahl et al. 2013a; Yamaguchi et al. 2015). Unfortunately, the total uncertainties of these two elements in the ICM are still large. Moreover, Mn is also affected by the initial metallicity of the WD progenitor, while Ni is also sensitive to the SNIa explosion mechanism itself. Therefore, the accurate predicted yields of more elements are also needed.

In Chapter 4, we have shown that our measured ICM abundance pattern does not match the yield predictions of a violent collision between two WDs of similar masses ($\sim 0.9 M_{\odot}$ each, Pakmor et al. 2010). This does not necessarily mean that all violent WD-WD collisions are to be discarded as SNIa progenitors, because at this stage the dependency of the relative

yields on the different parameters of the merger (e.g. the WD-WD mass ratio) is still unclear. Moreover, the DD scenario could even be possible in a sub- M_{Ch} case, where the most massive WD slowly accretes the disrupted material of the less massive WD (e.g. Piersanti et al. 2003). In that context, if efforts are pursued by the SNIa community to predict the differences between the yields of all the SD and DD scenarios, our ICM abundances will be a valuable legacy that may help to solve the SNIa progenitor problem.

7.2.2 High redshift clusters

Another question that arises is whether *XMM-Newton* can be useful for studying the enrichment at higher redshifts. Historically, after a first *ASCA* study showing no evidence of evolution in the ICM metallicity up to $z \sim 0.4$ (Mushotzky & Loewenstein 1997), *XMM-Newton* and *Chandra* allowed to investigate clusters up to $z \sim 1.3$, and more recent work suggests a slight decrease of Fe abundance with redshift (Balestra et al. 2007; Maughan et al. 2008; Anderson et al. 2009; Baldi et al. 2012). These results, however, are not always confirmed (e.g. Tozzi et al. 2003). In fact, if the core-excised regions only are considered, a flat trend even beyond $z \simeq 1$ would not be surprising, as the early enrichment in the outskirts is expected to have occurred already before that epoch (Chapters 1 and 6). That being said, a clear redshift-metallicity trend is difficult to confirm, because of possible intrinsic dispersion in the measurements. Moreover, the statistical errors on the metallicities of higher- z clusters are often large ($\gtrsim 30\%$).

Recently, de Plaa & Mernier (2017) estimated that, to clearly separate a flat from a decreasing trend with 90% of probability, observations of about 150 clusters within $0.3 < z < 1.0$ would be needed, with a total net exposure time of ~ 13.7 Ms. Although technically feasible, the chances to obtain such a large total exposure in the upcoming *XMM-Newton* observation rounds are low.

7.3 Future work on atomic data and spectral modelling

In Chapter 5, we showed that updates in atomic codes may provide significant effects on the abundance determination. This clearly illustrates the importance of such improvements if one wants to further constrain the abundances and better interpret the ICM enrichment.

Despite the remarkable improvements of SPEXACT v3 compared to its

previous version, current models hardly reproduce specific spectral features in cool ($kT \lesssim 1$ keV) plasmas, in particular in the Fe-L complex (Chapter 5). This clearly shows that further efforts toward more complete spectral modelling is desirable. These efforts can be led on different aspects: better calculations of the ionisation processes and the overall ionisation balance (e.g. Urdampilleta et al. 2017), better parametrisation of the radiative recombination rate coefficients (e.g. Mao & Kaastra 2016), implementing more spectral transitions into plasma codes (not only for H-like and He-like ions, but also for more complex electronic sequences), and / or a continuous and self-consistent update of the atomic data.

The optimal way to test our current knowledge of the radiation processes in CIE plasmas is to compare the current models with the most detailed data available. While laboratory experiments may be useful in some specific cases (e.g. Beiersdorfer et al. 2004; Shah et al. 2016), it is not possible to recreate the exact ICM conditions in laboratories (for instance, forbidden transitions observed in astrophysical plasmas require very low densities that cannot be currently achieved on Earth). Instead, the very first spectra of the ICM made by the new generation of X-ray satellites (Sect. 7.5) will be extremely useful to confront with the up-to-date models from SPEXACT (`cie` or `gdem`) and AtomDB (`apec`).

Above all, it is essential to understand the origin of the current discrepancies between the different spectral codes. Parallel ongoing improvement of SPEXACT and AtomDB will certainly improve the convergence between the prediction made by these two codes, and will clearly help to reduce the atomic uncertainties of our abundance measurements.

7.4 X-ray micro-calorimeters

In addition to atomic data, the most constraining limitation of the current X-ray instruments (i.e. CCDs and grating spectrometers) in the abundance measurements is their spectral resolution. In fact, many of the systematic uncertainties listed in Sect. 7.1 will be better understood with a better resolution of the emission lines in X-ray cluster spectra. More generally, improved spectral resolution will bring our understanding of the spectroscopy in the ICM (and hot plasmas in general) to another level. This will, in turn, considerably enlarge our current knowledge of metal enrichment in the ICM. Currently, the next step toward a better spectral resolution is the use of X-ray micro-calorimeters in future missions.

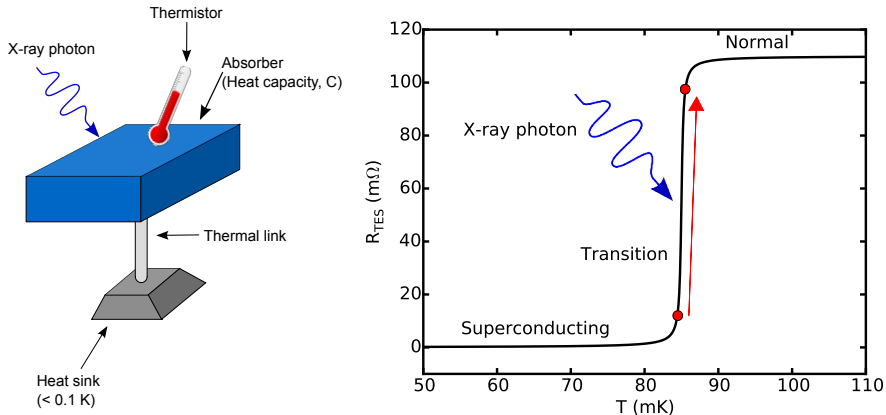


Figure 7.1: Left: Schematic illustration of a X-ray micro-calorimeter. Right: Electric resistance of a (TES type) thermistor as a function of its temperature. When a X-ray photon hits the absorber, the temperature increase occurs in the transition edge between the "superconducting" and "normal" regimes of the material, which makes it measurable.

A micro-calorimeter is essentially made of three components: a X-ray absorber, a thermistor and a heat sink (Fig. 7.1 left). The absorber and the heat sink are connected by a thermal link. On paper, the principle is quite simple. When a X-ray photon hits the absorber, its incoming energy is converted into a small heat increase, which is measured by the thermistor. This heat increase causes a change in resistance of the thermistor before being dissipated by the heat sink. The current through the thermistor is measured continuously, and from the pulse signal detected in the current, the photon energy can be derived with high precision. One good example of micro-calorimeter is the transition-edge sensor (TES), which will be used in the X-IFU instrument of *Athena* (Sect. 7.5.3). The material used as thermistor in TES-like micro-calorimeters is actually superconducting at very low temperature, while it quickly reaches a threshold of constant electrical resistance (R_{TES}) at higher temperature. In between (i.e. in the transition edge between the two regimes), a small change in temperature will result in a strong change in R_{TES} (Fig. 7.1 right). In that sense, the thermistor acts like an extremely sensitive thermometer, as its resistance can be used to efficiently measure small temperature changes caused by absorbed X-ray photons.

In the absorber, the incident photon energy (E) is simply proportional

to the heat variation (ΔT):

$$\Delta T \propto \frac{E}{C}, \quad (7.1)$$

where C is the heat capacity of the absorber. Since $\Delta T/T$ is typically of the order of 0.01%, the heat sink must keep the absorber as close as possible to the absolute zero in order to minimise the thermal noise. This implies the need for a complex unit efficiently cooling the detector. Moreover, the absorbing material should have its heat capacity as low as possible, and should be efficient in absorbing X-rays.

Compared to CCD (or proportional counter) detectors, the main advantage of micro-calorimeters resides in their remarkable energy resolution (ΔE). For CCDs, ΔE depends on both the photon energy and the number of the subsequent collected electrons (N), as

$$\Delta E \propto E \frac{\sqrt{N}}{N}. \quad (7.2)$$

On the other hand, it can be shown that for micro-calorimeters,

$$\Delta E \propto \sqrt{\frac{kT^2 C}{\alpha}}, \quad (7.3)$$

where α is the sensitivity of the thermistor. In other words, ΔE does not depend on E and can potentially reach very low values (a few eV at most) if the detector is kept at very low temperatures. One limitation to the energy resolution is when two photons hit the absorber within a short interval implying that their subsequent temperature jumps cannot be clearly separated. In most clusters, however, the count rate of the ICM emission is weak enough to limit such a pile-up effect.

One of the main challenges for the next X-ray detectors is to build an array of independent micro-calorimeter units, thereby recreating a full grid of pixels and allowing to perform spatially-resolved spectroscopy. So far (i.e. in the SXS instrument, Sect. 7.5.1 and 7.5.2), each pixel is wired independently to the read-out electronics, which limits the number of pixels on the detector (to 36 in the case of SXS). In future instruments (e.g. X-IFU, Sect. 7.5.3), multiple pixels will be connected to one read-out chain, although they can still be read-out independently using a multiplexing technique. This will allow to create more pixels per detector (~ 3500 approximately), and to reach a good spatial resolution while keeping an exquisite spectral resolution.

7.5 The upcoming generation of X-ray missions

As seen in Sect. 7.4, X-ray micro-calorimeters have a substantially improved spectral resolution compared to the instruments used in X-ray missions so far. This would be essential to further constrain abundances in cluster X-ray spectra. Fortunately, the upcoming generation of X-ray missions are (or will be) equipped with micro-calorimeters. In this section we briefly discuss the potential improvements that these missions may bring to the ICM enrichment.

7.5.1 *Hitomi*

On 17 February 2016, the Japanese satellite *Hitomi* (previously *ASTRO-H*, Fig. 7.2; Takahashi et al. 2014) was successfully launched. In addition to the two gamma-ray detectors and the two hard X-ray telescopes, the mission included two soft X-ray telescopes which focused light onto a soft X-ray imager (SXI) and a micro-calorimeter instrument — namely the soft X-ray spectrometer (SXS). The latter had a field of view of 3x3 arcmin and a very high spectral resolution of ~ 5 eV, allowing to do high-resolution spectroscopy in the 0.4–12 keV band at an unprecedented level. The first observation made by SXS (initially for calibration purposes) was the core region of the Perseus cluster in the 2–10 keV band. Unfortunately, about one month after the launch, the satellite experienced a loss of communication. It was later discovered that a chain of anomalies in the attitude control system caused an uncontrollable spinning of the satellite. Due to the subsequent accumulation of excessive momentum, several parts of the spacecraft eventually broke away. Despite all the efforts from JAXA to recover it, the mission was officially aborted on 28th April 2016.

Although this early end of *Hitomi* was very bad news for the whole X-ray astrophysics community, the observation of Perseus has been a great success in terms of technical capabilities (e.g. Hitomi Collaboration et al. 2016). Above all, the mission revealed the exquisite spectral resolution that micro-calorimeters can realistically achieve (Fig. 7.3), thereby opening a new window on the future of ICM enrichment studies. An overview of the prospects of *Hitomi* in cluster physics is given by Kitayama et al. (2014).



Figure 7.2: Artist impression of the *Hitomi* satellite (Credit: JAXA).

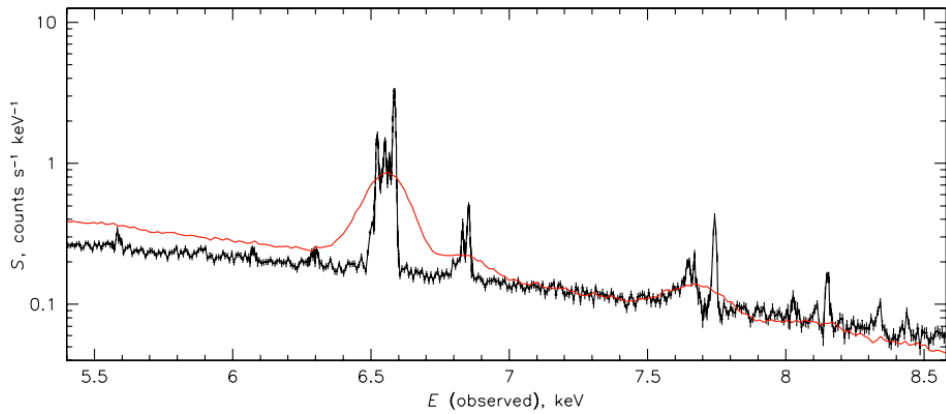


Figure 7.3: *Hitomi* SXS spectrum of the core of the Perseus cluster (Hitomi Collaboration et al. 2016). Overlaid in red is a typical CCD spectrum (*Suzaku* XIS) extracted from the same region.

7.5.2 XARM

The success of the SXS instrument onboard *Hitomi* to resolve metal lines in the spectrum of Perseus has been a strong motivation to recover the mission. On 14 July 2016, JAXA announced that a successor of *Hitomi* is actually planned for the year 2021. Named the *X-ray Astronomy Recovery Mission* (XARM), this satellite would be essentially centred on the SXS instrument.

If this mission is indeed confirmed, its SXS instrument will be highly valuable to future ICM enrichment studies. In Fig. 7.4, we simulate a SXS observation of 100 ks of cleaned exposure of the core region of Abell 4059 (see also Chapter 2). Here again, the simulated data illustrate the unprecedented spectral resolution we can achieve with a micro-calorimeter instrument.

One interesting direct application of the SXS capabilities is the improved measurement of the Ni/Fe ratio. As seen in Chapters 1, 4, and 5, the Ni/Fe ratio provides valuable constraints on the dominant SNIa explosion channel. Unfortunately, when measured with the EPIC instruments, this ratio suffers from large cross-calibration and background uncertainties (Chapter 3), and is very sensitive to the used spectral codes and atomic databases (Chapter 5). Moreover, at CCD spectral resolution, Ni-K lines are blended with Fe XXV (He-like) lines, thereby limiting the robustness of the Ni abundance measurement. In addition to be weakly affected by the instrumental background even at high energies², the SXS instrument is able to fully disentangle all the Ni and Fe lines, and will thus dramatically improve our measurement of the Ni/Fe ratio. Based on the simulation presented in Fig. 7.4, and assuming ongoing efforts are pursued toward an improvement of the plasma atomic codes, we estimate that the statistical errors on Ni/Fe should not be larger than $\sim 8\%$. At that level of accuracy, it will be easy to determine which of the deflagration or the delayed-detonation explosion mechanism is the dominant one in SNIa.

Another significant progress that SXS will be able to achieve is a better quantification of the radial variation in the relative number of SNIa (SNcc) enriching galaxy clusters. As shown in Chapter 6, we have provided interesting hints that SNIa and SNcc enrich the ICM at the same level in the centre and in the outer parts ($\sim 0.5r_{500}$). This could be further confirmed

²The main reason of the low background level of the SXS instrument is related to the choice of the low-Earth orbit of the *Hitomi*/XARM missions. This choice, however, also has drawbacks, like a shorter lifetime of the mission.

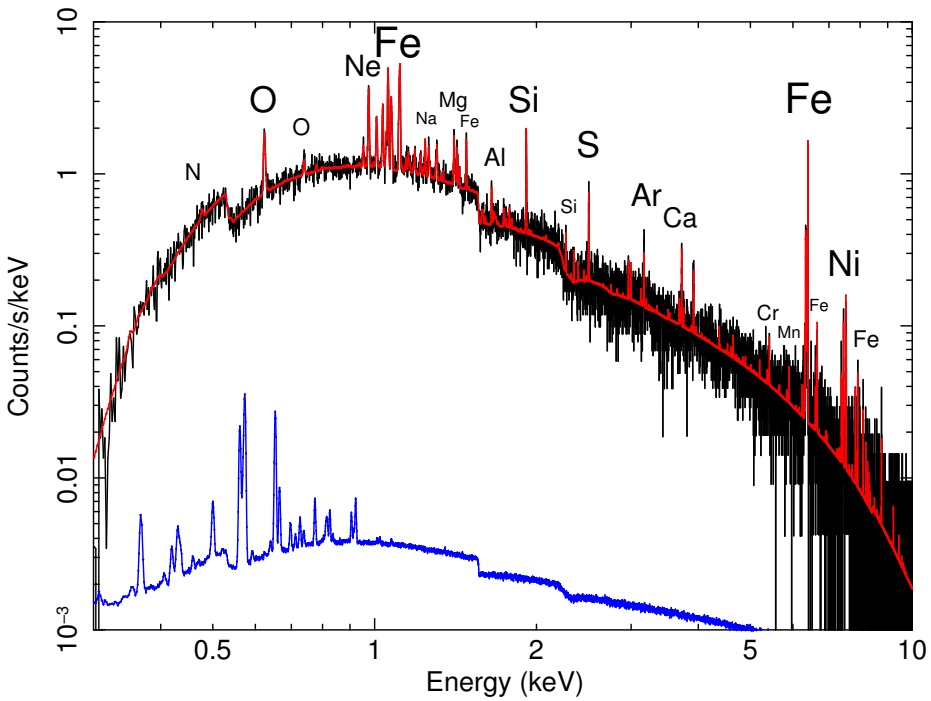


Figure 7.4: Simulated 100 ks spectrum of the core of Abell 4059 with SXS (*Hitomi/XARM*). Blue data points indicate the instrumental background (already subtracted in the upper spectrum). For clarity, error bars on the simulated data are not shown.

by pointing SXS successively toward the centre and an offset region of a cool-core cluster like Abell 4059. Since the instrumental background level of SXS is limited even at low surface brightness, it will be possible to measure the O/Fe and / or the Mg/Fe ratios with an excellent accuracy. Because O and Mg are produced in SNcc while Fe originates predominantly from SNIa, these two ratios are good indicators of the enriching SNcc-over-SNIa fraction in the studied regions of the ICM.

A third (and very interesting) contribution of SXS to the field resides in the substantial improvement of the measurement of the O, Ne, and Mg abundances. As discussed in Chapter 4, an accurate determination of the Ne/Mg ratio can in principle help to constrain the shape of the initial mass function (IMF) of the SNcc progenitors. This would be particularly valuable, since the question of the universality of the IMF is still under debate



Figure 7.5: Artist impression of the *Athena* satellite (Credit: ESA, MPE).

(e.g. Loewenstein 2013).

Finally, in addition to substantially improving the accuracy of the metal abundances discussed throughout this thesis, the SXS will also allow to detect the presence of rare elements (Na, Al, etc.) in the ICM for the first time. Measuring the abundance of these elements will be particularly useful to further constrain the initial metallicity of the SNcc progenitors (e.g. Nomoto et al. 2013).

7.5.3 Athena

Despite its very promising performances, the micro-calorimeter instrument onboard XARM is limited by its moderate spatial resolution (with a point spread function of $\sim 1.2'$) and effective area ($\sim 250 \text{ cm}^2$ at 1 keV). These limitations prevent studies of high-redshift clusters. Nevertheless, in a further future, the European mission *Athena* (Fig. 7.5, expected launch in 2028) is expected to overcome this issue.

Athena will be essentially composed of two key instruments: a micro-calorimeter — the X-ray Integral Field Unit (X-IFU; Barret et al. 2013) — for high spectral resolution imaging, and a Wide Field Imager (WFI; Rau et al. 2013) for moderate spectral resolution imaging, covering a larger field of view. Compared to SXS, the main improvements of X-IFU will be its significantly better spatial resolution (with an expected point spread function of $5''$) and effective area (expected to be $\sim 2 \text{ m}^2$ at 1 keV). This will allow to investigate metals with exquisite details not only in nearby clusters but also in more distant systems. For example, assuming 100 ks of cleaned ex-

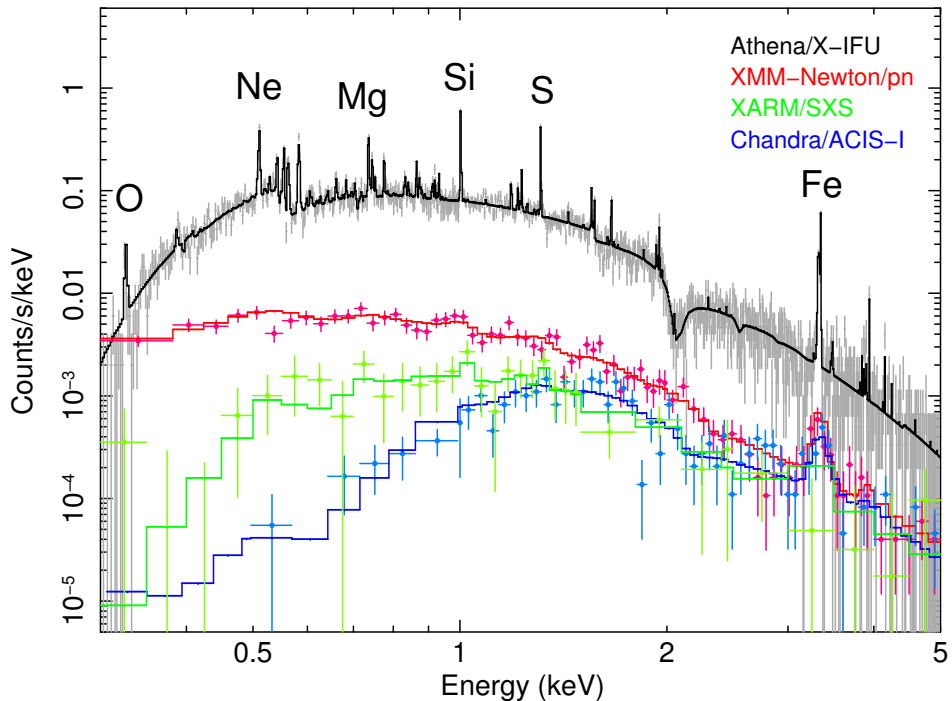


Figure 7.6: Simulated 250 ks spectrum of the core of a distant cluster ($kT = 3$ keV, $z = 1$) with the *Athena* X-IFU instrument. For comparison, similar simulated spectra are also shown for the *XMM-Newton* pn, *Chandra* ACIS-I, and *Hitomi*/XARM SXS instruments. For clarity, the data points have been rebinned to larger factors.

posure, X-IFU will be able to detect O, Si, and Fe in clusters up to $z = 1$ and to measure their abundances with at least 10% of accuracy (Pointecouteau et al. 2013). We illustrate this by simulating 250 ks of cleaned exposure of a bright distant ($z = 1$) cluster ($kT = 3$ keV) with X-IFU, and by comparing its simulated spectrum with that of other instruments (Fig. 7.6). An overview of the prospects of *Athena* in cluster physics is given by Ettori et al. (2013).

7.6 Concluding remarks

Since the launch of *Athena* is expected for 2028, patience will be required before entering into this completely new era. Nevertheless, there is no doubt that this mission — together with XARM and the possible other X-ray missions that may be planned in a near future — will considerably expand our knowledge on the origin and distribution of metals in the ICM. While systematic uncertainties should always be borne in mind (as discussed above and throughout this thesis), we can reasonably hope that simultaneous and continuous improvements in ICM observations, ICM simulations, supernova models, instrument calibration, and atomic calculations will substantially reduce them.

Clearly, the future of chemical enrichment studies at the largest scales of the Universe looks promising and full of surprising upcoming discoveries.

Bibliography

- Abramopoulos, F., Chanan, G. A., & Ku, W. H.-M. 1981, *ApJ*, 248, 429
- Allen, S. W. & Fabian, A. C. 1994, *MNRAS*, 269, 409
- Alpher, R. A., Bethe, H., & Gamow, G. 1948, *Physical Review*, 73, 803
- Andernach, H., Tago, E., Einasto, M., Einasto, J., & Jaaniste, J. 2005, in *Astronomical Society of the Pacific Conference Series*, Vol. 329, *Nearby Large-Scale Structures and the Zone of Avoidance*, ed. A. P. Fairall & P. A. Woudt, 283–287
- Anders, E. & Grevesse, N. 1989, *Geochim. Cosmochim. Acta*, 53, 197
- Anderson, M. E., Bregman, J. N., Butler, S. C., & Mullis, C. R. 2009, *ApJ*, 698, 317
- Arnaud, K. A. 1996, in *Astronomical Society of the Pacific Conference Series*, Vol. 101, *Astronomical Data Analysis Software and Systems V*, ed. G. H. Jacoby & J. Barnes, 17
- Arnett, D. 1995, *ARA&A*, 33, 115
- Arnett, W. D. 1973, *ARA&A*, 11, 73
- Arnett, W. D. 1977, *ApJS*, 35, 145
- Badenes, C., Borkowski, K. J., & Bravo, E. 2005, *ApJ*, 624, 198
- Badenes, C., Borkowski, K. J., Hughes, J. P., Hwang, U., & Bravo, E. 2006, *ApJ*, 645, 1373
- Badenes, C., Bravo, E., Borkowski, K. J., & Domínguez, I. 2003, *ApJ*, 593, 358
- Badnell, N. R. 2006, *ApJS*, 167, 334
- Baldi, A., Ettori, S., Molendi, S., & Gastaldello, F. 2012, *A&A*, 545, A41
- Balestra, I., Tozzi, P., Ettori, S., et al. 2007, *A&A*, 462, 429
- Barlow, M. J., Swinyard, B. M., Owen, P. J., et al. 2013, *Science*, 342, 1343
- Barret, D., den Herder, J. W., Piro, L., et al. 2013, ArXiv e-prints [arXiv:1308.6784]
- Baumgartner, V. & Breitschwerdt, D. 2009, *Astronomische Nachrichten*, 330, 898
- Baumgartner, W. H., Loewenstein, M., Horner, D. J., & Mushotzky, R. F. 2005, *ApJ*, 620, 680
- Beiersdorfer, P., Bitter, M., von Goeler, S., & Hill, K. W. 2004, *ApJ*, 610, 616
- Bethe, H. A. 1939, *Physical Review*, 55, 434

Bibliography

- Biffi, V., Planelles, S., Borgani, S., et al. 2017, MNRAS, 468, 531
- Bîrzan, L., Rafferty, D. A., Nulsen, P. E. J., et al. 2012, MNRAS, 427, 3468
- Böhringer, H., Belsole, E., Kennea, J., et al. 2001, A&A, 365, L181
- Böhringer, H., Matsushita, K., Churazov, E., Finoguenov, A., & Ikebe, Y. 2004a, A&A, 416, L21
- Böhringer, H., Matsushita, K., Finoguenov, A., Xue, Y., & Churazov, E. 2005, Advances in Space Research, 36, 677
- Böhringer, H., Schuecker, P., Guzzo, L., et al. 2004b, A&A, 425, 367
- Böhringer, H. & Werner, N. 2010, A&A Rev., 18, 127
- Boyarsky, A., Ruchayskiy, O., Iakubovskyi, D., & Franse, J. 2014, Physical Review Letters, 113, 251301
- Brachwitz, F., Dean, D. J., Hix, W. R., et al. 2000, ApJ, 536, 934
- Bradt, H., Mayer, W., Naranan, S., Rappaport, S., & Spada, G. 1967, ApJ, 150, L199
- Branch, D. 2001, PASP, 113, 169
- Branch, D., Thomas, R. C., Baron, E., et al. 2004, ApJ, 606, 413
- Bravo, E., Tornambe, A., Dominguez, I., & Isern, J. 1996, A&A, 306, 811
- Brickhouse, N. S., Dupree, A. K., Edgar, R. J., et al. 2000, ApJ, 530, 387
- Brickhouse, N. S. & Smith, R. K. 2005, Highlights of Astronomy, 13, 651
- Bryans, P., Landi, E., & Savin, D. W. 2009, ApJ, 691, 1540
- Bulbul, E., Markevitch, M., Foster, A., et al. 2014, ApJ, 789, 13
- Bulbul, E., Smith, R. K., & Loewenstein, M. 2012a, ApJ, 753, 54
- Bulbul, E., Smith, R. K., Foster, A., et al. 2012b, ApJ, 747, 32
- Buote, D. A. 2000, MNRAS, 311, 176
- Buote, D. A. & Canizares, C. R. 1994, ApJ, 427, 86
- Buote, D. A. & Fabian, A. C. 1998, MNRAS, 296, 977
- Buote, D. A., Lewis, A. D., Brighenti, F., & Mathews, W. G. 2003, ApJ, 595, 151
- Burbidge, E. M., Burbidge, G. R., Fowler, W. A., & Hoyle, F. 1957, Reviews of Modern Physics, 29, 547
- Burrows, A. 2013, Reviews of Modern Physics, 85, 245
- Byram, E. T., Chubb, T. A., & Friedman, H. 1966, Science, 152, 66
- Cameron, A. G. W. 1957a, PASP, 69, 201
- Cameron, A. G. W. 1957b, AJ, 62, 9
- Canizares, C. R., Clark, G. W., Markert, T. H., et al. 1979, ApJ, 234, L33
- Cao, Y., Kulkarni, S. R., Howell, D. A., et al. 2015, Nature, 521, 328
- Carter, J. A., Sembay, S., & Read, A. M. 2011, A&A, 527, A115
- Cash, W. 1979, ApJ, 228, 939
- Cattaneo, A. & Teyssier, R. 2007, MNRAS, 376, 1547
- Cavagnolo, K. W., Donahue, M., Voit, G. M., & Sun, M. 2009, ApJS, 182, 12
- Cavaliere, A. G., Gursky, H., & Tucker, W. H. 1971, Nature, 231, 437
- Chabrier, G. 2003, PASP, 115, 763

- Choi, Y.-Y., Reynolds, C. S., Heinz, S., et al. 2004, *ApJ*, 606, 185
- Churazov, E., Forman, W., Jones, C., & Böhringer, H. 2003, *ApJ*, 590, 225
- Cox, D. P. & Tucker, W. H. 1969, *ApJ*, 157, 1157
- Crosby, B. D., O'Shea, B. W., Beers, T. C., & Tumlinson, J. 2016, *ApJ*, 820, 71
- Dahlen, T., Strolger, L.-G., Riess, A. G., et al. 2004, *ApJ*, 613, 189
- De Grandi, S., Ettori, S., Longhetti, M., & Molendi, S. 2004, *A&A*, 419, 7
- De Grandi, S. & Molendi, S. 2001, *ApJ*, 551, 153
- De Grandi, S. & Molendi, S. 2009, *A&A*, 508, 565
- De Grandi, S., Santos, J. S., Nonino, M., et al. 2014, *A&A*, 567, A102
- De Luca, A. & Molendi, S. 2004, *A&A*, 419, 837
- de Plaa, J. 2013, *Astronomische Nachrichten*, 334, 416
- de Plaa, J., Kaastra, J. S., Tamura, T., et al. 2004, *A&A*, 423, 49
- de Plaa, J., Kaastra, J. S., Werner, N., et al. 2017, *A&A*, submitted
- de Plaa, J. & Mernier, F. 2017, *Astronomische Nachrichten*, in press [arXiv:1611.03723]
- de Plaa, J., Werner, N., Bleeker, J. A. M., et al. 2007, *A&A*, 465, 345
- de Plaa, J., Werner, N., Bykov, A. M., et al. 2006, *A&A*, 452, 397
- de Plaa, J., Zhuravleva, I., Werner, N., et al. 2012, *A&A*, 539, A34
- De Young, D. S. 1978, *ApJ*, 223, 47
- den Herder, J. W., Brinkman, A. C., Kahn, S. M., et al. 2001, *A&A*, 365, L7
- Dicke, R. H., Peebles, P. J. E., Roll, P. G., & Wilkinson, D. T. 1965, *ApJ*, 142, 414
- Diehl, S. & Statler, T. S. 2006, *MNRAS*, 368, 497
- Domainko, W., Gitti, M., Schindler, S., & Kapferer, W. 2004, *A&A*, 425, L21
- Domainko, W., Mair, M., Kapferer, W., et al. 2006, *A&A*, 452, 795
- Dupke, R. A. & White, III, R. E. 2000, *ApJ*, 528, 139
- Dutton, A. A., Mendel, J. T., & Simard, L. 2012, *MNRAS*, 422, 33
- Eddington, A. S. 1920, *The Observatory*, 43, 341
- Einstein, A. 1905, *Annalen der Physik*, 322, 891
- Einstein, A. 1916, *Annalen der Physik*, 354, 769
- Elkholy, T. Y., Bautz, M. W., & Canizares, C. R. 2015, *ApJ*, 805, 3
- Ettori, S. & Fabian, A. C. 2006, *MNRAS*, 369, L42
- Ettori, S., Pratt, G. W., de Plaa, J., et al. 2013, ArXiv e-prints [arXiv:1306.2322]
- Ezer, C., Bulbul, E., Nihal Ercan, E., et al. 2017, *ApJ*, 836, 110
- Fabian, A. C. 1994, *ARA&A*, 32, 277
- Fabian, A. C. & Pringle, J. E. 1977, *MNRAS*, 181, 5P
- Fabjan, D., Borgani, S., Tornatore, L., et al. 2010, *MNRAS*, 401, 1670
- Filippenko, A. V., Chornock, R., Swift, B., et al. 2003, *IAU Circ.*, 8159, 2
- Fink, M., Kromer, M., Seitzenzahl, I. R., et al. 2014, *MNRAS*, 438, 1762
- Finoguenov, A., Matsushita, K., Böhringer, H., Ikebe, Y., & Arnaud, M. 2002, *A&A*, 381, 21

Bibliography

- Foley, R. J. 2015, MNRAS, 452, 2463
- Frank, K. A., Peterson, J. R., Andersson, K., Fabian, A. C., & Sanders, J. S. 2013, ApJ, 764, 46
- Fujita, Y., Tawa, N., Hayashida, K., et al. 2008, PASJ, 60, S343
- Fukazawa, Y., Ohashi, T., Fabian, A. C., et al. 1994, PASJ, 46, L55
- Fuller, G. M., Fowler, W. A., & Newman, M. J. 1982, ApJS, 48, 279
- Gamezo, V. N., Khokhlov, A. M., & Oran, E. S. 2005, ApJ, 623, 337
- Gamow, G. 1946, Physical Review, 70, 572
- Gastaldello, F., Ettori, S., Balestra, I., et al. 2010, A&A, 522, A34
- Gastaldello, F. & Molendi, S. 2002, ApJ, 572, 160
- Gnedin, N. Y. 1998, MNRAS, 294, 407
- Grange, Y. G., de Plaa, J., Kaastra, J. S., et al. 2011, A&A, 531, A15
- Gu, L., Kaastra, J., Raassen, A. J. J., et al. 2015, A&A, 584, L11
- Gu, M. F. 2008, Canadian Journal of Physics, 86, 675
- Gunn, J. E. & Gott, III, J. R. 1972, ApJ, 176, 1
- Guo, F. & Mathews, W. G. 2010, ApJ, 717, 937
- Hamuy, M., Trager, S. C., Pinto, P. A., et al. 2000, AJ, 120, 1479
- Hatano, K., Branch, D., Lentz, E. J., et al. 2000, ApJ, 543, L49
- Heger, A. & Woosley, S. E. 2002, ApJ, 567, 532
- Heger, A. & Woosley, S. E. 2010, ApJ, 724, 341
- Heinz, S., Choi, Y.-Y., Reynolds, C. S., & Begelman, M. C. 2002, ApJ, 569, L79
- Hickox, R. C. & Markevitch, M. 2006, ApJ, 645, 95
- Hillebrandt, W., Kromer, M., Röpke, F. K., & Ruiter, A. J. 2013, Frontiers of Physics, 8, 116
- Hillebrandt, W. & Niemeyer, J. C. 2000, ARA&A, 38, 191
- Hitomi Collaboration, Aharonian, F., Akamatsu, H., et al. 2016, Nature, 535, 117
- Hopkins, A. M. & Beacom, J. F. 2006, ApJ, 651, 142
- Howell, D. A. 2011, Nature Communications, 2, 350
- Hoyle, F. 1946, MNRAS, 106, 343
- Huang, Z. & Sarazin, C. L. 1998, ApJ, 496, 728
- Hubble, E. 1929, Proceedings of the National Academy of Science, 15, 168
- Hubble, E. P. 1926, ApJ, 64
- Hudson, M. J., Lucey, J. R., Smith, R. J., Schlegel, D. J., & Davies, R. L. 2001, MNRAS, 327, 265
- Iakubovskyi, D. 2013, PhD thesis
- Iben, Jr., I. & Tutukov, A. V. 1984, ApJS, 54, 335
- Ichinohe, Y., Werner, N., Simionescu, A., et al. 2015, MNRAS, 448, 2971
- Iwamoto, K., Brachwitz, F., Nomoto, K., et al. 1999, ApJS, 125, 439
- Janka, H.-T. 2012, Annual Review of Nuclear and Particle Science, 62, 407
- Jansen, F., Lumb, D., Altieri, B., et al. 2001, A&A, 365, L1

- Jerkstrand, A., Timmes, F. X., Magkotsios, G., et al. 2015, *ApJ*, 807, 110
- Jha, S., Branch, D., Chornock, R., et al. 2006, *AJ*, 132, 189
- Johnstone, R. M., Allen, S. W., Fabian, A. C., & Sanders, J. S. 2002, *MNRAS*, 336, 299
- Johnstone, R. M., Fabian, A. C., Morris, R. G., & Taylor, G. B. 2005, *MNRAS*, 356, 237
- Jones, C. & Forman, W. 1984, *ApJ*, 276, 38
- Kaastra, J. S. & Bleeker, J. A. M. 2016, *A&A*, 587, A151
- Kaastra, J. S., Ferrigno, C., Tamura, T., et al. 2001, *A&A*, 365, L99
- Kaastra, J. S., Mewe, R., & Nieuwenhuijzen, H. 1996, in UV and X-ray Spectroscopy of Astrophysical and Laboratory Plasmas, ed. K. Yamashita & T. Watanabe, 411–414
- Kaastra, J. S., Tamura, T., Peterson, J. R., et al. 2004, *A&A*, 413, 415
- Kalberla, P. M. W., Burton, W. B., Hartmann, D., et al. 2005, *A&A*, 440, 775
- Kapferer, W., Knapp, A., Schindler, S., Kimeswenger, S., & van Kampen, E. 2005, *A&A*, 438, 87
- Kapferer, W., Kronberger, T., Breitschwerdt, D., et al. 2009, *A&A*, 504, 719
- Kapferer, W., Kronberger, T., Weratschnig, J., et al. 2007, *A&A*, 466, 813
- Kapferer, W., Schindler, S., Knollmann, S. R., & van Kampen, E. 2010, *A&A*, 516, A41
- Kapteyn, J. C. 1922, *ApJ*, 55, 302
- Karakas, A. I. 2010, *MNRAS*, 403, 1413
- Kasliwal, M. M., Kulkarni, S. R., Gal-Yam, A., et al. 2012, *ApJ*, 755, 161
- Kellogg, E., Murray, S., Giacconi, R., Tananbaum, T., & Gursky, H. 1973, *ApJ*, 185, L13
- Kellogg, E., Schreier, E., Tananbaum, H., Gursky, H., & Giacconi, R. 1972, in BAAS, Vol. 4, Bulletin of the American Astronomical Society, 336
- Khokhlov, A. M. 1989, *MNRAS*, 239, 785
- Khokhlov, A. M. 1991, *A&A*, 245, L25
- Kitayama, T., Bautz, M., Markevitch, M., et al. 2014, ArXiv e-prints [arXiv:1412.1176]
- Kobayashi, C., Karakas, A. I., & Umeda, H. 2011, *MNRAS*, 414, 3231
- Kobayashi, C. & Nomoto, K. 2009, *ApJ*, 707, 1466
- Kobayashi, C., Umeda, H., Nomoto, K., Tominaga, N., & Ohkubo, T. 2006, *ApJ*, 653, 1145
- Krick, J. E. & Bernstein, R. A. 2007, *AJ*, 134, 466
- Krick, J. E., Bernstein, R. A., & Pimbblet, K. A. 2006, *AJ*, 131, 168
- Kromer, M., Fink, M., Stanishev, V., et al. 2013, *MNRAS*, 429, 2287
- Kuntz, K. D. & Snowden, S. L. 2008, *ApJ*, 674, 209
- Langanke, K. & Martínez-Pinedo, G. 1998, *Physics Letters B*, 436, 19
- Langanke, K. & Martínez-Pinedo, G. 2001, *Atomic Data and Nuclear Data Tables*,

Bibliography

- 79, 1
- Leccardi, A. & Molendi, S. 2008, A&A, 487, 461
- Lehmer, B. D., Xue, Y. Q., Brandt, W. N., et al. 2012, ApJ, 752, 46
- Li, W., Chornock, R., Leaman, J., et al. 2011, MNRAS, 412, 1473
- Li, W., Filippenko, A. V., Treffers, R. R., et al. 2001, ApJ, 546, 734
- Liang, L., Durier, F., Babul, A., et al. 2016, MNRAS, 456, 4266
- Lin, Y.-T., Mohr, J. J., & Stanford, S. A. 2003, ApJ, 591, 749
- Lodders, K., Palme, H., & Gail, H.-P. 2009, Landolt Börnstein, 44
- Loewenstein, M. 2006, ApJ, 648, 230
- Loewenstein, M. 2013, ApJ, 773, 52
- Lovisari, L., Schindler, S., & Kapferer, W. 2011, A&A, 528, A60
- Lumb, D. H., Warwick, R. S., Page, M., & De Luca, A. 2002, A&A, 389, 93
- Madau, P. & Dickinson, M. 2014, ARA&A, 52, 415
- Maeda, K., Röpke, F. K., Fink, M., et al. 2010, ApJ, 712, 624
- Mahdavi, A. & Geller, M. J. 2001, ApJ, 554, L129
- Mannucci, F., Della Valle, M., & Panagia, N. 2006, MNRAS, 370, 773
- Mannucci, F., Della Valle, M., Panagia, N., et al. 2005, A&A, 433, 807
- Mao, J. & Kaastra, J. 2016, A&A, 587, A84
- Maoz, D. 2008, MNRAS, 384, 267
- Maoz, D. & Mannucci, F. 2012, PASA, 29, 447
- Maoz, D., Mannucci, F., & Nelemans, G. 2014, ARA&A, 52, 107
- Martin, D., Perego, A., Arcones, A., et al. 2015, ApJ, 813, 2
- Matsushita, K. 2011, A&A, 527, A134
- Matsushita, K., Finoguenov, A., & Böhringer, H. 2003, A&A, 401, 443
- Matsushita, K., Fukazawa, Y., Hughes, J. P., et al. 2007, PASJ, 59, 327
- Matsushita, K., Makishima, K., Rokutanda, E., Yamasaki, N. Y., & Ohashi, T. 1997, ApJ, 488, L125
- Matteucci, F. & Chiappini, C. 2005, PASA, 22, 49
- Matteucci, F. & Recchi, S. 2001, ApJ, 558, 351
- Maughan, B. J., Jones, C., Forman, W., & Van Speybroeck, L. 2008, ApJS, 174, 117
- McCarthy, I. G., Schaye, J., Bower, R. G., et al. 2011, MNRAS, 412, 1965
- McDonald, M., Stalder, B., Bayliss, M., et al. 2016, ApJ, 817, 86
- McDonald, M., Veilleux, S., Rupke, D. S. N., Mushotzky, R., & Reynolds, C. 2011, ApJ, 734, 95
- McQuinn, M. 2016, ARA&A, 54, 313
- Medvedev, P., Gilfanov, M., Sazonov, S., & Shtykovskiy, P. 2014, MNRAS, 440, 2464
- Merrill, P. W. 1952, in The National Academy of Sciences: Abstracts of Papers Presented at the Annual Meeting April 28-30, Science, Vol. 115, 479–489
- Mewe, R. 1972, A&A, 20, 215
- Mewe, R. & Gronenschild, E. H. B. M. 1981, A&AS, 45, 11

- Mewe, R., Gronenschild, E. H. B. M., & van den Oord, G. H. J. 1985, A&AS, 62, 197
 Mewe, R., Lemen, J. R., & van den Oord, G. H. J. 1986, A&AS, 65, 511
 Million, E. T., Werner, N., Simionescu, A., & Allen, S. W. 2011, MNRAS, 418, 2744
 Mitchell, R. J., Culhane, J. L., Davison, P. J. N., & Ives, J. C. 1976, MNRAS, 175, 29P
 Miyaji, T., Griffiths, R. E., Lumb, D., Sarajedini, V., & Siddiqui, H. 2003, Astronomische Nachrichten, 324, 24
 Molendi, S., Eckert, D., De Grandi, S., et al. 2016, A&A, 586, A32
 Molendi, S. & Pizzolato, F. 2001, ApJ, 560, 194
 Moretti, A., Pagani, C., Cusumano, G., et al. 2009, A&A, 493, 501
 Moretti, A., Portinari, L., & Chiosi, C. 2003, A&A, 408, 431
 Morris, R. A. H., Phillipps, S., Jones, J. B., et al. 2007, A&A, 476, 59
 Morsony, B. J., Heath, C., & Workman, J. C. 2014, MNRAS, 441, 2134
 Mulchaey, J. S., Kasliwal, M. M., & Kollmeier, J. A. 2014, ApJ, 780, L34
 Mushotzky, R., Loewenstein, M., Arnaud, K. A., et al. 1996, ApJ, 466, 686
 Mushotzky, R. F., Holt, S. S., Boldt, E. A., Serlemitsos, P. J., & Smith, B. W. 1981, ApJ, 244, L47
 Mushotzky, R. F. & Loewenstein, M. 1997, ApJ, 481, L63
 Nagashima, M., Lacey, C. G., Baugh, C. M., Frenk, C. S., & Cole, S. 2005, MNRAS, 358, 1247
 Nandra, K., Barret, D., Barcons, X., et al. 2013, ArXiv e-prints [arXiv:1306.2307]
 Niemeyer, J. C. & Woosley, S. E. 1997, ApJ, 475, 740
 Nomoto, K., Kobayashi, C., & Tominaga, N. 2013, ARA&A, 51, 457
 Nomoto, K., Thielemann, F.-K., & Wheeler, J. C. 1984, ApJ, 279, L23
 Nomoto, K., Tominaga, N., Umeda, H., Kobayashi, C., & Maeda, K. 2006, Nuclear Physics A, 777, 424
 O'Dea, C. P., Baum, S. A., Privon, G., et al. 2008, ApJ, 681, 1035
 Ohashi, T. 1995, in American Institute of Physics Conference Series, Vol. 336, Dark Matter, ed. S. S. Holt & C. L. Bennett, 255–263
 Olling, R. P., Mushotzky, R., Shaya, E. J., et al. 2015, Nature, 521, 332
 O'Sullivan, E., David, L. P., & Vrtilek, J. M. 2014, MNRAS, 437, 730
 Pakmor, R., Kromer, M., Röpke, F. K., et al. 2010, Nature, 463, 61
 Pakmor, R., Kromer, M., Taubenberger, S., et al. 2012, ApJ, 747, L10
 Panagoulia, E. K., Fabian, A. C., & Sanders, J. S. 2013, MNRAS, 433, 3290
 Panagoulia, E. K., Sanders, J. S., & Fabian, A. C. 2015, MNRAS, 447, 417
 Paterno-Mahler, R., Blanton, E. L., Randall, S. W., & Clarke, T. E. 2013, ApJ, 773, 114
 Peimbert, A., Peimbert, M., & Luridiana, V. 2016, Rev. Mexicana Astron. Astrofis., 52, 419
 Peng, F. & Nagai, D. 2009, ApJ, 693, 839
 Penzias, A. A. & Wilson, R. W. 1965, ApJ, 142, 419

Bibliography

- Perets, H. B., Gal-yam, A., Crockett, R. M., et al. 2011, *ApJ*, 728, L36
Perets, H. B., Gal-Yam, A., Mazzali, P. A., et al. 2010, *Nature*, 465, 322
Perrin, J. 1922, *L'Astronomie*, 36, 49
Peterson, J. R., Kahn, S. M., Paerels, F. B. S., et al. 2003, *ApJ*, 590, 207
Peterson, J. R., Paerels, F. B. S., Kaastra, J. S., et al. 2001, *A&A*, 365, L104
Phillips, M. M., Li, W., Frieman, J. A., et al. 2007, *PASP*, 119, 360
Piersanti, L., Gagliardi, S., Iben, Jr., I., & Tornambé, A. 2003, *ApJ*, 598, 1229
Pinto, C., Fabian, A. C., Werner, N., et al. 2014, *A&A*, 572, L8
Pinto, C., Sanders, J. S., Werner, N., et al. 2015, *A&A*, 575, A38
Planelles, S., Borgani, S., Fabjan, D., et al. 2014, *MNRAS*, 438, 195
Pointecouteau, E., Reiprich, T. H., Adami, C., et al. 2013, ArXiv e-prints [arXiv:1306.2319]
Rafferty, D. A., Bîrzan, L., Nulsen, P. E. J., et al. 2013, *MNRAS*, 428, 58
Ramirez-Ruiz, E., Trenti, M., MacLeod, M., et al. 2015, *ApJ*, 802, L22
Rasia, E., Borgani, S., Murante, G., et al. 2015, *ApJ*, 813, L17
Rasia, E., Mazzotta, P., Bourdin, H., et al. 2008, *ApJ*, 674, 728
Rasmussen, J. & Ponman, T. J. 2007, *MNRAS*, 380, 1554
Rasmussen, J. & Ponman, T. J. 2009, *MNRAS*, 399, 239
Rau, A., Meidinger, N., Nandra, K., et al. 2013, ArXiv e-prints [arXiv:1308.6785]
Raymond, J. C. & Smith, B. W. 1977, *ApJS*, 35, 419
Read, A. M., Guainazzi, M., & Sembay, S. 2014, *A&A*, 564, A75
Rebusco, P., Churazov, E., Böhringer, H., & Forman, W. 2005, *MNRAS*, 359, 1041
Rebusco, P., Churazov, E., Böhringer, H., & Forman, W. 2006, *MNRAS*, 372, 1840
Reiprich, T. H., Basu, K., Ettori, S., et al. 2013, *Space Sci. Rev.*, 177, 195
Reiprich, T. H. & Böhringer, H. 2002, *ApJ*, 567, 716
Renzini, A. & Andreon, S. 2014, *MNRAS*, 444, 3581
Renzini, A., Ciotti, L., D'Ercole, A., & Pellegrini, S. 1993, *ApJ*, 419, 52
Reynolds, C. S., Casper, E. A., & Heinz, S. 2008, *ApJ*, 679, 1181
 Riess, A. G., Filippenko, A. V., Challis, P., et al. 1998, *AJ*, 116, 1009
Roediger, E., Brüggen, M., Simionescu, A., et al. 2011, *MNRAS*, 413, 2057
Roediger, E., Lovisari, L., Dupke, R., et al. 2012, *MNRAS*, 420, 3632
Romano, D., Karakas, A. I., Tosi, M., & Matteucci, F. 2010, *A&A*, 522, A32
Rubin, V. C. & Ford, Jr., W. K. 1970, *ApJ*, 159, 379
Ruiter, A. J., Sim, S. A., Pakmor, R., et al. 2013, *MNRAS*, 429, 1425
Russell, H. R., McNamara, B. R., Edge, A. C., et al. 2013, *MNRAS*, 432, 530
Russell, H. R., Sanders, J. S., & Fabian, A. C. 2008, *MNRAS*, 390, 1207
Salpeter, E. E. 1955, *ApJ*, 121, 161
Sanders, J. S. & Fabian, A. C. 2002, *MNRAS*, 331, 273
Sanders, J. S. & Fabian, A. C. 2006a, *MNRAS*, 371, 1483
Sanders, J. S. & Fabian, A. C. 2006b, *MNRAS*, 370, 63

- Sanders, J. S. & Fabian, A. C. 2007, MNRAS, 381, 1381
- Sanders, J. S. & Fabian, A. C. 2011, MNRAS, 412, L35
- Sanders, J. S., Fabian, A. C., Allen, S. W., et al. 2008, MNRAS, 385, 1186
- Sanders, J. S., Fabian, A. C., Allen, S. W., & Schmidt, R. W. 2004, MNRAS, 349, 952
- Sanders, J. S., Fabian, A. C., Taylor, G. B., et al. 2016, MNRAS, 457, 82
- Sanderson, A. J. R., O'Sullivan, E., & Ponman, T. J. 2009, MNRAS, 395, 764
- Sarazin, C. L. 1986, *Reviews of Modern Physics*, 58, 1
- Sasaki, T., Matsushita, K., & Sato, K. 2014, ApJ, 781, 36
- Sato, K., Matsushita, K., Ishisaki, Y., et al. 2009, PASJ, 61, S353
- Sato, K., Matsushita, K., Ishisaki, Y., et al. 2008, PASJ, 60, S333
- Sato, K., Tokoi, K., Matsushita, K., et al. 2007a, ApJ, 667, L41
- Sato, K., Yamasaki, N. Y., Ishida, M., et al. 2007b, PASJ, 59, 299
- Scalzo, R. A., Ruiter, A. J., & Sim, S. A. 2014, MNRAS, 445, 2535
- Schellenberger, G., Reiprich, T. H., Lovisari, L., Nevalainen, J., & David, L. 2015, A&A, 575, A30
- Schindler, S. & Diaferio, A. 2008, Space Sci. Rev., 134, 363
- Schindler, S., Kapferer, W., Domainko, W., et al. 2005, A&A, 435, L25
- Schlegel, D. J., Finkbeiner, D. P., & Davis, M. 1998, ApJ, 500, 525
- Schmidt, B. P., Suntzeff, N. B., Phillips, M. M., et al. 1998, ApJ, 507, 46
- Seitenzahl, I. R., Cescutti, G., Röpke, F. K., Ruiter, A. J., & Pakmor, R. 2013a, A&A, 559, L5
- Seitenzahl, I. R., Ciaraldi-Schoolmann, F., Röpke, F. K., et al. 2013b, MNRAS, 429, 1156
- Seitenzahl, I. R., Summa, A., Krauß, F., et al. 2015, MNRAS, 447, 1484
- Serlemitsos, P. J., Smith, B. W., Boldt, E. A., Holt, S. S., & Swank, J. H. 1977, ApJ, 211, L63
- Shah, C., Dobrodey, S., Bernitt, S., et al. 2016, ApJ, 833, 52
- Simionescu, A., Roediger, E., Nulsen, P. E. J., et al. 2009a, A&A, 495, 721
- Simionescu, A., Werner, N., Böhringer, H., et al. 2009b, A&A, 493, 409
- Simionescu, A., Werner, N., Finoguenov, A., Böhringer, H., & Brüggen, M. 2008, A&A, 482, 97
- Simionescu, A., Werner, N., Forman, W. R., et al. 2010, MNRAS, 405, 91
- Simionescu, A., Werner, N., Urban, O., et al. 2015, ApJ, 811, L25
- Smartt, S. J. 2009, ARA&A, 47, 63
- Smith, R. J., Lucey, J. R., Hudson, M. J., Schlegel, D. J., & Davies, R. L. 2000, MNRAS, 313, 469
- Smith, R. K., Brickhouse, N. S., Liedahl, D. A., & Raymond, J. C. 2001, ApJ, 556, L91
- Snowden, S. L., Collier, M. R., & Kuntz, K. D. 2004, ApJ, 610, 1182
- Snowden, S. L. & Kuntz, K. D. 2013, XMM ESAS cookbook

Bibliography

- Stewart, G. C., Fabian, A. C., Jones, C., & Forman, W. 1984, ApJ, 285, 1
- Strüder, L., Briel, U., Dennerl, K., et al. 2001, A&A, 365, L18
- Sullivan, M., Le Borgne, D., Pritchett, C. J., et al. 2006, ApJ, 648, 868
- Sun, M. 2012, New Journal of Physics, 14, 045004
- Takahashi, T., Mitsuda, K., Kelley, R., et al. 2014, ArXiv e-prints [arXiv:1412.2351]
- Tamura, T., Bleeker, J. A. M., Kaastra, J. S., Ferrigno, C., & Molendi, S. 2001, A&A, 379, 107
- Tamura, T., Kaastra, J. S., den Herder, J. W. A., Bleeker, J. A. M., & Peterson, J. R. 2004, A&A, 420, 135
- Tamura, T., Maeda, Y., Mitsuda, K., et al. 2009, ApJ, 705, L62
- Taylor, G. B., Barton, E. J., & Ge, J. 1994, AJ, 107, 1942
- Thölken, S., Lovisari, L., Reiprich, T. H., & Hasenbusch, J. 2016, A&A, 592, A37
- Timmes, F. X., Woosley, S. E., & Weaver, T. A. 1995, ApJS, 98, 617
- Tinsley, B. M. 1980, Fund. Cosmic Phys., 5, 287
- Tornatore, L., Borgani, S., Dolag, K., & Matteucci, F. 2007, MNRAS, 382, 1050
- Tozzi, P., Rosati, P., Ettori, S., et al. 2003, ApJ, 593, 705
- Treu, T., Auger, M. W., Koopmans, L. V. E., et al. 2010, ApJ, 709, 1195
- Tsujimoto, T., Nomoto, K., Yoshii, Y., et al. 1995, MNRAS, 277, 945
- Turner, M. J. L., Abbey, A., Arnaud, M., et al. 2001, A&A, 365, L27
- Umeda, H. & Nomoto, K. 2002, ApJ, 565, 385
- Urdampilleta, I., Kaastra, J. S., & Mehdipour, M. 2017, A&A, in press [arXiv:1702.06007]
- Voit, G. M. & Donahue, M. 2011, ApJ, 738, L24
- Waldman, R., Sauer, D., Livne, E., et al. 2011, ApJ, 738, 21
- Weaver, T. A. & Woosley, S. E. 1980, in Annals of the New York Academy of Sciences, Vol. 336, Ninth Texas Symposium on Relativistic Astrophysics, ed. J. Ehlers, J. J. Perry, & M. Walker, 335–357
- Weaver, T. A., Zimmerman, G. B., & Woosley, S. E. 1978, ApJ, 225, 1021
- Webbink, R. F. 1984, ApJ, 277, 355
- Werner, N., Böhringer, H., Kaastra, J. S., et al. 2006a, A&A, 459, 353
- Werner, N., de Plaa, J., Kaastra, J. S., et al. 2006b, A&A, 449, 475
- Werner, N., Durret, F., Ohashi, T., Schindler, S., & Wiersma, R. P. C. 2008, Space Sci. Rev., 134, 337
- Werner, N., Urban, O., Simionescu, A., & Allen, S. W. 2013, Nature, 502, 656
- Whelan, J. & Iben, Jr., I. 1973, ApJ, 186, 1007
- Wiersma, R. P. C., Schaye, J., Theuns, T., Dalla Vecchia, C., & Tornatore, L. 2009, MNRAS, 399, 574
- Willingale, R., Starling, R. L. C., Beardmore, A. P., Tanvir, N. R., & O'Brien, P. T. 2013, MNRAS, 431, 394
- Willman, B., Governato, F., Wadsley, J., & Quinn, T. 2004, MNRAS, 355, 159

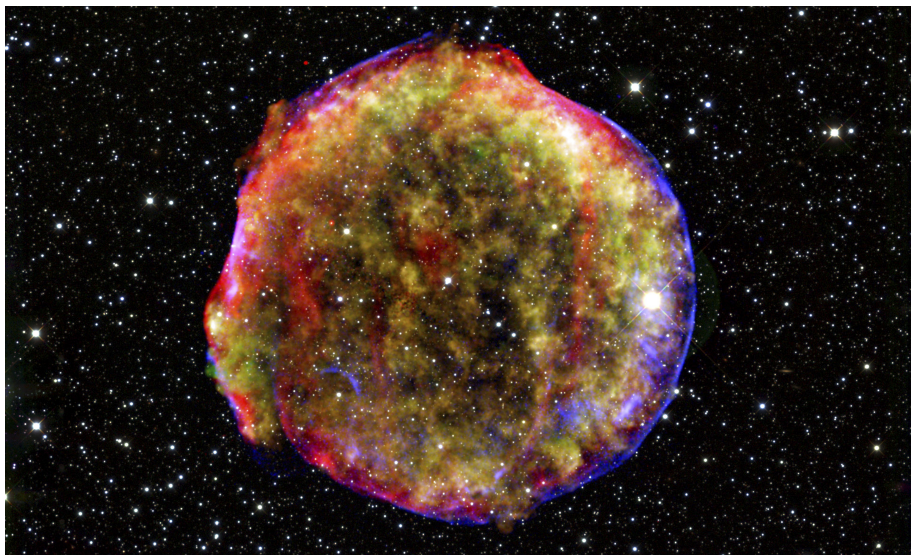
- Woosley, S. E. & Weaver, T. A. 1995, ApJS, 101, 181
Yamaguchi, H., Badenes, C., Foster, A. R., et al. 2015, ApJ, 801, L31
Yasumi, M., Nobukawa, M., Nakashima, S., et al. 2014, PASJ, 66, 68
Yates, R. M., Thomas, P. A., & Henriques, B. M. B. 2017, MNRAS, 464, 3169
Yoshii, Y., Tsujimoto, T., & Nomoto, K. 1996, ApJ, 462, 266
Yuan, F., Kobayashi, C., Schmidt, B. P., et al. 2013, MNRAS, 432, 1680
Zhang, Y.-Y., Andernach, H., Caretta, C. A., et al. 2011, A&A, 526, A105
Zhang, Y.-Y., Reiprich, T. H., Finoguenov, A., Hudson, D. S., & Sarazin, C. L. 2009,
ApJ, 699, 1178
Zwicky, F. 1933, Helvetica Physica Acta, 6, 110

Nederlandse samenvatting

Waar komen we vandaan? Deze vraag is natuurlijk heel breed omdat hij veel verschillende disciplines omvat (natuurkunde, biologie, sterrenkunde, filosofie, etc.). Het is moeilijk (of zelfs onmogelijk) om daar één duidelijk antwoord op te geven. Echter, één van de meest buitengewone ontdekkingen van de 20ste eeuw heeft voor een revolutie gezorgd in onze kennis over onze oorsprong. Zestig jaar geleden hebben we ontdekt dat de bouwstenen van planeten en het leven gevormd worden in de kern van sterren en wanneer die als supernova ontploffen. We zijn, met andere woorden, niets anders dan "sterrenstof".

De oorsprong van chemische elementen

De elementaire bouwstenen van alle stoffen die we kennen worden chemische elementen genoemd. Ze groeperen zich vaak in moleculen om zo planeten, rotsen, water, ijs, cellen, dieren etc. te vormen. Ze zijn de basis van de chemie en van het leven. Dankzij het werk van verschillende generaties van astronomen kennen we nu het verhaal over de oorsprong van chemische elementen in het Heelal. Zo'n 13.7 miljard jaar geleden hebben de extreme condities tijdens de eerste minuten na de Big Bang gezorgd voor de vorming van het waterstof en een groot deel van het helium dat we in ons Universum vinden. Zwaardere elementen, oftewel "metalen", zoals koolstof, stikstof, zuurstof, silicium en ijzer, konden in deze eerste minuten niet worden geproduceerd. Zij werden pas honderden miljoenen jaren na de Big Bang in de eerste sterren gevormd toen die ontploften als supernovae. Sindsdien hebben vele generaties van sterren mede door supernova explosies het Heelal verrijkt met zwaardere elementen.



Figuur 1: De Tycho supernova is een (Type Ia) overblijfsel van een supernova waarvan de explosie in het jaar 1572 werd waargenomen. De overblijfselen van deze voormalige witte dwerg en een geweldige hoeveelheid aan vers geproduceerd metaal verspreiden zich in de nabijgelegen interstellaire omgeving (Bronnen: NASA/SAO/CXC,JPL-Caltech/MPIA).

Niet alle supernovae zijn hetzelfde en verschillende typen supernovae kunnen elementen in verschillende hoeveelheden produceren. Ze kunnen in twee primaire categorieën worden ingedeeld:

1. Core-collapse supernovae (SNcc) zijn zware sterren met een massa die meer dan tien keer groter is dan de Zon en waarvan de kern aan het eind van zijn leven in elkaar stort. Dit zorgt voor een explosie in de laag rondom de kern die het meeste stellaire materiaal de ruimte in slingert. De kern van de ster wordt door de explosie samengeperst tot een neutronenster (voor sterren met een massa minder dan dertig keer de massa van de Zon) of een zwart gat (als de massa meer dan dertig keer groter was dan de massa van de Zon). Van deze supernovae denken we dat ze bijna al het zuurstof, neon en magnesium in het Heelal produceren. Omdat zulke massieve sterren op astronomische schaal een relatief korte levensduur hebben van maar een paar miljoen jaar, ontploffen die supernovae "snel" ten opzichte van de andere sterren.

2. Type Ia supernovae (SNIa) worden gevormd in een dubbelstersysteem dat bestaat uit minder zware sterren (met een massa die minder is dan acht keer de massa van de Zon). Ze zijn het resultaat van een explosie van een witte dwerg (een overblijfsel van de kern van een ster met een lage massa). Deze explosie wordt veroorzaakt door een begeleidende ster die samen met de witte dwerg in een nauwe baan om elkaar heen draaien. Als de afstand tussen de sterren kort genoeg is, kan er gas van de begeleidende ster naar de witte dwerg toe stromen. Dit gaat goed, totdat de temperatuur op het oppervlak van de witte dwerg zo hoog wordt dat het koolstof in de witte dwerg in één explosieve klap fuseert. De begeleidende ster kan ook een witte dwerg zijn. Dan ontstaat de explosie door een gewelddadige botsing tussen de twee witte dwergen. Zelfs vandaag is het voor astronomen nog onduidelijk welke van deze twee scenario's het vaakst voorkomt. In beide gevallen gaan we ervan uit dat deze supernovae zwaardere elementen zoals chroom, mangaan, ijzer en nikkel produceren en de omgeving in slingeren. In vergelijking tot de SNcc, hebben SNIa veel meer tijd nodig om te exploderen, omdat lichtere sterren die witte dwergen vormen veel langer leven dan zwaardere sterren (wel tot miljarden jaren).

Elementen die qua massa tussen magnesium en chroom in zitten, zoals silicium, zwavel, argon en calcium worden waarschijnlijk door zowel SNIa en SNcc in vergelijkbare hoeveelheden geproduceerd. Koolstof en stikstof, beiden essentieel voor het leven op aarde, worden waarschijnlijk niet in supernovae gevormd, maar gedurende de laatste levensfasen van sterren met een lage of middelmatige massa.

Toch begrijpen we nog lang niet alles over supernovae. Wat is bijvoorbeeld de precieze identiteit van het begeleidend object van explosieve SNIa? En, wat is het precieze fysische mechanisme dat leidt tot de explosie? Er zijn nog veel onopgeloste vragen over de massieve sterren die als supernova zijn ontploft. Hoeveel massieve sterren hebben zich er ontstaan in verhouding tot minder massieve sterren? Zijn deze massieve sterren eerder verrijkt door een vroegere generatie sterren?

De relatieve hoeveelheden van zware elementen in het heelal kunnen belangrijke aanwijzingen opleveren om deze vragen te beantwoorden, omdat de eigenschappen van de sterpopulatie bepalen hoeveel er van ieder element wordt geproduceerd. Als we de hoeveelheden (abundanties) van al deze elementen in SNIa en/of SNcc konden meten, moeten we in staat

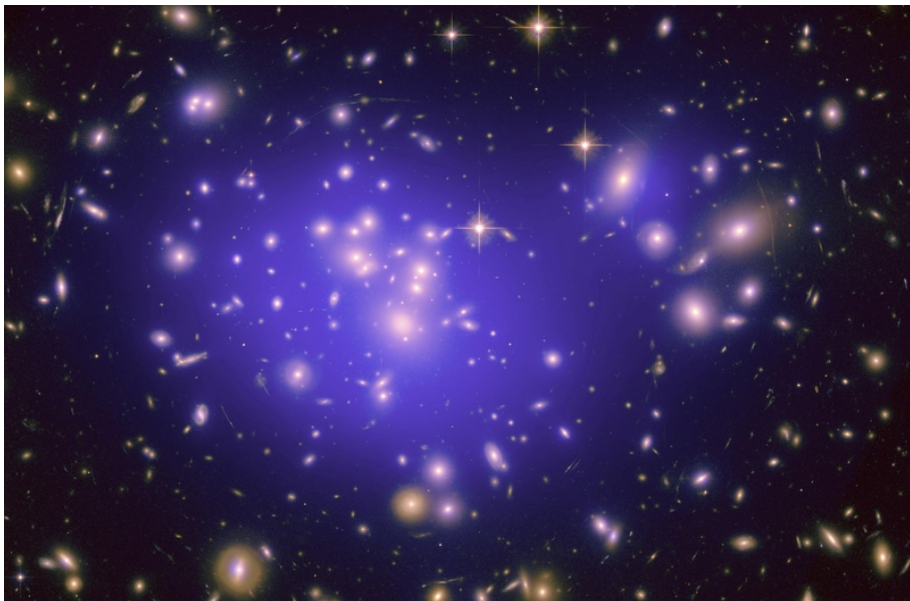
zijn om de fysica en de omgevingskenmerken van deze interessante objecten beter te begrijpen (Fig. 1). Er zijn maar enkele supernovae recent in ons eigen melkwegstelsel afgegaan die we goed kunnen bestuderen, wat ons nog geen goed algemeen beeld geeft van alle supernovae in het Universum. Als we de vorming van elementen beter willen begrijpen, dan is het nodig om op de grote schaal van het heelal te kijken.

Van supernovae tot clusters van sterrenstelsels

Op Universele schaal zijn clusters van melkwegstelsels de grootste door zwaartekracht gebonden objecten. In feite zijn melkwegstelsels niet willekeurig door de ruimte verspreid. In plaats daarvan vind je ze vaak in groepen (met daarin enkele tientallen sterrenstelsels) of in grotere clusters (van 100 tot 1000 sterrenstelsels). Alle sterren, planeten, het interstellair gas en het stof die bij de sterrenstelsels horen, vormen slechts 10 tot 20 procent van de totaal zichtbare (oftewel ‘normale’) materie in een cluster. 80 tot 90 procent van de normale materie in clusters bestaat uit een heel heet en diffuus gas. Door de hoge massa van de clusters vallen gassen en stelsels uit de omgeving naar het cluster toe. De gassen botsen met zichzelf en warmen daardoor op tot wel 10 tot 100 miljoen graden. Deze hete gaswolk noemen we het Intra-Cluster Medium (ICM). De extreme verhitting zorgt ervoor dat het röntgenstraling uit gaat zenden (Fig. 2). De meest recente generatie van röntgensatellieten, en dan met name de Europese missie *XMM-Newton* (Fig. 3 links), is erg geschikt om het ICM te observeren en om de eigenschappen ervan via röntgenspectroscopie te bestuderen.

Wat is röntgenspectroscopie?

Zoals veel andere telescopen op Aarde óf in een baan rond de Aarde, kunnen de röntgenruimtetelescopen van tegenwoordig veel meer dan het slechts ‘zien’ van astrofysische bronnen aan de hemel. Precies zoals een regenwolk zonlicht in een brede reeks van kleuren (of specifieke golflengten) kan ontleden in een regenboog, kunnen de instrumenten aan boord van de meest recente röntgensatellieten het röntgenlicht van het hete ICM ontleden. Door de binnenkomende röntgenlichtdeeltjes te sorteren op golflengte (of ‘kleur’) maken sterrenkundigen een grafiek die een röntgenspectrum genoemd wordt. Daarmee kunnen we verschillende kenmerken van het gas (bijvoorbeeld de temperatuur of dichtheid) bepalen.



Figuur 2: Cluster Abell 1689. In zichtbaar licht (hier in het geel), zie je de individuele sterrenstelsels. Er is echter veel meer 'normale' materie in het cluster in de vorm van een heet gas, dat zichtbaar is in röntgenlicht (hier in het paars). Dit gas is ook rijk aan metalen die de afgelopen miljoen jaar werden geproduceerd door SNIa en SNcc in de melkwegstelsels (Bronnen: NASA, ESA, E. Jullo, P. Natarajan, and J-P. Kneib).

Metalen in het hete intra-cluster medium

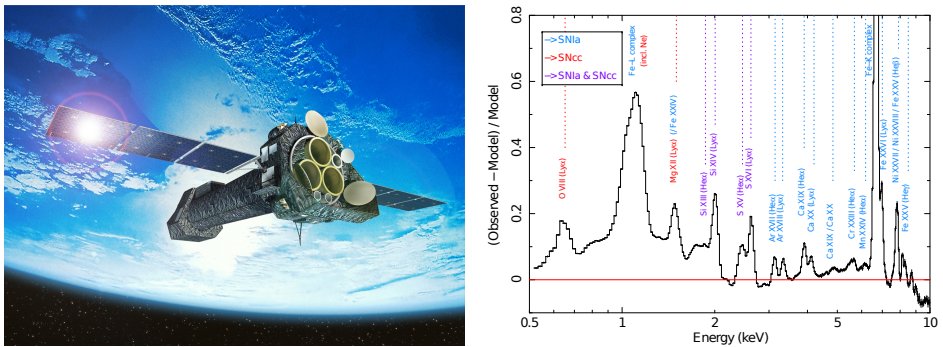
Ongeveer veertig jaar geleden ontdekten astronomen de aanwezigheid van emissielijnen in röntgenspectra van dit clustergas. Deze emissielijnen zijn een karakteristieke aanwijzing voor de aanwezigheid van zware elementen. Dit houdt in dat het ICM een significante hoeveelheid metalen bezit. Aangezien alleen supernovae zware elementen kunnen produceren, moeten die metalen afkomstig zijn van SNIa en SNcc in de individuele sterrenstelsels. De metalen zijn dus niet alleen in de nabije omgeving van de supernova beland, maar hebben ook het ICM buiten de melkwegstelsels bereikt. Met andere woorden, zelfs de grootste schalen van het Universum worden chemisch door sterren en supernovae verrijkt. Gelukkig is de röntgenemissie van het ICM makkelijk op computers te modelleren en kunnen we ook de metaalabundanties van dit gas meten door hun corresponde-

rende lijnen in de röntgenspectra van clusters te analyseren (Fig. 3 rechts). Omdat het hete gas de geproduceerde elementen van miljarden supernovae bevat die in het verleden in het cluster zijn ontploft, kan de abundantie van die elementen in het ICM direct worden vergeleken met de hoeveelheden die door de huidige moderne SNIa en SNcc modellen zijn voorspeld. Door deze vergelijking te doen, blijkt dat sommige scenario's voor het ontstaan en ontploffen van supernovae goed bij de waarnemingen passen en andere scenario's juist niet. Uiteindelijk helpt het meten van de hoeveelheid metalen in clusters ons om supernovae beter te kunnen begrijpen. Hoe zit het eigenlijk met de verspreiding van deze metalen in clusters? Zijn de metalen juist geconcentreerd in de kern van clusters of juist aan de rand van clusters? Worden ze gelijkmataig door het clustergas verspreid of vind je ze slechts in sommige specifieke gebieden? De antwoorden op deze vragen kunnen ons waardevolle informatie opleveren om te begrijpen hoe en wanneer sterren en supernovae het ICM hebben verrijkt.

Dit proefschrift

Voor dit proefschrift heb ik waarnemingen met *XMM-Newton* van 44 nabijgelegen clusters, groepen en massieve elliptische sterrenstelsels (de CHEMical Enrichment Rgs Sample, of CHEERS) verzameld. De waarnemingen vertegenwoordigen in totaal een ononderbroken waarneemtijd van bijna twee maanden.

Ik ben dit proefschrift begonnen met een introductie van de verschillende onderzoeksgebieden. Daarnaast ben ik ingegaan op de meest recente vooruitgang met betrekking tot de verrijking van het ICM (**Hoofdstuk 1**). Door zowel de hoge resolutie van RGS als de normale resolutie van de EPIC instrumenten van *XMM-Newton* te gebruiken, heb ik **Hoofdstuk 2** gewijd aan de uitgebreide studie van de temperaturen en abundanties in het ICM van het cluster Abell 4059. Ik heb deze studie uitgebreid naar alle CHEERS observaties (**Hoofdstuk 3**, Fig. 3 rechts), waarvan ik de gemiddelde abundanties van 11 essentiële elementen (zuurstof, neon, magnesium, silicium, zwavel, argon, calcium, chroom, mangaan, ijzer, en nikkel) kon meten. Ik heb deze abundantiemetingen vergeleken met de voorspellingen van de beste theoretische SNIa en SNcc modellen. Zo kon ik beter begrijpen hoe SNIa exploderen en hoe massief en verrijkt de massieve sterren waren die ontploften als SNcc (**Hoofdstuk 4**). Ik heb ook veel aandacht besteed aan alle onzekerheden die mijn uiteindelijke resultaten kunnen be-



Figuur 3: Links: Een artistieke impressie van de XMM-Newton satelliet in een baan rondom de Aarde (Bronnen: ESA). Rechts: Deze figuur laat de typische emissielijnen zien die je vindt in de röntgenspectra van de centrale gebieden in het ICM (Hoofdstuk 3). Elke lijn of onopgelost lijnencomplex komt overeen met de afdruk van een specifiek zwaar element. Samen verschaffen ze een robuuste bepaling van abundanties van de elementen in het ICM.

invloeden. Ik heb met name de effecten gemeten die de laatste grote update van de spectrale code SPEX (die gebruikt wordt om de röntgenemissie van het ICM op de computer te berekenen) heeft op de gemiddelde metingen van abundanties (**Hoofdstuk 5**). Uiteindelijk kunnen ook de EPIC instrumenten aan boord van *XMM-Newton* de ruimtelijke verspreiding van verschillende elementen in het ICM meten (**Hoofdstuk 6**). Dit verschafft ons belangrijke aanwijzingen over wanneer en hoe de verrijking van het ICM plaatsvindt. De conclusies van dit proefschrift zijn divers, maar kunnen als volgt worden samengevat.

- In sommige gevallen is de verspreiding van metalen in clusters allesbehalve symmetrisch. Abell 4059 is daar een schoolvoorbeeld van omdat er dicht naast de kern van het cluster een dichte metaalrijke wolk heet gas te vinden is. Dit suggereert dat sterrenstelsels hun omgeving met metalen kunnen verrijken als zij met hoge snelheid door het ICM bewegen en door de "tegenwind" van het ICM hun gas verliezen.
- Waarschijnlijk heb ik de meest nauwkeurige metingen van abundanties in het ICM tot nu toe gedaan door lange waarnemingen van *XMM-Newton* te combineren en de onzekerheden in de meting nauwkeurig in kaart te brengen. Verdere aanzienlijke verbeteringen van

deze metingen kunnen niet worden bereikt zonder betere instrumenten aan boord van toekomstige röntgenmissies, zoals XARM of *Athena* (**Hoofdstuk 7**), of zonder een wezenlijke vermindering van systematische onzekerheden (bijvoorbeeld door een betere ijking van de *XMM-Newton* instrumenten).

- De metingen van de gemiddelde ICM abundanties die ik heb gedaan zijn waardevol als het gaat om het beter begrijpen van supernovae. Ze suggereren dat de schokgolf die SNIa explosies aandrijft zich eerst met een snelheid lager dan de geluidssnelheid uitbreidt en later in de ontploffing een supersonische snelheid bereikt. Hierna wordt al het materiaal de ruimte in geslingerd. De metingen suggereren ook dat de meeste SNcc die clusters verrijken, voortkomen uit massieve sterren die al waren verrijkt door eerdere generaties sterren. Daarnaast is het ook mogelijk dat een specifieke subgroep van SNIa (namelijk de Ca-rich gap transients, die calcium in grote hoeveelheden produceren en vrijgeven) een belangrijke rol spelen in de verrijking van clusters.

In het hete gas van clusters en groepen van sterrenstelsels die in de afgelopen honderden miljoenen jaren geen grote samensmelting met een ander cluster hebben ondervonden, is de concentratie van zuurstof, magnesium, silicium, zwavel, argon, calcium, ijzer, en nikkel op zijn hoogst in de kern van het cluster. Gemiddeld genomen lijkt de verspreiding van de metalen als functie van straal allemaal erg op elkaar. Dit suggereert dat zowel SNIa èn SNcc clusters min of meer tegelijk hebben verrijkt. Het feit dat het in vergelijking tot SNcc bij SNIa langer duurt voordat ze exploderen, betekent waarschijnlijk dat het grootste deel van het ICM verrijking plaatsvond op vroegere tijdstippen, nog voordat het het ICM bestond en het heelal nog maar een leeftijd had van enkele miljarden jaren.

English summary

Where do we come from? This question is of course very broad, as it concerns many disciplines (physics, biology, astronomy, philosophy, etc.), and it is difficult (if not impossible) to provide one clear and trivial answer. One of the most extraordinary astronomical discoveries of the 20th century, however, has revolutionised our view of the Universe regarding this question. Sixty years ago, we understood that the building blocks of planets and life have been formed in the core of stars and in their powerful end-of-life explosions, namely supernovae. In other words, we are nothing else than "stardust".

The origin of chemical elements

These elemental building blocks are named chemical elements. They assemble into molecules to form stars, planets, rock, water, ice, cells, plants, animals, etc. They are the essence of matter and life. Thanks to the remarkable work of several generations of astrophysicists, we know the basic history of the production of chemical elements in the Universe. About 13.7 billion years ago, the extreme conditions following the first minutes of the Big Bang created all the hydrogen, and almost all the helium that are present in today's Universe. However, heavier elements (or "metals", including for example carbon, nitrogen, oxygen, silicon, iron, etc.) could not have been synthesised during these first minutes. Instead, they formed in the very hot and dense core of stars and, especially when these stars explode as supernovae.

Not all supernovae are the same, and different supernovae may produce elements in different amounts. In fact, supernovae can be broadly

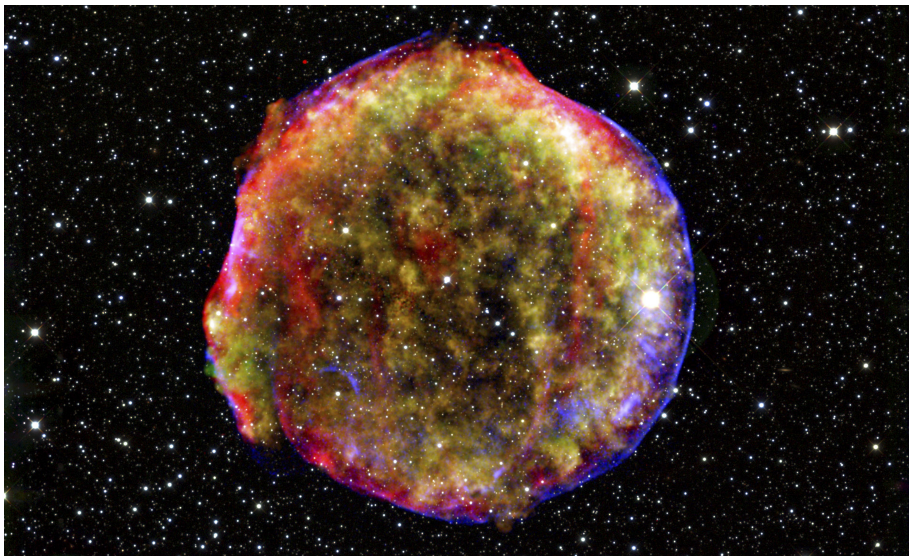


Figure 1: The Tycho supernova is a remnant of a (Type Ia) supernova whose explosion was observed in the year 1572. The remains of this former white dwarf, including a large amount of freshly produced metals, are being dispersed into the surrounding interstellar medium (Credit: NASA/SAO/CXC,JPL-Caltech/MPIA).

classified into two main categories.

1. Core-collapse supernovae (SNcc) are massive stars (more than ten times the mass of the Sun) undergoing a dramatic collapse of their core when they reach the end of their life. This results in an ultimate explosion that ejects most of the stellar material into space. The core remnant of the star becomes then either a neutron star (if the star was less than 30 times the mass of the Sun) or a black hole (if the star was more than 30 times the mass of the Sun). These supernovae are thought to produce almost all the oxygen, neon, and magnesium present in the Universe. Because the lifetime of massive stars is very short on astronomical scales (a few million years at most), these supernovae explode "quickly" relative to other stars.
2. Type Ia supernovae (SNIa) are formed in a double system of low-mass stars (less than eight times the mass of the Sun each). They are the result of the explosion of a white dwarf (the core remnant

of a low-mass star). This explosion is caused by the interaction of the white dwarf with its companion object. If that companion is a normal star, its material is progressively sucked by the white dwarf, until the temperature of the latter becomes too extreme and leads to a violent explosion. Alternatively, the companion object can be another white dwarf. In that case, the explosion may come from a violent collision between the two white dwarfs. Even today, it is unclear to astronomers which of these two scenarios is the correct one. In any case, these supernovae are thought to produce and eject heavier elements, in particular chromium, manganese, iron, and nickel. Compared to SNcc, SNIa take much more time to explode, because low-mass stars live much longer than massive stars (up to several billion years).

Intermediate elements, such as silicon, sulfur, argon, and calcium, are probably produced by SNIa and SNcc in comparable proportions. Finally, carbon and nitrogen, which are also essential for life on Earth, are thought to be produced by low- and intermediate-mass stars during their lifetime.

Nowadays, supernovae are far from being completely understood. For example, what is the precise nature of the companion of the exploding SNIa? What is the precise physical mechanism driving its explosion? Also, there are many unsolved questions left about the massive stars that turned into SNcc. How many very massive stars were typically formed with respect to less massive stars? Were these massive stars previously enriched by a former generation of stars?

The number of heavy elements produced by each supernova type are very sensitive to all these unknowns. This means that if we can measure the relative amounts, namely abundances, of all these elements in SNIa and / or SNcc, we will be able to better understand the physics and the environmental conditions of these fascinating objects (Fig. 1). However, studying the metals released by a couple of supernovae only would not give us a good picture of all the supernovae in the Universe. If we want to understand their general properties, it is necessary to zoom out to Universal scales.

From supernovae to galaxy clusters

On Universal scales, clusters of galaxies are the largest "bound" objects. In fact, galaxies are not randomly distributed in space. They are instead often found within groups (a few tens of galaxies) or larger clusters (100 to 1000

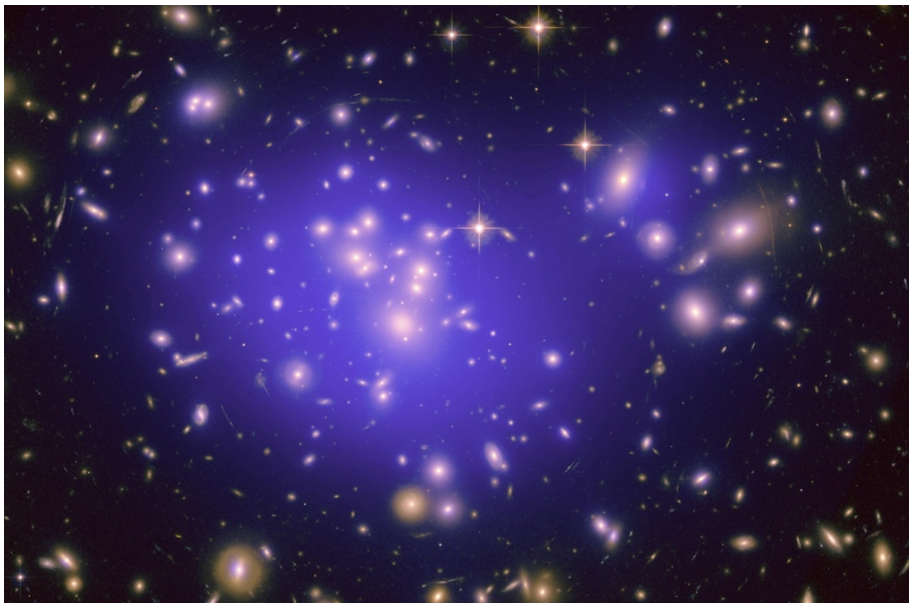


Figure 2: The galaxy cluster Abell 1689. At optical wavelengths (here in yellow), the individual galaxies can be seen. However, most of the "normal" matter of the cluster is present in the form of a hot gas, visible in X-ray (here in purple). This gas is also rich in metals, which are produced by SNIa and SNcc over the last billion years (Credit: NASA, ESA, E. Jullo, P. Natarajan, and J-P. Kneib).

galaxies). All the stars, planets, and the interstellar gas and dust belonging to the galaxies accounts for only 10 to 20 percent of the total visible (or "normal") matter in a galaxy cluster. The major "normal" component of galaxy clusters is, in fact, in the form of a very hot, diffuse gas. Because of the very large gravity in clusters, this intra-cluster medium (ICM) falls rapidly towards the centre, interacts and collides with itself, and is thus heated up to 10 to 100 million degrees. This extreme heating makes that gas visible in X-ray light (Fig. 2). The most recent generation of X-ray satellites, in particular the European mission *XMM-Newton* (Fig. 3 left), is well suited to observe the ICM and study its properties via X-ray spectroscopy.

What is X-ray spectroscopy?

Like many other telescopes on Earth or in orbit around the Earth, the current X-ray space telescopes can do much more than simply "see" astrophysical sources in the sky. Exactly like a rainy cloud is able to decompose sunlight into a wide range of colours (or more specifically, wavelengths), the instruments onboard the most recent X-ray satellites are able to decompose the X-ray light coming from the hot ICM. By analysing the relative amounts of all these X-ray "colours" we get (in other words, what its X-ray spectrum looks like), we can determine various features of that gas, such as its temperature or its density.

Metals in the hot intra-cluster medium

About forty years ago, astronomers discovered the presence of emission lines in the X-ray spectra of this intra-cluster gas. These emission lines are a characteristic imprint of the presence of heavy elements. This means that the ICM contains a significant fraction of metals. Since only supernovae can produce heavy elements, these metals must originate from SNIa and SNcc within the individual galaxies. Metals are thus not only located in the vicinity of supernovae, but also in the ICM, beyond galaxies. In other words, even the largest scales of the Universe are chemically enriched by stars and supernovae.

Luckily, the X-ray emission of the ICM is easy to model with computers, and the metal abundances of this gas can be accurately measured, by analysing their corresponding lines in the X-ray spectra of galaxy clusters (Fig. 3 right). In turn, because they trace the total yields of billions of supernovae over cosmic times, the abundances of these elements measured in the ICM can be directly compared to the yields predicted by the currently competing SNIa and SNcc theoretical models. This helps to favour some specific scenarios for supernovae, and to rule out some others. Eventually, measuring the amount of metals in galaxy clusters enables us to better understand supernovae.

How about the spatial distribution of these metals in galaxy clusters? Are they concentrated rather in the core of clusters, or rather in the outskirts? Are they distributed uniformly through the intra-cluster gas, or are they present in some specific regions only? Answering these questions may provide valuable information to understand how and when stars and su-

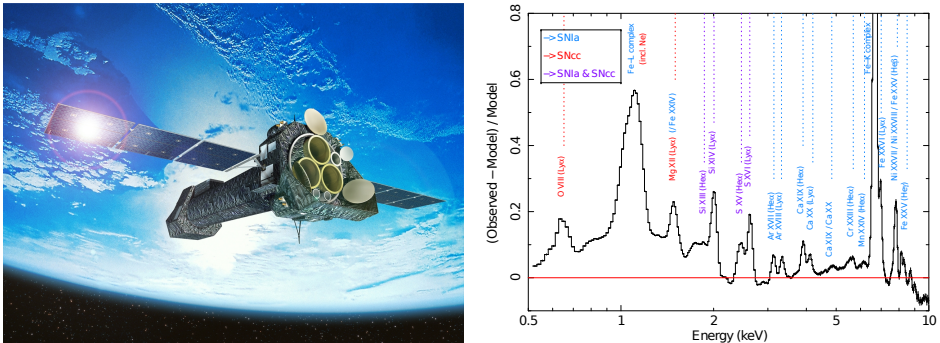


Figure 3: *Left:* Artist impression of the *XMM-Newton* satellite in orbit around the Earth (Credit: ESA). *Right:* This plot shows the typical emission lines that can be found in the X-ray spectra of the central ICM regions (Chapter 3). Each line, or unresolved line complex, corresponds to the imprint of a specific heavy element. Together, they provide a robust determination of the abundances of these elements in the ICM.

pernovae enriched the ICM.

This thesis

In this thesis, I have compiled the *XMM-Newton* observations of 44 nearby and relaxed galaxy clusters, groups, and giant ellipticals (the CHEMical Enrichment Rgs Sample, or CHEERS). These observations represent a total of almost two months of uninterrupted observing time.

I have started by summarising our current knowledge of the ICM enrichment, as well as the most recent progress achieved in this field of research (**Chapter 1**). Using both the high-resolution RGS and the moderate resolution EPIC instruments on board *XMM-Newton*, I have devoted **Chapter 2** to the extensive study of the temperature and abundances in the ICM of one galaxy cluster, Abell 4059. I have extended this study to the whole CHEERS sample (**Chapter 3**, Fig. 3 right), for which I could measure the average abundances of 11 key elements (oxygen, neon, magnesium, silicon, sulfur, argon, calcium, chromium, manganese, iron, and nickel). I have compared these abundance measurements to the yields predicted by the best SNIa and SNcc theoretical models, in order to better understand how SNIa explode, and how massive and enriched were the massive stars that gave birth to SNcc (**Chapter 4**). I have also devoted a lot of attention to

all the uncertainties that may affect the final results. In particular, I have investigated the effects that the latest major update of the spectral code SPEX, which is used to model the X-ray emission of the ICM, has on the average abundance measurements (**Chapter 5**). Finally, the EPIC instruments on board *XMM-Newton* also allow for a study of the radial distribution of the different elements in the ICM (**Chapter 6**). In turn, this provides important clues on the main epoch and the dynamics driving the ICM enrichment. The conclusions of this thesis are various, but can be summarised as follows.

- In some cases, the metal distribution in galaxy clusters is far from being symmetric. Abell 4059 is a textbook example, where a dense, metal-rich region of the hot gas is found outside of the cluster centre. This suggests that galaxies can enrich their surroundings with metals when they travel so fast that their gas gets stripped by the ambient ICM pressure.
- I have probably obtained the most accurate ICM abundance measurements that are ever possible to obtain with *XMM-Newton*. Further significant improvements of these measurements cannot be achieved without better instruments on board future X-ray missions, such as *XARM* or *Athena* (**Chapter 7**), or without a substantial reduction of the systematic uncertainties (for example a better calibration of the *XMM-Newton* instruments).
- The average ICM abundance measurements I have obtained are valuable to better understand supernovae. In particular, they suggest that the burning flame driving SNIa explosions propagates first below the speed of sound, then reaches a supersonic speed before ejecting the stellar material into space. They also suggest that most of the SNcc having enriched galaxy clusters come from massive stars that had been already enriched by a former generation of stars. Finally, it is possible that a specific sub-class of SNIa, namely the Ca-rich gap transients, which produce and release calcium in very large quantities, play an important role in enriching galaxy clusters.
- In the hot gas of relaxed galaxy clusters and groups, the radial distribution of oxygen, magnesium, silicon, sulfur, argon, calcium, iron, and nickel are all peaked: there is more of these metals in the centre than in the outskirts of clusters. On average, these profiles are all very

similar to each other. This strongly suggests that both SNIa and SNcc enrich clusters in a very similar way. Given that SNIa take longer to explode than SNcc, this probably means that the bulk of the ICM enrichment occurred at early times, before the Universe was half of its current age.

Résumé en français

D'où venous-nous? Cette question est bien-sûr très vaste puisqu'elle concerne de nombreuses disciplines (physique, biologie, astronomie, philosophie, etc.), et il est difficile (sinon impossible) d'y apporter une seule et même réponse. Une des plus extraordinaires découvertes astronomiques du XX^e siècle a pourtant révolutionné notre conception de l'Univers par rapport à cette question. Il y a soixante ans, on a compris que les briques élémentaires essentielles à la formation des planètes et de la vie ont été forgées au coeur même des étoiles, et dans la puissante explosion qu'elles générèrent à la fin de leur vie: les supernovae. Finalement, nous ne sommes rien d'autre que des "poussières d'étoiles".

L'origine des éléments chimiques

Ces briques élémentaires sont appelées les éléments chimiques. Elles s'assemblent en molécules pour ensuite former les étoiles, les planètes, la roche, l'eau, les cellules, les plantes, les animaux, etc. Elles sont l'essence même de la matière et de la vie. Grâce au travail remarquable de plusieurs générations d'astrophysiciens au cours des dernières décennies, nous connaissons l'histoire de la production des éléments chimiques dans l'Univers. Il y a environ 13.7 milliards d'années, les conditions extrêmes qui suivirent les premières minutes du Big Bang ont créé tout l'hydrogène et presque tout l'hélium que l'on retrouve aujourd'hui dans le Cosmos. Par contre, les éléments plus lourds (ou "métaux", par exemple le carbone, l'azote, l'oxygène, le silicium, le fer, etc.) n'ont pas pu se former lors de ces premières minutes. Ces métaux sont en fait fabriqués dans la dense et bouillonnante fournaise du coeur des étoiles, et en particulier lorsque ces étoiles

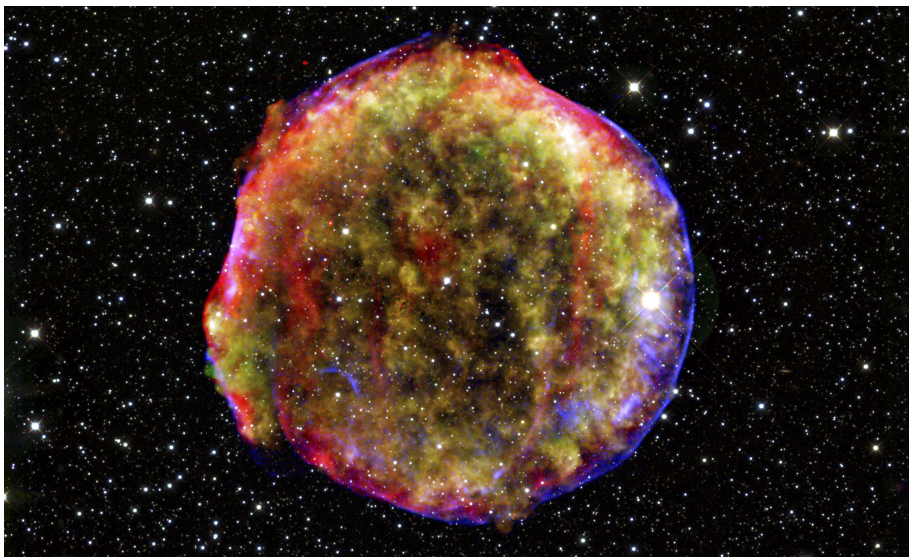


Figure 1: La supernova de Tycho est un rémanent de supernova (de Type Ia) dont l'explosion fut observée depuis la Terre en 1572. Les vestiges de cette ancienne naine blanche, parmi lesquels une énorme quantité de métaux fraîchement créés, se dispersent actuellement dans son milieu interstellaire environnant. (Crédits: NASA/ESA).

explosent en supernovae.

Bien-sûr, les supernovae ne sont pas toutes identiques, et différents types de supernovae peuvent produire des éléments chimiques en quantités très variées. En général, on peut regrouper les supernovae en deux grandes catégories.

1. Les supernovae à effondrement de coeur (ou "core-collapse"; SNcc) sont des étoiles massives (plus de dix fois la masse du Soleil) qui sont soumises à un brusque effondrement de leur coeur lorsqu'elles arrivent à la fin de leur vie. Cet effondrement donne naissance à une formidable et ultime explosion qui éjecte la plus grande partie de la matière de l'étoile dans l'espace. Le coeur restant de l'étoile devient alors une étoile à neutrons (si l'étoile était plus légère que 30 fois la masse du Soleil) ou un trou noir (si l'étoile était plus lourde que 30 fois la masse du Soleil). Les modèles actuels prédisent que les SNcc ont produit presque tout l'oxygène, le néon, et le magnésium présents dans l'Univers. Puisque la durée de vie d'une étoile massive est rel-

ativement courte à l'échelle cosmique (quelques millions d'années tout au plus), ces supernovae explosent "rapidement" par rapport aux autres étoiles.

2. Les supernovae de Type Ia (SNIa) se forment à partir d'un système double, constitué de deux étoiles de faible masse (moins de huit fois la masse du Soleil). Ces supernovae correspondent en fait à l'explosion dévastatrice d'une naine blanche (le cadavre stellaire d'une étoile de faible masse). Cette explosion est causée par l'interaction de cette naine blanche avec son astre compagnon. Si ce compagnon est une étoile normale, sa matière est progressivement aspirée par la naine blanche, jusqu'à ce que la température de cette dernière devienne trop extrême et mène à une violente explosion. Le compagnon pourrait également être une autre naine blanche. Dans ce cas, l'explosion pourrait résulter d'une violente collision entre les deux naines blanches du système. Encore aujourd'hui, les astronomes ne savent pas lequel de ces deux scénarios est le bon. Quoi qu'il en soit, ces supernovae produisent et éjectent des éléments plus lourds, en particulier du chrome, du manganèse, du fer, et du nickel. Comparées aux SNcc, les SNIa prennent beaucoup plus de temps à exploser, car les étoiles de faible masse dont elles sont issues vivent beaucoup plus longtemps que les étoiles massives (de l'ordre de plusieurs milliards d'années).

Les éléments chimiques intermédiaires, tels que le silicium, le soufre, l'argon, et le calcium, sont probablement produits par les SNIa et les SNcc dans des proportions comparables. Enfin, le carbone et l'azote, si indispensables à la vie sur Terre, sont produits par les étoiles de masse faible et/ou intermédiaire au cours de leur vie.

De nos jours, les supernovae sont encore très loin d'être comprises. Par exemple, quelle est la nature précise de l'astre compagnon d'une SNIa? Et quel est le mécanisme physique précis qui régit une telle explosion? De plus, il reste beaucoup de questions non résolues quant aux étoiles massives qui ont engendré les SNcc que l'on observe aujourd'hui. Combien d'étoiles très massives ont typiquement été formées par rapport aux étoiles moins massives? Ces étoiles massives ont-elles été, elles aussi, préalablement enrichies en métaux par une génération antérieure d'étoiles?

Le nombre d'éléments chimiques lourds produits dans chaque type de supernova est très sensible à toutes ces inconnues. Cela signifie que si l'on peut mesurer les quantités relatives — ou abondances — de tous ces élé-

ments dans les SNIa et / ou les SNcc, on sera à même de mieux comprendre la physique et les conditions environnementales de ces objets fascinants (Fig. 1). Cependant, étudier des métaux libérés par quelques supernovae bien connues ne nous permet pas d'avoir pas une vue d'ensemble de toutes les supernovae dans le Cosmos. Si l'on veut comprendre leur propriétés d'un point de vue général, il est nécessaire de contempler l'Univers à ses plus grandes échelles.

Des supernovae aux amas de galaxies

À l'échelle de l'Univers, les amas de galaxies sont les plus larges objets retenus par leur propre gravité. En fait, les galaxies ne sont pas distribuées de manière aléatoire dans l'espace. Elles sont, au contraire, souvent observées faisant partie de groupes (quelques dizaines de galaxies) ou de plus larges amas (de 100 à 1000 galaxies). Toutes les étoiles, planètes, et les poussières et gaz interstellaires appartenant aux galaxies ne représentent que 10 à 20 pourcent de la matière visible (ou "normale") totale d'un amas. La plus grande partie de la matière "normale" dans les amas de galaxies se trouve en fait sous la forme d'un gaz extrêmement chaud et diffus. En raison du pouvoir d'attraction gravifique très important des amas, ce milieu intra-amas "tombe" rapidement vers le centre, interagit et entre en collision avec lui-même, et se retrouve alors chauffé à des températures de l'ordre de 10 à 100 millions de degrés. Ce chauffage intense rend ce gaz visible en rayons X (Fig. 2). La plus récente génération des télescopes spatiaux à rayons X, en particulier la mission européenne *XMM-Newton* (Fig. 3 gauche), est taillée sur mesure pour observer le milieu intra-amas, et pour étudier ses propriétés par le biais de la spectroscopie à rayons X.

Qu'est-ce que la spectroscopie à rayons X?

À l'instar de nombreux autres télescopes au sol ou en orbite autour de la Terre, les télescopes spatiaux à rayons X utilisés aujourd'hui font bien davantage que simplement "voir" des sources astrophysiques dans le ciel. Tout comme un nuage de pluie est capable de décomposer la lumière du soleil en un large panel de couleurs (ou, plus précisément, de longueurs d'ondes), les instruments à bord des plus récents satellites à rayons X sont capables de décomposer la lumière provenant du gaz intra-amas. En analysant

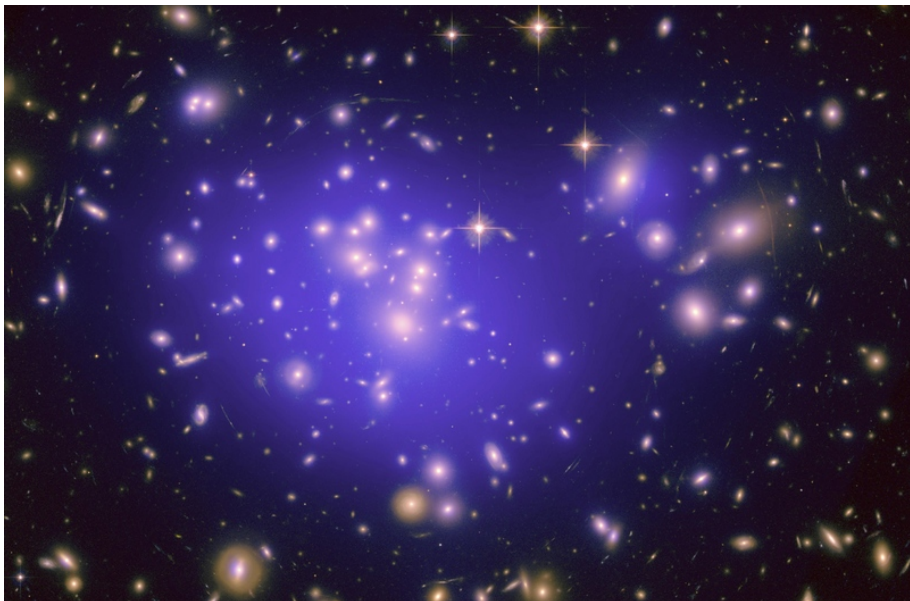


Figure 2: L'amas de galaxies Abell 1689. Les galaxies individuelles peuvent être vues en lumière optique (ici en jaune). Cependant, la plupart de la matière "normale" de l'amas est présente sous la forme d'un gaz très chaud, visible uniquement en rayons X (ici en mauve). Ce gaz est, en outre, riche en métaux, eux-mêmes produits par les SNIa et les SNcc des galaxies durant des milliards d'années (Crédits: NASA, ESA, E. Jullo, P. Natarajan, and J-P. Kneib).

les intensités relatives de toutes les "couleurs" que l'on obtient en rayons X (ou, en d'autres mots, à quoi ressemble son spectre à rayons X), on peut déterminer des propriétés intéressantes de ce gaz (par exemple sa température ou sa densité).

Des métaux dans le milieu intra-amas

Il y a quarante ans, les astronomes découvrirent la présence de raies en émission dans les spectres à rayons X de ce gaz. Ces raies en émission sont en fait caractéristiques de la présence d'éléments lourds. Cela signifie que le milieu intra-amas contient une fraction non-négligeable de métaux. Puisque seules les supernovae sont capables forger ces éléments lourds, ces derniers doivent provenir des SNIa et SNcc qui ont explosé au sein des galaxies de l'amas. Les métaux ne se retrouvent donc pas uniquement

autour des supernovae, ils sont au contraire capables de s'échapper des galaxies et de finir leur course dans le milieu intra-amas. Autrement dit, même les plus grandes échelles de l'Univers sont enrichies chimiquement par les étoiles et les supernovae.

Fort heureusement, l'émission en rayons X du milieu intra-amas est relativement facile à modéliser par ordinateur. Les abondances en métaux de ce gaz peuvent donc être mesurées de manière très précise en observant les spectres à rayons X des amas de galaxies (Fig. 3 droite). À leur tour, parce qu'elles sont la signature des produits de l'explosion de milliards de supernovae tout au long de l'histoire de l'Univers, les abondances de ces éléments mesurées dans le gaz intra-amas peuvent être directement comparées aux abondances prédictes par les modèles théoriques de SNIa et de SNcc qui sont actuellement proposés au sein de la communauté astronomique. Une telle comparaison permet de favoriser certains scénarios de formation des supernovae, et d'en écarter d'autres. Au final, et pour résumer, mesurer la quantité de métaux dans les amas de galaxies nous aiderait à mieux comprendre les supernovae.

Qu'en est-il de la répartition précise des métaux à travers les amas de galaxies? Sont-ils concentrés au centre des amas, ou en périphérie? Se répartissent-ils de manière uniforme partout dans le gaz intra-amas, ou ne sont-ils présents que dans certaines zones spécifiques? Répondre à ces questions nous fournirait des informations essentielles pour comprendre quand et comment les étoiles et les supernovae ont enrichi le milieu intra-amas.

Cette thèse

Dans cette thèse, j'ai collecté les observations de 44 amas de galaxies, groupes de galaxies, et galaxies elliptiques géantes, obtenues par télescope spatial *XMM-Newton* (le "CHEMical Enrichment Rgs Sample", ou CHEERS). Ces observations représentent un total de presque deux mois de temps d'observation ininterrompu.

J'ai commencé par résumer nos connaissances actuelles sur l'enrichissement du milieu intra-amas, ainsi que les récents progrès accomplis dans ce domaine de recherche (**Chapitre 1**). En utilisant à la fois l'instrument à haute résolution RGS et celui à résolution plus modérée EPIC, tous deux à bord du satellite *XMM-Newton*, j'ai consacré le **Chapitre 2** à l'étude extensive des températures et des abondances dans le gaz très chaud d'un amas

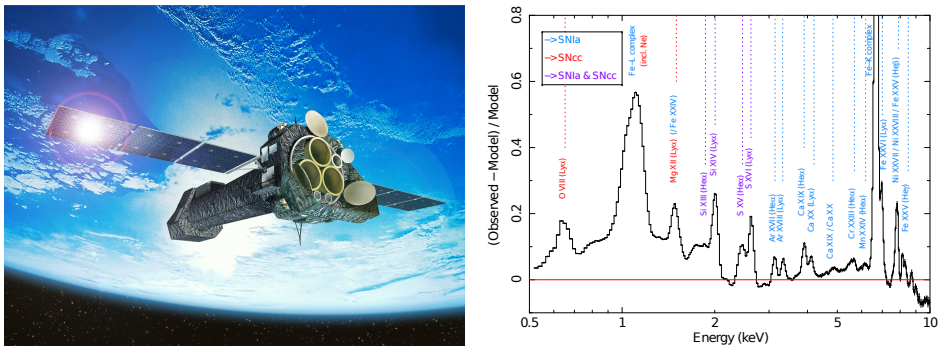


Figure 3: *Gauche:* Impression d'artiste du satellite *XMM-Newton* en orbite autour de la Terre (Crédits: ESA). *Droite:* Cette figure montre les raies en émission typiques qui peuvent être détectées au sein du gaz intra-amas. Chaque raie, ou complexe de raies non résolues par le télescope, correspond à la signature d'un élément lourd spécifique. Prises dans leur ensemble, ces raies permettent une mesure robuste des abondances de ces éléments dans le milieu intra-amas (Chapitre 3).

bien particulier, Abell 4059. J'ai ensuite étendu cette étude à l'ensemble des observations CHEERS (Chapitre 3, Fig. 3 droite), pour lesquelles j'ai pu mesurer les abondances moyennes de 11 éléments chimiques clés (oxygène, néon, magnésium, silicium, soufre, argon, calcium, chrome, manganèse, fer, et nickel). J'ai comparé ces abondances aux quantités d'éléments chimiques prédites par les meilleurs modèles théoriques de SNIa et de SNcc, afin de mieux comprendre comment explosent les SNIa, et combien massives et riches en métaux sont les étoiles qui donnent naissance aux SNcc (Chapitre 4). J'ai aussi accordé beaucoup d'attention à toutes les incertitudes qui pourraient affecter ces résultats. En particulier, j'ai exploré les effets que la dernière mise à jour du code spectral SPEX, utilisé pour reproduire par ordinateur l'émission à rayons X du milieu intra-amas, produit sur les abondances moyennes que j'ai mesurées (Chapitre 5). Enfin, l'instrument EPIC permet aussi d'étudier la distribution des différents éléments chimiques du milieu intra-amas (Chapitre 6). Cela fournit des indices précieux sur l'époque principale et la dynamique ayant régi l'enrichissement du milieu intra-amas. Les conclusions de cette thèse sont variées, mais peuvent être résumées comme suit.

- Dans certains cas, la distribution des métaux dans les amas de galaxies est loin d'être parfaitement symétrique. Abell 4059 en est un exemple.

ple typique, où une région dense et riche en métaux est observée en dehors du centre de l'amas. Cela suggère que les galaxies peuvent enrichir leurs environs en métaux lorsqu'elles voyagent tellement vite que leur gaz s'arrache sous l'effet de la pression du milieu intra-amas environnant.

- J'ai probablement obtenu les mesures d'abondances du milieu intra-amas les plus précises qu'il soit jamais possible d'obtenir avec les télescopes spatiaux actuels. Des améliorations de ces mesures ne peuvent être atteintes sans de meilleurs instruments à bord de futures missions à rayons X, telles que XARM ou *Athena* (**Chapitre 7**), ou sans une réduction drastique des incertitudes systématiques (par exemple via une meilleure calibration des instruments de *XMM-Newton*).
- Les mesures moyennes d'abondances du gaz intra-amas que j'ai obtenues sont précieuses pour mieux comprendre les supernovae. En particulier, elles suggèrent que la déflagration qui se propage lorsqu'une SNIa explose se déplace d'abord à une vitesse raisonnable — en dessous de la vitesse du son, ensuite s'accélère et atteint des vitesses superpersoniques avant d'éjecter sa matière dans l'espace. Mes résultats suggèrent aussi que la plupart des SNcc qui ont enrichi les amas de galaxies proviennent d'étoiles massives qui avaient déjà été auparavant enrichies par une précédente génération d'étoiles. Pour finir, il est possible qu'une sous-classe spécifique de SNIa, les "Ca-rich gap transients", qui fabriquent et éjectent du calcium en très grandes quantités, jouent un rôle important dans l'enrichissement des amas de galaxies.
- Dans le gaz chaud des amas et groupes de galaxies, les distributions radiales de l'oxygène, du magnésium, du silicium, du soufre, de l'argon, du calcium, du fer, et du nickel sont toutes piquées: il y a bien plus de métaux dans le centre des amas qu'en périphérie. En moyenne, ces profils sont très semblables les uns par rapport aux autres. Cela suggère fortement que les SNIa et les SNcc enrichissent toutes deux le milieu intra-amas de manière très similaire. Étant donné que les SNIa mettent plus de temps à exploser que les SNcc, cela implique probablement que la majeure partie de cet enrichissement a eu lieu en des temps très lointains, avant même que l'Univers n'atteigne la moitié de son âge actuel.

Curriculum Vitae

I was born on June 27, 1989, in Uccle (in Dutch, "Ukkel"), one of the 19 municipalities of Brussels, in Belgium. Except for a period of two or three years (which I barely remember), in which we moved to a small town named Hannut, I spent almost the 20 first years of my life in Brussels. It was during my primary school (Le Jardin des Écoliers), after a class on the Solar System (and on the mysteries of Pluto, which was still a planet at that time, and for which we had no picture yet) that I naively decided to become an astronomer. I did my secondary studies at the Lycée Émile Jacqmain, where I graduated in "Latin-mathematics" in 2007 (cum laude). During those years, I regularly attended astronomy camps in Modave, where my interest for astronomy and astrophysics kept growing.

I did my Bachelor degree in physics at the Université Libre de Bruxelles, where I graduated in 2010 (cum laude). My Bachelor project was focused on the observation of variable stars using the telescope of the university, and was supervised by Sophie Van Eck. I finally left my home town in 2010, when I started my Master degree in space sciences at the University of Liège. On that time, I developed a strong interest for high-energy astrophysics on one hand, and extragalactic astrophysics on the other hand. I did my Master thesis with Gregor Rauw on the X-ray emission of massive stars in the M 17 nebula as observed by *XMM-Newton*. After my graduation in 2012 (magna cum laude), I stayed four more months at the University of Liège to work with Thierry Morel on optical observations of the massive star ζ Puppis. I devoted the next few months to tutor high school students in mathematics, physics, and chemistry before I moved to the Netherlands in June 2013 to start my PhD.

This thesis summarises the results of my PhD project, and on which I

worked both at SRON (Utrecht) and Leiden Observatory with Jelle Kaasstra and Jelle de Plaa. During these four years, I had the opportunity to present my work at several conferences and workshops, in Dublin (Ireland), Tokyo (Japan), Sexten (Italy), Madrid (Spain), Paris (France), and Beijing (China). I was also the lucky laureate of the "poster prize" of the 71st Dutch Astronomy Conference in Nunspeet (The Netherlands) in 2016. I spent a few weeks of my PhD to visit colleagues in other institutes: Yu-Ying Zhang, Lorenzo Lovisari, Thomas Reiprich, and Gerrit Schellenberger (Argelander-Institut für Astronomie, Bonn, Germany), as well as Norbert Werner (MTA-Eötvös University Lendület Hot Universe Research Group, Budapest, Hungary), with whom I will work as a postdoc from September 2017. From the first years of my academic studies up to now, I occasionally go back to Modave, this time as a "teacher", to share my knowledge of astronomy with younger students (with the secret hope they will want to become astronomer, too).

List of publications

First author publications

- **Mernier, F.**, de Plaa, J., Kaastra, Raassen, A. J. J., Gu, L., Mao, and Urdampilleta, I.
Origin of central abundances in the hot intra-cluster medium - III. The impact of spectral model improvements on the abundance ratios
2017, A&A, submitted (this thesis, Chapter 5)
- **Mernier, F.**, de Plaa, J., Kaastra, J. S., Zhang, Y.-Y., Akamatsu, H., Gu, L., Kosec, P., Mao, J., Pinto, C., Reiprich, T. H., Sanders J. S., Simionescu, A., and Werner, N.
Radial metal abundance profiles in the intra-cluster medium of cool-core galaxy clusters, groups, and ellipticals
2017, A&A, in press (this thesis, Chapter 6)
- **Mernier, F.**, de Plaa, J., Pinto, C., Kaastra, J. S., Kosec, P., Zhang, Y.-Y., Mao, J., Werner, N., Pols, O. R., and Vink, J.
Origin of central abundances in the hot intra-cluster medium - II. Chemical enrichment and supernova yield models
2016b, A&A, **595**, A126 (this thesis, Chapter 4)
- **Mernier, F.**, de Plaa, J., Pinto, C., Kaastra, J. S., Kosec, P., Zhang, Y.-Y., Mao, J., and Werner, N.
Origin of central abundances in the hot intra-cluster medium - I. Individual and average abundance ratios from XMM-Newton EPIC
2016a, A&A, **592**, A157 (this thesis, Chapter 3)
- **Mernier, F.**, de Plaa, J., Lovisari, L., Pinto, C., Zhang, Y.-Y., Kaastra, J. S., Werner, N., and Simionescu, A.

Co-author publications

- Mao, J., de Plaa, J., Kaastra, J. S., Pinto, C., Gu, L., **Mernier, F.**, Hong-Liang, Y., Zhang, Y.-Y., and Akamatsu, H.
Nitrogen abundance in X-ray halos of clusters and groups of galaxies
2017, A&A, submitted
- Albert, J. G., Sifón, C., Stroe, A., **Mernier, F.**, Intema, H. T., Röttgering, H. J. A., Brunetti, G.
Complex Diffuse Emission in the z=0.52 Cluster PLCK G004.5-19.5
2017, A&A, submitted
- de Plaa, J., Kaastra, J. S., Werner, N., Pinto, C., Kosec, P., **Mernier, F.**, Lovisari, L., Akamatsu, H., Schellenberger, G., Hofmann, F., Reiprich, T. H., Finoguenov, A., Ahoranta, J., Sanders, J. S., Fabian, A. C., Pols, O. R., Simionescu, A., Vink, J., and Böhringer, H.
CHEERS: The chemical evolution RGS sample
2017, A&A, submitted
- Akamatsu, H., Fujita, Y., Akahori, T., Ishisaki, Y., Hayashida, K., Hoshino, A., **Mernier, F.**, Yoshikawa, K., Sato, K., and Kaastra, J. S.
Properties of the cosmological filament between two clusters: A possible detection of a large-scale accretion shock by Suzaku
2017, A&A, in press
- de Plaa, J., and **Mernier, F.**
CHEERS: Future perspectives for abundance measurements in clusters with XMM-Newton
2017, Astron. Nachr., in press
- Akamatsu, H., Gu, L., Shimwell, T., **Mernier, F.**, Mao, J., Urdampilleta, I., de Plaa, J., Röttgering, H. J. A., and Kaastra, J. S.
Suzaku and XMM-Newton observations of the newly discovered early-stage cluster merger 1E2216.0-0401 and 1E2215.7-0404
2016, A&A, 593, L7
- Ichinohe, Y., Werner, N., Simionescu, A., Allen, S. W., Canning, R. E. A., Elhert, S., **Mernier, F.**, and Takahashi, T.
The growth of the galaxy cluster Abell 85: mergers, shocks, stripping and seeding of clumping
2015, MNRAS, 448, 2971

Acknowledgements

Here we are: the end of four rich and exciting years spent at both Leiden observatory and SRON, but also full of great moments outside work. Writing the "acknowledgements" part of this manuscript is rather easy (because this thesis would not have been possible without the valuable help of so many people), and at the same time rather difficult (because I must take care of not forgetting anyone to thank).

First of all, this thesis was made possible thanks to Jelle de Plaa, who successfully obtained most of the very deep *XMM-Newton* data analysed here, and who built the entire CHEERS project. But far beyond that, Jelle was always available and ready to help me, from the very first days to the very last steps of my PhD thesis. I will never be grateful enough for all the expertise I have learned from him. Thank you Jelle! One Jelle may hide another, and I'm also very grateful to Jelle Kaastra for all his useful scientific and non-scientific advice, as well as for his constant optimism and support throughout these four years.

To become a doctor, you first need to get a PhD position. This requires two ingredients: (i) a deep passion for astronomy and (ii) people who greatly support you and recommend you. This is why I deeply thank: (i) my high school physics teacher Albert Friadt and all the members of the association "Jeunesse et Science" for having made me an astro-addict, and (ii) Gregor Rauw, Yaël Nazé, Thierry Morel, and Michaël De Becker for all their help and support during my Master thesis and during my search for a PhD position.

A PhD thesis is nothing either without excellent collaborators. It was a pleasure for me to work with Hiroki, Junjie, Igone, Liyi, and Ton as great colleagues within the cluster group at SRON. I also enjoyed working with

the whole CHEERS collaboration, in particular Yu-Ying (to the memory of whom I would like to dedicate most of the chapters of this thesis), Ciro, Norbert (I'm looking forward to starting my postdoc in your group!), Aurora, Lorenzo, Yuto, Thomas, Jeremy, Florian, Onno, Jacco, Peter, and Gerriet. All these friendly colleagues (and many more I may have forgotten) helped me to learn about chemical enrichment in clusters, but also about other fascinating aspects of cluster physics in general. I also had very nice discussions with cluster people from Leiden, and I would like to thank Huub, Jit, Huib, Josh, Tim, Duy, Francesco, Andra, Jeroen, and Raymond. Igone, let me thank you once more for having helped me to organise the cluster meetings. You brought awesome ideas to make these meetings attractive and convivial! Finally, I really appreciated the availability and amiability of the supporting staff in Leiden: thanks a lot to Evelijn, Els, Erik, Eric, Alexandra, Marjan, Caroline, Anita, and Liesbeth for your assistance!

A nice advantage of doing a PhD in two different places is that the number of awesome colleagues and friends increases by a factor of 2. Thanks to the "followers of evolutionism" (they will recognise themselves), and to Marianne, Tullio, Laura, Zuzanna, Missagh, Lucien, Wim, Jean, Cor, Esther, Elisa, Theo, Jan-Willem, and all the other Astro-U members for the great and dynamical atmosphere you bring every day to SRON. Besides, I've been very lucky to be part of one of the weakest indoor football teams that have ever existed. However, nothing is impossible. From "Village Bike FC" to "The Supermassive Black Goals" (via "WTFITDMYT FC"), we managed to greatly improve our level, and to win two trophies (including one that was not just to eat)! For all those great moments, thanks a lot to all of you, team mates: Emanuele, Clément, Jit (again!), Sasha, Ahmad, Christos, Pedro, Santiago, Duy (again!), Zanjar, Fabian, Iulian, and Andrea. Clément: le foot, les débats politiques, les discussions sur l'émission radio des galaxies elliptiques géantes, les pauses café, et les borrels auraient été bien fades sans toi. Merci pour tout, et bonne suite pour ton futur postdoc! Also thanks to Darko, Edwin, David, Aayush, Mieke, Andrej, Ricardo, Valeriya, Andrew, Tomasso, Nico, and Eleonora for the friendly moments you brought in the Kaiser Lounge and outside of the observatory.

Finally, the huge amount of work that a PhD thesis represents would be impossible to achieve without a strong support from friends and family. A huge thanks to all my friends, who are disseminated between Brussels, Liège, and the Netherlands! Lieselot, if these last four years have been the happiest ones in my life, it's thanks to you. Thank you for having ac-

accompanied me and supported me during this great adventure! Whatever will happen in the months / years to come, remember that I will be always there for you. Also, my "Nederlandse samenvatting" would have looked so ridiculous without your valuable help to translate it. Thank you so much for this as well! Le dernier mot de remerciement sera pour ma famille. Lise, il n'est jamais trop tard pour arrêter ton cinéma et faire de l'astronomie! Paul, un doctorat, ça vaut pas un fifa! Enfin, je termine cette thèse comme je l'ai commencée, en la dédiant à mes parents. On dit souvent qu'on ne choisit pas sa famille, mais qu'est-ce que je suis chanceux de vous avoir! Je ne vous remercierai jamais assez pour votre soutien inconditionnel depuis toujours, en particulier durant ces quatre dernières années... et pour toutes celles à venir.

